

---

---

# Fc Antigen-Binding Fragment- Drug Conjugates as Novel Antibody-Based Format for Targeted Drug Delivery



TECHNISCHE  
UNIVERSITÄT  
DARMSTADT

**vom Fachbereich Chemie  
der Technischen Universität Darmstadt**

zur Erlangung des Grades  
Doctor rerum naturalium  
(Dr. rer. nat.)

**genehmigte Dissertation  
von Sebastian Michael Jäger, M.Sc.**

Erstgutachter: Prof. Dr. Harald Kolmar  
Zweitgutachter: Prof. Dr. Dr. Siegfried Neumann

Darmstadt 2022

---

---

Jäger, Sebastian Michael

***Fc Antigen-Binding Fragment-Drug Conjugates  
as Novel Antibody-Based Format for Targeted Drug Delivery***

Darmstadt, Technische Universität Darmstadt

Tag der Einreichung: 16. November 2021

Tag der mündlichen Prüfung: 17. Januar 2022

Jahr der Veröffentlichung der Dissertation auf TUpriints: 2022

Lizenz: Veröffentlicht unter CC BY 4.0 International

URN: urn:nbn:de:tuda-tuprints-203609

URL: <https://tuprints.ulb.tu-darmstadt.de/id/eprint/20360>

---

---

Die vorliegende Arbeit wurde unter der Leitung von Herrn Prof. Dr. Harald Kolmar am Clemens-Schöpf-Institut für Organische Chemie und Biochemie der Technischen Universität Darmstadt sowie bei der Merck KGaA in Darmstadt von Januar 2018 bis Januar 2021 angefertigt.

---

---

## Publications or patents derived from the presented work

Parts of this work have been published.

**Jäger S.**, Wagner T.R., Rasche N., Kolmar H., Hecht S., Schröter C. (2021) Generation and Biological Evaluation of Fc Antigen Binding Fragment-Drug Conjugates as a Novel Antibody-Based Format for Targeted Drug Delivery. *Bioconjugate Chem.* **32**, 1699 – 1710.

**Jäger S.**, Dickgiesser S., Tonillo J., Hecht S., Kolmar H., Schröter C. (2021) EGFR Binding Fc Domain-Drug Conjugates: Stable and Highly Potent Cytotoxic Molecules Mediate Selective Cell Killing. *Biol. Chem.*, doi: 10.1515/hsz-2021-0321, *ahead of print*.

**Jäger S.**, Schröter C. (2021) HER2 targeting Fc antigen binding fragment-drug conjugates, European Patent Application EP 21 171 859.8

**Jäger S.**, Schröter C. (2021) EGFR targeting Fc antigen binding fragment-drug conjugates, European Patent Application EP 21 175 808.1

## Publications to other projects

**Jäger S.**, Gude L, Arias-Pérez M.S. (2018) 4,5-Diazafluorene *N*-glycopyranosyl hydrazones as scaffolds for potential bioactive metallo-organic compounds: Synthesis, structural study and cytotoxic activity. *Bioorg. Chem.* **81**, 405 – 413.

**Jäger S.**, Krah S., Könning D., Roskopf J., Dickgiesser S., Rasche N., Kolmar H., Hecht S., Schröter C. (2020) Isolation of Anti-Hapten Antibodies by Fluorescence-Activated Cell Sorting of Yeast-Displayed B-Cell Receptor Gene Repertoires. *Methods in Molecular Biology. Vol 2070: Genotype Phenotype Coupling: Methods and Protocols* (Zielonka S., Krah S., Eds.) pp 267-287, Chapter 15, Springer US, New York.

Kaempffe A.\*, **Jäger S.\***, Könning D., Kolmar H., Schröter C. (2020) Isolation of Tailor-Made Antibody Fragments from Yeast-Displayed B-Cell Receptor Repertoires by Multiparameter Fluorescence-Activated Cell Sorting. *Methods in Molecular Biology. Vol 2070: Genotype Phenotype Coupling: Methods and Protocols* (Zielonka S., Krah S., Eds.) pp 249-266, Chapter 14, Springer US, New York.

Könning D., Zielonka S., Kaempffe A., **Jäger S.**, Kolmar H., Schröter C. (2020) Selection and Characterization of Anti-idiotypic Shark Antibody Domains. *Methods in Molecular Biology. Vol 2070: Genotype Phenotype Coupling: Methods and Protocols* (Zielonka S., Krah S., Eds.) pp 191-209, Chapter 11, Springer US, New York.

\* *contributed equally to this work.*

---

---

---

## 1. Table of Contents

---

1.....	TABLE OF CONTENTS .....	I
2.....	ABSTRACT .....	V
3.....	ZUSAMMENFASSUNG.....	VI
4.....	INTRODUCTION.....	8
4.1.	The Biology of Cancer .....	8
4.1.1.	The Transformation of Normal Cells to Cancer Cells.....	8
4.1.2.	The Architecture of a Malignant Solid Tumor .....	11
4.2.	From Conventional Cancer Therapy to Targeted Cancer Therapy.....	13
4.2.1.	Cancer Treatment at a Glance .....	13
4.3.	Monoclonal Antibodies as Targeted Therapeutics.....	15
4.3.1.	Structure and Function of Antibodies .....	15
4.3.2.	Human Epidermal Growth Factor Receptors (HER) as Important Solid Tumor Targets for Targeted Monoclonal Antibody Therapy.....	18
4.4.	Antibody-Drug Conjugates as Targeted Therapeutics .....	23
4.4.1.	Structure and Mode of Action.....	23
4.4.2.	Advancements in the ADC Field .....	24
4.4.3.	Clinically validated ADCs.....	27
4.5.	Limitations of Antibody-based Therapies.....	29
4.5.1.	Solid Tumor Exposure and Efficacy .....	29
4.5.2.	Solid Tumor Penetration – A Complex Interplay of Various Factors.....	30
4.6.	Small Format-Based Drug Conjugates .....	37
4.6.1.	Antibody Fragment-Based Binding Scaffolds .....	37
4.6.2.	Alternative Binding Scaffolds.....	38
4.6.3.	Binding Scaffolds with Half-Life Extension .....	39
4.7.	Fc Antigen Binding Fragments (Fcabs) as Novel Drug Conjugate Scaffold .....	42
4.7.1.	Structure and Function of Fcabs.....	42
4.7.2.	Generation and Screening of Fcabs.....	45
4.7.3.	Application and Therapeutic Use of Fcabs .....	46

<b>5. .... OBJECTIVE OF THIS WORK.....</b>	<b>47</b>
<b>6. .... MATERIAL AND METHODS .....</b>	<b>49</b>
<b>6.1. Human Cell Lines and Bacterial Strains.....</b>	<b>49</b>
<b>6.2. Antibody Sequences.....</b>	<b>49</b>
<b>6.3. Plasmids .....</b>	<b>54</b>
<b>6.4. Enzymes and Proteins .....</b>	<b>55</b>
6.4.1. Commercial Antibodies.....	56
<b>6.5. Chemicals .....</b>	<b>56</b>
<b>6.6. Cell Culture Media.....</b>	<b>59</b>
<b>6.7. Solutions, Media and Buffer Preparation .....</b>	<b>59</b>
<b>6.8. Kits and Consumables .....</b>	<b>60</b>
<b>6.9. Devices and Equipment .....</b>	<b>61</b>
<b>6.10. Software.....</b>	<b>63</b>
<b>6.11. Molecular Biological Methods .....</b>	<b>64</b>
6.11.1. Determination of DNA Concentration .....	64
6.11.2. Transformation in <i>E. coli</i> .....	64
6.11.3. Plasmid Preparation.....	64
<b>6.12. Biophysical and Biochemical Methods .....</b>	<b>65</b>
6.12.1. Determination of Protein Concentration.....	65
6.12.2. SDS-PAGE .....	65
6.12.3. Protein A Affinity Chromatography .....	65
6.12.4. Immobilized Metal Ion Affinity Chromatography (IMAC).....	66
6.12.5. Preparative Size Exclusion Chromatography (SEC).....	66
6.12.6. Analytical Size Exclusion Chromatography (SE-HPLC) .....	66
6.12.7. Reversed Phase HPLC (RP-HPLC) .....	67
6.12.8. Hydrophobic Interaction HPLC (HI-HPLC).....	67
6.12.9. LC-MS Intact Mass Analysis .....	67
6.12.10. LC-MS DAR Determination.....	68
6.12.11. Peptide Mapping.....	68

---

6.12.12. Thermal Stability.....	69
6.12.13. Biolayer Interferometry.....	69
6.12.14. Proteolytic Cleavage Reaction.....	70
6.12.15. pHAb-Dye Labeling.....	71
6.12.16. Cysteine Conjugation.....	71
6.12.17. Sortase A Conjugation.....	71
6.12.18. Transglutaminase Conjugation.....	72
6.12.19. Serum Stability.....	72
6.12.20. Degree of pHAb-Dye Labeling.....	73
<b>6.13. Cell Biological Methods.....</b>	<b>75</b>
6.13.1. Cultivation of Mammalian Cells.....	75
6.13.2. Protein Production.....	76
6.13.3. Cellular Binding Assay.....	76
6.13.4. Cellular Uptake Assay.....	76
6.13.5. Cell Viability Assay.....	77
6.13.6. Tumor Spheroid Penetration.....	77
<b>7..... RESULTS AND DISCUSSION.....</b>	<b>80</b>
<b>7.1. Design and Generation of Fcabs and Controls.....</b>	<b>80</b>
7.1.1. Selection and Design.....	80
7.1.2. Expression and Purification.....	83
7.1.3. Biophysical Characterization.....	84
<b>7.2. Evaluation of Fcab Suitability for ADC Generation.....</b>	<b>86</b>
7.2.1. Cellular Binding of Fcabs to Tumor Cells.....	86
7.2.2. Generation of pHAb-Dye Labeled Fcabs and Controls.....	89
7.2.3. Cellular Uptake of Fcabs into Tumor Cells.....	91
<b>7.3. Selection, Design and Generation of Fcab-Drug Conjugates.....</b>	<b>95</b>
7.3.1. Design Rationale.....	95
7.3.2. Conjugation, Purification and Biophysical Characterization.....	96
<b>7.4. Evaluation of Fcab-Drug Conjugates.....</b>	<b>100</b>

---

---

7.4.1.	Hydrophobicity of Drug Conjugates.....	100
7.4.2.	Receptor Binding Properties of Drug Conjugates.....	103
7.4.3.	Serum Stability of Drug Conjugates.....	105
7.4.4.	<i>In Vitro</i> Cytotoxicity of Drug Conjugates.....	106
<b>7.5.</b>	<b>3D Tumor Cell Spheroid Penetration Studies.....</b>	<b>112</b>
<b>8.....</b>	<b>CONCLUSION.....</b>	<b>118</b>
<b>9.....</b>	<b>OUTLOOK.....</b>	<b>120</b>
9.1.	Solid Tumor Penetration and Efficacy Predictions by Mechanistic Modelling.....	120
9.2.	<i>In Vivo</i> Evaluation of Fcab-Drug Conjugates.....	120
9.3.	Cleavable (Fab) <sub>2</sub> -Fcab-drug conjugates – Reducing Size Right at the Tumor Site.....	121
<b>10....</b>	<b>REFERENCES.....</b>	<b>123</b>
<b>11....</b>	<b>APPENDIX.....</b>	<b>139</b>
11.1.	Abbreviations.....	162
11.2.	List of Figures.....	167
11.3.	List of Tables.....	169
11.4.	Acknowledgements.....	170
<b>12....</b>	<b>AFFIRMATIONS.....</b>	<b>172</b>

---

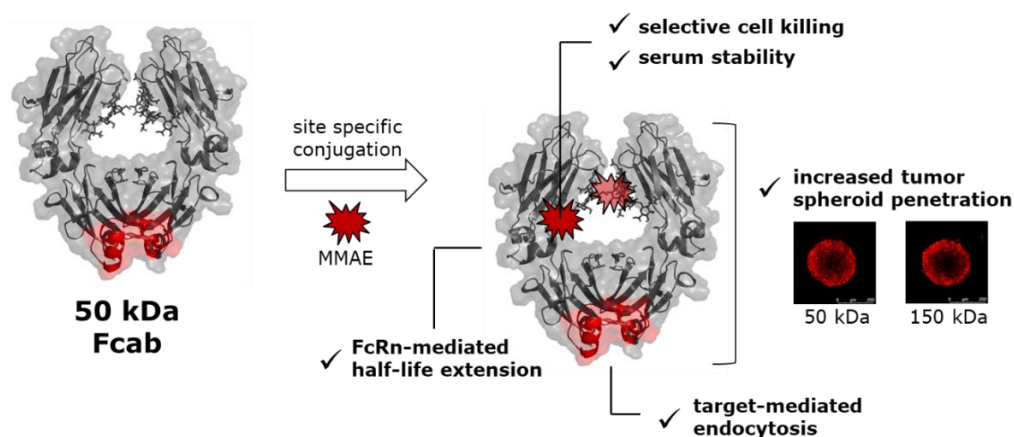
## 2. Abstract

---

The fundamental prerequisite of therapeutic efficacy of antibody drug conjugates (ADCs) in solid tumors is the exposition of cancer cells to a therapeutically active dose of drug. One prominent strategy to maximize drug exposure, is to increase tissue penetration by smaller sized drug conjugates that extravasate faster and distribute deeper into the tumor.

Fc antigen binding fragments (Fcabs) are engineered homodimeric 50 kDa Fc regions that incorporate all essential immunoglobulin G (IgG) functionalities such as neonatal Fc receptor (FcRn)-mediated recycling and antigen binding at only one-third of the size. The combination of reduced size and favorable pharmacokinetics makes Fcabs an attractive alternative to the conventional IgG scaffold employed in ADCs, with potentially improved tissue penetration capabilities. In the present study, Fcabs were explored for the first time as a novel scaffold for ADCs.

For proof-of-principle, HER2- and EGFR-targeting Fcabs were selected, coupled to a pH sensitive dye, and subsequently tested for receptor-mediated endocytosis on tumor cells. Target-dependent cellular binding and uptake confirmed the suitability of the selected Fcabs for targeted intracellular drug delivery. Moreover, Fcabs were conjugated to cytotoxic monomethyl auristatin E (MMAE) employing site-specific enzymatic or cysteine coupling. The feasibility of Fcab-drug conjugates could be demonstrated by retained binding to target receptor and half-life prolonging FcRn, conjugation site dependent serum stability and target-mediated cell killing at sub-nanomolar to double digit nanomolar concentrations. Moreover, HER2-targeting Fcab-dye constructs were tested in a tumor cell spheroid model and showed elevated penetration compared to a 150 kDa Fcab derivative with unrelated Fab arms or to the clinically validated HER2-targeting antibody Trastuzumab.



Overall, this study demonstrates the applicability of the Fcab format as targeting scaffold for the generation of drug conjugates and emphasizes the potential of Fcab-drug conjugates for improved tumor penetration in solid cancers.

---

### 3. Zusammenfassung

---

Die Grundvoraussetzung für die therapeutische Wirksamkeit von Antikörper-Wirkstoff-Konjugaten (ADCs) bei soliden Tumoren ist die Exposition der Krebszellen gegenüber einer therapeutisch wirksamen Dosis des Wirkstoffs. Eine mögliche Strategie zur Maximierung der Wirkstoffexposition besteht darin, die Gewebepenetration durch Verwendung kleinerer Wirkstoffkonjugate zu erhöhen. Diese extravasieren schneller und können sich tiefer im Tumorgewebe verteilen. Hier stellen Fc-Antigenbindungsfragmente (Fcabs) eine attraktive Alternative zu dem, in ADCs üblicherweise als Targetierungseinheit verwendeten, Immunglobulin G (IgG) dar.

Fcabs sind gentechnisch veränderte, homodimere Fc Fragmente, die alle wesentlichen IgG Funktionen wie die Antigenbindung und das neonatale Fc-Rezeptor (FcRn) vermittelte Recycling in einem Molekül vereinen. Dabei weisen die 50 kDa schweren Fcabs nur ein Drittel der IgG Größe auf. Durch die Kombination aus geringerer Größe und guter Pharmakokinetik besitzen Fcabs eine potentiell verbesserte Gewebepenetration. In der vorliegenden Studie wurden Fcabs erstmalig als Targetierungseinheit für ADCs untersucht. Hierzu wurden verschiedene Fcabs ausgewählt, die an epidermale Wachstumsfaktorrezeptoren (HER2 oder EGFR) binden. Um deren Aufnahme in Tumorzellen zu untersuchen, wurden sie an einen pH sensitiven Farbstoff gekoppelt. Die rezeptorvermittelte zelluläre Aufnahme bestätigte die Eignung der ausgewählten Fcabs für die gezielte intrazelluläre Pharmakotherapie. Dementsprechend wurde durch ortsspezifische, enzymatische Konjugation oder Cystein-Kopplung der zytotoxische Wirkstoff Monomethyl-Auristatin E (MMAE) an die Fcab Moleküle konjugiert. Dabei blieb die Bindungsfähigkeit der erzeugten Fcab-Wirkstoffkonjugate an deren Zielrezeptor und den halbwertszeitverlängernden FcRn Rezeptor erhalten. Die Fcab-Wirkstoffkonjugate zeigten eine Target-vermittelte Zytotoxizität im subnanomolaren bis zweistellig nanomolaren Konzentrationsbereich und eine konjugationsstellenabhängige Serumstabilität. Darüber hinaus wurden HER2-targetierende Fcab-Farbstoffkonjugate in einem Tumorzell-Sphäroid-Modell getestet. Diese zeigten eine höhere Penetration im Vergleich zu einem 150 kDa Fcab-Derivat mit nicht targetierenden Fab-Armen oder dem klinisch zugelassenen HER2-targetierenden Antikörper Trastuzumab.

Die vorliegende Arbeit erbringt den Machbarkeitsnachweis für die Anwendung des Fcab-Formats als Targetierungseinheit in Wirkstoff-Konjugaten. Die Studie zeigt außerdem das Potential von Fcab-Wirkstoffkonjugaten für eine verbesserte Tumورpenetration bei soliden Krebserkrankungen auf.

---

# INTRODUCTION

---

---

---

## 4. Introduction

---

This doctoral thesis is settled in the exploration of novel targeted therapeutics aiming for an improved solid tumor therapy.

To elucidate the targeting concept, special attention was given to tumor biology, the structure of solid tumors followed by a short overview on general aspects in cancer treatment. Herein, the use of monoclonal antibodies, antibody-drug conjugates for relevant solid tumor targets is outlined, including the limitations of these targeted therapy forms and current solution strategies. Finally, Fc antigen binding fragments are highlighted due to its special importance for this work.

### 4.1. The Biology of Cancer

Cancer is a generic term describing a plethora of genetic diseases related to an abnormal and rapid cell growth. Cancer can affect any part of the body, form local masses called neoplasm or tumors and potentially invade other tissues or organs developing new settlements, termed metastases.<sup>1</sup> The formation of metastases cause the majority of all human cancer cell deaths and discriminates malignant tumors from benign tumors which do not spread to distant parts of the body.<sup>1,2</sup> Cancer develops slowly. It has been estimated that for most human solid tumors, there can be 20-years between initial carcinogen exposure and detection of the tumor.<sup>3</sup> To understand how cancer develops, the multistep process of tumorigenesis and common characteristics of cancer cells are described in the following section.

#### 4.1.1. The Transformation of Normal Cells to Cancer Cells

Cancer results from a combination of various mutations into central genes of the genome. The affected genes are classified into oncogenes and tumor suppressor genes. Oncogenes promote cell growth while tumor suppressor genes inhibit cell growth. During tumorigenesis, a cell acquires mutations in these genes which reconfigure its capabilities. Weinberg and Hanahan postulated that cells must acquire a set of eight common capabilities, “The Hallmarks of Cancer” in order to transform into cancer cells: (1) sustained proliferative signaling, (2) evading growth suppressors, (3) resisting cell death, (4) enabling replicative immortality, (5) inducing angiogenesis, (6) activating invasion and metastasis, (7) reprogramming of energy metabolism and (8) evading immune destruction.<sup>4,5</sup> According to Weinberg and Hanahan these hallmarks underlie most types of cancer and their acquisition is made possible by two enabling characteristics: (1) genomic instability and (2) tumor promoting inflammation.<sup>5</sup>

Genomic instability refers to the elevated mutability in cancer cells which drives tumorigenesis to completion. In hereditary cancers, genomic instability originates from germline mutations in DNA repair

---

genes, which result in an increased frequency of base-pair changes upon loss of the remaining wild-type allele.<sup>6</sup> Prominent examples are the *BRCA1* or *BRCA2* genes in which certain mutations lead to improper function of the respective DNA repair proteins and an increased risk of developing breast cancer up to 80% by age 70.<sup>7,8</sup> By contrast, the cause of genomic instability in sporadic cancers is less well understood.<sup>6</sup> Tumor sequencing studies revealed that mutations in classical DNA repair genes are less frequent in early cancer development.<sup>9–12</sup> Alternatively, an oncogene-induced DNA replication stress model was proposed to explain genomic instability.<sup>13</sup> Activated oncogenes such as *ras* or *myc* can induce stalling and collapse of DNA replication forks which lead to DNA double strand breaks (DSBs). DSBs result in activation of the DNA damage response machinery (DDR) including DNA damage checkpoint gene *p53* – the “guardian of the genome”.<sup>14</sup> *p53* preserves genomic stability by activating DNA repair proteins, arresting the cellular cycle to give these proteins time for repair or by inducing senescence or apoptosis if DNA damage is irreparable. DSBs increase selective pressure on *p53* mutations which fundamentally accelerate cancer development due to the outstanding role of *p53* for cellular health.<sup>15,16</sup> Its importance for the development of cancer is emphasized by the fact that *p53* is one of the most frequently mutated genes in sporadic cancers.<sup>17,18</sup>

Another enabling characteristic is tumor-promoting inflammation.<sup>5</sup> Tumors represent a chronic site of inflammation and can be seen as “wounds that do not heal”.<sup>19</sup> Consequently, immune cells invade the tumor site where they fulfill tumor antagonizing and, counterintuitively, tumor-promoting roles. Subclasses of macrophages, neutrophils and myeloid progenitors stimulate mistakenly cancer cell proliferation by releasing wound healing factors such as epidermal growth factor (EGF), angiogenesis promoting vascular endothelial growth factor A (VEGF-A), inflammation promoting cytokines and matrix modifying proteases.<sup>5,19</sup>

In the following the 8 hallmark capabilities will be discussed in more detail.<sup>4,5</sup>

In normal tissues cell growth and cell death rates are kept in balance by the strict regulation of mitogenic growth signals. Cancer cells can bypass this regulatory mechanism and are capable to sustain proliferative signaling in different ways. They may synthesize their own growth factor ligands or stimulate adjacent normal cells of the supporting tumor-associated stroma to provide needed growth factors.<sup>20,21</sup> Alternatively, cancer cells may upregulate growth factor receptors displayed on their surface. For example, the epidermal growth factor receptor (EGFR) is overexpressed in many types of solid tumors such as head and neck cancer or colon and rectum cancer, while levels of human epidermal growth factor receptor 2 (HER2) are increased in breast (~ 15% of all breast cancers<sup>22,23</sup>), bladder esophageal and gastric cancer.<sup>24,25</sup>

In addition to growth promoting signals, tissue homeostasis can be also maintained by antiproliferative signals and cell death. Cancer cells must evade growth suppressing signals and apoptosis which typically involve the action of tumor suppressing proteins like the cell cycle controlling *p53*. Mutations in the *p53* gene allow cancer cells to continuously proliferate and evade apoptosis even if DNA is severely damaged due to hyper proliferation.<sup>5</sup>

---

Another hallmark is replicative immortality. Normal cells can undergo only a limited number of successive cell growth and division cycles before they enter a nonproliferating but viable senescent state and eventually cell crisis resulting in apoptosis.<sup>26</sup> The key enzyme in circumventing the finite replicative potential of cells is the reverse transcriptase telomerase. Telomerase restores telomere repeat sequences at the end of chromosomes which protect chromosomal DNA but continuously shorten during consecutive cell division cycles thereby defining a cells' lifespan. Telomerase is almost absent in somatic cells but expressed in 90% of tested primary tumors.<sup>27</sup>

The progressive tumor growth makes an infrastructure necessary that supplies the tumor with oxygen, nutrients and removes metabolic waste and carbon dioxide. This is accomplished by the induction of angiogenesis. The sprout of new blood vessels into the tumor mass is almost constantly activated by hypoxia- or oncogene-induced upregulation of VEGF-A expression in cancer cells.<sup>28</sup> The structure of tumor vasculature is described in more detail in section 4.1.2.

Vascularization is also required for the metastatic process. At some stage in cancer development, tumor cells leave the primary tumor site and spread to secondary locations. This is often associated with a downregulation or loss of cell adhesion molecules such as E-cadherin or claudin.<sup>29,30</sup> The invasion-metastasis cascade typically starts with local invasion, followed by intravasation of tumor cells into close-by blood and lymphatic vessels, circulation within the hematologic and lymphatic vascular system and extravasation into distant tissues where tumor cells form micro-metastases and eventually a macroscopic tumor which reinitiate the cascade.<sup>31</sup>

Most macroscopic tumors have regions where little vascularization results in a permanent or transient hypoxic state. Cancer cells counter this state of low oxygen supply by reprogramming their energy metabolism to glycolysis. Compared to oxidative phosphorylation under aerobic conditions, ATP production is 18-fold less efficient. Cancer cells compensate lower energy yield by upregulating glucose transporters and other enzymes of the glycolytic pathway.<sup>5</sup> Paradoxically, proliferating cancer cells still derive most of their energy from glycolysis even under oxygen sufficiency (Warburg effect).<sup>5</sup> It is assumed that this energy-economically irrational behavior may be beneficial to cancer cells as it allows them to redirect glycolytic intermediates into biosynthetic pathways of macromolecules and organelles required for assembling new cells.<sup>32</sup>

Finally, cancer cells can be characterized by their capability to evade immune destruction. The interaction of cancer cells with the host immune system is summarized in the "three E's theory" comprising three steps: 1) Elimination of the developing tumor by the innate and adaptive immune system at an early stage, 2) Equilibrium when the host immune system controls but not fully extinguish tumor cells that have survived the initial elimination phase (this phase probably occurs over many years in humans), and 3) Escape when tumor cells selected in the equilibrium phase have acquired resistance to immune detection and/or

---

elimination and become clinically detectable.<sup>33</sup> One example for such an escape strategy is the overexpression of the programmed death-ligand 1 (PD-L1) on the surface of cancer cells. After a cytotoxic T-cell has recognized a cancer cell, PD-L1 binds the programmed cell death protein 1 (PD-1) on the surface of the T-cells and the tumor cell evades its destruction by inhibiting T-cell proliferation and cytotoxic cytokine secretion.<sup>34</sup>

#### **4.1.2. The Architecture of a Malignant Solid Tumor**

Solid tumors are complex organ-like structures. They consist not only of malignant tumor cells but also of stromal and immune cells, vasculature and an extracellular matrix (ECM). The non-malignant tumor components are summarized as the tumor microenvironment (TME). A tumors' TME composition is highly heterogeneous and dynamic. It varies during tumorigenesis, at different tumor stages/ between different tumor types and as response to therapeutic interventions.<sup>35,36</sup>

In the following, the components of a solid tumor and its TME are described in more detail.

##### ***Tumor Cells and Intratumoral Heterogeneity***

Cancer development is a highly dynamic process driven by genomic instability and subjected to evolutionary pressure. Even after a single tumor cell has acquired all 8 hallmark capabilities, it continues to evolve. As a result, the number of genetically distinct tumor-cell subpopulations within a tumor mass grows over time – the tumor becomes more heterogeneous. The appearance of different subpopulations in one patient does not have to follow a linear evolution where a new clone outcompetes its ancestral clones (temporal heterogeneity). Especially solid tumors adopt a branched pattern of evolution where multiple subclonal populations emerge from a common ancestral clone.<sup>37</sup> Clonal subpopulations can distribute across different regions within the primary tumor mass and/or across different metastatic sites (spatial heterogeneity). They do not necessarily outcompete each other but might even cooperate for tumor propagation.<sup>38</sup>

Intratumoral temporal and spatial heterogeneity complicate treatment of cancer as distinct molecular signatures of clonal subpopulations lead to different responsiveness. Moreover, the selection pressure built up by targeted therapies, chemotherapies, or immunotherapies inevitably causes cancer cells to escape from growth suppression fostering the development of drug resistant clones.<sup>37</sup>

##### ***Stromal cells in the tumor microenvironment***

During tumorigenesis cancer cells recruit stromal cells (e.g. endothelial cells, pericytes, cancer-associated fibroblasts, adipocytes, stellate cells) from surrounding tissues to promote cancer progression.<sup>36,39</sup> For example, tissue-resident fibroblasts can be activated by TGF- $\beta$  and inflammatory modulators of the perpetual inflammatory state of a tumor to become cancer-associated fibroblasts (CAF). CAFs are often found in the

---

invasive margins of a solid tumor and shape the tumor microenvironment in different ways. CAF induce angiogenesis and tumor growth by secreting growth factors such as VEGF-A, produce extracellular matrix remodeling enzymes (e.g. matrix proteases) that promote cancer invasion and metastasis and maintain the chronic inflammatory tumor state by the release of numerous cytokines and chemokines.<sup>40</sup>

### ***Immune cells in the tumor microenvironment***

The persistent inflammatory state of a tumor causes infiltration by different adaptive and innate immune cells, namely T-cells, B-cells, natural killer (NK) cells as well as macrophages, neutrophils and dendritic cells.<sup>36</sup> As already described in section 4.1.1. immune cells in the TME can either suppress or promote tumor growth.

### ***Tumor vasculature***

Fast growing tumor tissue causes several structural abnormalities of tumor blood vessels compared to normal vasculature. Typically, new blood vessels form by splitting or sprouting from a pre-existing vascular network, a process termed as angiogenesis. In adults, normal physiological angiogenesis occurs during wound healing or the female reproductive act but is otherwise very rare.<sup>41</sup> The single layer of endothelial cells lining blood vessels are low proliferative and their estimated turnover times are in the order of years.<sup>42</sup> In contrast, endothelial cells in solid tumors proliferate 50 – 200 times faster due to the excessive secretion of pro-angiogenic factors (mainly VEGF-A) by hypoxic cancer, stromal and immune cells.<sup>42,43</sup> VEGF-A binds to the VEGF receptor on endothelial cells of nearby blood vessels and initiates angiogenesis. The excess of VEGF-A impairs adequate maturation of newly formed blood vessels. As a result, the morphology of the tumor vasculature is rather chaotic and loses a hierarchical branching pattern of arteries, capillaries and veins. Vessels are irregularly shaped, dilated, tortuous, abnormally branched, compressed by proliferating tumor cells and end abruptly.<sup>41</sup> Abnormal vessel growth and tortuosity tend to increase blood flow resistance leading to ineffective delivery of oxygen and drugs, even when the tumoral vascular network is rather dense.<sup>44,45</sup> Endothelial cells lining blood vessel walls form only loose cell contacts causing vascular leakiness and an increased permeability.<sup>42,46</sup> In addition to morphological changes, endothelial cells reprogram their energy metabolism to glycolysis during angiogenesis and increase their metabolic activity similar to tumor cells.<sup>47</sup>

The vascular network consists not only of blood vessels, but also of lymphatic vessels. Lymphatic vessels are structured like blood vessels. They collect excess interstitial fluid, immune cells and macromolecules that have extravasated from blood vessels into tissues and return them *via* lymph nodes to the circulatory system. In solid tumors, lymphatic vessels play an important role for metastasis but are often collapsed within the tumor mass.<sup>48</sup> Functional lymphatic vessels are found only at the tumor margin (defined as < 100 μm from the tumor edge)<sup>49</sup> where their surface is often increased due to lymphangiogenesis stimulated by the

---

overexpression and release of VEGF-C and VEGF-D from tumor cells themselves, stromal cells, tumor-infiltrating macrophages or activated platelets.<sup>50-53</sup> Increased vessel surface only in the tumor periphery, seems to be sufficient for lymphatic metastasis.<sup>49</sup> Furthermore, lymphatic deficiencies limit the drainage of fluid from the tumor which consequently increases the interstitial fluid pressure (IFP) uniformly within the tumor mass (except at margin).<sup>54,55</sup> The hyperpermeability of tumor blood vessels and the dense extracellular matrix of the tumor interstitial space increase tumor IFP additionally.<sup>54</sup> The consequences of an elevated IFP for drug delivery are further elucidated in section 4.5.

### ***Extracellular matrix in the tumor microenvironment***

The tissue space in between blood vessels and cells is termed as tumor interstitial space and comprises the ECM as well as fluids with soluble biomolecules (interstitial fluid). The ECM comprise the non-cellular solid components of a tissue that provide structural support and integrity, namely collagen, fibronectin, elastin, proteoglycans, laminins and hyaluronic acid.<sup>36,56</sup> Its composition, organization and amount differs significantly between tumors and normal tissues. In many solid tumors the ECM contributes up to 60% to tumor mass.<sup>56</sup> ECM molecules render a tumor more rigid and contribute to the palpability of solid tumors. They are mainly deposited and remodeled by CAFs but also by tumor cells themselves.<sup>40</sup> The ECM influences tumor growth and metastasis *via* epithelial-to-mesenchymal transition and ECM stiffness.<sup>57,58</sup> In this context, matrix metalloproteinases (MMPs) are critical for ECM degradation, remodeling and thus tumor progression. Furthermore, the ECM serves as a deposit for cytokines and different proangiogenic factors such as VEGF and TGF- $\beta$ .<sup>36</sup>

## **4.2. From Conventional Cancer Therapy to Targeted Cancer Therapy**

In order to put the therapeutic approach presented later in this thesis into a larger context, current treatment approaches for cancer will be briefly discussed in the following section.

### **4.2.1. Cancer Treatment at a Glance**

Several types of cancer therapies were developed over the last 150 years.<sup>59</sup> Treatment approaches can be divided into local therapies (surgery, radiation therapy) or systemic therapies affecting the whole body (chemotherapy, endocrine/ hormone therapy, immunotherapy, targeted therapy).<sup>1</sup>

These therapeutic approaches rely on different previously mentioned characteristics of cancer. For example, a localized primary solid tumor and affected associated lymphatics can be efficiently treated by surgical removal in combination with preceding (neoadjuvant) or subsequent (adjuvant) radiation or chemotherapy to decrease tumor size or to minimize the statistical risk of relapse due to remaining micrometastases.<sup>60,61</sup>

In the case where a tumor has already metastasized to several distant parts of the body and removal by surgery no longer seems possible, a systemic therapy is often chosen. For example, chemotherapy seems most promising for treating rapidly growing cancers. Chemotherapeutic agents affect mainly fast dividing cells and include DNA damager<sup>62</sup> (e.g. doxorubicin, cyclophosphamide, irinotecan), antimetabolites<sup>63</sup> (e.g. 5-fluorouracil, methotrexate) and microtubule inhibitors<sup>64</sup> (e.g. vincristine, docetaxel). Typically, chemotherapeutic agents with distinct modes of action and different side effects are administered in combination to minimize the probability that cancer cells become resistant to the therapy.<sup>65</sup> Chemotherapeutics are relatively non-specific and must be administered at the maximum tolerated dose (MTD) to achieve a therapeutic effect. As a consequence, they induce severe side effects due to the damage of other fast-dividing cells, such as blood cells or hair follicles.<sup>66</sup>

Within the last decades considerable progress was made to understand underlying molecular mechanisms of cancer pathogenesis. This led to the development of systemic treatments which act on specific targets associated with cancer cells or within the TME. Such treatments, termed targeted therapies, are more selective than chemotherapy. A higher selectivity of a drug results in a higher MTD and a lower minimum effective dose (MED). Thus, the dose range in which the drug has a therapeutic effect but no toxic effect, also termed as the therapeutic index (TI), is increased (**Figure 1**). Consequently, targeted therapies and immunotherapies can be administered at doses where less severe side effects are observed compared to chemotherapy.<sup>67</sup>

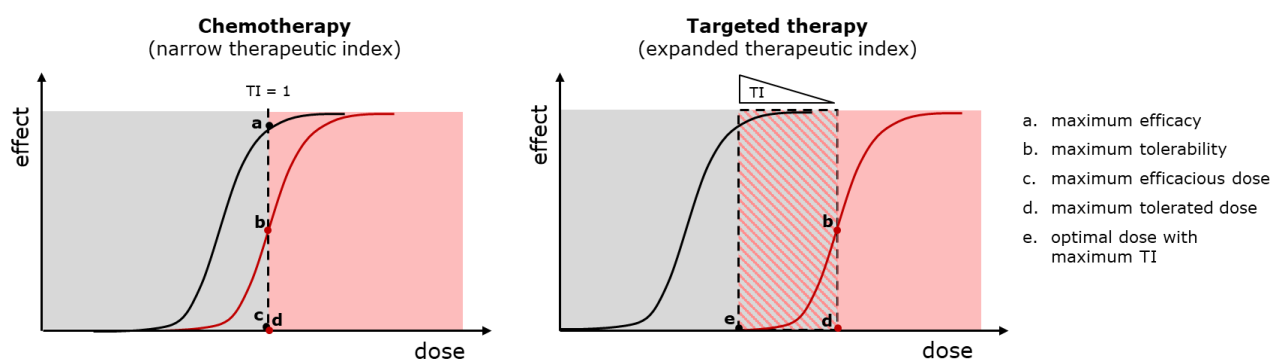


**Figure 1. Therapeutic index.** Schematic representation adapted from Tarcsa *et al.* to illustrate the improvement of therapeutic index from small molecule chemotherapeutics to targeted therapeutics (e.g., small molecule inhibitors, monoclonal antibodies or antibody-drug conjugates (ADCs)).<sup>68</sup>

In the following, examples are given of how selectivity is achieved in targeted therapies. For instance, immunotherapy reverses a cancer's capability to evade immune destruction redirecting immune cells to attack tumor cells again. Recently, immune checkpoint inhibitors attracted great attention in this context.<sup>69</sup> They bind for example PD-L1 which is overexpressed on the surface of many cancer cells or PD-1 on the

---

surface of immune cells and block the interaction between these two proteins thereby preventing tumor cells from masking themselves as non-altered self.<sup>70</sup> Other targeted therapeutics confer tumor selectivity by acting on oncoproteins which are involved in essential signaling pathways for tumor growth and survival.<sup>59</sup> Molecular targets include growth factor receptors such as overexpressed HER2 or EGFR, mutated tyrosine kinases such as FLT3 and angiogenic ligands and receptors such as VEGF and VEGFR to name only a few.<sup>71</sup> Currently, two classes of molecules are applied in targeted therapy: monoclonal antibodies (mAbs), which are designed to target specific receptors and ligands expressed on the surface of cancer cells and small-molecule inhibitors, which can cross cell membranes and block signaling pathways intracellularly.<sup>59</sup> In the scope of this work, mAbs and epidermal growth factor receptors are of special relevance and will be discussed in more detail in the following sections.

### 4.3. Monoclonal Antibodies as Targeted Therapeutics

In principle, antibodies can attack tumors by three general mechanisms: (1) opsonization, which induces killing by immune cells, (2) blocking proliferative signaling pathways and processes, or (3) delivery of cytotoxic drugs. Before mechanism (1) and (2) are described in section 4.3.2, the general structure and function of antibodies should be explained first. Afterwards, mechanism (3) will be presented in section 4.4.

#### 4.3.1. Structure and Function of Antibodies

Antibodies or immunoglobulins (Ig) form a class of proteins that are produced as part of the body's humoral immune response to bind and neutralize pathogens. These ~ 150 kDa proteins are composed of two identical light chains (LC; ~ 25 kDa) and two identical heavy chains (HC; ~ 50 kDa) arranged in a LC-HC paired heterodimer (**Figure 2A, B**). LC and HC as well as both HCs are bridged by interchain disulfide bonds conferring additional stability to the non-covalent interactions that hold HC and LC together. Both LC and HC can be structurally divided into variable domains ( $V_L$  and  $V_H$ ) responsible for antigen binding and the constant domains ( $C_L$  and  $C_{H1}$ ,  $C_{H2}$ ,  $C_{H3}$ ) that specify effector functions of the antibody. In mammals, the LC can consist either of a  $\kappa$  or  $\lambda$  chain whereas the HC consists either of an  $\alpha$ ,  $\gamma$ ,  $\delta$ ,  $\epsilon$ , or  $\mu$  constant domain and defines the isotype or class of an antibody ( $\alpha$ : IgA;  $\gamma$ : IgG;  $\delta$ : IgD;  $\epsilon$ : IgE;  $\mu$ : IgM). The IgG class is the most common in human serum (~ 75%) and can be further split into four IgG isotype subclasses, IgG1, IgG2, IgG3 and IgG4. The isotype of an antibody provides different biological properties and can be switched in order to alter effector functions while antigen specificity is maintained. Within the HC, a spacer hinge region separates the  $C_{H1}$  and  $C_{H2}$  domains and contributes flexibility to the antibody structure resulting in its characteristic bivalent Y-shaped form. The hinge region also contains various protease cleavage sites. For example, papain cuts in the upper hinge region giving rise to the ~ 50 kDa fragment crystallizable (Fc) and two ~ 50 kDa

fragment antigen binding (Fab). The Fc portion consists of a hinge interchain disulfide-bridged C<sub>H</sub>2-C<sub>H</sub>3 homodimer whereas Fab fragments include the variable domains V<sub>H</sub>, V<sub>L</sub> as well as the interchain disulfide-bridged C<sub>H</sub>1 and C<sub>L</sub> domains. On the other hand, pepsin digests the Fc portion into small fragments and cuts within the lower hinge region yielding an interchain disulfide-bridged ~ 100 kDa F(ab')<sub>2</sub> fragment. Besides classical Ig-based antibodies found in nature or enzymatically derived fragments, there are several other antibody-based formats currently in clinical or exploratory use such as Fabs, diabodies or single domain antibodies (sdAbs) (**Figure 2C**).

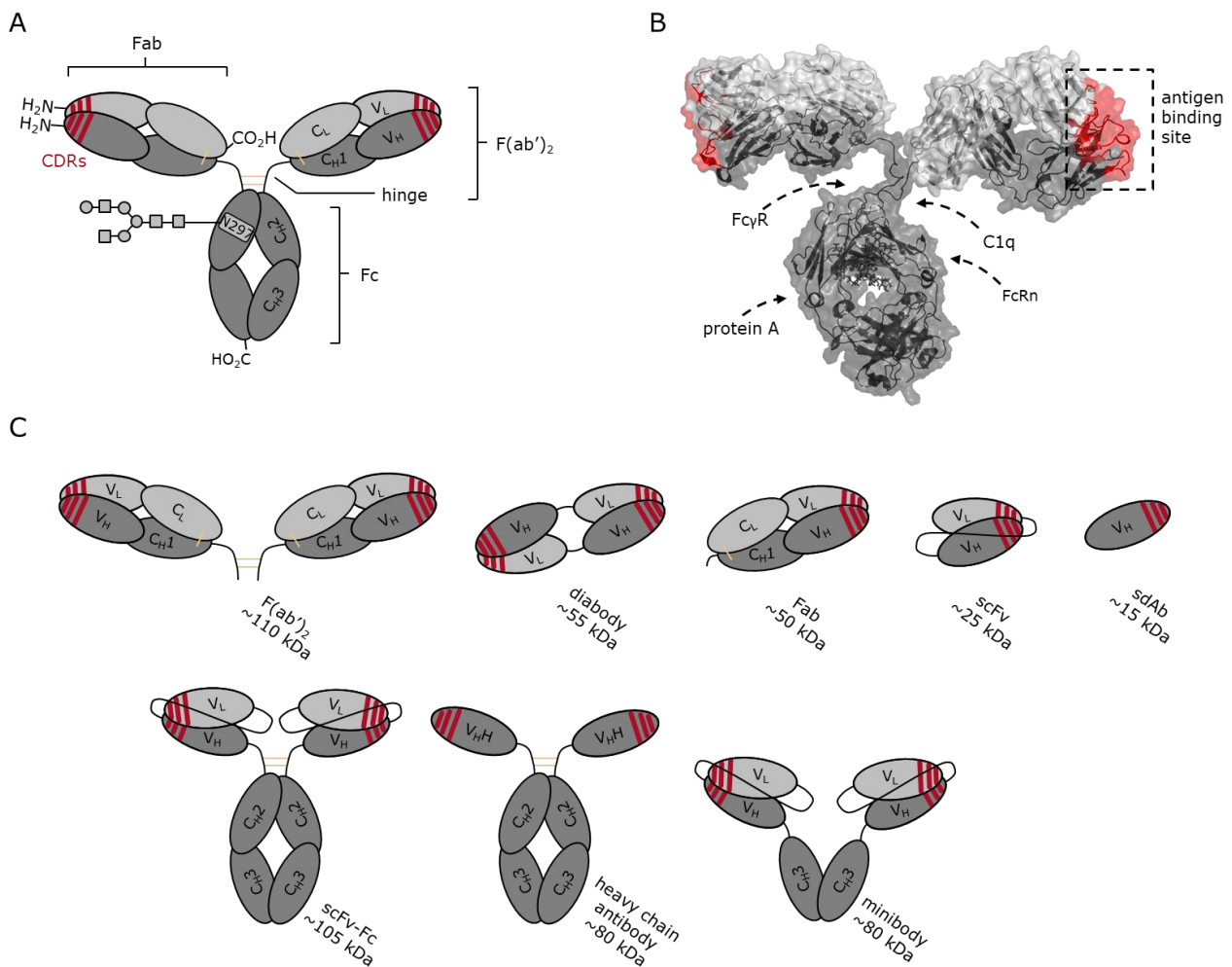


**Figure 2. Antibody structure.** (A) Schematic representation of IgG structure comprising two heavy (depicted in dark grey) and two light chains (depicted in light grey), assembled *via* disulfide bonds (depicted as yellow lines). Hypervariable CDR regions forming the antigen binding site are marked in red. The glycosylation site (N297) is highly conserved across IgG subclasses. In humans and rodents the core glycan consists of *N*-acetylglucosamine and mannose units.<sup>72</sup> (B) Murine IgG2 crystal structure (PDB: 1IGT<sup>73</sup>). The binding sites of its natural ligands at the Fc portion and hinge region are indicated by arrows.<sup>74</sup> (C) Schematic representation of selected antibody-derived formats. F(ab')<sub>2</sub> and Fab can be accessed *via* enzymatic digestion of IgG. HC antibodies lack an associated LC and occur naturally in camelids and cartilaginous fishes. The HC variable domain is characterized by high stability and can be expressed as a single domain antibody (sdAb), also known as nanobody. Diabodies, single chain variable fragments (scFv), scFv-Fc fusions or minibodies are generated by genetic antibody engineering.

---

A special feature of antibodies or related Fab and F(ab')<sub>2</sub> fragments is that they can specifically bind a target antigen structure with high affinity. The binding site of an antibody (also referred to as paratope) is predominantly formed by three hypervariable CDR loop structures in the V<sub>L</sub> and three CDR loops in the V<sub>H</sub> domain (**Figure 2A, B**). Binding to an antigen involves non-covalent interactions between residues of the CDRs and residues of the binding site on the antigen (epitope). It is noteworthy that an antibody is a bivalent molecule meaning that it has one paratope in each Fab arm and can potentially bind two antigens.

Besides specific binding, another main feature of an antibody is to activate components of the immune system by its effector functions. This includes antibody-dependent cellular cytotoxicity (ADCC) and complement-dependent cytotoxicity (CDC). ADCC implies that antibody-coated antigens recruit Fcγ receptor (FcγR) presenting effector cells, e.g. natural killer cells or monocytes, to destroy the antibody-decorated target. In contrast, CDC is dependent on the binding of C1q to the antibody which activates the classical complement pathway to destroy the target cell. Both, FcγR and C1q bind to overlapping epitopes in the upper C<sub>H2</sub> domain and the hinge region (**Figure 2B**). Thus, differences between the Ig classes and IgG subclasses are mostly located in this region. In addition, ADCC and CDC activity was shown to be significantly dependent on the glycan composition at the conserved asparagine 297 (N297).<sup>72</sup>

For the IgG class, extraordinary long plasma half-lives are observed. For example, the half-life of human IgG1, IgG2 and IgG4 is approximately 21 days at normal IgG serum levels (~ 12 g/L).<sup>75</sup> IgG half-life extension can be attributed to the neonatal Fc receptor (FcRn) which is expressed in endothelial cells lining the blood vessels (**Figure 3**).<sup>76</sup> Due to the large surface area of endothelial cells in the body (> 1000 m<sup>2</sup>), IgG, serum albumin and other proteins are continuously and efficiently internalized into endothelial cells through unspecific pinocytosis (**Figure 3A**).<sup>75</sup> Typically, internalized soluble proteins are transported from the endosome to the lysosome, where they are degraded. Soluble IgG and serum albumin are captured by the membrane associated FcRn at the slightly acidic pH (< 6.5) in the endosome and are recycled in receptor bound state back to the cell surface where they dissociate from the FcRn at the neutral pH (7.4) of blood.<sup>76,77</sup> In this way, approximately two thirds of IgGs taken up into endosomes bypass lysosomal degradation.<sup>78</sup> The efficiency of the FcRn-mediated recycling was illustrated in FcRn<sup>-/-</sup> deficient mice where the circulatory half-life of IgG is reduced from 9 days (FcRn wild type) to only 1 day.<sup>76</sup> Similarly, reduction in circulatory half-life can be observed when residues of the FcRn binding site at the C<sub>H2</sub>-C<sub>H3</sub> interface of the Fc portion are mutated and FcRn cannot bind anymore (**Figure 3B**). Shah and coworkers found in a mouse tumor PK model that half-life of Trastuzumab dropped from 9 days to 7 hours for an FcRn non-binding (I253A, H310A, H435A) Trastuzumab.<sup>79</sup>

In the next section, two clinically relevant solid tumor targets for monoclonal antibody therapy are described before the mode of action of corresponding mAbs is illustrated using these targets as an example. Both solid tumor targets as well as the corresponding mAbs are of special interest for this work.

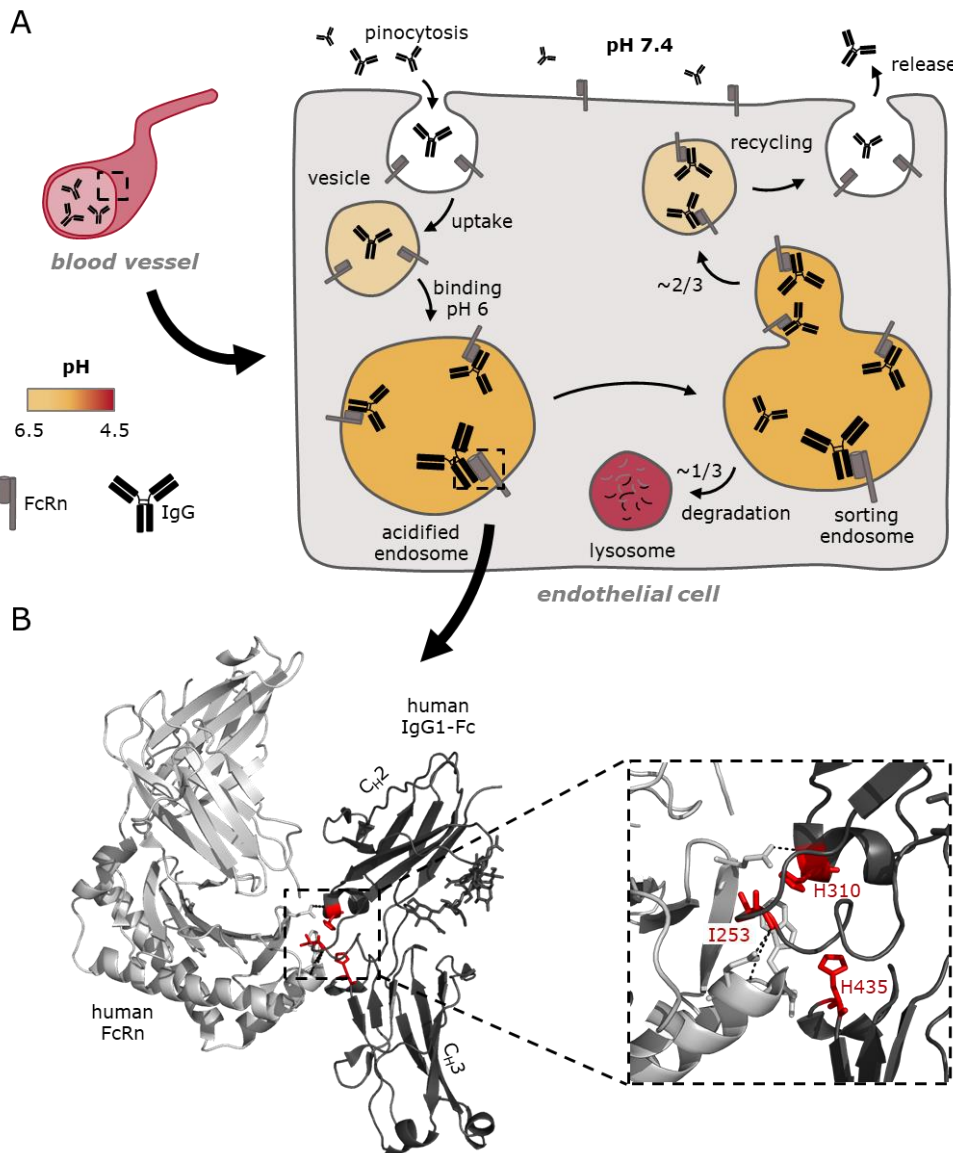


**Figure 3. IgG half-life extension by FcRn.** (A) FcRn recycling mechanism in endothelial cells lining blood vessels. Serum proteins are taken up *via* fluid phase pinocytosis and travel in vesicular transport carriers to the endosome where IgG and serum albumin are bound by the FcRn at acidic pH (< 6). Approximately two thirds of IgG are returned to the plasma membrane in FcRn-bound state where they are released into the extracellular fluid upon dissociation from FcRn at neutral pH. About one-third of IgGs is degraded in the lysosome together with other FcRn non-bound proteins. (B) FcRn binding site at the Fc C<sub>H</sub>2-C<sub>H</sub>3 interface. Three residues (His435, Ile253, His310) that were identified to be most critical for binding at acidic pH are highlighted in red.<sup>80</sup> (PDB: 4NOU<sup>81</sup>).

### 4.3.2. Human Epidermal Growth Factor Receptors (HER) as Important Solid Tumor Targets for Targeted Monoclonal Antibody Therapy

As mentioned in section 4.1.1, in many epithelial solid tumors the epidermal growth factor receptor (EGFR, also HER1, ErbB-1) and the human epidermal growth factor receptor 2 (HER2, also ErbB-2) are subjected to a number of genetic changes such as receptor overexpression, kinase domain mutations and coexpression of receptors and associated ligands. Each of these changes leads to constitutive activated downstream signaling that triggers nuclear gene activation and eventually promotes cancer development *via* sustained cell

proliferation.<sup>82</sup> In the following, the biology of HER receptors is briefly outlined before targeted therapy options are discussed.

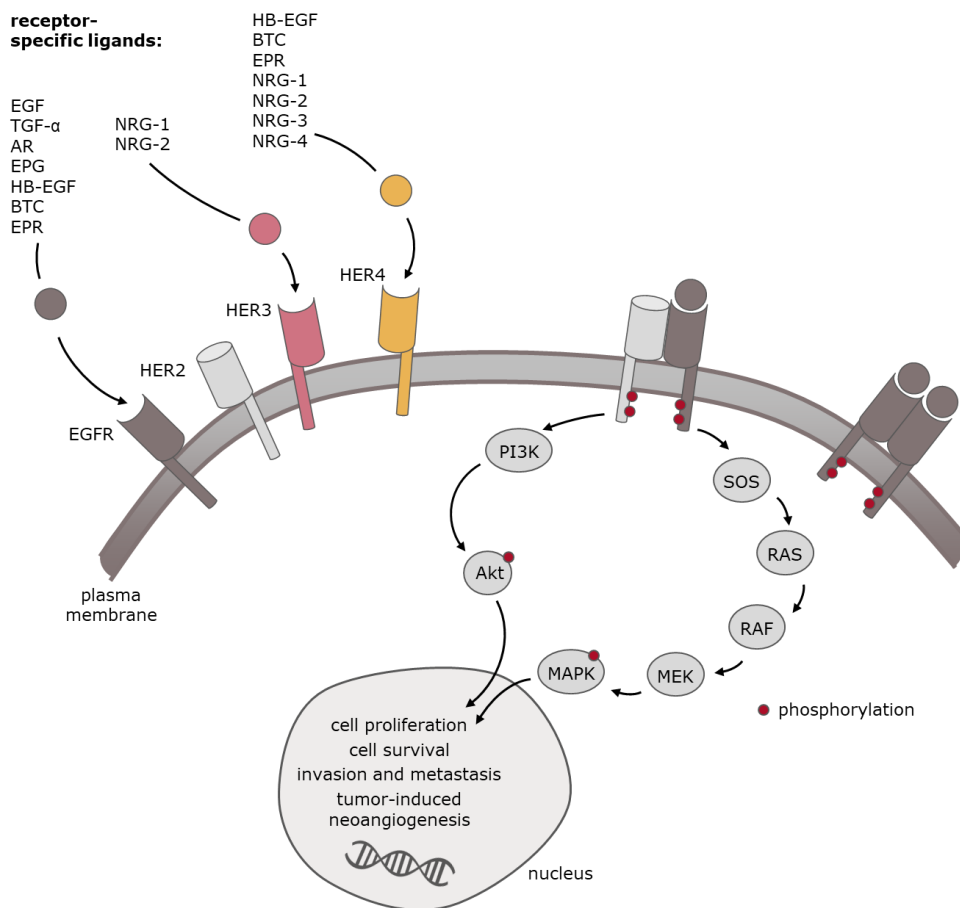


**Figure 4. HER receptors, ligands and major downstream signal transduction pathways.** HER2 does not have any known ligand but is the preferred association partner of all other HER receptors. Here, intracellular signaling pathways controlled by the activation of EGFR and HER2 are shown. Further details are given in the text. AR – amphiregulin; BTC – betacellulin; EGF – epidermal growth factor; EPG – epigen; EPR – epiregulin; HB-EGF – heparin-binding EGF; MAPK – mitogen-activated protein kinase; NRG – neuregulin; PI3K – phosphatidylinositol 3,4,5-kinase; TGF- $\alpha$  – transforming growth factor  $\alpha$ . Adapted from Ciardiello and Tortora.<sup>83</sup>

EGFR and HER2 belong to a family comprising four homologous receptor tyrosine kinases: EGFR (HER1), HER2, HER3 and HER4 (**Figure 4**). The 180 – 190 kDa sized HER receptors are located at the cell membrane and consist of an extracellular ligand binding domain, a lipophilic transmembrane segment and a cytoplasmic tyrosine kinase domain. Upon ligand binding the four monomeric receptors can associate with each other to form more stable homo- or heterodimers.<sup>84</sup> To date, several growth factor receptor ligands are known. They all share an EGF-like domain and possess different specificity towards the four HER receptors. EGF, transforming growth factor  $\alpha$  (TGF- $\alpha$ ), amphiregulin (AR), and epigen (EPG) bind specifically to EGFR; betacellulin (BTC), heparin-binding EGF (HB-EGF) and epiregulin (EPR) bind both EGFR and HER4; the neuregulins NRG-1 and NRG-2 bind HER3 and HER4; and NRG-3 and NRG-4 bind only HER4. HER2 does not have any known ligand but is the preferred association partner of all other HER receptors.<sup>85</sup> Consequently, it

can be activated upon heterodimerization with another ligand-bound receptor. In tumors, many of the same signaling pathways as in normal cells are stimulated by activated EGFR and HER2. Autophosphorylation triggers the RAS–RAF–MEK–MAPK pathway, which controls gene transcription, cell-cycle progression from the G1 phase to the S phase, and cell proliferation. Furthermore, the PI3K–Akt pathway is triggered, which activates a cascade of anti-apoptotic and pro-survival signals.<sup>82,83</sup>

Although HER receptors reside at the cell surface, they undergo constant trafficking between the plasma membrane and endosomal compartments (**Figure 5**). In the absence of ligands, constitutive trafficking of EGFR and HER2 seem to be very similar.<sup>86</sup> For example, inactive EGFR is internalized relatively slowly ( $t_{1/2} \sim 20 - 50 \text{ min}$ )<sup>87–89</sup> and rapidly recycled back to the cell surface ( $t_{1/2} \sim 5 \text{ min}$ ) resulting in the predominant localization (80 – 90%) of EGFR at the cell surface.<sup>86</sup>

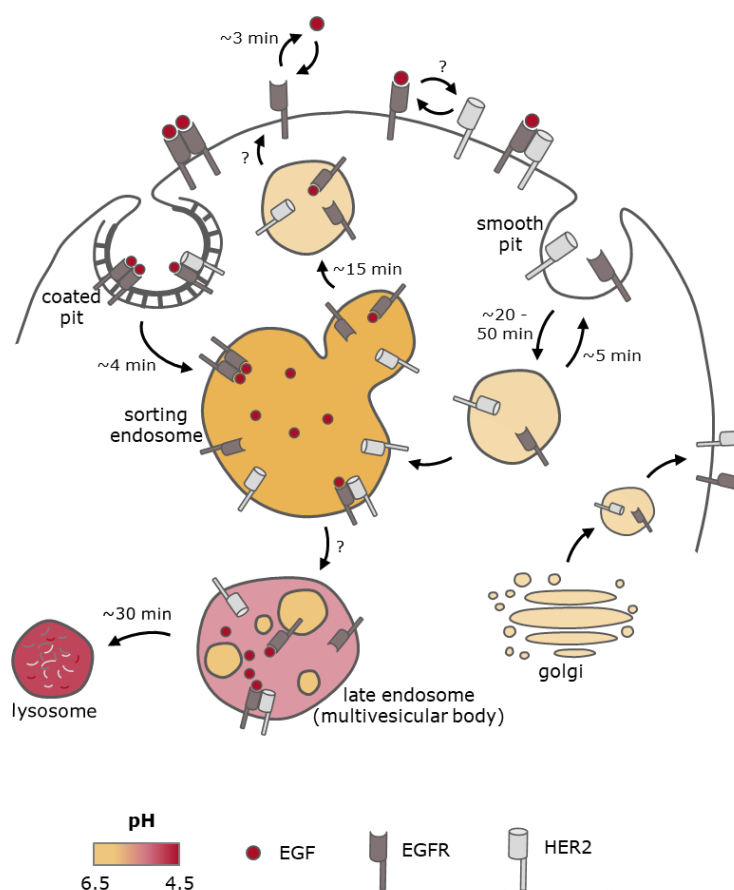


**Figure 5. Trafficking of HER receptors.** Activated EGFR homodimer and EGFR-HER2 heterodimer internalize quickly in clathrin-coated pits *via* receptor-mediated endocytosis. Inactive HER receptors internalize relatively slowly by a smooth pit pathway. Given are the approximate mean times for the specific trafficking processes. Time constants for heterodimerization and formation of multivesicular bodies are unknown. Time for lysosomal fusion includes the time for multivesicular body formation. Further details are explained in the text. Adapted from H. Wiley.<sup>86</sup>

In addition to this major rapid recycling pathway, some EGFR recycles *via* sorting endosomes in a more prolonged pathway ( $t_{1/2} \sim 20 \text{ min}$ ) back to the surface.<sup>86</sup> Through this sorting endosomal route, a small

---

fraction of EGFR ends up in the late endosome and the lysosome where it is degraded. In low to moderate EGFR expressing cells (< 200,000 copies /cell), inactivated EGFR undergoes metabolic turnover with  $t_{1/2} \sim 6 - 10 \text{ h}^{90,91}$ , whereas in EGFR overexpressing cells (e.g. human epidermoid carcinoma A431),  $t_{1/2}$  is 24 h or longer.<sup>92</sup> Consequently, during its life span a receptor shuttles and recycles dozens of times through the cell before it is finally degraded.

In contrast to inactivated EGFR, internalization of ligand activated EGFR is 5 – 10-fold increased ( $t_{1/2} \sim 4 \text{ min}$ )<sup>87</sup> whereas its lysosomal degradation is 3 – 4-fold enhanced.<sup>93</sup> Interestingly, ligand-induced internalization or degradation is not observed for other members of the HER family probably due to the absence of specific internalization sequences in their cytoplasmic domains.<sup>86,93</sup> As a consequence, most signaling from activated EGFR comes from endosomal compartments while other HER family members generate signals mostly from the cell surface.<sup>86</sup>

Currently, there are two approved anti-EGFR mAbs (Cetuximab and Panitumumab) and two approved anti-HER2 mAbs (Trastuzumab and Pertuzumab) on the market. Cetuximab is a human-mouse chimeric IgG1 that received FDA approval for advanced colorectal cancer in 2004 and for squamous cell carcinoma of the head and neck in 2006.<sup>94</sup> Cetuximab binds to the extracellular domain of EGFR with twice the affinity of the natural ligands, thereby blocking ligand binding and subsequent receptor dimerization and activation (**Figure 6C**).<sup>67</sup> In analogy to natural ligand binding, cetuximab induces receptor internalization (**Figure 6A**) and degradation.<sup>95</sup> Interestingly, receptor degradation with natural ligand is faster than with cetuximab engagement (EGFR turnover  $t_{1/2}$  on A431 cells decreases from 17.8 h to 5.6 h upon addition of EGF and to 8.5 h in response to addition of Cetuximab murine precursor mAb 225).<sup>96</sup> Moreover, Cetuximab's IgG1 scaffold could elicit host immune response including antibody-dependent cell mediated cytotoxicity (ADCC) resulting in recruitment of immune effector cells which induce tumor cell lysis (**Figure 6B**).

In contrast to chimeric Cetuximab, Trastuzumab is a humanized IgG1 which was first approved by the FDA in 1998 for patients with metastatic HER2 overexpressing breast cancers.<sup>97</sup> It binds to the juxtamembrane region of the extracellular HER2 domain and blocks receptor dimerization, autophosphorylation and downstream signaling pathways (**Figure 6D**). Furthermore, Trastuzumab binding prevents proteolytic shedding of the extracellular domain which would leave a truncated membrane bound and phosphorylated HER2 fragment (p95) with increased kinase activity (**Figure 6E**).<sup>98</sup>

To which extent Trastuzumab induces HER2 degradation (**Figure 6A**) depends strongly on HER2 expression levels. HER2 high expressing human cancer cell lines (e.g. SKBR-3, HCC-1954, BT-474) exhibit efficient HER2 recycling and only a small fraction of Trastuzumab-HER2 complexes enter the lysosomal pathway. By contrast, in HER2 low expressing cells (e.g. LNCaP, HCC-2185) the lysosomal pathway appears to be the major trafficking route for Trastuzumab-HER2 complexes and Trastuzumab treatment substantially reduces HER2 levels.<sup>99</sup>

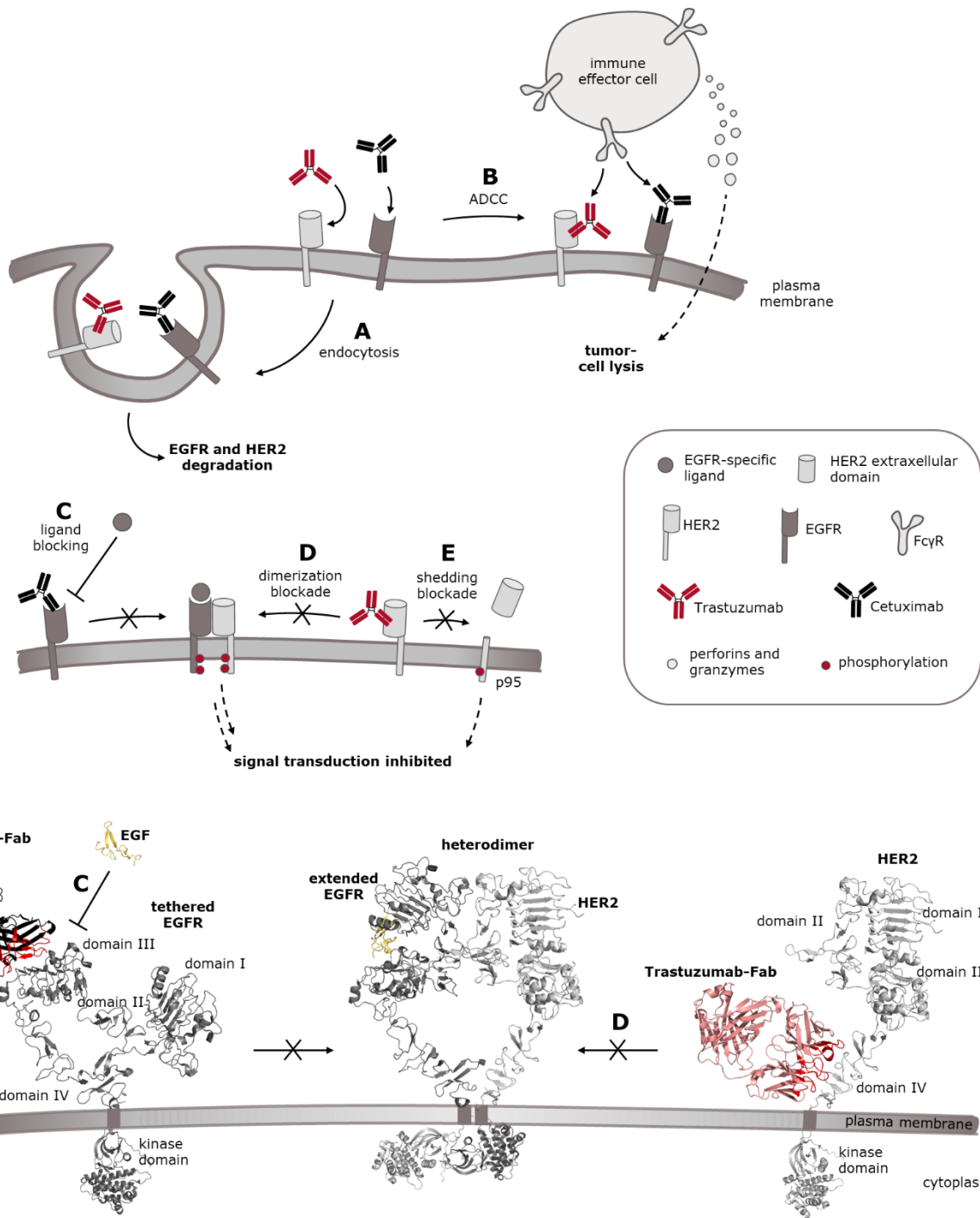


**Figure 6. Cetuximab and Trastuzumab mode of action.** (A) Both Cetuximab and Trastuzumab induce EGFR and HER2 internalization and lysosomal degradation which result in decreased number of surface receptors and reduced signal transduction. For Trastuzumab, the rate of degradation depends strongly on the HER2 surface density.<sup>99</sup> (B) Furthermore, binding of Cetuximab and Trastuzumab leads to ADCC causing tumor cell lysis by released perforins and granzymes from immune effector cells. (C) As Cetuximab binds to the EGFR ligand binding site at domain III with higher affinity than natural ligands, it blocks ligand binding and subsequent receptor activation. (D) Trastuzumab inhibits HER2 heterodimerization and downstream signaling by binding to the HER2 region IV. (E) In addition, Trastuzumab blocks proteolytic shedding of the extracellular HER2 domain which would leave a truncated membrane bound and phosphorylated HER2 fragment (p95) with increased kinase activity.<sup>83,100</sup> CDR regions of Cetuximab- and Trastuzumab-Fab crystal structures are colored in red. EGFR-HER2 heterodimer crystal structure and kinase domains were arranged manually for illustration. (PDB: Cetuximab-Fab-tethered EGFR: 1YY9<sup>101</sup>; EGFR inactivated kinase domain: 1M14<sup>102</sup>; extended EGFR-EGF: 3NJP<sup>103</sup>; Trastuzumab-HER2: 1N8Z<sup>104</sup>; HER2 inactivated kinase domain: 3PP0<sup>104</sup>).

Furthermore, ADCC appears to play also an important role in the mode of action of Trastuzumab (**Figure 6B**). For example, in mice with suppressed immune effector NK cells, Trastuzumab inhibited tumor growth only by 29% whereas in mice with intact NK cells, 96% tumor growth inhibition was observed upon Trastuzumab treatment.<sup>105</sup>

The great success and selectivity of monoclonal antibodies led to the development of antibody-drug conjugates as another therapeutic modality for cancer treatment which is described in the following.

#### 4.4. Antibody-Drug Conjugates as Targeted Therapeutics

Antibody-drug conjugates (ADCs) are one of the fastest growing classes of targeted anticancer therapeutics with alone six new ADCs approved by the FDA between 2019 and April 2021.<sup>68,106</sup> ADCs link the great selectivity of monoclonal antibodies with cell killing abilities of cytotoxic drugs and expand the therapeutic index by guiding these highly potent toxins to tumor cells (**Figure 7**).

##### 4.4.1. Structure and Mode of Action

ADCs are composed of a cytotoxic drug (often referred to as payload or warhead) attached *via* a cleavable or non-cleavable linker to a humanized or fully human mAb (**Figure 7A**).

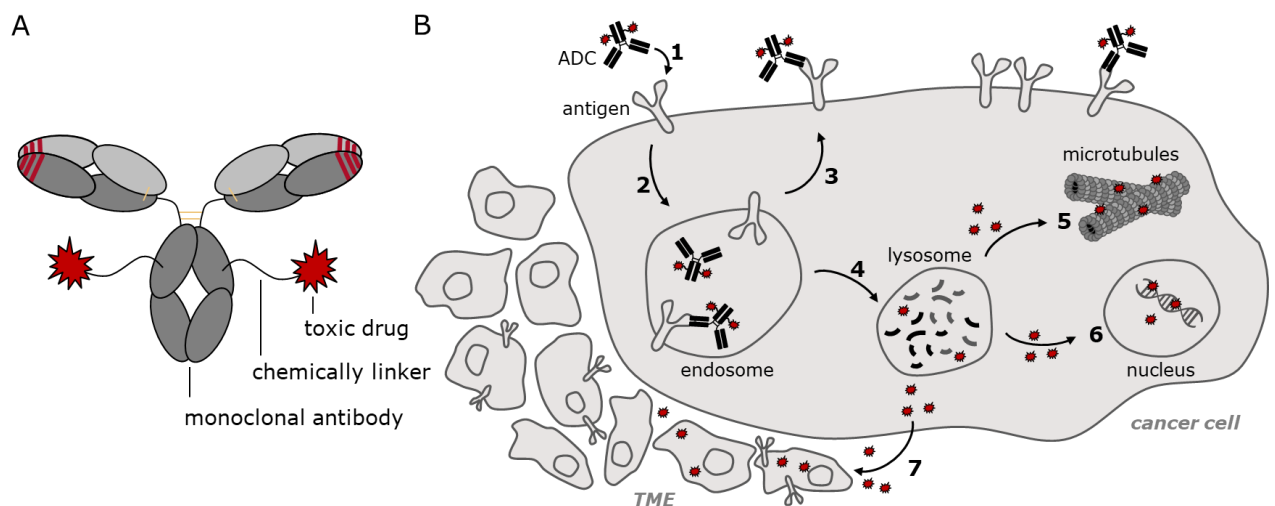


**Figure 7. ADC structure and mode of action.** (A) Schematic representation of an IgG-based ADC. (B) The ADC binds *via* the mAb selectively to its target antigen on the membrane of a cancer cell (1). After receptor-mediated endocytosis and travelling to the endosome (2), a fraction of receptor bound ADC returns directly back to the plasma membrane (3) while unbound ADC and the other fraction of receptor bound ADC travel to the lysosome (4). There, ADCs release their toxic payload by linker cleavage or mAb degradation. The released toxic drug diffuses into the cytoplasm and nucleus where it disrupts microtubules (5) or induces DNA damage (6). Moreover, hydrophobic drugs can diffuse out of the (dying) cancer cell and enter and kill adjacent tumor and healthy cells (7). This effect is known as “bystander effect” in the literature.<sup>107</sup>

---

ADCs act in analogy to a Trojan horse (**Figure 7B**): Once the antibody has bound selectively to its target on a tumor cell, it is internalized *via* receptor-mediated endocytosis. Depending on the target receptor, a certain fraction of receptor bound ADC can be recycled from early endosomes back to the cell surface while the other fraction, including soluble ADCs, may end up in lysosomes. Herein, the payload is liberated by e.g., the action of hydrolytic enzymes which can either specifically cleave the linker motif or degrade the antibody in its entirety. Finally, the cytotoxic drug is released into the cytoplasm where it interferes with critical cellular machinery inducing cell apoptosis. A special feature of ADCs carrying hydrophobic payloads is that a cell does not necessarily have to be exposed to the intact ADC itself as released hydrophobic payload from a targeted neighboring cell can cross membranes and diffuse into non-targeted cells (**Figure 7B**). This “bystander effect” increases exposure and induces cell killing in adjacent target positive and negative cells paying also tribute to tumor heterogeneity.<sup>108,109</sup>

The individual components of ADCs were already extensively reviewed elsewhere.<sup>110–114</sup> In the following some of the most recent advancements in the ADC field are highlighted.

#### 4.4.2. Advancements in the ADC Field

First and second-generation ADCs were mainly manufactured using random lysine coupling chemistry or interchain cysteine conjugation to link the payload to the antibody.<sup>115</sup> The resultant products were highly heterogeneous mixtures of ADCs having varying numbers of payloads attached at different positions. ADC subgroups typically have different stability properties, with some subgroups showing unfavorable pharmacokinetics or premature payload release and thus, reduced effectiveness and possibly toxicity.<sup>116–118</sup> It was soon recognized that site-specific conjugation yielded more homogeneous ADCs with defined physical properties and enhanced preclinical therapeutic indices.<sup>119</sup> For example, the genetically incorporation of cysteine residues at specific positions in the antibody scaffold allowed for selective chemical conjugation of maleimide- and disulfide-based linkers. Several positions were identified (e.g. S239C, D265C) where conjugation was highly efficient and generated ADCs had low aggregation tendency without showing premature drug release in circulation.<sup>116,117,119–123</sup>

Another site-specific conjugation technique involves the enzyme microbial transglutaminase (mTG). mTG catalyzes the formation of isopeptide bonds between glutamine residues and substrates possessing amino groups, e.g. lysines. Reactive glutamines were either genetically incorporated, often by LC or HC C-terminally fused tags (e.g. LLQGA), or were uncovered within the native mAb structure (Q295) by enzymatic or genetic removal (N297A) of glycosylation at position N297.<sup>124</sup> Recently, Dickgiesser *et al.* published genetically engineered mTG variants which enable efficient site-specific conjugation to position Q295 of native, fully glycosylated antibodies.<sup>125</sup> This method allows to use off-the-shelf antibodies and makes antibody engineering or processing before conjugation obsolete. Other recent site-specific conjugation

techniques include for example, genetically encoded non-natural amino acids<sup>126</sup>, glycan conjugation<sup>127</sup> and non-covalent affinity peptides<sup>128,129</sup> and ligands<sup>130</sup>.

In addition to the conjugation site, the linker structure can confer stability to an ADC and prevent premature drug release as well.<sup>131</sup> Widely applied valine-citrulline (Val-Cit) linkers can be efficiently cleaved by lysosomal cathepsins overexpressed in tumor cells but also by extracellular murine carboxylesterase 1c (mCes1c), which complicates preclinical development (**Figure 8A**).<sup>132,133</sup> Several groups showed that structural modifications at the position prior to Val did not drastically alter cathepsin cleavage but prevented Val-Cit linkers from mCes1c-mediated cleavage in mouse serum (**Figure 8B**).<sup>133–135</sup> Besides improving established linker structures, other enzymatically-cleavable linkers were explored in the ADC context such as  $\beta$ -glucuronidase<sup>136,137</sup>,  $\beta$ -galactosidase<sup>138</sup> or legumain<sup>139</sup> cleavable linkers (**Figure 8C**). Moreover, linkers for non-internalizing ADCs were recently reported.<sup>140,141</sup>

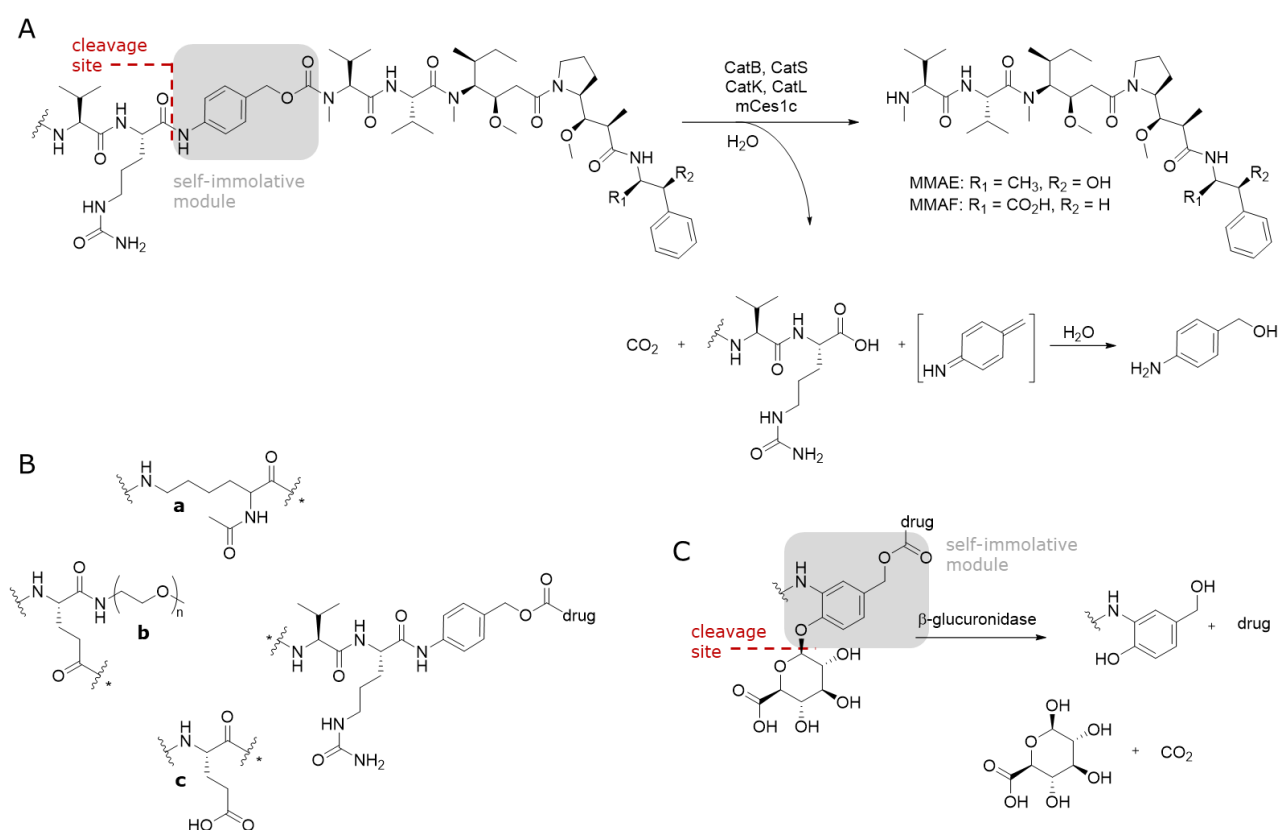


**Figure 8. ADC linker structures.** (A) Conventional Val-Cit linker with monomethyl auristatin E (MMAE) as applied in approved ADCs Brentuximab vedotin, Polatuzumab vedotin and Enfortumab vedotin. Val-Cit linkers are not only cleaved by lysosomal cathepsin B (CatB) but also equally efficient by lysosomal cathepsin S (CatS) and less efficiently by lysosomal cathepsins K and L (CatK, CatL).<sup>132</sup> In mouse serum, murine carboxylesterase 1c (mCes1c) cleaves Val-Cit at the same position as cathepsins thereby interfering with proper preclinical ADC assessment in this species.<sup>133</sup> (B) Several groups found that linker modifications (a<sup>133</sup>, b<sup>134</sup>, c<sup>135</sup>) at the position prior to Val prevented cleavage by mCes1c while cathepsin linker processing was not affected. (C)  $\beta$ -glucuronidase sensitive linkers are more hydrophilic than Val-Cit linkers and exhibit great plasma stability in humans and preclinical species.<sup>136,137</sup>

The overwhelming majority of ADC payloads currently in use are DNA damaging agents and tubulin inhibitors. Other payload classes with a different mode of action include, e.g. amanitins and proteolysis targeting

chimeras (PROTACs) (Figure 9). Of these, the naturally RNA polymerase II inhibiting amanitin from the green death cap mushroom *Amanita Phalloides* is more advanced as ADC payload with one amanitin-ADC candidate already at the gate to enter clinical development.<sup>142</sup> In contrast, PROTACs are the newcomers in the ADC payload field<sup>143–147</sup> and in drug discovery at all.<sup>148</sup> PROTACs are fully synthetic small molecules without relation to natural products. They bind to a protein of interest (POI) and an E3 ligase, thereby forming a ternary complex in which the E3 ligase transfers ubiquitin onto the POI. Subsequently, the ubiquitylated POI is degraded by the proteasome and the unmodified PROTAC is released, ready to initiate another protein degradation cycle. PROTACs are currently causing a lot of excitement because their mode of action promises to expand the target space for the drug discovery process.<sup>148</sup> Attaching PROTACs to antibodies would allow for targeted delivery since they are not cell-type selective.<sup>143–147</sup>

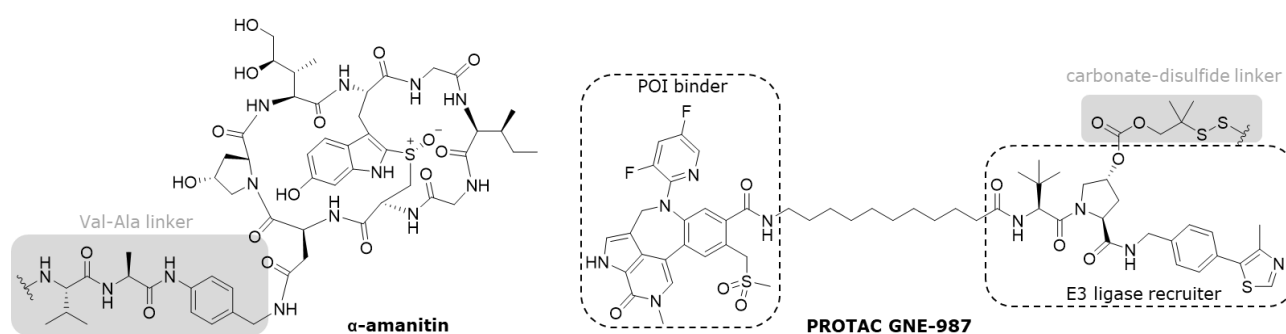


**Figure 9. Novel ADC payloads.**  $\alpha$ -amanitin with cleavable Val-Ala linker as employed in preclinical ADC HDP-101.<sup>142</sup> Bromodomain-containing protein 4 (BRD4) degrading PROTAC GNE-987 with disulfide-containing linker attached *via* a carbonate to the von-Hippel Lindau (VHL) E3 ligase recruiter VH032.<sup>143</sup> POI – protein of interest.

Most ADC payloads possess a hydrophobic nature and highly toxin-loaded, hydrophobic ADCs are prone to aggregation and accelerated undesired non-specific uptake *via* normal cells.<sup>149</sup> Therefore, highly hydrophilic polymeric polyol-<sup>150</sup> and dextran polysaccharide<sup>151</sup> scaffolds were developed to achieve high DAR loadings and enhanced efficacy without compromising physicochemical and pharmacokinetic properties.

To date, clinically approved ADCs and the vast majority in clinical and pre-clinical development consist of a monoclonal IgG for targeting.<sup>111</sup> However, several other antibody- or antibody-like formats were recently explored, mainly with the objective to increase solid tumor penetration. These small-format drug conjugates are discussed in more detail in section 4.6. At this point, the use of bispecific antibodies (bsAbs) in ADCs should be mentioned. De Goeij *et al.* could demonstrate that a bispecific ADC targeting HER2 and the lysosome-associated membrane glycoprotein 3 (LAMP3 or CD63) showed superior *in vivo* efficacy compared to monospecific HER2 and LAMP3 ADC constructs due to enhanced lysosomal trafficking.<sup>152</sup> Furthermore, bsAbs can enhance the tumor specificity of ADCs as recently shown for the first-in-class bispecific ADC

---

M1231.<sup>153</sup> M1231 binds to solid tumor targets MUC1 and EGFR and also showed higher efficacy compared to monospecific EGFR and MUC1 ADCs in patient-derived xenograft (PDX) models.<sup>153</sup>

Classical ADCs are directed against internalizing targets since their mode of action requires lysosomal degradation for efficient payload release. However, Neri and coworkers demonstrated that ADCs targeting non-internalizing antigens (e.g. fibronectin, tenascin-C) are also therapeutically active when linkers can be cleaved in the extracellular space.<sup>140,154–156</sup>

The highly complex interplay between the individual components of an ADC and external factors such as target biology led to modelling and simulation approaches to better understand and assess the impact of design parameters on pharmacokinetics and pharmacodynamics. Especially the academic research of Aman P. Singh and Dhaval K. Shah as well as Greg M. Thurber should be mentioned here. They built up several mechanistic models based on experimentally accessible kinetic rate constants (e.g. internalization, payload lysosomal liberation, payload cellular efflux) to simulate for example the *in vitro* potency<sup>157,158</sup> but also the *in vivo* efficacy<sup>159–161</sup> or the biodistribution<sup>108,162,163</sup> of ADCs. Moreover, the developed models were validated with experimental data. Other groups from industry seem to adopt to modelling and simulation approaches to guide their ADC design and development.<sup>164,165</sup>

#### 4.4.3. Clinically validated ADCs

To date, ten ADCs have been approved by the FDA (**Table 1**). The first ADC, Gemtuzumab ozogamicin, was initially approved for the treatment of relapsed acute myeloid leukemia (AML) in 2000. It consists of an acid-labile hydrazone linker which is attached *via* random lysine coupling to the anti CD33 IgG4 Gemtuzumab. Since then, the understanding of ADC design parameters increased tremendously, resulting in more homogeneous ADCs such as Brentuximab vedotin or Trastuzumab deruxtecan. In both ADCs, a cathepsin B cleavable linker-payload is site-specifically attached to reduced interchain cysteins yielding a defined drug-to-antibody ratio (DAR) of 4 or 8.

Compared to conventional chemotherapy, ADCs have an improved tolerability. However, new ADC-associated toxicities have emerged and their origin is not always fully understood.<sup>166,167</sup> Toxic effects are typically driven by the payload, but target and linker may specify the organ where toxicity is observed.<sup>166</sup>

Dose-limiting toxicities prevent currently approved ADCs from reaching their full potential leading to only moderate efficacy and improvements in overall survival. However, the results of the last years are promising as those ADCs for which important findings have been considered in ADC design and development are still ahead of approval. Nevertheless, several factors that limit the success of ADCs are still not sufficiently considered in the current design of advanced clinical candidates. In the next section limited exposure is outlined as one mayor limiting factor for the success of antibody-based therapies.<sup>168</sup>

**Table 1. Main characteristics of approved ADCs.** The first approved ADC Mylotarg received accelerated approval in 2000, was withdrawn from market in 2010 and re-approved in 2017. ALCL – anaplastic large-cell lymphoma; ALL – acute lymphoblastic leukemia; AML – acute myeloid leukemia; BCMA – B-cell maturation antigen; CL – cleavable linker; Cys – interchain cysteine conjugation; DLBCL – diffuse large B-cell lymphoma; HL – Hodgkin lymphoma; Lys – random lysine coupling; nCL – non-cleavable linker; TNBC – triple negative breast cancer.

drug	company	ADC	year appr.	indication	target	Ab	conjug.	drug	drug MOA	linker	DAR
<b>Mylotarg</b>	Pfizer	Gemtuzumab ozogamicin	2000/ 2017	AML	CD33	IgG4	Lys	calichea micin	DNA damager	CL hydrarzone disulfide	2.5
<b>Adcetris</b>	Seagen	Brentuximab vedotin	2011	HL, ALCL	CD30	IgG1	Cys	MMAE	tubulin inhibitor	CL Val-Cit	4
<b>Kadcyla</b>	Roche	Ado-Trastuzumab emtansine	2013	HER2+ breast c.	HER2	IgG1	Lys	DM1	tubulin inhibitor	nCL thioether	3.5
<b>Besponsa</b>	Pfizer	Inotuzumab ozogamicin	2017	ALL	CD22	IgG4	Lys	calichea micin	DNA damager	CL hydrarzone disulfide	6
<b>Polivy</b>	Roche/ Seagen	Polatuzumab vedotin	2019	DLBCL	CD79b	IgG1	Cys	MMAE	tubulin inhibitor	CL Val-Cit	3.5
<b>Padcev</b>	Astellas/ Seagen	Enfortumab vedotin	2019	urothelial	Nectin-4	IgG1	Cys	MMAE	tubulin inhibitor	CL Val-Cit	4
<b>Enhertu</b>	Daiichi S./ Astraz.	Fam-Trastuzumab deruxtecan	2019	HER2+ breast c.	HER2	IgG1	Cys	Dxd	topoisom. I inhib.	CL Gly-Gly-Phe-Gly	8
<b>Trodelyv</b>	Immunom edics	Sacituzumab govitecan	2020	TNBC	Trop-2	IgG1	Cys	SN-38	topoisom. I inhib.	CL carbonate	8
<b>Blenrep</b>	GSK	Belantamab mafodotin	2020	multiple myeloma	BCMA	IgG1	Cys	MMAF	tubulin inhibitor	nCL	3-4
<b>Zynlonta</b>	ADC Therapeut	Loncastuximab tesirine	2021	DLBCL	CD19	IgG1	Cys	PBD dimer	DNA damager	CL Val-Ala	2.3

## 4.5. Limitations of Antibody-based Therapies

### 4.5.1. Solid Tumor Exposure and Efficacy

The fundamental prerequisite of therapeutic efficacy of mAbs or ADCs in solid cancers is the exposition of cancer cells to cytotoxic doses of antibody or payload. The obvious assumption to increase exposure by administering higher doses is generally true but cannot be applied for any drug including the class of ADCs due to dose limiting toxicities (DLTs). The major factor limiting exposure of antibody-based therapeutics is incomplete penetration into the tumor. Consequently, cancer cells in the core of a solid tumor survive treatment or may even develop resistance to therapy due to exposure to non-efficacious drug doses. **Figure 10** illustrates schematically the fundamental relationship of solid tumor penetration/ exposure, efficacy, administered dose and DLT by plotting drug concentration against tumor depth. Here, drug A (grey line) shows an unfavorable solid tumor penetration profile and remains mainly in the outer periphery of the tumor. Increasing the dose of drug A (red line) exposes more tumor cells to therapeutically active drug concentrations but induces also toxic side effects since the MTD is exceeded (filled red area). Drug B (black solid line) shows a more homogeneous and favorable penetration profile exposing additional tumor cells to an efficacious dose while preventing dose limiting toxicities.

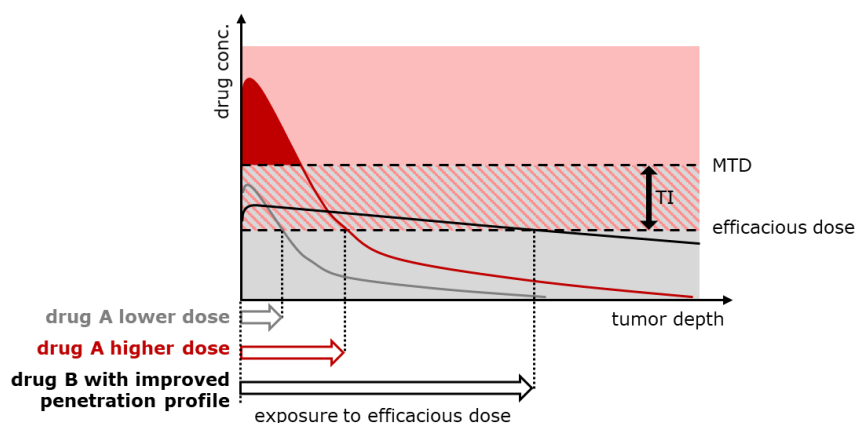


**Figure 10. Solid tumor exposure and efficacy.** Another factor influencing efficacy is the time which cells need to be exposed to a certain concentration to achieve a pharmacodynamic effect. For the sake of simplicity, the time factor has been neglected in the graph above. *MTD* – maximum tolerated dose; *TI* – therapeutic index.

The tumor penetration profile of a drug is governed by multiple factors such as the biological properties of the tumor and the target as well as the physical and pharmacokinetic properties of the antibody construct.<sup>169</sup> This will be explained in more detail in the following section.

#### 4.5.2. Solid Tumor Penetration – A Complex Interplay of Various Factors

Antibody targeting of solid tumors is a complex process that involves extravasation across tumor blood capillaries, diffusion and binding within the tumor interstitial space, endocytotic uptake and catabolism in tumor cells as well as systemic clearance (Figure 11).<sup>170–172</sup>

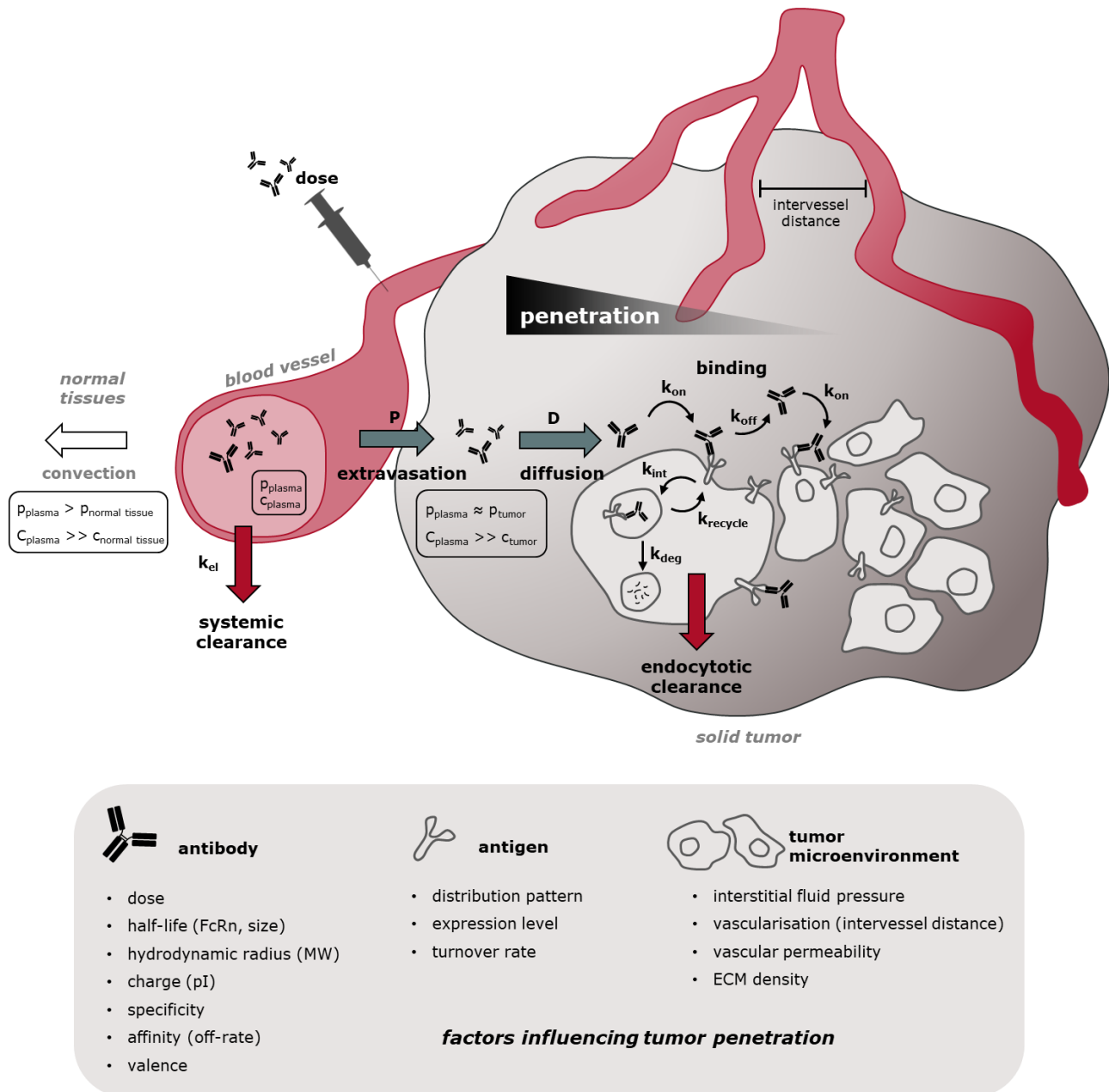


**Figure 11. Factors influencing antibody tumor penetration.** Tumor penetration depends on a variety of different factors including properties of the antibody, the antigen and the tumor microenvironment. Antibody extravasation and diffusion drive tumor penetration while antigen binding, endocytotic and systemic clearance prevent tumor penetration.  $c$  – antibody concentration;  $D$  – diffusion coefficient;  $k_{deg}$  – antigen degradation rate;  $k_{el}$  – antibody plasma elimination rate;  $k_{int}$  – antigen internalization rate;  $k_{off}$  – antibody binding off rate;  $k_{on}$  – antibody binding on-rate;  $k_{recycle}$  – antigen recycling rate;  $P$  – permeability coefficient;  $p$  – pressure;  $pI$  – antibody isoelectric point.

---

The interplay of all these factors results in a dynamic, tumor penetrating boundary with high antibody concentrations on one side and almost no antibody present on the other side. This boundary shifts towards the center of the tumor until the opposing rates that either drive or prevent tumor penetration are in equilibrium. If an equilibrium is reached before the tumor is fully penetrated, the boundary apparently gets stuck leaving tumor regions unexposed – an effect also referred to as binding site barrier. This situation occurs when extravasation and diffusion are limited by target binding and antibody degradation inside tumor cells or by systemic clearance.<sup>170,171</sup>

In the following the molecular background of these processes is explained in more detail.

### **Extravasation**

After intravenous infusion, antibodies distribute in the human body into a volume approximately equal to the plasma volume ( $V_c$  0.045 L/kg). When reaching steady state, the overall volume of distribution approximately has doubled ( $V_{d,ss}$  0.1 L/kg), reflecting only limited distribution into extravascular space.<sup>75,169</sup> In normal tissues the extravasation process of antibodies mainly relies on convective transport driven by a blood-tissue hydrostatic gradient.<sup>75</sup> In contrast, in solid tumors the leaky blood vasculature and poor lymphatic drainage elevate the interstitial fluid pressure (see also section 4.1.2) neutralizing or even inverting the hydrostatic gradient.<sup>172</sup> Consequently, antibodies must diffuse against the pressure gradient to extravasate across the vessel wall into solid tumors. However, the leakiness (e.g. pore size) of tumor blood vessels and the lack of lymphatics also facilitate the accumulation and retention of macromolecules > 45 kDa in solid tumors.<sup>169</sup> This phenomenon is termed the enhanced permeability and retention (EPR) effect and is responsible for tumor accumulation of even untargeted macromolecules such as serum albumin.<sup>173,174</sup> It is evident that the more vascularized a solid tumor is, the higher is the amount of drug that can extravasate into the tumor and the shorter is the distances a drug must travel within the tumor for complete penetration (typically intercapillary distances are between 100 – 200  $\mu\text{m}$  in the tumor core<sup>175</sup>).

Extravasation can be characterized by the vascular permeability coefficient  $P$ :

$$J_{extravasation} = P \cdot \frac{\partial[\text{drug}]}{\partial x} \quad (1)$$

where  $J$  is the molar flux of antibody across the capillary wall and  $\partial[\text{drug}]/\partial x$  is the antibody concentration gradient across the capillary wall.  $P$  is a function of antibody properties (e.g. size, shape and charge) and the vessel wall (e.g. pore size).<sup>176</sup> In the context of solid tumor penetration the inversely proportional relationship between  $P$  and the molecular size was modeled and fitted to experimental data demonstrating clearly that reducing drug size increases permeability  $P$  and extravasation  $J$ .<sup>79,177</sup>

---

A tumor pharmacokinetic model of Thurber and Weissleder demonstrated that tumor penetration by macromolecules such as antibodies is typically limited by permeability and blood vessel surface area, even in tumors with fenestrated vessels.<sup>178</sup> As a result, typical antibody plasma concentrations of 1  $\mu\text{M}$  correspond to only 1 nM at the capillary surface in contact with the tumor tissue after extravasation.<sup>170</sup>

### **Diffusion**

After successful extravasation, the antibody moves away from the capillary surface and penetrates the extracellular matrix of the tumor tissue. In contrast to normal tissues, tumor penetration is governed by diffusion as the pressure gradient in tumors is negligible. The process of diffusion where molecules move from regions with high concentration to regions of lower concentration can be described by Fick's law:

$$J_{diffusion} = -D \cdot \frac{\partial[drug]}{\partial x} \quad (2)$$

In analogy to the extravasation process, the molar flux  $J$  is characterized by a diffusion coefficient  $D$  and a concentration gradient  $\partial[drug]/\partial x$  as main driving force.<sup>171</sup>  $D$  is inversely proportional to molecular size and transport barriers within the densely packed ECM. It can be modeled as a function of molecular size<sup>177</sup> or approximated by the more descriptive Stokes-Einstein equation for diffusion of spherical particles in a liquid:

$$D = \frac{k_B \cdot T}{6 \cdot \pi \cdot \eta \cdot r_H} \quad (3)$$

where  $k_B$  is Boltzmann's constant,  $T$  is the absolute temperature,  $\eta$  is the dynamic viscosity and  $r_H$  is the hydrodynamic radius of the spherical particle.

In addition to size, i.e.  $r_H$ , the shape and the charge of a macromolecule impacts diffusivity. For example, a 150 kDa IgG molecule diffuses more slowly than a more globular-like 150 kDa dextran molecule.<sup>169</sup> Furthermore, molecules with an isoelectric point (pI) between 5 and 9 show superior tumor penetration compared to molecules with a pI outside that range.<sup>169</sup>

### **Target Binding**

As soon as the antibody diffuses into the tumor tissue, it encounters a tumor cell and binds the target antigen on its surface. The interaction of the antibody and the antigen is characterized by the affinity of the antibody usually expressed as dissociation constant  $K_D$  ( $K_D = k_{off}/k_{on}$ ). The affinity of an antibody must balance several competing processes: (1) It must be high enough to retain the antibody in the tumor tissue and (2) allow the antibody to remain sufficient time in receptor-bound state to trigger its pharmacodynamic effect.

---

Simultaneously, affinity must be (3) as low as possible to allow for substantial dissociation and tumor penetration.

Adams *et al.* studied tumor uptake and retention of five radiolabeled mutant scFv fragments targeting the same HER2 epitope with varying affinities ( $K_D$   $10^{-7}$  –  $10^{-11}$  M) in normal and anephric mice after 24 h.<sup>179</sup> While the lowest affinity variant ( $K_D$   $3.2 \cdot 10^{-7}$  M) only showed appreciable retention after elimination of the fast clearance term by rendering the mice anephric, maximum tumor retention was obtained with the  $K_D$   $10^{-9}$  M affinity variant in both normal and anephric mice. Higher affinity ( $K_D$   $10^{-10}$  –  $10^{-11}$  M) did not result in better tumor retention.<sup>179</sup> Computational model data from Wittrup and coworkers support the existence of the  $K_D \sim 10^{-9}$  M affinity threshold for 25 kDa sized scFv tumor uptake and retention.<sup>177,180</sup> Their model data demonstrate also that the affinity threshold is size dependent, with smaller molecules (particularly < 50 kDa renal clearance cutoff) requiring higher affinity to be retained in the tumor.<sup>177</sup> This is due to their faster systemic clearance and higher permeability that facilitates unbound molecules to diffuse back from the tumor into the circulation once the circulatory concentration has dropped below the tumor concentration.<sup>177</sup> That lower affinity leaves more molecules in unbound state and reduces retention was also demonstrated experimentally by Thurber and Wittrup in a tumor spheroid model applying scFvs with varying affinities ( $K_D$  8 nM and 30 pM).<sup>181</sup> Antibody retention can not only be increased by higher affinity but also by bivalency as shown for scFv dimers or diabodies.<sup>182,183</sup> This becomes obvious when considering avidity as the accumulated strength of multiple affinities.

The off-rate ( $k_{off}$ ) of an antibody determines its residence time at the target receptor and thus the time to trigger the pharmacodynamic effect (e.g. ADCC, signal inhibition, internalization).<sup>169</sup> Generally, it does not make sense to prolong receptor residence time beyond the time necessary for the therapeutic effect, as this would just prevent homogeneous tumor penetration. This was also comprehensively demonstrated in a study by Rudnick *et al.*<sup>184</sup> They showed for a set of four mutant IgGs targeting the same HER2 epitope with different affinities that the amount of internalized and degraded antibody does not increase under receptor saturating conditions when  $k_{off} < k_{int}$ .<sup>184</sup> Instead, tumor penetration distance from blood vessels was increased for antibodies with  $K_D$  in the order: 0.6 nM < 7 nM < 23 nM < 270 nM.<sup>184</sup> These results indicate that for efficient drug delivery by ADCs, the off-rate should be equal or slightly slower than the internalization rate to prevent ADC dissociation before the receptor is internalized. However, depending on the potency of the drug, internalization and lysosomal degradation of only a fraction of receptor bound ADC may be sufficient for efficient cell killing.<sup>169</sup> In this case, an off-rate in the range of the internalization rate could provoke an “overkilling” of cells and unnecessarily limit tumor penetration.

That lower affinity or monovalency results in more homogeneous tumor penetration was repeatedly demonstrated for antibodies *in vitro*<sup>181</sup> and *in vivo*<sup>184–187</sup>. More recently it was shown that lower affinity drug conjugates showed superior efficacy in xenograft models possibly due to their improved tumor

---

penetration.<sup>188,189</sup> In addition, lower affinity ADCs seem to be beneficial for drug safety as they do not mediate strong toxic effects in non-cancerous cells expressing only low levels of the target.<sup>190,191</sup>

When choosing the appropriate affinity for an antibody, the applicable antibody dose and antigen density must also be considered. For example, when the antibody-based therapeutic can only be administered at low doses or when antigen density is high, a lower affinity seems more appropriate to prevent a binding site barrier in the tumor periphery.

### **Local Endocytotic Clearance**

Endocytotic uptake and degradation is indispensable for the mode of action of a classical ADC but represents also a significant sink for antibody clearance in the tumor tissue if  $k_{off} < k_{int}$  and if receptor recycling rates are low. Consequently, tumor penetration is enhanced when endocytotic clearance is low. Endocytotic clearance and antibody net uptake is reduced when intact antibody is recycled back to the surface in receptor bound state and prevents binding of another antibody.<sup>171</sup> This is typically observed for Trastuzumab in HER2 high expressing cell lines.<sup>99</sup> In contrast, high antigen turnover rates can set an inherent limit to tumor penetration of antibodies as demonstrated by Ackerman *et al.* in tumor spheroid experiments with cells expressing targets with different metabolic turnover half-lives.<sup>192</sup> If the antigen is replaced at a rate similar to the diffusion of the antibody, complete penetration may be impossible.<sup>192</sup> Besides antigen turnover, the antigen density has significant impact on tumor penetration. Several groups demonstrated in tumor spheroids with different target expression levels that higher antigen density decreases antibody penetration distance.<sup>192,193</sup> Antigen expression above levels necessary for the therapeutic effect, only negatively impact tumor penetration.

Higher dosing is a general strategy to overcome endocytotic clearance and to increase tumor penetration but is less applicable for highly toxic ADCs. Groups around Greg M. Thurber and Dhaval K. Shah pointed out two possible solutions of this dilemma: (1) lowering the DAR so that higher ADC doses can be administered at equal payload doses<sup>108</sup> or (2) increasing the number of target binders and lowering the effective DAR by co-administering unconjugated antibody together with high DAR ADC<sup>161,194,195</sup>. Recently, another group reported an alternative strategy to overcome endocytotic clearance of ADCs by co-administration of anti-idiotypic nanobodies which transiently competitively inhibit the ADC-antigen binding thereby increasing tumor penetration.<sup>196</sup> All strategies aim to “match the single-cell potency with single cell delivery” to maximize ADC efficacy.<sup>194</sup>

### **Systemic Clearance**

Besides local endocytotic clearance in the tumor, solid tumor penetration is also reduced by systemic clearance in kidneys, liver or endothelia. Systemic clearance from the plasma decreases the antibody

concentration gradient that drives extravasation into the tumor and diffusion within the tumor. Whether a tumor can be fully penetrated depends on whether this is achieved before the antibody is cleared from circulation. As repeatedly mentioned, antibodies have long circulatory half-lives mainly due to FcRn-mediated salvage recycling maintaining a sufficiently high plasma-tissue concentration gradient over several days. In contrast, smaller proteins and antibody fragments below the cutoff size of glomerular filtration (~ 60-70 kDa) lacking FcRn binding, are cleared rapidly through the kidneys.<sup>177,197</sup> Resultant half-lives in the range of minutes mean that the concentration gradient can only be maintained for a short time. Consequently, long-living IgGs or 100 kDa sized F(ab')<sub>2</sub> fragments usually outcompete the initial fast tumor accumulation of smaller short-living antibody fragments by higher overall tumor uptake in the long term.<sup>169,185,186,198</sup>

### ***Semiquantitatively Scaling Relationships of Tumor Penetration***

The complex interplay and interdependencies of all above-mentioned factors makes it difficult to understand the impact of a single factor on tumor penetration without the help of computational modeling. Nevertheless, the qualitative influence of key factors and the overall limiting process can be estimated by the help of dimensionless numbers proposed by Thurber, Schmidt and Wittrup.<sup>170,171,199</sup> These numbers compare either endocytotic or systemic clearance rates with the transport rates into the tumor (diffusion or extravasation) to predict whether an antibody can saturate a tumor up to a certain distance  $R$  or whether it will be cleared prior to reaching  $R$ .

The Thiele modulus  $\varphi^2$  compares the time to saturate a tumor ( $t_{sat}$ ) up to the distance  $R$  with the characteristic time for endocytosis ( $t_{int} = 1/k_{int}$ ) in the absence of any systemic clearance. In case that diffusion limits transport into the tumor and not extravasation, the diffusion-limited form of  $\varphi^2$  is given as:<sup>171</sup>

$$\varphi^2 \equiv \frac{k_{int}R^2([Ag]/\varepsilon)}{D([Ab]_{surf} + K_D)} = \frac{t_{sat}}{t_{int}} \quad (4)$$

where  $D$  is the antibody diffusion coefficient;  $[Ab]_{surf}$  is the antibody concentration at the surface of the tumor after extravasation;  $k_{int}$  is the effective internalization rate;  $[Ag]$  is the concentration of antigen; and  $\varepsilon$  is the tumor void fraction accessible to antibody. Only when diffusion is faster than endocytotic consumption ( $\varphi^2 \leq 1$ ) the moving antibody front will successfully saturate the antigen up to the distance  $R$ .<sup>171</sup> The antibody continues to penetrate into tumor tissue until reaching a steady state where the diffusion rate and the effective internalization rate are equal. In this situation is  $\varphi^2 = 1$  and the maximum penetration distance  $R$  can be solved:

$$R \approx \sqrt{\frac{D([\text{Ab}]_{\text{surf}} + K_D)}{k_{\text{int}}([\text{Ag}]/\varepsilon)}} \quad (5)$$

Equation (5) clearly shows that tumor penetration can be increased by: (1) increasing the diffusion coefficient  $D$ , i.e. making the antibody smaller; (2) increasing the antibody concentration at the tumor surface  $[\text{Ab}]_{\text{surf}}$  by increasing the dose or (3) by increasing the extravasation, i.e. again by reducing the antibody size. (4) Lowering the antibody affinity  $K_D$ ; (5) selecting a slowly internalizing ( $k_{\text{int}}$ ) and (6) low expressed target antigen in (7) a less densely ( $\varepsilon$ ) packed tumor would also increase tumor penetration.<sup>171</sup> It should be noted that the square-root relationship between penetration distance and above-mentioned factors indicate that, e.g. a 4-fold increase in antibody concentration only doubles  $R$ .

For the case that extravasation is the transport limiting rate into the tumor and not diffusion, Thurber *et al.* derived an extravasation-limited form of  $\varphi^2$ :<sup>171</sup>

$$\varphi^2 \equiv \frac{k_{\text{int}} R^2 ([\text{Ag}]/\varepsilon)}{2PR_{\text{capillary}}[\text{Ab}]_{\text{plasma}}} = \frac{t_{\text{sat}}}{t_{\text{ext}}} \quad (6)$$

where  $t_{\text{ext}}$  is the time for extravasation;  $P$  is the permeability coefficient;  $R_{\text{capillary}}$  is the blood vessel radius; and  $[\text{Ab}]_{\text{plasma}}$  is the antibody concentration in the plasma.

To estimate whether systemic clearance limits tumor penetration and not endocytotic clearance, the clearance modulus  $\Gamma$  compares the time  $t_{\text{sat}}$  to saturate a tumor with the radius  $R$  and the time for systemic clearance  $t_{\text{clear}}$ . Given are the diffusion- (7) and extravasation-limited (8) form of  $\Gamma$ :<sup>171</sup>

$$\Gamma \equiv \frac{R^2 ([\text{Ag}]/\varepsilon)}{D([\text{Ab}]_{\text{surf},0} + K_D) \left(\frac{A+B}{\alpha+\beta}\right)} = \frac{t_{\text{sat}}}{t_{\text{clear}}} \quad (7)$$

$$\Gamma \equiv \frac{R^2 ([\text{Ag}]/\varepsilon)}{2PR_{\text{capillary}}[\text{Ab}]_{\text{plasma}} \left(\frac{A+B}{\alpha+\beta}\right)} = \frac{t_{\text{sat}}}{t_{\text{clear}}} \quad (8)$$

where  $[\text{Ab}]_{\text{surf},0}$  is the initial antibody concentration at the surface of the tumor after capillary extravasation; and  $\alpha$ ,  $\beta$ ,  $A$  and  $B$  describe the systemic antibody clearance by a typical biexponential decrease in antibody plasma concentration:

$$[\text{Ab}]_{\text{plasma}} = [\text{Ab}]_{\text{plasma},0} (Ae^{-\alpha t} + Be^{-\beta t}) \quad (9)$$

$\Gamma > 1$  describes the situation where the antibody will have cleared before reaching the distance  $R$ , while  $\Gamma \leq 1$  denotes the situation in which the antibody persists sufficient time in the plasma to saturate the tumor to the distance  $R$ . Typically,  $\alpha$  and  $\beta$  are small for IgGs and IgG-based ADCs and  $\Gamma$  is often  $\ll 1$  indicating that systemic clearance usually does not limit their tumor penetration. However, the time an IgG or ADC needs to fully saturate a tumor up to the distance  $R$  can be very long.

#### 4.6. Small Format-Based Drug Conjugates

Beside clinically successful IgG-based ADCs, small format-based drug conjugates were explored aiming for a broader therapeutic window by a combination of better efficacy through enhanced solid tumor penetration (smaller size) and reduced adverse effects mediated by faster systemic clearance.<sup>200–204</sup> The different drug conjugates that fall under this classification can be categorized into antibody-based (**Figure 12**) and non-antibody-based small format drug conjugates (**Figure 13**). In this section, the recent literature is reviewed.

##### 4.6.1. Antibody Fragment-Based Binding Scaffolds

Fab fragments are probably the most easily accessible antibody-based scaffolds for the generation of smaller drug conjugates. Zhou *et al.* and Badescu *et al.* used 50 kDa Fab fragments from papain digested CD20 and HER2 targeting IgGs and coupled doxorubicin to reduced hinge cysteines (DAR 2.0), or MMAE *via* a re-bridging Val-Cit linker construct to reduced interchain cysteines between LC and HC (DAR 1.0).<sup>205,206</sup> Ruddle *et al.* addressed the same reduced LC/HC interchain cysteines of an anti-HER2 Fab and conjugated a highly toxic pyrrolobenzodiazepine (PBD) dimer *via* an alternative re-bridging Val-Ala linker (DAR 1.0).<sup>207</sup>

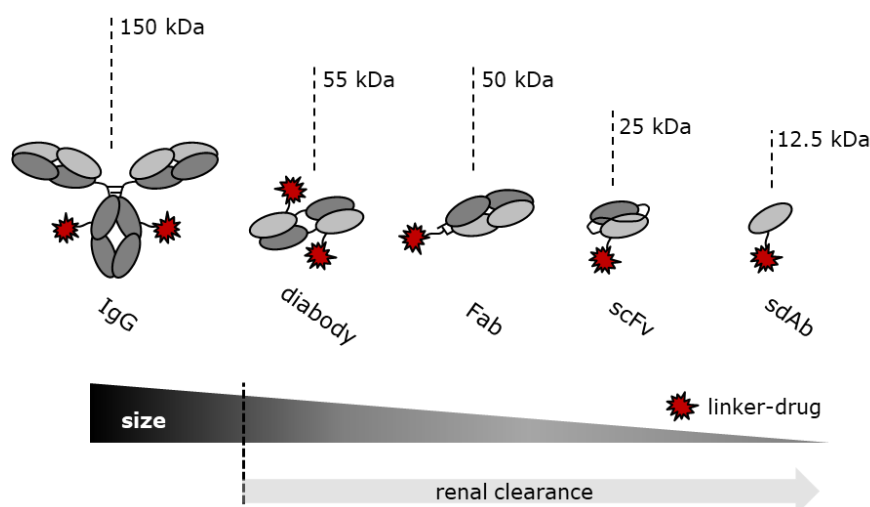


**Figure 12. IgG- and antibody fragment-based drug conjugates.** Approximate molecular weight of scaffold is given. Renal clearance cutoff at approximately 60 – 70 kDa is indicated. *sdAb* - single domain antibody (e.g., nanobody, humabody).

That not only cysteine conjugation is possible, but also enzymatic conjugation, was shown by Liu and coworkers. They generated a DAR ~ 1 anti-CD20 Fab-Val-Cit-MMAE conjugate by sortase A (SrtA) coupling to a genetically incorporated SrtA tag (LPETG) at the C-terminal end of the HC.<sup>208</sup> CD20 and HER2 targeting Fab-drug conjugates were evaluated together with corresponding IgG-drug conjugates in xenograft studies but could not show superior efficacy or tolerability compared to the 150 kDa IgG constructs.<sup>206,208</sup>

Like Fab fragments, diabodies are similar in size (50-55 kDa) but have two antigen binding sites. Here, CD30 and oncofetal antigen 5T4 targeting diabody-drug conjugates were generated *via* site-specific cysteine conjugation of Val-Cit-auristatin or a non-cleavable PBD dimer construct.<sup>209,210</sup>

Variable fragments (Fv) are the next smaller antibody-based fragments (~ 25 - 30 kDa). Numerous single chain Fv (scFv) drug conjugates (DAR ~ 1) are reported where different auristatins and the DNA-damager duocarmycin SA were attached by cysteine coupling techniques.<sup>211-213</sup> Although scFv-drug conjugates showed potent cell killing *in vitro* they were not further investigated in animal models. It should be mentioned that in 2018 the FDA approved an anti-CD22 Fv *Pseudomonas* exotoxin A (PE38) recombinant fusion protein for a rare form of B-cell leukemia. Strictly speaking, the 63 kDa sized immunotoxin is not a drug conjugate, but its clinical elimination half-life of  $t_{1/2}$  1.4 h in humans seems worth to be mentioned here. Recently, even smaller HER2-specific immunotoxins based on 15 kDa sized single domain nanobodies and a less immunogenic version of PE38 were reported.<sup>214</sup>

#### 4.6.2. Alternative Binding Scaffolds

In contrast to antibody-based scaffolds, non-antibody based alternative binding scaffolds were explored for drug conjugate generation (**Figure 13**). They can be subdivided into (1) antibody mimetic proteins<sup>215-218</sup>, (2) aptamers<sup>219-222</sup>, (3) peptide-like scaffolds<sup>223-227</sup> and (4) small molecule ligands<sup>228-232</sup>.

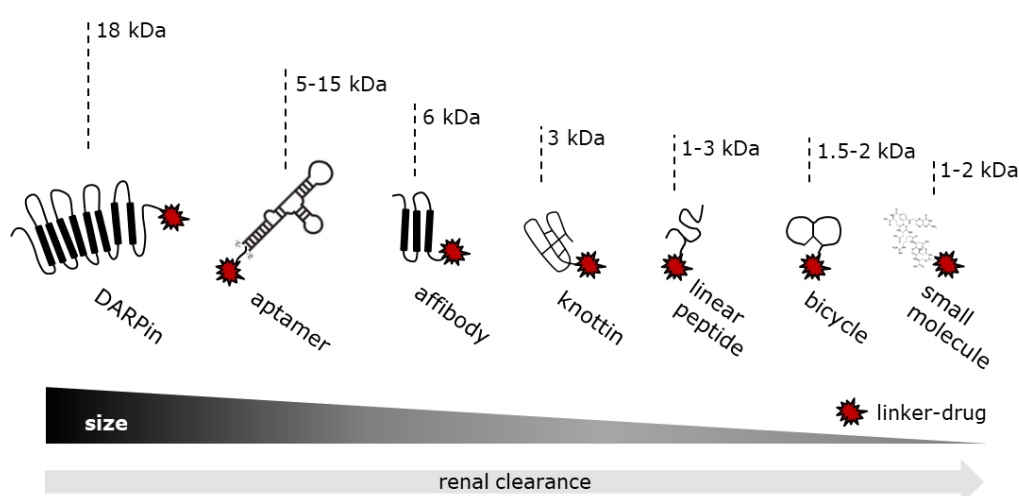


**Figure 13. Small drug conjugates based on non-antibody alternative binding scaffolds.** Approximate molecular weight of scaffold is given.

---

Antibody mimetics are artificial proteins that can specifically bind antigens with high affinity but are not structurally related to antibodies. In this context, a HER2 targeting affibody (~ 6 kDa) maytansine derivate DM1 conjugate<sup>216,218</sup> and an EpCAM-targeting Designed Ankyrin Repeat Protein (DARPin) (~ 19 kDa) MMAF conjugate<sup>217</sup> were recently described. Both proteins were conjugated *via* maleimide chemistry to C-terminal cysteine residues and showed target selective activity *in vitro* and *in vivo*.<sup>216–218</sup>

Peptidic-like scaffolds are even smaller and from this subgroup bicycle-drug conjugates (~ 4 kDa) attracted much attention.<sup>225,226</sup> Bicycles are chemically stabilized bicyclic peptides whose constrained structure gives rise to antibody-like high binding affinities and selectivity. Moreover, bicycles can be displayed on phages which allows for rapid binder identification from large bicycle libraries (> 10<sup>15</sup>).<sup>225</sup> The preclinical profile of the EphA2-targeting bicycle ( $K_D$  1.9 nM) MMAE conjugate (DAR 1) BT5528 indicated a good balance between tumor accumulation and plasma clearance which justified its recent entry into clinical development.<sup>226</sup>

Of all the formats presented here, small molecule-drug conjugates (SMDCs) are the smallest (~ 1 – 2.5 kDa). SMDCs consist of a targeting ligand (e.g. folic acid) which is attached *via* a cleavable or non-cleavable linker to a cytotoxic payload.<sup>233</sup> Due to the smallest size, SMDCs possess the highest diffusion coefficient. However, the good diffusion properties come at the cost of a short half-life which is for SMDCs typically in the range of minutes to few hours.<sup>230</sup> Fast elimination makes a high affinity of the targeting ligand necessary to achieve sufficient retention at the tumor. For example, the tumor targeting folic acid ligand in the approved SMDC Vintafolide binds to the folate receptor with subnanomolar affinity ( $K_D$  ~ 0.1 nM).<sup>229</sup>

#### 4.6.3. Binding Scaffolds with Half-Life Extension

As repeatedly mentioned, *in vivo* efficacy of small format-based drug conjugates was moderate to inferior compared to IgG-based drug conjugates.<sup>189,206,208</sup> This may relate to the absence of the Fc domain and its half-life extending function as detailed in section 4.5. To improve the pharmacokinetic profile of small format-based drug conjugates, two strategies were applied so far: (1) Increasing the hydrodynamic radius by PASylation<sup>217</sup> or polymer attachment<sup>209,221</sup> to bypass renal filtration or (2) fusing the construct to albumin binding domains<sup>189,198,209,216,234–237</sup>, serum albumin<sup>238</sup> or Fc portions<sup>215,220,239–241</sup> which allows for FcRn-mediated recycling (**Figure 14**). Contradictorily, both strategies increase the hydrodynamic radius which limits the tumor penetration.

Brandl *et al.* reported that the half-life of EpCAM targeting DARPins could be improved from  $t_{1/2,\beta}$  11 min up to  $t_{1/2,\beta}$  17 h depending on the length of the attached linear Pro, Ala and Ser (termed PAS) polypeptide.<sup>238,242</sup> The corresponding apparent molecular weight ( $MW_{app}$ ) increased from 29 kDa to 807 kDa.<sup>242</sup> Recently, Brandl *et al.* demonstrated in a xenograft study (100 mm<sup>3</sup> starting tumor volume) that PASylated EpCAM targeting ( $K_D$  0.06 – 0.26 nM) DARPin-MMAF conjugates with  $MW_{app}$  284 kDa and 591 kDa showed better efficacy than a larger  $MW_{app}$  807 kDa construct while the 29 kDa variant lacking PASylation showed no efficacy at all.<sup>217</sup> As

extravasation played only a minor role in their tumor model (well fenestrated tumor vasculature), they deduced that this effect was a compromise of serum half-life and diffusion within the tumor.<sup>217</sup> Similarly, Li *et al.* improved the half-life of their anti-oncofetal antigen 5T4 diabody from  $t_{1/2}$  40 min to 33 h by attaching two branched 20 kDa PEG chains. In a tumor xenograft model (200 mm<sup>3</sup> starting tumor volume), a PEGylated diabody-PBD conjugate showed moderate but improved efficacy compared to a diabody-PBD conjugate.<sup>209</sup> In the same study, Li *et al.* included also a diabody with two albumin binding domains attached ( $t_{1/2}$  45 h). When administered at the same dose, the albumin-binding diabody-PBD conjugate induced greater tumor growth suppression than the PEGylated version.<sup>209</sup>

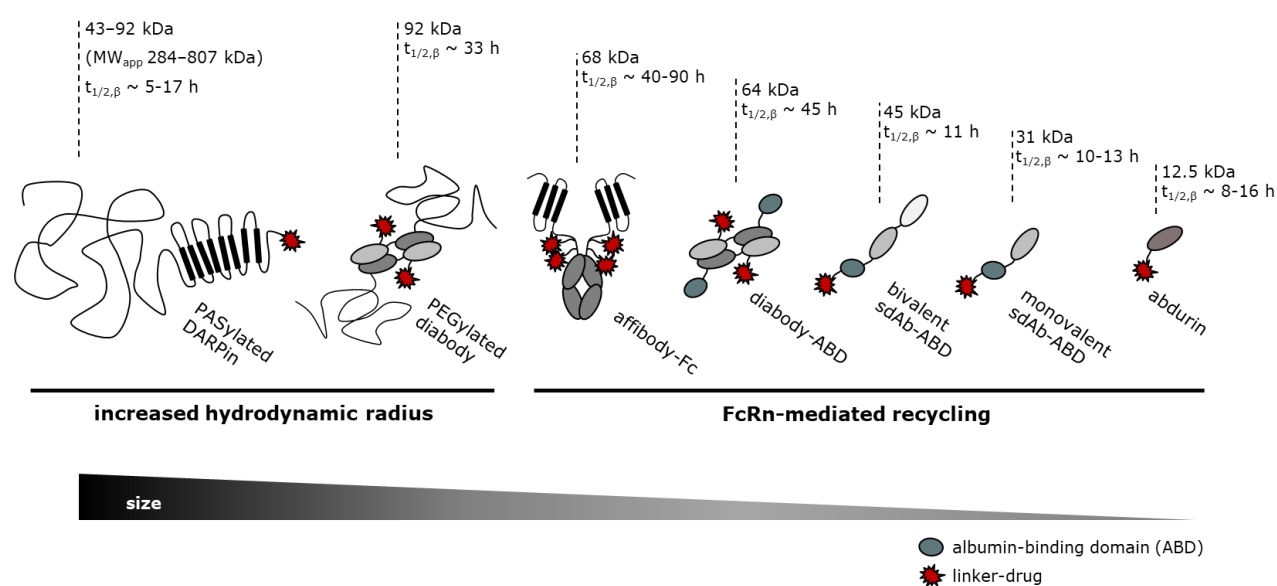


**Figure 14. Small format-based drug conjugates with half-life extending function.** Two strategies were applied to improve pharmacokinetics of small-format based drug conjugates: (1) Increasing the hydrodynamic radius and (2) incorporation of domains that allow for FcRn-mediated recycling. Approximate molecular weight and terminal half-life (mouse) of scaffold is given.<sup>189,209,215,235,239,242,243</sup>

Besides albumin binding diabody-drug conjugates<sup>209</sup>, also albumin binding affibody-<sup>216</sup>, nanobody-<sup>234,235,244</sup> and humabody-drug conjugates<sup>189</sup> were reported. In these studies affinities for serum albumin were relatively high ( $K_D$  0.6 nM<sup>216</sup>, 5.8 nM<sup>235</sup> and 52 nM<sup>189</sup>, respectively). To date, it is not fully understood whether or to what extent permanent albumin binding plays a role in albumin-binding constructs and how an additional 67 kDa albumin appendage would affect extravasation and tissue diffusion.<sup>198</sup> In a recent study by Xenaki *et al.*, the presence of albumin did not negatively impact the spheroid penetration of an albumin-binding nanobody-drug conjugate.<sup>244</sup>

The most comprehensive study for albumin-binding constructs was published by Nessler *et al.*<sup>189</sup> They generated fusions of either one or two distinct fully human, anti PSMA single heavy chain variable ( $V_H$ ) domains (Humabody) and an albumin binding domain. The 31 kDa mono- and 45 kDa biparatopic constructs

---

had half-lives of  $t_{1/2,\beta}$  10 h and 11 h. They were site-specifically conjugated to a monoimine indolinobenzodiazepine alkylator (DAR 1.0) and compared to a biparatopic construct lacking the albumin binding domain (31 kDa,  $t_{1/2,\alpha}$  0.2 h) as well as a full-length IgG-based ADC (150 kDa,  $t_{1/2,\beta}$  28 h) in a xenograft study (250 mm<sup>3</sup> starting tumor volume). The albumin binding mono- and biparatopic conjugates showed best efficacy in this model probably due to a combination of favorable tumor penetration and increased half-life. Furthermore, targeting scaffolds can be fused to 50 kDa Fc portions to improve half-life. This was realized e.g. for affibodies<sup>215</sup>, peptides<sup>239,240</sup> and aptamers<sup>220</sup>. Half-life of peptides or other small fragments after Fc fusion is usually in the range  $t_{1/2,\beta}$  40 – 90 h.<sup>239</sup>

Among the small format drug conjugates mentioned above, abdurin-drug conjugates have a special position because they fit in several groups. Abdurins are IgG-derived, disulfide stabilized C<sub>H2</sub> domains with an engineered binding site in the loop region and a retained FcRn binding site.<sup>245,246</sup> This targeting scaffold combines by design a relatively long FcRn-mediated half-life ( $t_{1/2,\beta}$  ~ 8 – 16 h) with a small size of 12.5 kDa.<sup>243</sup> Conjugation of Val-Cit-MMAE (DAR 2.0) to an EphA2 binding abdurin ( $K_D$  3.2 nM) resulted in a 10-fold reduced affinity for EphA2 and FcRn binding.<sup>247</sup> Nevertheless, the molecules showed efficacy in a xenograft model (100 mm<sup>3</sup> starting tumor volume).<sup>247</sup>

---

## 4.7. Fc Antigen Binding Fragments (Fcabs) as Novel Drug Conjugate Scaffold

Another antibody-fragment based format that incorporates a smaller size and an Fc-mediated half-life extension and, to the best of our knowledge was never explored as drug conjugate, is the Fc antigen binding fragment (Fcab).

### 4.7.1. Structure and Function of Fcabs

Fcabs are 55 kDa sized IgG1-based homodimeric Fc regions that combine Fc effector functions with two engineered antigen binding sites located at the C-terminal structural loops in each C<sub>H</sub>3 domain (**Figure 15A**).<sup>74,248,249</sup> The structural loops form part of the most flexible region within the Fc portion and each C<sub>H</sub>3 domain contains three (AB, CD and EF loop) (**Figure 15B, C**). In Fcabs, mainly the adjacent AB (residues 358 – 362) and EF loop (residues 413 – 422) harbor mutated and, in some cases, additional amino acids to enlarge the potential binding surface (**Figure 16**). The CD loop (residues 383 – 391) is unmodified in most Fcabs due to its spatial distance to the AB and EF loop. But there exist also examples where an engineered, extended CD loop forms part of the paratope of VEGF<sup>250,251</sup> and EGFR<sup>252</sup> targeting Fcabs. Engineered loop structures form one of two Fcab antigen binding sites at each HC (**Figure 15D**). Compared with the Fab antigen binding sites of a typical IgG, Fcab binding sites are closer together (20 – 40 Å *versus* 120 – 170 Å) and relatively inflexible.<sup>74</sup> This raised the question whether an Fcab can bind one or two of its antigens. A structural analysis performed by Lobner *et al.* revealed that the HER2 targeting Fcabs H10-03-6 and STAB19 can bind two HER2 molecules in a negative cooperative binding mode (**Figure 15E**).<sup>249</sup> Isothermal titration calorimetry indicated that the first HER2 molecule is bound with higher affinity ( $K_{D1}$  0.07 μM) than the second HER2 ( $K_{D2}$  1.1 μM).<sup>249</sup> Superimposition of the crystal structures of unbound STAB19 and STAB19 in complex with HER2 showed no significant structural changes suggesting that allosteric mechanisms within the STAB19 molecule are not responsible for the negative cooperativity. Alternatively, Lobner *et al.* proposed that steric hindrance for the second HER2 molecule could be a reasonable explanation.<sup>249</sup> However, whether soluble Fcab is able to simultaneously interact with two membrane-bound HER2 molecules on cells remains unknown.

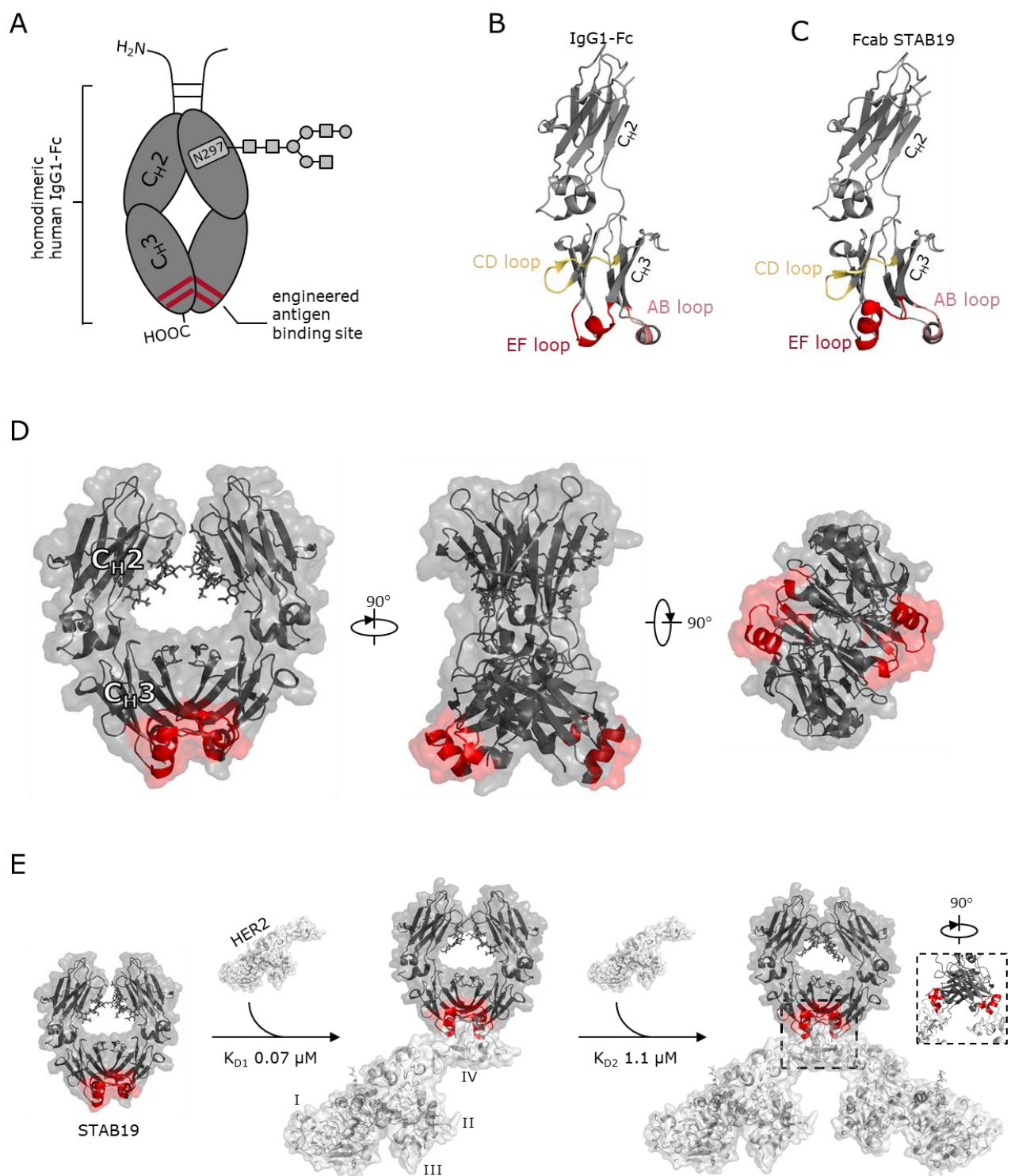


**Figure 15. Fcab structure and binding.** (A) Schematic representation of Fcab. The engineered binding site in the  $C_{H3}$  domain is marked red. The asparagine at position 297 in the  $C_{H2}$  domain carries the glycan. (B) IgG1-Fc monomer with  $C_{H3}$  AB, CD and EF loop marked in pale red, yellow and red. Glycosylation is not shown for clarity. (C) Fcab STAB19 HC monomer with engineered  $C_{H3}$  AB and EF loop. Compared to IgG1-Fc the EF loop of STAB19 is expanded by 5 additional amino acids that enlarge the binding surface. Glycosylation is not shown for clarity. (D) Three distinct perspectives of Fcab STAB19. Glycosylation at position N297 is shown as well as engineered  $C_{H3}$  AB and EF loop (both marked in red). (E) Crystal structures of Fcab STAB19-HER2 complexes illustrating the negative cooperative binding of STAB19 and HER2 extracellular domain IV.<sup>249</sup> The first HER2 receptor is bound with higher affinity than the second. (PDB: IgG1-Fc: 5JII<sup>249</sup>; STAB19: 5JIH<sup>249</sup>; STAB19-HER2: 5K33<sup>249</sup>).

In contrast to antigen binding that solely takes place at the C<sub>H</sub>3 domains, interactions with Fc natural binding partners involve mostly the N-terminal site of the C<sub>H</sub>2 domain (e.g., C1q, FcγRI – III) or the C<sub>H</sub>2-C<sub>H</sub>3 interface (e.g., FcRn, protein A) (see also **Figure 2B**). It was repeatedly shown for several Fcabs that binding to recombinant FcγRI – III<sup>252–256</sup>, FcRn<sup>255,256</sup> or protein A<sup>253,254,256</sup> was not impaired by the engineered antigen binding site. Moreover, it could be shown that Fcabs induce selective cell killing *via* FcγR-mediated ADCC.<sup>252–254,257</sup> The retained FcRn binding of the Fcab mediates extraordinary long half-life ( $t_{1/2,\beta}$  60 – 85 h in mice) for a 55 kDa molecule, similar to human wildtype Fc ( $t_{1/2,\beta}$  40 h).<sup>248,255</sup>

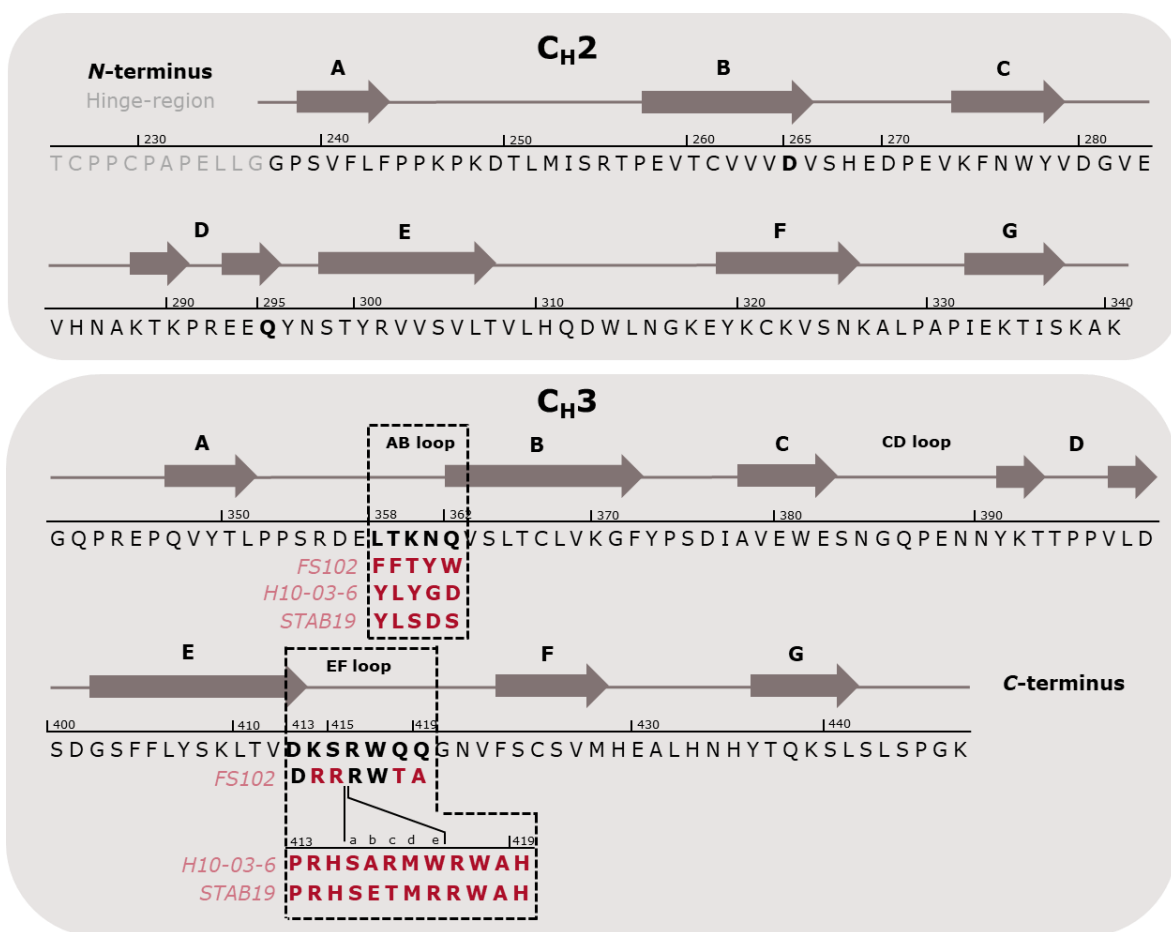


**Figure 16. Amino acid sequence of human IgG1-Fc and HER2 targeting Fcabs H10-03-6, STAB19 and FS102.**<sup>248,255,258</sup> Mutated and additional amino acids (a – e) within AB (residues 358 – 362) and EF loop (residues 413 – 422) forming the paratope of Fcabs are marked in red. Positions are numbered according to EU numbering. Figure adapted from Lobner *et al.*<sup>249</sup>

## 4.7.2. Generation and Screening of Fcabs

To date, Fcabs against six different targets have been published (**Table 2**). Of these variants, some were used in this work and are therefore described in more detail here.

The first incorporation of an antigen binding site into a human IgG1 Fc fragment was reported by Wozniak-Knopp *et al.* in 2010. The reported Fcab H10-03-6 ( $K_D$  23 - 69 nM<sup>248,258</sup>) was an affinity matured HER2 binder from a yeast surface display (YSD) library of IgG1 Fc regions containing randomized AB and EF loop sequences.<sup>248</sup> H10-03-6 showed reduced thermostability and was subsequently stabilized by either incorporation of additional disulfide bonds yielding, e.g. H10-03-6 CysP2 Cys<sup>259,260</sup> or by applying a YSD-based directed evolution heat shock protocol<sup>261,262</sup> resulting in stabilized variants with altered affinity, e.g. STAB5 ( $K_D$  19 nM) and STAB19 ( $K_D$  109 nM)<sup>258</sup>. In contrast to parental H10-03-6, both STAB5 and STAB19 showed largely unchanged SEC profiles after 4 weeks at 22 or 37°C indicating for an acquired resistance to aggregation.

Furthermore, Traxlmayr *et al.* demonstrated that YSD can be used to screen for Fcabs with pH-dependent binding sites.<sup>263</sup> They generated a YSD library of H10-03-6 with softly re-randomized AB and EF loops and isolated a clone with an 8-fold higher  $K_D$  at pH 6.0 by alternating selection rounds for binding at pH 7.4 and non-binding at pH 6.0.<sup>263</sup> In addition, Traxlmayr *et al.* showed that it is possible to generate integrin binding Fcabs by grafting a known  $\alpha\beta3$  binding peptide motif into the CD or EF loop.<sup>256</sup>

**Table 2. Overview of published and characterized Fcab variants.** Lower  $T_m$  represents melting point of C<sub>H</sub>2 domain, whereas higher  $T_m$  characterizes the melting temperature of the C<sub>H</sub>3 domain. Due to engineered C<sub>H</sub>3 loop regions melting temperature decreases resulting in only one visible thermal transition. Terminal half-life was determined in Balb/c mice. \**adjacent but not overlapping epitope with Trastuzumab*; \*\**no overlapping epitope with Trastuzumab*; †*Lower  $T_m$  for C<sub>H</sub>2 domain due to *P. pastoris* glycosylation pattern*; ‡*measured at pH 6.0*; ‡*no overlapping epitope with Cetuximab, but blocks EGF binding*; n.r. – not reported.

Fcab	target	$K_D$ target [nM]	target epitope	$T_m$ [°C]	FcRn binding	FcγR binding	$t_{1/2,\beta}$ [h]	PDB ID	ref.
H10-03-6	HER2	69	domain IV*	68	x	x	86	5JIK, 5KWG	248,249
H10-03-6 CysP2 Cys	HER2	69	domain IV*	64, 81	n.r.	n.r.	n.r.	-	260
H10-03-6 P1	HER2	152/1201 <sup>†</sup>	domain IV*	65	x	n.r.	n.r.	-	263
STAB19	HER2	109	domain IV*	71, 76	x	n.r.	n.r.	5JIH, 5K33	249,258
STAB5	HER2	19	domain IV*	~ 72	x	n.r.	n.r.	-	258
FS102	HER2	0.8	n.r.**	71, 76	x	x	60	-	255
Fc-RGD-CD-EF	$\alpha\beta3$	~ nM	n.r.	~ 63 <sup>‡</sup>	x	x	n.r.	-	256
448	VEGF	26	known	70	n.r.	n.r.	n.r.	5K64	250,251
CT6	VEGF	4	known	70, 75	x	n.r.	n.r.	5K65, 5O4E	250,251
FS18-7-9	LAG-3	0.056	n.r.	n.r.	n.r.	n.r.	n.r.	-	264,265
FS1-60	EGFR	2.6	‡	n.r.	n.r.	x	n.r.	-	252
FS1-65	EGFR	0.7	‡	n.r.	n.r.	x	n.r.	-	252
FS1-67	EGFR	1.3	‡	n.r.	n.r.	x	n.r.	-	252
TV	TfR	120	known	n.r.	x	n.r.	n.r.	6W3H	266
human Fc	-	-	-	71, 82	x	x	40	5JII	248,249

---

### 4.7.3. Application and Therapeutic Use of Fcabs

Since the HER2 binding Fcab H10-03-6 elicit ADCC, its anti-tumor activity was tested in a BT-474 xenograft model. Although H10-03-6 slowed down tumor growth, its efficacy was only moderate.<sup>257</sup> One year later very promising preclinical results of another HER2 binding Fcab, FS102, were reported.<sup>255</sup> FS102 was developed by F-star Therapeutics and contained 5 amino acid substitutions in the AB loop and 4 in the EF loop.<sup>267</sup> It bound recombinant HER2 with high affinity ( $K_D$  0.8 nM) at a non-overlapping epitope with Trastuzumab or Pertuzumab and exhibited biophysical properties similar to an IgG1 Fc portion.<sup>255</sup> In HER2 high expressing cell lines FS102 induced profound HER2 internalization and degradation leading to apoptosis. Moreover, FS102 showed also a superior antitumor effect over Trastuzumab or a combination of Trastuzumab and Pertuzumab in several PDX models.<sup>255</sup> This led to the phase I clinical evaluation of FS102 in patients with HER2 overexpressing solid tumors (NCT02286219).

At the moment, Fcabs are primarily developed as bispecific “mAb<sup>2</sup>” for therapeutic use by F-star Therapeutics.<sup>268</sup> A mAb<sup>2</sup> is a 150 kDa IgG molecule in which the Fc region has been replaced by an Fcab bearing a second distinct antigen binding site. For example, Kraman *et al.* published preclinical data of the dual immune checkpoint inhibitor FS118.<sup>265</sup> FS118 is a mAb<sup>2</sup> combining a human LAG-3 binding Fcab<sup>264</sup> with two human anti-PD-L1 Fab arms. It is currently being evaluated in a phase I clinical trial in patients with advanced malignancies (NCT03440437).

Other examples of recent use of the Fcab format include another IgG-based bispecific format where the Fab C<sub>H1</sub>/C<sub>L</sub> domains are replaced by VEGF-binding CH3 domains or a bispecific blood-brain barrier transport vehicle.<sup>266,269</sup> Moreover, a tetravalent biparatopic HER2-binding antibody based on Pertuzumab Fab arms and a HER2-specific Fcab was reported that showed a stronger anti-proliferative effect than the mixture of Pertuzumab and the parental Fcab.<sup>270</sup>

---

## 5. Objective of this Work

---

The presented work aims to evaluate Fc antigen binding (Fcab) fragments as novel targeting scaffold for the generation of antibody-based drug conjugates with improved solid tumor penetration capabilities. In the ADC field an improvement in tumor penetration is of special interest because it allows more cells to be exposed to cytotoxic doses of payload, aiming at an increased therapeutic efficacy (**Figure 17**).

Fcabs are engineered homodimeric Fc portions that incorporate all essential IgG functionalities such as antigen binding and FcRn-mediated half-life prolongation at only one third of the size. In contrast to IgG-based ADCs, Fcabs' smaller size holds promise to improve solid tumor penetration of Fcab-based drug conjugates by enhancing the extravasation from the circulation into the interstitial space and increasing diffusion rates throughout interstitium and tumor tissue. Additionally, the half-life extending FcRn binding site delays systemic clearance of the Fcab-drug conjugates whereby a high plasma

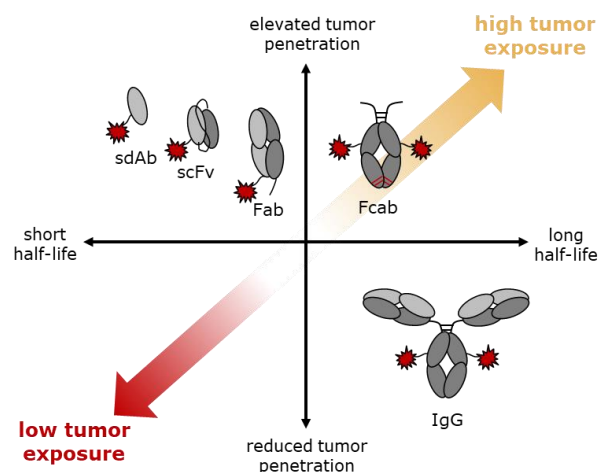


**Figure 17.** Conceptual representation of potential advantages of Fcab-drug conjugates over other small antibody-fragment based drug conjugates and conventional IgG-based ADCs.

concentration is maintained that further drives penetration into tissues. FcRn binding provides Fcab-drug conjugates with a significant advantage over other reported small format-based drug conjugates that lack an FcRn binding site and consequently suffer from a short half-life *in vivo*.

The main objective of this work was to assess the generation and functionality of Fcab-drug conjugates for the first time. Therefore, Fcabs that bind to the solid tumor targets HER2 and EGFR were selected and genetically engineered at different positions for subsequent site-specific conjugation. As endocytotic uptake and lysosomal delivery is a prerequisite for an ADC approach, target-dependent intracellular accumulation of Fcabs had to be investigated on different cancer cell lines, before the most promising variants in terms of biophysical behavior and cellular uptake should be coupled to the well-established microtubule inhibitor monomethyl auristatin E (MMAE) employing different conjugation techniques. The resultant Fcab-MMAE conjugates had to be characterized for retained target and FcRn binding as well as hydrophobicity, serum stability and target-dependent cytotoxicity. Finally, a tumor cell spheroid penetration assay should be set up in order to study penetration capabilities of selected Fcab variants and to assess the impact of target affinity, intracellular uptake and size.

---

# MATERIAL AND METHODS

---

---

---

## 6. Material and Methods

---

### 6.1. Human Cell Lines and Bacterial Strains

#### Mammalian cell lines

Cancer cell lines were purchased from the American Type Culture Collection (ATCC<sup>®</sup>, Manassas, USA) or companies as listed below.

**Table 3. Mammalian cell lines used in this work.**

cell line	cell type	medium	origin
A431	human epidermoid carcinoma	A	ATCC <sup>®</sup> CRL-1555 <sup>™</sup>
BT-474	human ductal carcinoma (mammary gland)	C	ATCC <sup>®</sup> HTB-20 <sup>™</sup>
Expi293F <sup>™</sup>	human embryonic kidney	B	Life Technologies <sup>™</sup>
HCC-1143	human invasive ductal carcinoma	D	ATCC <sup>®</sup> CRL-2321 <sup>™</sup>
HCC-1937	human primary ductal carcinoma	D	ATCC <sup>®</sup> CRL-2336 <sup>™</sup>
HCC-1954	human ductal carcinoma (mammary gland)	D	ATCC <sup>®</sup> CRL-2338 <sup>™</sup>
LNCaP	human prostate carcinoma	D	ATCC <sup>®</sup> CRL-1740 <sup>™</sup>
MCF-7	human breast adenocarcinoma (mammary gland)	A	ATCC <sup>®</sup> HTB-22 <sup>™</sup>
MDA-MB-468	human breast adenocarcinoma (mammary gland)	D	ATCC <sup>®</sup> HTB 132 <sup>™</sup>
SKBR-3	human breast adenocarcinoma (mammary gland)	A	ATCC <sup>®</sup> HTB-30 <sup>™</sup>

#### Bacterial strains

One Shot<sup>™</sup> TOP10 Chemically Competent *E. coli* cells (#C4040-10, Invitrogen<sup>™</sup>, Carlsbad, USA);

Genotype: F<sup>-</sup> *mcrA*  $\Delta$ (*mrr-hsdRMS-mcrBC*)  $\phi$ 80*lacZ* $\Delta$ M15  $\Delta$ *lacX74* *recA1* *araD139*  $\Delta$ (*ara-leu*) 7697 *galU* *galK* *rpsL* (Str<sup>R</sup>) *endA1* *nupG* $\lambda$ -

### 6.2. Antibody Sequences

*hinge region*, *G<sub>4</sub>S-His-Tag*, *D265A*, *Engineered C<sub>H</sub>3 loops forming Fcab binding site*

---

**HER2-binding Fcabs**<sup>255,258</sup>

**$\alpha$ H-H10 (Q295)**

TCPPCPAPELLGGPSVFLFPPKPKDTLMISRTPEVTCVVVAVSHEDPEVKFNWYVDGVEVHNAKTKPREEQYNSTYRVVSVLTVLHQDWLNGKEYKCKVSNKALPAPIEKTISKAKGQCREPQVYTLPPSRDEYLYGQVSLTCLVKGFYPSDIAVEWESNGQPE  
NNYKTTTPVLDSDGSFFLYSKLTVPRHSARMWRWAHGNVFSCSVMHECLHNHYTQKSLSLSGEC

**$\alpha$ H-H10<sup>C265</sup> (D265C)**

TCPPCPAPELLGGPSVFLFPPKPKDTLMISRTPEVTCVVVCVSHEDPEVKFNWYVDGVEVHNAKTKPREEQYNSTYRVVSVLTVLHQDWLNGKEYKCKVSNKALPAPIEKTISKAKGQCREPQVYTLPPSRDEYLYGQVSLTCLVKGFYPSDIAVEWESNGQPE  
NNYKTTTPVLDSDGSFFLYSKLTVPRHSARMWRWAHGNVFSCSVMHECLHNHYTQKSLSLSGEC

**$\alpha$ H-S5 (Q295)**

TCPPCPAPELLGGPSVFLFPPKPKDTLMISRTPEVTCVVVAVSHEDPEVKFNWYVDGVEVHNAKTKPREEQYNSTYRVVSVLTVLHQDWLNGKEYKCKVSNKALPAPIEKTISKAKGQPREPQVYTLPPSRDEYLSGNVSLTCLVKGFYPSDIAVEWESNGQPE  
NNYKTTTPVLDSDGSFFLYSKLTVPRHSERMWRWAHGNVFSCSVMHEALHNHYTQKSLSLSPG

**$\alpha$ H-S5<sup>C265</sup> (D265C)**

TCPPCPAPELLGGPSVFLFPPKPKDTLMISRTPEVTCVVVCVSHEDPEVKFNWYVDGVEVHNAKTKPREEQYNSTYRVVSVLTVLHQDWLNGKEYKCKVSNKALPAPIEKTISKAKGQPREPQVYTLPPSRDEYLSGNVSLTCLVKGFYPSDIAVEWESNGQPE  
NNYKTTTPVLDSDGSFFLYSKLTVPRHSERMWRWAHGNVFSCSVMHEALHNHYTQKSLSLSPG

**$\alpha$ H-S5<sup>LLQGA-N</sup>**

LLQGATCPPCPAPELLGGPSVFLFPPKPKDTLMISRTPEVTCVVVAVSHEDPEVKFNWYVDGVEVHNAKTKPREEQYNSTYRVVSVLTVLHQDWLNGKEYKCKVSNKALPAPIEKTISKAKGQPREPQVYTLPPSRDEYLSGNVSLTCLVKGFYPSDIAVEWESNGQPE  
NNYKTTTPVLDSDGSFFLYSKLTVPRHSERMWRWAHGNVFSCSVMHEALHNHYTQKSLSLSPG

**$\alpha$ H-S5<sup>LLQGA-G4S-N</sup>**

LLQGAGGGGSTCPPCPAPELLGGPSVFLFPPKPKDTLMISRTPEVTCVVVAVSHEDPEVKFNWYVDGVEVHNAKTKPREEQYNSTYRVVSVLTVLHQDWLNGKEYKCKVSNKALPAPIEKTISKAKGQPREPQVYTLPPSRDEYLSGNVSLTCLVKGFYPSDIAVEWESNGQPE  
NNYKTTTPVLDSDGSFFLYSKLTVPRHSERMWRWAHGNVFSCSVMHEALHNHYTQKSLSLSPG

**$\alpha$ H-S5<sup>C-G4S-LLQGA</sup>**

TCPPCPAPELLGGPSVFLFPPKPKDTLMISRTPEVTCVVVAVSHEDPEVKFNWYVDGVEVHNAKTKPREEQYNSTYRVVSVLTVLHQDWLNGKEYKCKVSNKALPAPIEKTISKAKGQPREPQVYTLPPSRDEYLSGNVSLTCLVKGFYPSDIAVEWESNGQPE  
NNYKTTTPVLDSDGSFFLYSKLTVPRHSERMWRWAHGNVFSCSVMHEALHNHYTQKSLSLSPGGGGGSLLOGA

**$\alpha$ H-S5<sup>C-(G4S)2-LLQGA</sup>**

TCPPCPAPELLGGPSVFLFPPKPKDTLMISRTPEVTCVVVAVSHEDPEVKFNWYVDGVEVHNAKTKPREEQYNSTYRVVSVLTVLHQDWLNGKEYKCKVSNKALPAPIEKTISKAKGQPREPQVYTLPPSRDEYLSGNVSLTCLVKGFYPSDIAVEWESNGQPE  
NNYKTTTPVLDSDGSFFLYSKLTVPRHSERMWRWAHGNVFSCSVMHEALHNHYTQKSLSLSPGGGGGSGGGSLLOGA

**$\alpha$ H-S19 (Q295)**

TCPPCPAPELLGGPSVFLFPPKPKDTLMISRTPEVTCVVVAVSHEDPEVKFNWYVDGVEVHNAKTKPREEQYNSTYRVVSVLTVLHQDWLNGKEYKCKVSNKALPAPIEKTISKAKGQPREPQVYTLPPSRDEYLSDSVSLTCLVKGFYPSDIAVEWESNGQPE  
NNYKTTTPVLDSDGSFFLYSKLTVPRHSETMRRWAHGNVFSCSVMHEALHNHYTQKSLSLSPG

---

### **$\alpha$ H-S19<sup>C265</sup> (D265C)**

TCPPCPAPELLGGPSVFLFPPKPKDTLMISRTPEVTCVVVAVSHEDPEVKFNWYVDGVEVHNAKTKPREEQYNSTYRVVSVLTVLHQDWLNGKEYKCKVSNKALPAPIEKTISKAKGQPREPQVYTLPPSRDEYLSDSVSLTCLVKGFYPSDIAVEWESNGQPE  
NNYKTPPVLDSDGSFFLYSKLTVPRHSETMRRWAHGNVFSCSVMHEALHNHYTQKSLSLSPG

### **$\alpha$ H-FS (Q295)**

TCPPCPAPELLGGPSVFLFPPKPKDTLMISRTPEVTCVVVAVSHEDPEVKFNWYVDGVEVHNAKTKPREEQYNSTYRVVSVLTVLHQDWLNGKEYKCKVSNKALPAPIEKTISKAKGQPREPQVYTLPPSRDEFFTYWVSLTCLVKGFYPSDIAVEWESNGQPE  
NNYKTPPVLDSDGSFFLYSKLTVDRRRWTAGNVFSCSVMHEALHNHYTQKSLSLSPG

### **EGFR-binding Fcabs<sup>252</sup>**

EGFR-binding Fcabs were modified by removing the core hinge region (*TCPPCP*).

#### **$\alpha$ E-60 (Q295, Q311, Q438)**

APELLGGPSVFLFPPKPKDTLMISRTPEVTCVVVAVSHEDPEVKFNWYVDGVEVHNAKTKPREEQYNSTYRVVSVLTVLHQDWLNGKEYKCKVSNKALPAPIEKTISKAKGQPREPQVYTLPPSRDELDEGGPVSLTCLVKGFYPSDIAVEWESTYGPENNYK  
TTPPVLDSDGSFFLYSRLTVSHWRWYSGNVFSCSVMHEALHNHYTQKSLSLSPG

#### **$\alpha$ E-65 (Q295, Q311, Q438)**

APELLGGPSVFLFPPKPKDTLMISRTPEVTCVVVAVSHEDPEVKFNWYVDGVEVHNAKTKPREEQYNSTYRVVSVLTVLHQDWLNGKEYKCKVSNKALPAPIEKTISKAKGQPREPQVYTLPPSRDELDEGGPVSLTCLVKGFYPSDIAVEWESTYGPENNYK  
TTPPVLDSDGSFFLYSKLTVSYWRWVKGNVFSCSVMHEALHNHYTQKSLSLSPG

#### **$\alpha$ E-67 (Q295, Q311, Q438)**

APELLGGPSVFLFPPKPKDTLMISRTPEVTCVVVAVSHEDPEVKFNWYVDGVEVHNAKTKPREEQYNSTYRVVSVLTVLHQDWLNGKEYKCKVSNKALPAPIEKTISKAKGQPREPQVYTLPPSRDETDGDPVSLTCLVKGFYPSDIAVEWESTYGPENNYKT  
TTPPVLDSDGSFFLYSKLTVSYWRWYKGNVFSCSVMHEALHNHYTQKSLSLSPG

### **Reference molecules<sup>249,271</sup>**

#### **$\alpha$ HxH-S5-IgG**

##### *Light Chain:*

DIQMTQSPSSLSASVGDRVTITCRASGNIHNYLAWYQQKPGKAPKLLIYTTTLDAGVPSRFSGSGSDYFTFTISSLQPEDIA  
TYYCQHFWSPTPTFGQGTKVEIKRTVAAPSVFIFPPSDEQLKSGTASVCLLNNFYPREAKVQWKVDNALQSGNSQESVTE  
QDSKDYSLSSLTLSKADYEKHKVYACEVTHQGLSSPVTKSFNRGEC

##### *Heavy Chain:*

QVQLQESGPGGLVRSQTLSTCTVSGFSLTGYGVNWVRQPPGRGLEWIGMIWGDGNTDYNALKSRVTMLKDTSKNQFS  
LRLSSVTAADTAVYYCARERDYRLDYWGQGLVTVSSASTKGPSVFPLAPSSKSTSGGTAALGLCLVKDYFPEPVTVSWNSGA  
LTSGVHTFPAVLQSSGLYSLSSVTVPSSSLGTQTYICNVNHKPSNTKVDKRVEPKSCDKTHTCPPCPAPELLGGPSVFLFPPK  
PKDTLMISRTPEVTCVVVAVSHEDPEVKFNWYVDGVEVHNAKTKPREEQYNSTYRVVSVLTVLHQDWLNGKEYKCKVSNK  
ALPAPIEKTISKAKGQPREPQVYTLPPSRDEYLSGNVSLTCLVKGFYPSDIAVEWESNGQPENNYKTPPVLDSDGSFFLYSKL  
TVPRHSERMWRWAHGNVFSCSVMHEALHNHYTQKSLSLSPG

---

**$\alpha$ H-T-IgG (unmodified Trastuzumab)**

*Light chain:*

DIQMTQSPSSLSASVGDRTITCRASQDVNTAVAWYQQKPGKAPKLLIYSASFLYSGVPSRFSGSRSGTDFTLTISSLQPEDF  
ATYYCQQHYTTPPTFGQGTKVEIKRTVAAPSVFIFPPSDEQLKSGTASVVCLLNNFYPREAKVQWKVDNALQSGNSQESVT  
EQDSKDSTYLSSTLTLSKADYEKHKVYACEVTHQGLSSPVTKSFNRGEC

*Heavy chain:*

EVQLVESGGGLVQPGGSLRLSCAASGFNIKDTYIHWVRQAPGKGLEWVARIYPTNGYTRYADSVKGRFTISADTSKNTAYL  
QMNSLR AEDTAVYYCSRWGGDGFYAMDYWGQGLVTVSSASTKGPSVFPLAPSSKSTSGGTAALGCLVKDYFPEPVTVS  
WNSGALTSGVHTFPAVLQSSGLYSLSSVTVPSSSLGTQTYICNVNHKPSNTKVDKKVEPKSCDKTHTCPPCPAPELLGGPS  
VFLFPPPKDITLMISRTEVTCVVVDVSHEDPEVKFNWYVDGVEVHNAKTKPREEQYNSTYRVVSVLTVLHQDWLNGKEY  
KCKVSNKALPAPIEKTISKAKGQPREPQVYTLPPSREEMTKNQVSLTCLVKGFYPSDIAVEWESNGQPENNYKTTTPVLDS  
GSFFLYSKLTVDKSRWQQGNVFCFSVMHEALHNHYTQKSLSLSPGK

**$\alpha$ H-T-Fab (K183C, V205C)**

*Light chain:*

DIQMTQSPSSLSASVGDRTITCRASQDVNTAVAWYQQKPGKAPKLLIYSASFLYSGVPSRFSGSRSGTDFTLTISSLQPEDF  
ATYYCQQHYTTPPTFGQGTKVEIKRTVAAPSVFIFPPSDEQLKSGTASVVCLLNNFYPREAKVQWKVDNALQSGNSQESVT  
EQDSKDSTYLSSTLTLSCADYEKHKVYACEVTHQGLSSPCTKSFNRGEC

*Heavy chain:*

EVQLVESGGGLVQPGGSLRLSCAASGFNIKDTYIHWVRQAPGKGLEWVARIYPTNGYTRYADSVKGRFTISADTSKNTAYL  
QMNSLR AEDTAVYYCSRWGGDGFYAMDYWGQGLVTVSSASTKGPSVFPLAPSSKSTSGGTAALGCLVKDYFPEPVTVS  
WNSGALTSGVHTFPAVLQSSGLYSLSSVTVPSSSLGTQTYICNVNHKPSNTKVDKKVEPKSCDKTHTGGGGSHHHHHH

**$\alpha$ E-C-Fab (LC-C-(G<sub>4</sub>S)<sub>3</sub>-LPETGS)**

*Light chain:*

DILLTQSPVILSVSPGERVSFSCRASQSIGTNIHWYQQRTNGSPRLLIKYASESISGIPSRFSGSGSGTDFTLSINSVESEDIADYY  
CQQNNNWPTTFGAGTKLELKRVAAPSVFIFPPSDEQLKSGTASVVCLLNNFYPREAKVQWKVDNALQSGNSQESVTEQ  
DSKDSTYLSSTLTLSKADYEKHKVYACEVTHQGLSSPVTKSFNRGECGGGGSGGGSGGGGSLPETGS

*Heavy chain:*

QVQLKQSGPGLVQPSQLSITCTVSGFSLTNYGVHWVRQSPGKLEWLGVWVSGGNTDYNTPFTSRLSINKDNSKSQVFF  
KMNSLQSNDAIYYCARALTYDYEFAYWGQGLVTVSAASTKGPSVFPLAPSSKSTSGGTAALGCLVKDYFPEPVTVSWN  
SGALTSGVHTFPAVLQSSGLYSLSSVTVPSSSLGTQTYICNVNHKPSNTKVDKRVEPKSCDKTHTGGGGSHHHHHH

**$\alpha$ E-C-IgG (LC-C-(G<sub>4</sub>S)<sub>3</sub>-LPETGS)**

*Light chain:*

DILLTQSPVILSVSPGERVSFSCRASQSIGTNIHWYQQRTNGSPRLLIKYASESISGIPSRFSGSGSGTDFTLSINSVESEDIADYY  
CQQNNNWPTTFGAGTKLELKRVAAPSVFIFPPSDEQLKSGTASVVCLLNNFYPREAKVQWKVDNALQSGNSQESVTEQ  
DSKDSTYLSSTLTLSKADYEKHKVYACEVTHQGLSSPVTKSFNRGECGGGGSGGGSGGGGSLPETGS

---

*Heavy chain:*

QVQLKQSGPGLVQPSSQLSITCTVSGFSLTNYGVHWRQSPGKGLEWLGVIWSGGNTDYNTPTFTSRLSINKDNSKSQVFF  
KMNSLQSNDAIYYCARALTYDYEFAYWGQGLVTVSAASTKGPSVFPLAPSSKSTSGGTAALGCLVKDYFPEPVTVSWN  
SGALTSKVHTFPAVLQSSGLYSLSVVTVPSSSLGTQTYICNVNHKPSNTKVDKRVEPKSCDKTHTCPPCPAPELLGGPSVFLF  
PPKPKDTLMISRTPEVTCVVVDVSHEDPEVKFNWYVDGVEVHNAKTKPREEQYNSTYRVVSVLTVLHQDWLNGKEYKCKV  
SNKALPAPIEKTISKAKGQPREPQVYTLPPSREEMTKNQVSLTCLVKGFYPSDIAVEWESNGQPENNYKTTTPVLDSDGSFFL  
YSKLTVDKSRWQQGNVFCFSVMHEALHNHYTQKSLSLSPGK

**$\alpha$ H-T-CL-S5** (Trastuzumab with STAB5 Fcab and **matriptase**, **uPA cleavage site** within hinge region)

*Light chain:*

DIQMTQSPSSLSASVGDRVTITCRASQDVNTAVAWYQQKPGKAPKLLIYSASFLYSGVPSRFSGRSGTDFTLTISLQPEDF  
ATYYCQQHYTTPPTFGQGTKVEIKRTVAAPSVFIFPPSDEQLKSGTASVVCLLNNFYPREAKVQWKVDNALQSGNSQESVT  
EQDSDKSTYLSSTLTLSKADYEKHKVYACEVTHQGLSSPVTKSFNRGECGGGGSGGGGSGGGGSLPETGS

*Heavy chain:*

EVQLVESGGGLVQPGGSLRLSCAASGFNIKDTYIHWVRQAPGKGLEWVARIYPTNGYTRYADSVKGRFTISADTSKNTAYL  
QMNSLRAEDTAVYYCSRWGGDGFYAMDYWGQGLVTVSSASTKGPSVFPLAPSSKSTSGGTAALGCLVKDYFPEPVTVS  
WNSGALTSKVHTFPAVLQSSGLYSLSVVTVPSSSLGTQTYICNVNHKPSNTKVDKKEPKSCDKTHTLSGRSDNHCPPCPA  
PELLGGPSVFLFPPKPKDTLMISRTPEVTCVVVAVSHEDPEVKFNWYVDGVEVHNAKTKPREEQYNSTYRVVSVLTVLHQD  
WLNGKEYKCKVSNKALPAPIEKTISKAKGQPREPQVYTLPPSRDEYLSGNVSLTCLVKGFYPSDIAVEWESNGQPENNYKTT  
PPVLDSDGSFFLYSKLTVPRHSEMRRWAHGNVFCFSVMHEALHNHYTQKSLSLSPG

**$\alpha$ H-T-CL-S19** (Trastuzumab with STAB19 Fcab and **matriptase**, **uPA cleavage site** within hinge region)

*Light chain:*

DIQMTQSPSSLSASVGDRVTITCRASQDVNTAVAWYQQKPGKAPKLLIYSASFLYSGVPSRFSGRSGTDFTLTISLQPEDF  
ATYYCQQHYTTPPTFGQGTKVEIKRTVAAPSVFIFPPSDEQLKSGTASVVCLLNNFYPREAKVQWKVDNALQSGNSQESVT  
EQDSDKSTYLSSTLTLSKADYEKHKVYACEVTHQGLSSPVTKSFNRGECGGGGSGGGGSGGGGSLPETGS

*Heavy chain:*

EVQLVESGGGLVQPGGSLRLSCAASGFNIKDTYIHWVRQAPGKGLEWVARIYPTNGYTRYADSVKGRFTISADTSKNTAYL  
QMNSLRAEDTAVYYCSRWGGDGFYAMDYWGQGLVTVSSASTKGPSVFPLAPSSKSTSGGTAALGCLVKDYFPEPVTVS  
WNSGALTSKVHTFPAVLQSSGLYSLSVVTVPSSSLGTQTYICNVNHKPSNTKVDKKEPKSCDKTHTLSGRSDNHCPPCPA  
PELLGGPSVFLFPPKPKDTLMISRTPEVTCVVVAVSHEDPEVKFNWYVDGVEVHNAKTKPREEQYNSTYRVVSVLTVLHQD  
WLNGKEYKCKVSNKALPAPIEKTISKAKGQPREPQVYTLPPSRDEYLSDSVSLTCLVKGFYPSDIAVEWESNGQPENNYKTT  
PVLDSDGSFFLYSKLTVPRHSETMRWAHGNVFCFSVMHEALHNHYTQKSLSLSPG

---

## Human IgG1-Fc control molecules

### huFc (Q295)

TCPPCPAPELLGGPSVFLFPPKPKDTLMISRTPEVTCVVVAVSHEDPEVKFNWYVDGVEVHNAKTKPREEQYNSTYRVVSVLTVLHQDWLNGKEYKCKVSNKALPAPIEKTISKAKGQPREPQVYTLPPSRDELTKNQVSLTCLVKGFYPSDIAVEWESNGQPE  
NNYKTTTPVLDSDGSFFLYSKLTVDKSRWQQGNVFSCSVMHEALHNHYTQKSLSLSPG

### huFc<sup>C265</sup> (D265C)

TCPPCPAPELLGGPSVFLFPPKPKDTLMISRTPEVTCVVVAVSHEDPEVKFNWYVDGVEVHNAKTKPREEQYNSTYRVVSVLTVLHQDWLNGKEYKCKVSNKALPAPIEKTISKAKGQPREPQVYTLPPSRDELTKNQVSLTCLVKGFYPSDIAVEWESNGQPE  
NNYKTTTPVLDSDGSFFLYSKLTVDKSRWQQGNVFSCSVMHEALHNHYTQKSLSLSPG

### huFc<sup>LLQGA-N</sup>

LLQGATCPPCPAPELLGGPSVFLFPPKPKDTLMISRTPEVTCVVVAVSHEDPEVKFNWYVDGVEVHNAKTKPREEQYNSTYRVVSVLTVLHQDWLNGKEYKCKVSNKALPAPIEKTISKAKGQPREPQVYTLPPSRDELTKNQVSLTCLVKGFYPSDIAVEWES  
NGQPENNYKTTTPVLDSDGSFFLYSKLTVDKSRWQQGNVFSCSVMHEALHNHYTQKSLSLSPG

### huFc<sup>LLQGA-G4S-N</sup>

LLQGAGGGGSTCPPCPAPELLGGPSVFLFPPKPKDTLMISRTPEVTCVVVAVSHEDPEVKFNWYVDGVEVHNAKTKPREEQYNSTYRVVSVLTVLHQDWLNGKEYKCKVSNKALPAPIEKTISKAKGQPREPQVYTLPPSRDELTKNQVSLTCLVKGFYPSDIAVEWESNGQPENNYKTTTPVLDSDGSFFLYSKLTVDKSRWQQGNVFSCSVMHEALHNHYTQKSLSLSPG

### huFc<sup>C-G4S-LLQGA</sup>

TCPPCPAPELLGGPSVFLFPPKPKDTLMISRTPEVTCVVVAVSHEDPEVKFNWYVDGVEVHNAKTKPREEQYNSTYRVVSVLTVLHQDWLNGKEYKCKVSNKALPAPIEKTISKAKGQPREPQVYTLPPSRDELTKNQVSLTCLVKGFYPSDIAVEWESNGQPE  
NNYKTTTPVLDSDGSFFLYSKLTVDKSRWQQGNVFSCSVMHEALHNHYTQKSLSLSPGGGGGSLQGA

### huFc<sup>C-(G4S)2-LLQGA</sup>

TCPPCPAPELLGGPSVFLFPPKPKDTLMISRTPEVTCVVVAVSHEDPEVKFNWYVDGVEVHNAKTKPREEQYNSTYRVVSVLTVLHQDWLNGKEYKCKVSNKALPAPIEKTISKAKGQPREPQVYTLPPSRDELTKNQVSLTCLVKGFYPSDIAVEWESNGQPE  
NNYKTTTPVLDSDGSFFLYSKLTVDKSRWQQGNVFSCSVMHEALHNHYTQKSLSLSPGGGGGSGGGSLQGA

## 6.3. Plasmids

pTT5 plasmids containing the modified antibody, antibody fragment or Fcab sequences were ordered from GeneArt (Thermo Fisher Scientific, Waltham, USA) as human codon-optimized versions for mammalian expression. For all constructs the following leader sequence was used: METDTLLLWVLLLWVPGSTG.

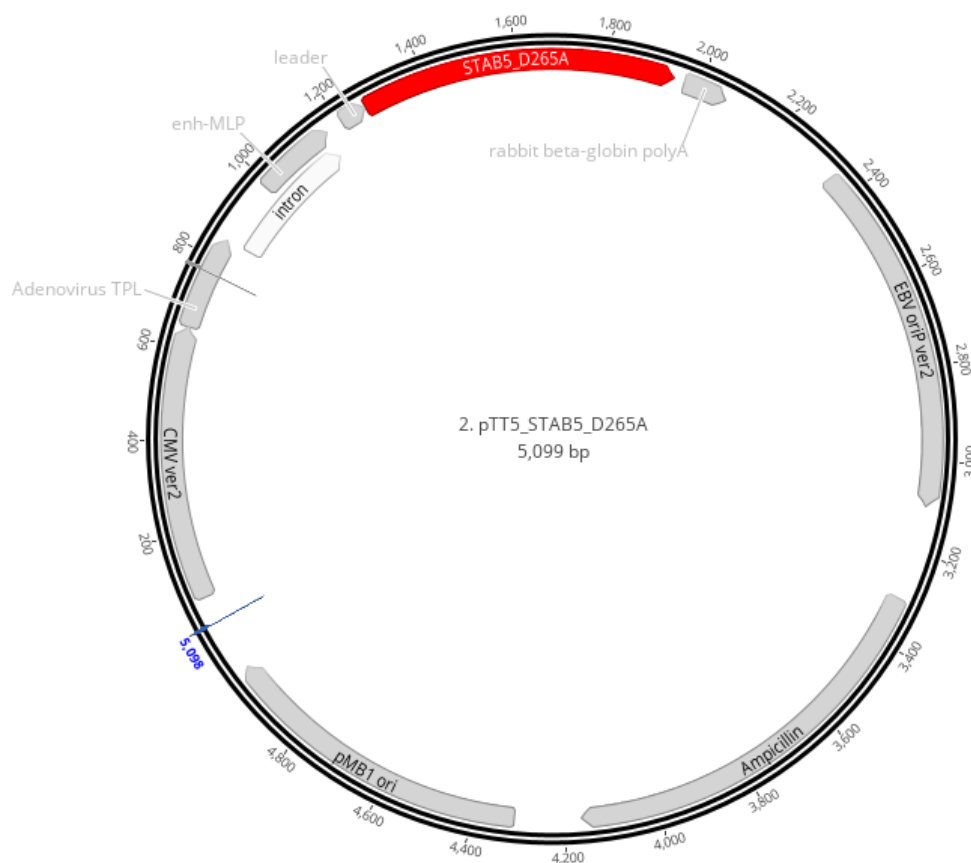


**Figure 18. Exemplary pTT5 vector for mammalian expression.** The pTT5 vector (National Research Council, Canada) contains an origin of replication for mammalian cells (EBV oriP), a bacterial origin of replication (pMB1 ori), an ampicillin resistance gene, a cytomegalovirus immediate early promoter (CMV), a rabbit  $\beta$ -globin polyadenylation signal located downstream of the antibody sequence and the adenovirus tripartite leader (TPL), which is an synthetic intron including an enhancer element from the adenovirus major late promoter enhancing protein expression (enh MLP).

#### 6.4. Enzymes and Proteins

Albumin fraction V from bovine serum (BSA)	Merck, Darmstadt, Germany
EGFR extracellular domain (1-618 aa)-His <sub>6</sub> , recombinant, human	produced in-house; Merck, Darmstadt, Germany
EndoS2 (GlycINATOR®)	Genovis, Lund, Sweden
FcRn-His <sub>6</sub> , biotinylated, human	produced in-house; Merck, Darmstadt, Germany
Fetal Bovine Serum (FBS)	Gibco® Thermo Fisher Scientific, Waltham, USA
Furin, recombinant human (#1503-SE)	R&D Systems, Minneapolis, USA
HER2 extracellular domain (1-607 aa)-muFc-His <sub>6</sub> dimer	produced in-house; Merck, Darmstadt, Germany
HER2-His <sub>6</sub> , recombinant, human (#CP69)	Novoprotein, Fremont, USA

Human serum (#S4200)	BioWest, Nuaille, France
IdeS (FabRICATOR®)	Genovis, Lund, Sweden
Insulin, from bovine pancreas; 10 mg/mL	Sigma Aldrich, St. Louis, USA
Matriptase/ST14 Catalytic Domain (#3946-SEB)	R&D Systems, Minneapolis, USA
MMP-14, recombinant, human (#918-MP)	R&D Systems, Minneapolis, USA
Mouse serum (#S2160)	BioWest, Nuaille, France
Sortase A, recombinant, <i>S. aureus</i>	produced in-house; Merck, Darmstadt, Germany
Transglutaminase, genetically engineered <sup>125</sup>	produced in-house; Merck, Darmstadt, Germany
Transglutaminase, recombinant, <i>S. mobaraensis</i>	Zedira®, Darmstadt, Germany
Trypsin-EDTA; 0.05%, (1x)	Gibco® Thermo Fisher Scientific, Waltham, USA
Trypsin Gold, Mass Spectrometry Grade	Promega, Madison, USA
uPA, recombinant human (#1310-SE)	R&D Systems, Minneapolis, USA

#### 6.4.1. Commercial Antibodies

Alexa Fluor 488 conjugated AffiniPure Fab Fragment Goat Anti-Human IgG (H+L) (#109-547-003)	Jackson ImmunoResearch, Suffolk, GB
Alexa Fluor 488 conjugated AffiniPure F(ab') <sub>2</sub> Fragment Goat Anti-Human IgG Fcγ Fragment specific (#109-546-008)	Jackson ImmunoResearch, Suffolk, GB
Trastuzumab (Herceptin®)	Roche, Basel, Switzerland

#### 6.5. Chemicals

Acetic acid, glacial	Sigma Aldrich, St. Louis, USA
Acetonitrile (LC-MS grade)	LiChrosolv® Merck, Darmstadt, Germany
Agar, extra pure	Merck, Darmstadt, Germany
Ammonium sulfate (NH <sub>4</sub> ) <sub>2</sub> SO <sub>4</sub>	Merck, Darmstadt, Germany
Ammonium bicarbonate NH <sub>4</sub> HCO <sub>3</sub>	Merck, Darmstadt, Germany
Ampicillin, sodium salt	Life Technologies, Carlsbad, USA
Bleach, Attune™	Thermo Fisher Scientific, Waltham, USA
Brij-35	Merck, Darmstadt, Germany
Calcium chloride (CaCl <sub>2</sub> ·2H <sub>2</sub> O)	Merck, Darmstadt, Germany

Chloroacetamide	Merck, Darmstadt, Germany
Cytometer Focusing Fluid (1x), Attune™ NxT	Life Technologies, Carlsbad, USA
1,5-Dansyl-Glu-Gly-Arg chloromethyl ketone	Merck, Darmstadt, Germany
L-Dehydroascorbic acid (L-DHA)	Sigma Aldrich, St. Louis, USA
Deuterated D8-MMAE	MedChemExpress, Monmouth Junction, USA
Disodium hydrogen phosphate (Na <sub>2</sub> HPO <sub>4</sub> ·2H <sub>2</sub> O)	Merck, Darmstadt, Germany
Dithiothreitol (DTT)	Merck, Darmstadt, Germany
DMEM (#D5796)	Sigma Aldrich, St. Louis, USA
DMEM without phenol red (#31053-028)	Gibco® Thermo Fisher Scientific, Waltham, USA
DMSO	VWR International, Radnor, USA
Doxorubicin, hydrochlorid	Calbiochem, San Diego, USA
Dulbecco's PBS (DPBS, w/o CaCl <sub>2</sub> , MgCl <sub>2</sub> )	Gibco® Thermo Fisher Scientific, Waltham, USA
EDTA (ethylenediaminetetraacetic acid)	Sigma Aldrich, St. Louis, USA
Ethanol	Merck, Darmstadt, Germany
Expi293F™ Expression Medium	Gibco® Thermo Fisher Scientific, Waltham, USA
Formic acid	Sigma Aldrich, St. Louis, USA
Gel filtration standard (#151-1901)	Bio-Rad, Hercules, USA
Glucose	Sigma Aldrich, St. Louis, USA
L-Glutamine; 200 mM, (100x)	Gibco® Thermo Fisher Scientific, Waltham, USA
Gly <sub>3</sub> -Val-Cit-MMAE	Levena Biopharma, San Diego, USA
Ham's F-12 Nutrient Mix	Gibco® Thermo Fisher Scientific, Waltham, USA
HEPES buffer; 1 M	Gibco® Thermo Fisher Scientific, Waltham, USA
Hoechst 33342, trihydrochloride dye; 10 mg/mL	Thermo Fisher Scientific, Waltham, USA
Hydrochloric acid (HCl); 1 M	Merck, Darmstadt, Germany
Imidazole	Merck, Darmstadt, Germany
InstantBlue™ Coomassie-based protein stain	Expedeon Ltd, San Diego, USA
Iodoacetamide	Merck, Darmstadt, Germany
Isopropyl alcohol	Merck, Darmstadt, Germany
LDS sample buffer (4x)	NuPAGE® Life Technologies, Carlsbad, USA
Magnesium chloride (MgCl <sub>2</sub> ·6H <sub>2</sub> O)	Merck, Darmstadt, Germany
mc-Val-Cit-MMAE	Levena Biopharma, San Diego, USA
MES SDS running buffer (20x)	NuPAGE® Life Technologies, Carlsbad, USA
Methanol	Merck, Darmstadt, Germany

Methylcellulose solution; 3% (w/v)	R&D Systems, Minneapolis, USA
Monomethyl auristatin E (MMAE)	produced in-house; Merck, Darmstadt, Germany
<i>N</i> -acetylcysteine	Sigma Aldrich, St. Louis, USA
Nickel sulfate (NiSO <sub>4</sub> ·6H <sub>2</sub> O)	Merck, Darmstadt, Germany
Opti-MEM, Reduced Serum Media	Gibco® Thermo Fisher Scientific, Waltham, USA
Paclitaxel, <i>Taxus sp.</i> (Taxol)	Calbiochem, San Diego, USA
Peptone, from casein	Merck, Darmstadt, Germany
pHAb amine reactive dye	Promega, Madison, USA
pHAb thiol reactive dye	Promega, Madison, USA
Potassium di-hydrogen phosphate (KH <sub>2</sub> PO <sub>4</sub> )	Merck, Darmstadt, Germany
Precision Plus Protein™ Unstained Protein Standards (#161-0363)	Bio-Rad, Hercules, USA
RPMI-1640 (#R0883)	Sigma Aldrich, St. Louis, USA
RPMI-1640 without phenol red (#R7509)	Sigma Aldrich, St. Louis, USA
Sample Reducing Agent (10x)	NuPAGE® Life Technologies, Carlsbad, USA
S.O.C. medium	Thermo Fisher Scientific, Waltham, USA
Sodium azide (NaN <sub>3</sub> )	Merck, Darmstadt, Germany
Sodium chloride (NaCl)	Merck, Darmstadt, Germany
Sodium dihydrogen phosphate (NaH <sub>2</sub> PO <sub>4</sub> ·H <sub>2</sub> O)	Merck, Darmstadt, Germany
Sodium hydroxide (NaOH)	Merck, Darmstadt, Germany
Sodium hydroxide solution; 2 M	Merck, Darmstadt, Germany
Sodium perchlorate (NaClO <sub>4</sub> ·H <sub>2</sub> O)	Merck, Darmstadt, Germany
Sodium pyruvate; 100 mM, (100x)	Gibco® Thermo Fisher Scientific, Waltham, USA
Sucrose	Merck, Darmstadt, Germany
Trifluoroacetic acid (TFA) HPLC Grade	Applied Biosystems™, Waltham, USA
Tris(hydroxymethyl)aminomethane-HCl (Tris)	Merck, Darmstadt, Germany
Tris(2-carboxyethyl)phosphine (TCEP); 0.5 M	Sigma Aldrich, St. Louis, USA
Tween-20 (polysorbate 20)	Merck, Darmstadt, Germany
Water (LC-MS grade)	LiChrosolv® Merck, Darmstadt, Germany
Water, milli-Q, autoclaved	Merck, Darmstadt, Germany
Yeast extract, granulated	Merck, Darmstadt, Germany
Zinc chloride (ZnCl <sub>2</sub> )	Merck, Darmstadt, Germany

---

## 6.6. Cell Culture Media

A	DMEM, 10% (v/v) FBS, 1 mM sodium pyruvate, 2 mM L-glutamine
B	Expi293™ expression medium
C	Ham's F-12, 10% (v/v) FBS, 1 mM sodium pyruvate, 2 mM L-glutamine, 10 µg/mL insulin
D	RPMI-1640, 10% (v/v) FBS, 1 mM sodium pyruvate, 2 mM L-glutamine

## 6.7. Solutions, Media and Buffer Preparation

Unless otherwise stated, deionized water was used as solvent

Flow cytometry binding buffer	1% (w/v) BSA in DPBS
FcRn binding assay buffer for BLI	100 mM sodium phosphate (NaH <sub>2</sub> PO <sub>4</sub> , Na <sub>2</sub> HPO <sub>4</sub> ), 150 mM NaCl, 0.05% (v/v) Tween-20, pH 6.0
HI-HPLC mobile phase	A: 1.5 M (NH <sub>4</sub> ) <sub>2</sub> SO <sub>4</sub> , 25 mM Tris, pH 7.5 B: 20% (v/v) isopropyl alcohol, 25 mM Tris, pH 7.5
IMAC elution buffer	500 mM imidazole, pH 7.4
Kinetics buffer (KB) for BLI	0.1% (w/v) BSA, 0.02% (v/v) Tween-20 in PBS pH 7.4
LB agar	1.5% (w/v) agar in LB medium
LB-ampicillin selective agar plates	LB agar, 50 µg/mL (w/v) ampicillin, poured into plates
LB-ampicillin selective medium	LB medium, 50 µg/mL (w/v) ampicillin
LB medium	10 g/L peptone, 5 g/L yeast extract, 10 g/L NaCl
LC-MS mobile phase	A: water (LC-MS grade), 0.1% (v/v) formic acid B: acetonitrile (LC-MS grade), 0.1% (v/v) formic acid
LC-MS sample buffer	water (LC-MS grade), 10% acetonitrile (LC-MS grade), 2% (v/v) formic acid
LC MS/MS mobile phase	A: water (LC-MS grade), 0.1% (v/v) formic acid B: acetonitrile (LC-MS grade)
MMP-14 activation buffer	50 mM Tris, 1 mM CaCl <sub>2</sub> , 0.5% (w/v) Brij-35, pH 9.0
MMP-14 assay buffer	50 mM Tris, 3 mM CaCl <sub>2</sub> , 1 µM ZnCl <sub>2</sub> , pH 8.5
mTG conjugation buffer	PBS pH 6 – 7
Nickel sulfate solution	0.5 M Ni <sub>2</sub> SO <sub>4</sub>

PBS formulation buffer	PBS pH 6.0 – 7.4; pH depends on pI of antibodies, antibody-fragments and Fcabs and should be pH $\leq$ pI – 0.5
pHAb amine reactive dye conjugation buffer	10 mM NaHCO <sub>3</sub> , pH 8.5
Phosphate buffered saline	150 mM NaCl, 8.4 mM Na <sub>2</sub> HPO <sub>4</sub> ·2H <sub>2</sub> O, 1.6 mM KH <sub>2</sub> PO <sub>4</sub> , pH 7.4
Protein A chromatography elution buffer	50 mM acetic acid, pH 3.2
RP-HPLC mobile phase	A: water (LC-MS grade), 0.1% (v/v) TFA B: acetonitrile (LC-MS grade), 0.1% (v/v) TFA
SE-HPLC mobile phase	50 mM sodium phosphate (NaH <sub>2</sub> PO <sub>4</sub> , Na <sub>2</sub> HPO <sub>4</sub> ), 0.4 M NaClO <sub>4</sub> , pH 6.3
SrtA conjugation buffer	150 mM NaCl, 50 mM Tris, 5 mM CaCl <sub>2</sub> , pH 7.5

## 6.8. Kits and Consumables

BLI biosensor, anti-human IgG Fc capture (AHC)	FortéBio, Fremont, USA
BLI biosensor, anti-mouse IgG Fc capture (AMC)	FortéBio, Fremont, USA
BLI biosensor, streptavidin (SA)	FortéBio, Fremont, USA
BLI biosensor, Fab-CH1 2 <sup>nd</sup> Generation (FAB2G)	FortéBio, Fremont, USA
Cell culture flasks T25, T75, T175	Greiner Bio-One, Kremsmünster, Austria
Cryogenic tubes for long-term storage	Nalgene™ Thermo Fisher Scientific, Waltham, USA
Deep well plates, 96 square well, PP, 2 mL	VWR International, Radnor, USA
Desalting spin columns, MWCO 7 k, 75 $\mu$ L, 2 mL	Zeba™ Life Technologies, Carlsbad, USA
Dialysis Membrane MWCO 6-8 kDa, $\varnothing$ 25.5 mm	Spectra/Por® Repligen, Waltham, USA
Dispensehead cassettes D4+ (#F0L60A)	HP, Palo Alto, USA
Dispensehead cassettes T8+ (#F0L59A)	HP, Palo Alto, USA
Erlenmeyer shake flasks, PC, 0.5 L, 1 L, 3 L	Corning® Corning, USA
Glas autosampler vials	VWR International, Radnor, USA
Glas autosampler insert micro vials, 100 $\mu$ L	VWR International, Radnor, USA
Luminescent cell viability assay	CellTiter-Glo® Promega, Madison, USA
Microplates 384 well, black, PS (#781091)	Greiner Bio-One, Kremsmünster, Austria
Microplates 384 well, white, clear, PS (#781080)	Greiner Bio-One, Kremsmünster, Austria



Microplates 384 well spheroid, black/clear round bottom, PS (#3830)	Corning® Corning, USA
Microplates 96-well U-shaped-bottom PS (#168136)	Nunclon™ Thermo Fisher Scientific, Waltham, USA
Microplates 96-well, black, F-bottom, PP (#655209)	Greiner Bio-One, Kremsmünster, Austria
PCR tubes	Thermo Fisher Scientific, Waltham, USA
Plasmid Maxiprep Kit	QIAfilter® Venlo, Netherlands
SDS-PAGE 4 - 12% Bis-Tris gels	NuPAGE® Life Technologies, Carlsbad, USA
Standard capillary chips	NanoTemper Technologies, Munich, Germany
Sterile filters, 0.22 µm, bottle top	Steritop™ Merck, Darmstadt, Germany
Sterile filters, 0.22 µm, centrifugal units	Ultrafree®-CL/MC Merck, Darmstadt, Germany
Sterile filters, 0.22 µm, 50 mL device	Steriflip™ Merck, Darmstadt, Germany
Transfection kit, ExpiFectamine™ 293	Life Technologies, Carlsbad, USA
Transglutaminase activity assay kit, ZediXclusive	Zedira®, Darmstadt, Germany
Tubes 0.2, 1.5, 2.0, 5.0 mL, safe-lock	Eppendorf, Hamburg, Germany
Tubes, 15 mL and 50 mL	Falcon® VWR International, Radnor, USA
Ultra centrifugal filter devices, MWCO 10 K and 30 K, 15 mL, 4 mL, 0.5 mL	Amicon® Merck, Darmstadt, Germany

## 6.9. Devices and Equipment

Analytical balance AE200 or AE240	Mettler-Toledo, Columbus, USA
Automated incubator, BioSpa 8	BioTeK, Winooski, USA
BLI system, Octet® RED96	FortéBio, Fremont, USA
Cell imaging reader, Cytation 5	BioTeK, Winooski, USA
Cell imaging reader, IncuCyte® S3	Sartorius, Göttingen, Germany
Cell imaging system, EVOS FL Auto 2	Life Technologies, Carlsbad, USA
Cell viability analyzer Vi-CELL™ XR	Beckmann Coulter, Brea, USA
Centrifuge 5415D	Eppendorf, Hamburg, Germany
Centrifuge 5810R	Eppendorf, Hamburg, Germany
Centrifuge Galaxy Ministar	VWR International, Radnor, USA

Centrifuge Megafuge 1.0R	Thermo Fisher Scientific, Waltham, USA
Centrifuge Multifuge 3 SR+	Heraeus, Hanau, Germany
Chromatography system ÄKTA avant	GE Healthcare, Buckinghamshire, GB
Chromatography system ÄKTA pure	GE Healthcare, Buckinghamshire, GB
Chromatography system ÄKTAexpress	GE Healthcare, Buckinghamshire, GB
Confocal Laser Scanning Microscope TCS SP8	Leica, Wetzlar, Germany
Cryo 1°C freezing container	Thermo Fisher Scientific, Waltham, USA
Dispenser, D300e	Tecan, Männedorf, Switzerland
Electrophoresis chambers	Novex® Invitrogen, Carlsbad, USA
Erlenmeyer flasks with baffles	Schott, Mainz, Germany
Flow Cytometer, Attune™ NxT	Life Technologies, Carlsbad, USA
HiLoad™ Superdex 200 pg 26/60 column	GE Healthcare, Buckinghamshire, GB
HiPrep™ 26/10 desalting column	GE Healthcare, Buckinghamshire, GB
HisTrap™ HP column, 1 mL	GE Healthcare, Buckinghamshire, GB
HiTrap™ Desalting column, 5 mL	GE Healthcare, Buckinghamshire, GB
HiTrap™ Mab Select SuRe column, 5 mL	GE Healthcare, Buckinghamshire, GB
HPLC column MAB PAK Butyl 5 µm 4.6 x 100 mm	Thermo Fisher Scientific, Waltham, USA
HPLC column PLRP-S 4000 Å, 5 µm, 50 x 2.1 mm	Agilent Technologies, Santa Clara, USA
HPLC column TSKgel SuperSW3000, 4.6 x 300 mm	Tosoh Bioscience, Tokyo, Japan
HPLC column TSKgel SuperSW2000, 4.6 x 300 mm	Tosoh Bioscience, Tokyo, Japan
HPLC 1260 Infinity, ChemStation LC 3D	Agilent Technologies, Santa Clara, USA
Incubation shaker Multitron	Infors HT, Bottmingen, Switzerland
Incubator BBD 6220	Thermo Fisher Scientific, Waltham, USA
Incubator Heracell™ 150	Thermo Fisher Scientific, Waltham, USA
Incubator Heracell™ VIOS 160i	Thermo Fisher Scientific, Waltham, USA
LC-MS system, Exion HPLC system with bioZen™ 3.6 µm Intact C4, 2.1 mm x 100 mm column and TripleTOF® 6600+ mass spectrometer	Shimadzu, Kyoto, Japan; Phenomenex®, Torrance, USA; AB Sciex, Framingham, USA
LC-MS system, U3000 HPLC system equipped with Proteomix RP-1000 1000 Å, 5 µm, 1.0 x 100 mm column and Synapt-G2 mass spectrometer	Dionex, Sunnyvale, USA; Sepax, Newark, USA; Waters, Milford, USA

LC MS/MS system, Acquity UPLC H-Class system equipped with Acquity BEH C18 1.7 $\mu$ m 2.1 x 50 mm and Sciex Triple Quad 6500 system	Waters, Milford, USA; AB Sciex, Framingham, USA
NanoDSF, Prometheus NT.PLEX	NanoTemper Technologies, Munich, Germany
Optical microscope Labovert	Leitz, Wetzlar, Germany
pH meter Seven Easy	Mettler-Toledo, Columbus, USA
Pipette, ViaFlow 16 channel	Integra Biosciences, Zizers, Switzerland
Plate reader, EnVision 2104	Perkin Elmer, Boston, USA
Plate reader, Synergy™ 4	BioTeK, Winooski, USA
Spectrophotometer, Nanodrop ND-1000	Thermo Fisher Scientific, Waltham, USA
Spectrophotometer, Nanodrop One <sup>C</sup>	Thermo Fisher Scientific, Waltham, USA
Sterile bench, laminar air flow, HeraSafe®	Thermo Fisher Scientific, Waltham, USA
ThermoMixer® comfort	Eppendorf, Hamburg, Germany
Vacuum centrifuge concentrator 5301	Eppendorf, Hamburg, Germany

## 6.10. Software

AB Sciex Analyst ver. 1.7	AB Sciex, Framingham, USA
ÄKTA UNICORN software ver. 5.31 (Build 407)	GE Healthcare, Buckinghamshire, GB
Attune™ NxT Software ver. 2.7.0	Life Technologies, Carlsbad, USA
BioSpa OnDemand software ver. 1.03	BioTeK, Winooski, USA
ChemBioDraw Prime ver. 19.1.0.8	Perkin Elmer, Boston, USA
D300e control software ver. 3.4.0	Tecan, Maennedorf, Switzerland
FortéBio Octet Data Acquisition ver. 12.0.1.8	FortéBio, Fremont, USA
FortéBio Octet Data Analysis ver. 12.0.1.2	FortéBio, Fremont, USA
Gen5™ microplate reader Software ver. 3.08.01	BioTeK, Winooski, USA
Genedata Expressionist	Genedata, Basel, Switzerland
Geneious prime® ver. 11.0.4	Biomatters, Auckland, New Zealand
HPLC Software ChemStation	Agilent Technologies, Santa Clara, USA
ImageJ ver. 1.49 with Radial Profile Plot plugin <sup>272</sup>	NIH, Bethesda, USA
Incucyte S3 ver. 2018A	Sartorius, Göttingen, Germany
Leica Application Suite X ver. 3.5.2.18963	Leica, Wetzlar, Germany

---

Prism ver. 8.0.0	GraphPad Software, La Jolla, USA
PR.Thermo Control software ver. 2.1.2	NanoTemper Technologies, Munich, Germany
PyMOL ver. 1.8.6.0	Schrodinger, San Diego, USA
Vi-CELL™ XR Cell viability analyzer ver. 2.04	Beckmann Coulter, Brea, USA
Wallac EnVision Manager ver. 1.12	Perkin Elmer, Boston, USA

## 6.11. Molecular Biological Methods

### 6.11.1. Determination of DNA Concentration

The concentration of nucleic acids in aqueous solutions was measured by spectrophotometer Nanodrop ND-1000 applying 1.5 µL of blank or sample. For blank measurement milli-Q water was used. The law of Lambert-Beer is the fundamental physical principle as well as the absorption of aromatic nucleobases of DNA at 260 nm. The ratios of absorbance  $A_{260}/A_{280}$  and  $A_{260}/A_{230}$  can be used as quality criteria for the purity of the DNA and should be in the range 1.8 and 2.0 - 2.2, respectively. Lower values indicate a contamination with undesired products, typically proteins or aromatic compounds.

### 6.11.2. Transformation in *E. coli*

Typically, synthesized plasmid DNA from GeneArt was dissolved in sterile water and further amplified in *E. coli*. Therefore, One Shot™ TOP10 Chemically Competent *E. coli* cells were transformed with plasmid DNA by heat shock. Briefly, 50 µL chemically competent *E. coli* cells were thawed on ice, followed by the addition of 1 µL plasmid DNA (approximately 500 ng/µL) and incubation for 30 min on ice. Cells were placed in a 42°C water bath for exactly 30 sec, removed and incubated on ice for 3 min. After transformation, 250 µL pre-warmed S.O.C. medium was added, and cells were incubated at 37°C, 450 rpm for 1 h. 50 µL cell suspension were plated on each LB-ampicillin selective agar plate and plates were incubated at 37°C overnight.

### 6.11.3. Plasmid Preparation

Single *E. coli* colonies were picked from the agar plates and inoculated overnight at 37°C, 250 rpm in 100 mL LB-ampicillin selective medium. The next day, bacterial culture was harvested by centrifugation (4800 x g, 4°C for 30 min). Plasmid preparation was performed using a QIAfilter® Plasmid Maxiprep Kit according to the manufacturer's instruction. The washed DNA pellet was dried by vacuum centrifugation and dissolved in sterile milli-Q water. Plasmid DNA was stored at -20°C until transfection.

---

## 6.12. Biophysical and Biochemical Methods

### 6.12.1. Determination of Protein Concentration

Protein concentration was determined by measuring absorbance of aromatic amino acids at 280 nm ( $A_{280}$ ) with a spectrophotometer Nanodrop One<sup>C</sup>. Sample volume was 1.5  $\mu$ L. For blank measurement the PBS formulation buffer was used. Protein concentration (in mg/mL) was calculated by dividing the measured  $A_{280}$  value by theoretical  $A_{280}$  of a 1 mg/mL solution of the protein calculated from the protein sequence by e.g., ExPASy Prot Param tool.<sup>273</sup>

### 6.12.2. SDS-PAGE

Sodium dodecyl sulfate polyacrylamide gel electrophoresis (SDS-PAGE) separates proteins primarily according to molecular weight (sieving effect) when migrating to the anode in an electric field. For this purpose, protein samples were mixed with 4x LDS sample buffer (not-reduced samples) or 4x LDS sample buffer supplemented with 10x sample reducing agent (reduced samples) to reduce disulfide bonds. Reduced samples were incubated in a ThermoMixer for 10 min at 75°C before samples (2  $\mu$ g protein/ lane) were loaded together with a molecular weight marker onto a Bis-Tris gel (4 - 12%), installed in a electrophoreses chamber filled with 1x MES SDS running buffer. Gels were run for 40 min at 200 V. Afterwards, gels were rinsed with deionized water and protein bands were visualized by Coomassie staining. Therefore, gels were incubated for 1 h in InstantBlue™ Protein Stain on an orbital shaker, rinsed with deionized water and incubated in deionized water at gentle orbital shaking overnight.

### 6.12.3. Protein A Affinity Chromatography

Antibodies, Fcabs and huFc controls from cell free Expi293F™ supernatants were purified by affinity chromatography using ÄKTExpress or ÄKTA pure systems equipped with 5 mL HiTrap™ Mab Select SuRe and HiPrep™ 26/10 desalting columns. Mab Select columns were equilibrated with 5 column volumes (CV) PBS formulation buffer at a flow rate of 2.5 mL/min and desalting columns were equilibrated with 3 CV PBS formulation buffer at 7.5 mL/min. Subsequently, supernatant was loaded (2.5 mL/min) on Mab Select column followed by a wash out step with 5 CV. Isocratic elution was carried out with 3 CV using 50 mM acetic acid, pH 3.2. Eluate was directly buffered through desalting column with PBS formulation buffer. 1 mL fractions were collected in 96 deep well plates and fractions containing the target protein were pooled and checked for purity with SDS-PAGE and SE-HPLC. Proteins were concentrated ( $\geq 5$  mg/mL) with Ultra centrifugal filter units (Fcabs, huFc: 10K MWCO, IgG: 30k MWCO; Amicon®) and subjected to preparative size exclusion chromatography (SEC), if SE-HPLC homodimer content was < 95%. Identity of proteins was

---

confirmed *via* intact mass analysis. Proteins were sterile filtered, and protein concentration was determined by UV–VIS spectroscopy at 280 nm. Finally, proteins were snap-frozen in liquid nitrogen and stored at -80°C.

#### **6.12.4. Immobilized Metal Ion Affinity Chromatography (IMAC)**

Fab fragments containing a His<sub>6</sub>-tag were purified by IMAC using an ÄKTA pure system equipped with a 1 mL HisTrap™ HP column. Prior to purification, the Ni<sup>2+</sup> sepharose column was equilibrated with 5 CV PBS pH 7.4 at 4.0 mL/min and the cell free Expi293F™ supernatant was dialyzed against PBS formulation buffer overnight. The dialyzed solution was concentrated and loaded at 4.0 mL/min onto the Ni<sup>2+</sup> sepharose column, followed by a wash out step with 5 CV PBS pH 7.4. Complexed His<sub>6</sub>-tagged Fabs and other bound proteins were stepwise eluted with a 6-step gradient (15 CV each step) using 20 mM, 50 mM, 100 mM, 200 mM, 300 mM, 500 mM imidazole in PBS pH 7.4 (4.0 mL/min). 1 mL fractions were collected in 96 deep well plates and fractions containing the Fab fragment were identified by SDS-PAGE, pooled and checked for purity by SE-HPLC. Protein was concentrated ( $\geq 5$  mg/mL) with Ultra centrifugal filter units (10K MWCO, Amicon®) and subjected to preparative SEC, if SE-HPLC monomer content was  $< 95\%$ . Identity of Fab fragments was confirmed *via* intact mass analysis. Fabs were sterile filtered and protein concentration was determined by UV–VIS spectroscopy at 280 nm. Finally, proteins were snap-frozen in liquid nitrogen and stored at -80°C.

#### **6.12.5. Preparative Size Exclusion Chromatography (SEC)**

Antibodies, antibody fragments, Fcabs and corresponding MMAE conjugates were purified by preparative SEC to remove high molecular weight (aggregates) or low molecular weight species. For this, an ÄKTA pure or ÄKTA avant system equipped with a HiLoad™ Superdex 200 pg 26/60 column was used. The column was equilibrated with 5 CV PBS formulation buffer at 10.0 mL/min, before  $\leq 2$  mL concentrated protein solution was loaded onto the column (2.5 mL/min) *via* a sample loop. 1 mL fractions were collected in a 96 deep well plate and fractions containing the target protein were pooled and checked for purity with SE-HPLC. Proteins were concentrated ( $\geq 5$  mg/mL) using Ultra centrifugal filter units (10K MWCO, Amicon®), sterile filtered, and protein concentration was determined by UV–VIS spectroscopy at 280 nm. Finally, proteins or protein-conjugates were snap-frozen in liquid nitrogen and stored at -80°C.

#### **6.12.6. Analytical Size Exclusion Chromatography (SE-HPLC)**

Protein purity, aggregation status and molecular size of expressed and conjugated proteins was analyzed by SE-HPLC using an Agilent 1260 Infinity system equipped with a TSKgel® SuperSW3000 column. The column was equilibrated with mobile phase buffer (50 mM sodium phosphate, 0.4 M NaClO<sub>4</sub>, pH 6.3) at 0.35 mL/min until a stable baseline was observed. Typically, a gel filtration standard was injected before and after sample

---

runs to allow for the calculation of apparent molecular weights ( $MW_{app}$ ). 10  $\mu$ g protein was applied per SE-HPLC run and chromatograms were recorded at 214 nm or 280 nm. Peaks were analyzed and integrated by the ChemStation software and target protein purity as well as content of high and low molecular weight species were determined from peak area.

#### **6.12.7. Reversed Phase HPLC (RP-HPLC)**

RP-DAR of conjugated protein was determined by RP-HPLC using an Agilent 1260 Infinity system equipped with a PLRP-S column (4000 Å, 5  $\mu$ m, 2.1  $\times$  50 mm; Agilent). Prior to analysis, conjugated protein and its unconjugated parental protein were diluted with PBS formulation buffer to 1 mg/mL. 5  $\mu$ g protein were loaded onto the 65°C preheated column and a gradient of 30% to 45% solvent B over 7.5 min at a flow rate of 1 mL/min was applied (solvent A: water, 0.1% (v/v) TFA, B: acetonitrile, 0.1% (v/v) TFA). Eluted protein peaks were detected at 214 nm. Subsequently, RP-DAR was calculated from peak areas of individual DAR species using the unconjugated parent as reference.

#### **6.12.8. Hydrophobic Interaction HPLC (HI-HPLC)**

To analyze conjugate overall hydrophobicity and the shielding of the hydrophobic payload, HI-HPLC was performed. Therefore, samples were adjusted to 0.5 M  $(NH_4)_2SO_4$  and assessed *via* an Agilent 1260 Infinity system equipped with a MAB PAK Butyl column (5  $\mu$ m, 4.6  $\times$  100 mm, Thermo Scientific). Samples were separated applying a full gradient from A (1.5 M  $(NH_4)_2SO_4$ , 25 mM Tris, pH 7.5) to B (20% (v/v) isopropyl alcohol, 25 mM Tris, pH 7.5) over 20 min at 1 mL/min and 30°C. Typically, 40  $\mu$ g sample were used and signals were recorded at 280 nm.

Relative retention times (RRT) were calculated by dividing the absolute retention time of the DAR 2 species by the retention time of the respective unconjugated protein.

#### **6.12.9. LC-MS Intact Mass Analysis**

Identity of proteins was confirmed *via* LC-MS intact mass analysis using either (1) a Shimadzu HPLC system with a Phenomenex® bioZEN column (3.6  $\mu$ m Intact C4, 2.1 mm  $\times$  100 mm) coupled to a TripleTOF® 6600+ mass spectrometer (AB Sciex) or (2) a Dionex U3000 HPLC system equipped with a Proteomix RP-1000 column (1000 Å, 5  $\mu$ m, 1.0  $\times$  100 mm; Sepax) coupled to a Synapt-G2 mass spectrometer (Waters). Both devices were run with a gradient of solvent A (water, 0.1% (v/v) formic acid) and solvent B (acetonitrile, 0.1% (v/v) formic acid). Protein samples were diluted in LC-MS sample buffer to a final concentration of 0.5 mg/mL and reduced with TCEP (final 50 mM) for 5 min at room temperature before subjected to LC-MS analysis. Recorded TIC

---

chromatograms were deconvoluted and protein fragments were identified by comparing observed masses with calculated masses considering different glycosylation patterns.

#### 6.12.10. LC-MS DAR Determination

Prior to LC-MS DAR determination, conjugates were diluted with  $\text{NH}_4\text{HCO}_3$  (25 mM) to a final concentration of 0.025 mg/mL and reduced with TCEP (final 12 mM) for 5 min at room temperature. Subsequently, conjugates were alkylated by adding chloroacetamide (final 50 mM), followed by overnight incubation at 37°C in the dark.

For DAR determination the same LC-MS systems as for intact mass analysis were used following two distinct procedures: (1) The reduced and alkylated sample was loaded onto the RP column of a Dionex U3000 HPLC system and separated by a gradient from 30 – 55% (v/v) solvent B over the course of 14 min before entering the Synapt-G2 mass spectrometer for identification of the DAR species. (2) The reduced and alkylated sample was injected directly in the TripleTOF® 6600+ mass spectrometer without HPLC separation.

Recorded TIC chromatograms were deconvoluted and protein fragments were identified by comparing observed masses with calculated masses considering different glycosylation patterns and numbers of attached drugs. MS-DAR was calculated from TIC peak areas (**Figure A13**). LC-MS DAR was calculated from RP-HPLC peak areas (**Figure A14, Figure A15**).

#### 6.12.11. Peptide Mapping

Fcab and corresponding Fcab-MMAE conjugate were deglycosylated with endoglycosidase from *S. pyogenes* (EndoS2) (GlycINATOR®, Genovis) according to the instruction manual. Deglycosylated molecules were then reduced with 10 mM DTT for 30 min at 56°C and alkylated with 55 mM iodoacetamide for 30 min at room temperature in the dark. 10 µg protein was digested with 0.5 µg trypsin gold (Promega) at 37°C overnight.

LC-MS analysis was performed using an Exion HPLC system coupled to a TripleTOF 6600+ mass spectrometer (Sciex). 7.5 µg peptide solution was loaded onto an Aeris PEPTIDE XB-C18 column (Phenomenex) and eluted with a linear gradient from 5% to 50% solvent B (acetonitrile, 0.1% formic acid; solvent A: water, 0.1% formic acid) within 49 min. Data were acquired with positive polarity and in a TOF-MS mass range from 350 to 2500 m/z and a TOF-MS/MS mass range from 50 to 2500 m/z. Other instrument settings were as follows: ion spray voltage 5.5 kV, source temperature 450°C, accumulation time 0.25 s for TOF-MS and 0.08 s for TOF-MS/MS, gas1 45 psi, gas2 45 psi, curtain gas 35 psi, declustering potential 80 V, and collision energy was set to dynamic. Data was processed with Genedata Expressionist.

---

### 6.12.12. Thermal Stability

Thermal unfolding of Fcabs and huFc was assessed by differential scanning fluorimetry (DSF). Therefore, the molecules (in PBS formulation buffer) were loaded into nanoDSF grade standard capillaries which were then transferred into a Prometheus NT.PLEX nanoDSF instrument. Samples were subjected to a linear thermal ramp from 20°C to 95°C at a slope of 1°C/min with simultaneous recording of fluorescence at 350 and 330 nm. Unfolding transition midpoints ( $T_m$ ) were determined from the first derivative of the fluorescence ratio 350 nm/330 nm. All samples were measured in duplicates.

### 6.12.13. Biolayer Interferometry

Kinetic binding parameters were determined by BLI using the Octet® RED96 system (FortéBio) at 30°C and 1,000 rpm agitation speed.

#### **HER2 Binding**

For HER2 binding analysis of Fcab variants,  $\alpha$ H-T-Fab and respective MMAE conjugates (analytes), anti-mouse IgG Fc capture biosensors (AMC) were loaded with murine Fc-HER2 dimer (20  $\mu$ g/mL diluted in DPBS) for 360 s. Biosensors were then transferred into kinetics buffer and incubated for 45 s followed by an association step to the analytes. Analytes were diluted in kinetics buffer in a concentration range varying from 200 nM to 3.13 nM. Association was monitored for 180 s or 240 s followed by a dissociation step in kinetics buffer for 480 s to determine  $k_{on}$  and  $k_{off}$  values. Analytes were replaced by kinetics buffer, serving as a negative control and reference measurement. Respective non-binding human Fc fragments were used as negative controls in each experiment. The buffer reference measurement (control curve) was subtracted from antibody measurements for data fitting and kinetics parameter were determined by using FortéBio data analysis software applying a 1:1 global full-fit binding model after Savitzky-Golay filtering.

For HER2 binding analysis of  $\alpha$ H-T-IgG and its MMAE conjugate, a reversed assay set-up using monomeric HER2-His<sub>6</sub> (Novoprotein) as analyte was chosen to avoid avidity effects. After a 60 s baseline step in DPBS, antibodies (10  $\mu$ g/mL in DPBS) were loaded for 60 s on anti-human IgG Fc capture biosensors (AHC) followed by a 45 s kinetics buffer step. Association of HER2-His<sub>6</sub> (50 – 0.78 nM, diluted in kinetics buffer) was monitored for 180 s before a final dissociation step in kinetics buffer for 420 s. Buffer reference measurements and controls were included and data was processed as mentioned before.

#### **EGFR Binding**

For EGFR binding analysis, Fcab variants (10  $\mu$ g/mL in DPBS),  $\alpha$ E-C-IgG (2.5  $\mu$ g/mL in DPBS) and respective MMAE conjugates were loaded onto anti-human IgG Fc capture biosensors (AHC) for 60 – 180 s.  $\alpha$ E-C-Fab

---

(2.5 µg/mL in DPBS) was loaded onto anti-human Fab-CH1 2<sup>nd</sup> Generation biosensors (FAB2G) for 180 s. Biosensors were then transferred into kinetics buffer and incubated for 60 s followed by an association step to EGFR-His<sub>6</sub>. EGFR-His<sub>6</sub> was serially diluted in kinetics buffer in a concentration range varying from 20 nM to 0.313 nM. Association was monitored for 180 s, 240 s or 300 s, followed by a dissociation step in kinetics buffer for 600 s. Buffer reference measurements and controls were included and data was processed as mentioned before.

### ***FcRn Binding***

The FcRn binding assay was adapted from a published FortéBio application note.<sup>274</sup> Baseline, association and dissociation steps were performed in FcRn binding assay buffer. The same buffer was used for dilution of analytes and ligands. Streptavidin biosensors were used and sensorgrams were recorded at 10 Hz starting with a 60 s baseline step, before biotinylated FcRn-His<sub>6</sub> (2 µg/mL) was captured for 120 s. Subsequently, association of Fcabs, IgGs and corresponding MMAE conjugates was measured at varying concentrations (1 µM to 15.63 nM) for 60 s followed by dissociation for 60 s. A reference measurement with loaded biosensor omitting analyte association was included in each run to account for ligand dissociation. To subtract unspecific binding to the sensor tips, the assay was run again with unloaded reference biosensors. After subtracting the reference measurement and the reference sensor run (double referencing), a Savitzky-Golay filtering was performed and data was fitted using a 1:1 global partial-dissociation model. Due to the typical biphasic dissociation, the dissociation step was only fitted for 4 s to cover the initial fast dissociation rate.<sup>274</sup>

### **6.12.14. Proteolytic Cleavage Reaction**

Proteolytic hinge cleavage of cleavable αH-T-CL-S5 and αH-T-CL-S19 was performed with recombinant human TME proteases uPA and matriptase (MT-SP1). MMP-14 was included as a negative control TME protease that does not recognize the engineered hinge cleavage site. Prior to cleavage, MMP-14 (final 2.6 µM) was activated with human recombinant furin (final 26 nM) in MMP-14 activation buffer for 1.5 h at 37°C. Protease cleavage was performed by adding antibodies (final 1 µM) to proteases uPA (final 100 nM, in PBS pH 7.4), matriptase (final 40 nM, in PBS pH 7.4), or activated MMP-14 (final 100 nM, in MMP-14 assay buffer) and incubation of the mixtures (150 µL total volume each) at 37°C for 24 h. Samples (13 µL) were taken at 0.5 h, 1 h, 2 h, 3 h, 4 h, 5 h, 6 h and 24 h, immediately mixed with 2 µL of the protease inhibitor 1,5-dansyl-Glu-Gly-Arg chloromethyl ketone (1.43 mM in PBS pH 7.4) and frozen at -80°C until analysis. Upon completing time series, 15 µL samples were mixed with 5 µL 4x LDS sample buffer and 20 µL/ lane (2 µg protein) were loaded together with intact antibody onto a Bis-Tris gel (4 - 12%) for SDS-PAGE analysis.

---

### 6.12.15. pHAb-Dye Labeling

For thiol coupling, antibodies, antibody fragments and Fcabs were reduced with 2.5 mM DTT in DPBS, 1 mM EDTA, pH 7.0 for 1.5 h at 25°C, 450 rpm. DTT was removed by Zeba™ Spin desalting columns, previously equilibrated with DPBS, 1 mM EDTA, pH 7.0 according to the manufacturer's instructions. 2.0 molar equivalents (pHAb:antibody) of pHAb thiol reactive dye (10 mg/mL in 1:1 (v/v) DMSO/water) were added to the reduced antibodies, antibody fragments and Fcabs and incubated for 3 h at 25°C, 450 rpm in the absence of light. Typically, no unreacted pHAb-dye was left.

For amine coupling, antibodies, antibody fragments and Fcabs were formulated in 10 mM sodium-bicarbonate buffer pH 8.5. pHAb amine reactive dye (10 mg/mL 1:1 (v/v) DMSO/water) was either added at a 2:1 molar ratio (pHAb:antibody) ( $\alpha$ E-60,  $\alpha$ E-65,  $\alpha$ E-67,  $\alpha$ E-C-IgG,  $\alpha$ E-C-Fab) or a 10:1 molar ratio (huFc), followed by incubation at 25°C, 450 rpm for 1 h in the absence of light. Excess dye was removed by DPBS equilibrated Zeba™ Spin desalting columns.

The degree of labeling (DOL) could be determined by UV–VIS spectroscopy according to the manufacturer's instructions or by an SE-HPLC method described in section 6.12.20.

### 6.12.16. Cysteine Conjugation

Antibody fragments and Fcabs were diluted to a final concentration of 5 mg/mL in PBS pH 7.4, 1 mM EDTA and partially reduced with an excess of 40 equivalents TCEP for 2 h at 37°C. TCEP was removed by desalting using an ÄKTA avant equipped with two consecutively connected 5 mL HiTrap™ desalting columns pre-equilibrated with PBS formulation buffer. Subsequently, the purified, reduced antibody fragments were reoxidized with 20 equivalents L-dehydroascorbic acid (L-DHA) for 2 h at 25°C. To this mixture, 8 equivalents of mc-Val-Cit-MMAE were added and incubated for 1 h at 25°C before the reaction was stopped by the addition of 25 equivalents of *N*-acetylcysteine (15 min at 25°C) and purified by preparative SEC. Purified conjugates were concentrated using Ultra centrifugal filter units (10K MWCO, Amicon®), sterile filtered and protein concentration was determined by UV–VIS spectroscopy at 280 nm. The purified conjugates were subjected to analysis by SE-HPLC and DAR determination (RP-HPLC, HI-HPLC, LC-MS), snap-frozen in liquid nitrogen and stored at -80°C.

### 6.12.17. Sortase A Conjugation

For SrtA conjugation to LC-C-terminal LPETGS tags,  $\alpha$ E-C-IgG or  $\alpha$ E-C-Fab were formulated in SrtA conjugation buffer (final 5 mg/mL) using Ultra centrifugal filter units ( $\alpha$ E-C-Fab: 10K MWCO,  $\alpha$ E-C-IgG: 30k MWCO; Amicon®). SrtA<sup>275</sup> was added to a final concentration of 13  $\mu$ M along with 10 equivalents of Gly<sub>3</sub>-Va-Cit-MMAE per SrtA recognition motif. The reaction mixture was incubated for 90 min at 25°C,

---

stopped by the addition of EDTA as Ca<sup>2+</sup> chelator (final 10 mM) and purified by preparative SEC. Purified conjugates were concentrated using Ultra centrifugal filter units, sterile filtered and protein concentration was determined by UV–VIS spectroscopy at 280 nm. The purified conjugates were subjected to analysis by SE-HPLC and DAR determination (RP-HPLC, HI-HPLC, LC-MS), snap-frozen in liquid nitrogen and stored at -80°C.

#### **6.12.18. Transglutaminase Conjugation**

mTG-mediated antibody conjugation was assessed in PBS formulation buffer with up to 10% (v/v) DMSO. 5 mg/mL antibody, antibody-fragments or Fcabs and 20 equivalents of linker-drug Gly<sub>3</sub>-Val-Cit-MMAE were mixed with 60 U/mL genetically engineered mTG (made in-house<sup>125</sup>) for conjugation on Q295 or 6 U/mL mTG from *S. mobaraensis* (Zedira) for conjugation on N-terminal LLQGA tags. Reaction mixes were incubated at 37°C for 18 h with gentle shaking, chilled to 10°C and purified by preparative SEC. Purified conjugates were concentrated using Ultra centrifugal filter units (Fcab, huFc: 10K MWCO, IgG: 30k MWCO; Amicon®), sterile filtered and protein concentration was determined by UV–VIS spectroscopy at 280 nm. The purified conjugates were subjected to analysis by SE-HPLC and DAR determination (RP-HPLC, HI-HPLC, LC-MS), snap-frozen in liquid nitrogen and stored at -80°C.

Activity of mTG (U/mL) was determined using the ZediXclusive microbial transglutaminase (Zedira) photometric assay according to the manufacturer's instructions.<sup>125</sup>

#### **6.12.19. Serum Stability**

Mouse and human serum were thawed at ambient temperature and supplemented with HEPES buffer (final 0.3 M HEPES) in order to maintain serum pH levels close to physiological pH ranging between pH 7.3 and pH 7.4. Buffered serum was sterile filtered and MMAE conjugate stock solutions were added to the serum sample at final concentrations of 5 µM conjugated MMAE (considering the DAR of each construct). In addition, samples were supplemented with deuterated D8-MMAE internal standard (final 5 µM). Samples were mixed and transferred to PCR tubes with a final volume of 20 µL per aliquot, followed by incubation at 37°C, 5% CO<sub>2</sub>, 95% H<sub>2</sub>O. Triplicates were prepared for each sample. Sample time series were collected at timepoints 0, 2, 4, 6, 24, 48, 72 and 96 h and stored at -80°C until further analysis. Serum samples (5 µL) were transferred to PCR tubes, mixed with 150 µL methanol and MMAE as well as D8-MMAE concentrations were analyzed by UPLC MS/MS. For the UPLC system, an ACQUITY UPLC H-Class System (Waters) was used along with an Acquity UPLC BEH C18 1.7 µm 2.1 × 50 mm column (Waters). For the mobile phase, solvent A was used with 0.1% formic acid in water and acetonitrile for solvent B. Mass spectrometer measurements were performed using a Sciex Triple Quad 6500 system and AB Sciex Analyst for data analysis.

## 6.12.20. Degree of pHAb-Dye Labeling

SE-HPLC was performed on a 1260 Infinity device from Agilent Technologies equipped with a diode array (DAD) and a fluorescence (FLD) detector module and either a TSKgel SuperSW3000 or a SuperSW2000 column. The mobile phase consisted of 50 mM sodium phosphate, 400 mM sodium perchlorate, pH 6.3 and its flow rate was set to 0.35 mL/min. The DAD was set to detect absorption at 280 nm (aromatic amino acids) and 535 nm (pHAb-dye). The excitation and emission wavelengths of the FLD were set to 535 nm and 566 nm to record fluorescence of pHAb-dye (see also **Figure 24B**).

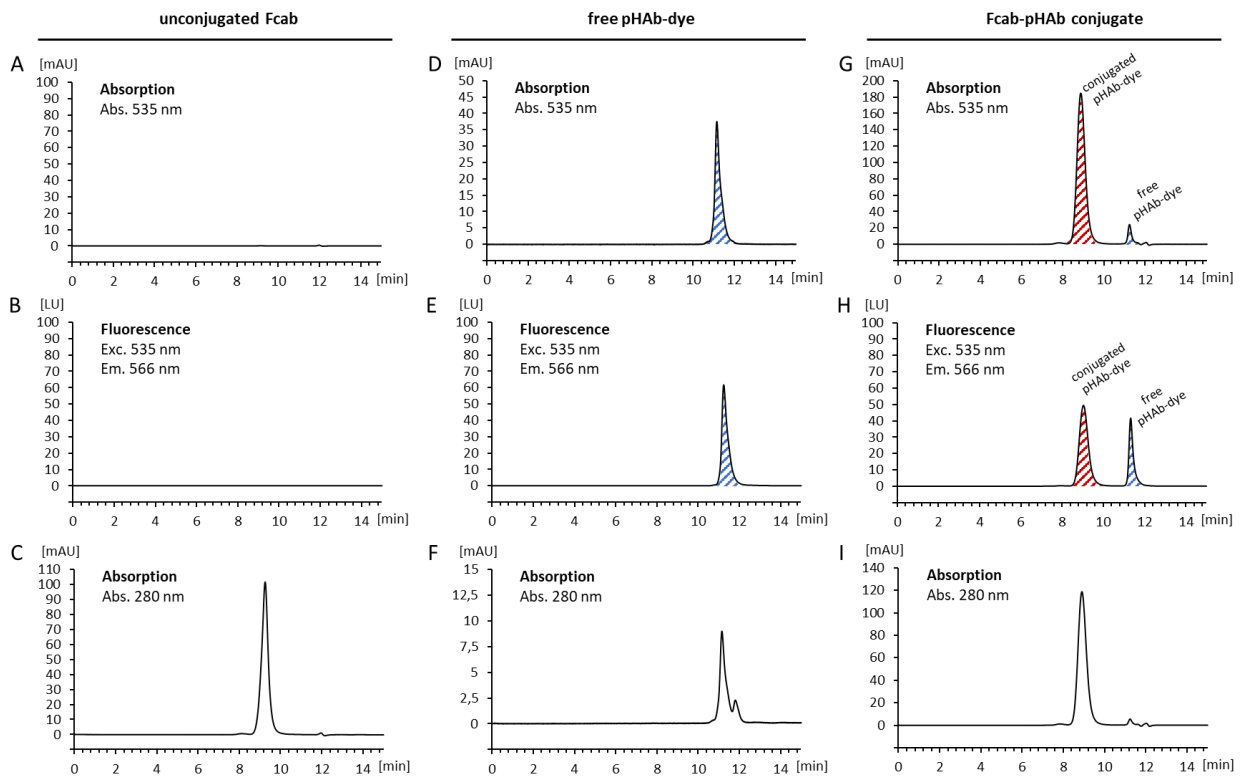


**Figure 19.** SE-HPLC analysis for the determination of pHAb-dye DOL, exemplarily shown for a pHAb-dye conjugated Fcab. (A) Unconjugated Fcab does not absorb light at 535 nm. (B) Hence, Fcab does not show fluorescence at 566 nm when excited at 535 nm (pHAb-dye absorption maximum). (C) Absorption of Fcab at 280 nm (aromatic amino acids). Fcab (54 kDa) elutes at 9.3 min. (D) Absorption of free pHAb-dye at its absorption maximum at 535 nm. According to its smaller size, free pHAb-dye (786 g/mol, carboxylic acid form) elutes at higher  $t_R$  11.2 min. (E) Fluorescence at 566 nm (pHAb-dye fluorescence maximum) of free pHAb-dye when excited at 535 nm. (F) Free pHAb-dye absorbs also at 280 nm. The smaller peak at 11.8 min is caused by buffer components and was neglected for peak integration. (G) Absorption at 535 nm of Fcab-pHAb conjugate. The first peak marked in red represents the absorption of conjugated pHAb-dye molecules while the second peak marked in blue shows free pHAb-dye which could not be removed entirely by Zeba™ spin desalting column purification. (H) Fluorescence at 566 nm of Fcab-pHAb conjugate. The peak depicted in red shows fluorescence of conjugated pHAb-dye while the blue peak shows fluorescence of free pHAb-dye. With respect to the peak area of the absorption signal (535 nm) of conjugated pHAb-dye depicted in (G), its relative fluorescence signal (H) is reduced compared to the fluorescence signal of free pHAb-dye. This indicates that the local molecular environment influences the fluorophore quantum yield. (I) Absorption of Fcab-pHAb at 280 nm is composed of the absorption of its protein and pHAb-dye components.

Free pHAb-dye, pHAb-dye conjugated proteins and the corresponding unconjugated proteins were then analyzed by SE-HPLC. **Figure 19** depicts exemplarily the resulting chromatograms for unconjugated protein, free pHAb-dye and pHAb-dye conjugated protein.

#### **Calculating molar extinction coefficients (MEC) of unconjugated protein and free pHAb-dye from SE-HPLC peak area**

In a next step, the molar extinction coefficients (MEC) of unconjugated protein and free pHAb-dye were calculated from SE-HPLC peak areas. Exemplary chromatograms can be found in **Figure 19C** (unconjugated protein) and **Figure 19D-F** (free pHAb-dye). Relevant peaks were integrated using the ChemStation analysis software by Agilent. From the corresponding peak area, the  $MEC_{280nm}$  of the unconjugated protein and the  $MEC_{535nm}$  of free pHAb-dye could be determined applying the following equation derived from Wang *et al.*<sup>276</sup>

$$\varepsilon_i = \frac{Ar \cdot F}{l \cdot c \cdot v_{inj}} \quad (10)$$

where  $\varepsilon_i$  is the MEC at wavelength  $\lambda_i$ ,  $Ar$  is the calculated peak area,  $F$  is the SE-HPLC flow rate,  $l$  is the flow cell path length,  $c$  is the concentration of the injected sample, and  $v_{inj}$  is the injected sample volume. **Table 4** summarizes the resulting MEC of unconjugated proteins and free pHAb-dye.

**Table 4. Molar extinction coefficient at different wavelengths.** MEC are given as the mean ( $\pm$  SD). Different volumes of unconjugated protein or free pHAb-dye solution were injected in three consecutive SE-HPLC runs and the resulting peak areas were used to calculate MEC from equation (10). For example, when injecting  $v_{inj} = 7.5 \mu\text{L}$  of  $c = 18.3 \mu\text{M}$  Fcab a single peak with a peak area  $Ar_{280nm}$  of 1825 eluted at 9.3 min (**Figure 19C**). With a constant SE-HPLC flow rate of  $F = 5.8 \mu\text{L/s}$ , a  $MEC_{280nm}$  of  $77122 \text{ (mM}\cdot\text{cm)}^{-1}$  was calculated.

analyte	$MEC_{280nm}$ [mM·cm] <sup>-1</sup>	$MEC_{535nm}$ [mM·cm] <sup>-1</sup>
$\alpha\text{E-60}$	94582 $\pm$ 685	-
$\alpha\text{E-65}$	94608 $\pm$ 1	-
$\alpha\text{E-67}$	96964 $\pm$ 155	-
huFc	75217 $\pm$ 306	-
$\alpha\text{E-C-Fab}$	72828 $\pm$ 26	-
$\alpha\text{E-C-IgG}$	107610 $\pm$ 182	-
free pHAb-dye	14825 $\pm$ 257	60813 $\pm$ 823

#### **Calculating the DOL from SE-HPLC peak area of pHAb-dye conjugated protein and MEC**

To calculate the DOL value from a pHAb-dye labeled construct, the molar amount of conjugated pHAb-dye ( $n_{\text{pHAb},535nm}$ ) and protein ( $n_{\text{protein},280nm}$ ) was calculated first. Therefore, pHAb-dye labeled constructs were analyzed by SE-HPLC and the absorption peak area of conjugated pHAb-dye (**Figure 19G** peak marked in red), as well as peak area from absorption at 280 nm (**Figure 19I**) were calculated. Absorption at 280 nm is caused not only by the protein structure but also by the conjugated pHAb-dye (**Figure 19F**). To calculate the amount

of injected protein from this peak, the peak area that is contributed by pHAb-dye must be subtracted. The portion of pHAb-dye absorption at 280 nm can be derived from its peak area at 535 nm ( $Ar_{535nm}$ ) and subtracted from total peak area at 280 nm ( $Ar_{280nm}$ ) as shown in equation (11):

$$Ar_{280nm,corrected} = Ar_{280nm} - \left( Ar_{535nm} \cdot \frac{MEC_{pHAb,280nm}}{MEC_{pHAb,535nm}} \right) \quad (11)$$

Subsequently, the amount of injected protein can be calculated from the corrected peak area ( $Ar_{280nm,corrected}$ ) by equation (12):

$$n_{protein,280nm} = \frac{Ar_{280nm,corrected} \cdot F}{MEC_{protein,280nm}} \quad (12)$$

Similarly, the amount of conjugated pHAb-dye can be calculated from the peak area of its absorption signal at 535 nm ( $Ar_{535nm}$ ):

$$n_{pHAb,535nm} = \frac{Ar_{535nm} \cdot F}{MEC_{pHAb,535nm}} \quad (13)$$

The ratio between the amount of conjugated pHAb-dye molecules and protein defines the DOL value of a construct:

$$DOL = \frac{n_{pHAb,535nm}}{n_{protein,280nm}} \quad (14)$$

The SE-HPLC chromatograms of relevant pHAb-dye conjugates as well as derived DOL values are shown in **Figure A8** and **Table 10**.

## 6.13. Cell Biological Methods

### 6.13.1. Cultivation of Mammalian Cells

Cells were thawed rapidly in a water bath at 37°C, resuspended in 10 mL of pre-warmed medium and centrifuged for 10 min, 250 x g at ambient temperature. The supernatant was removed, and the pellet was resuspended in 10 mL cell culture medium and seeded into a cell culture flask of appropriate size.

Adherent cancer cells were maintained according to standard culture conditions in T25, T75 or T175 flasks (37°C, 5% CO<sub>2</sub>, 95% humidity) and usually subcultured every 3-4 days. For example, confluent grown cells in T175 flasks were washed two times with 13 mL pre-warmed DPBS and detached with 1 mL 0.05% trypsin-EDTA. Trypsin activity was stopped by addition of 9 mL fresh medium and cell viability as well as cell number were measured by Vi-CELL™ XR. For subculturing, an appropriate number of cells was transferred into a new culturing flask, diluted with fresh medium to 13 mL and returned to the incubator.

Expi293F™ cells were cultured in Erlenmeyer shake flasks (Corning®) according to the manufacturer's instructions.

---

### 6.13.2. Protein Production

Antibodies, antibody-fragments and Fcabs were expressed by transient transfection of heavy chains (and light chains) in Expi293F™ cells following the manufacturer's instructions using the corresponding transfection kit and media from Life Technologies. HC and LC plasmids were used at a HC:LC 1:2 ratio for transfection. Expression volumes were either 100 mL (0.5 L flask) or 200 mL (1 L flask).

Supernatant was harvested by centrifugation (4800 x g, 4°C for 1 h) after 5 days post transfection and sterile filtered before purification *via* affinity chromatography.

### 6.13.3. Cellular Binding Assay

Cellular binding of antibodies, antibody-fragments or Fcabs was studied *via* a flow cytometry-based assay. Therefore, the cells were centrifuged (10 min at 500 x g, 4°C), the supernatant was carefully aspirated and cells were resuspended in a suitable volume of DPBS, 1% (w/v) BSA to obtain a final concentration of  $1 \cdot 10^6$  cells/mL. 100  $\mu$ L of cell suspension was added to each well of a 96 well round bottom microplate ( $1 \cdot 10^5$  cells/well). The plate was centrifuged for 5 min at 660 x g and 4°C and the supernatant was discarded. Analytes (100  $\mu$ L/well) were added in 1:2 dilution series starting at concentrations approximately 100-fold higher than the expected  $K_D$  value. Plates were incubated for 60 min on ice to prevent internalization and centrifuged afterwards (5 min at 660 x g and 4°C). The supernatant was discarded, and cell pellets were washed twice with 150  $\mu$ L chilled DPBS, 1% (w/v) BSA. Microplates were centrifuged again, and the resulting cell pellets were taken up in 100  $\mu$ L chilled AF488-labeled detection antibody (final 500 nM in DPBS, 1% (w/v) BSA; IgGs, huFc, Fcabs: #109-546-008; Fabs: #109-547-003; Jackson ImmunoResearch). Cells were incubated with labeling antibodies for 30 min on ice in the absence of light, washed twice, centrifuged, and taken up in 200  $\mu$ L chilled DPBS, 1% (w/v) BSA. The plate was immediately transferred to an Attune NxT flow cytometer and fluorescence (Exc. 488 nm, Em. 574 nm) of cells was analyzed (30,000 counts/well). Cellular binding was typically analyzed on one target-negative and two target-positive cell lines.

### 6.13.4. Cellular Uptake Assay

Cells were centrifuged at 500 x g for 10 min. The supernatant was discarded, and cells were resuspended in the respective medium without phenol red (SKBR-3, HCC-1954, BT-474, MDA-MB-468: 200,000 cells/mL; MDA-MB-468, A431, MCF-7: 300,000 cells/mL). The cell suspension (40  $\mu$ L/well) was seeded into a black 384 clear bottom plate followed by incubation (37°C, 5% CO<sub>2</sub>) in a humid chamber overnight. pHAb-dye constructs were supplemented with 0.3% Tween-20 (final), diluted to 3  $\mu$ M and added in triplicates to the cells (final 100 nM) using a D300e digital dispenser. The cells were immediately transferred to a Cytation 5 cell imaging reader equipped with DAPI and RFP filter cubes and a BioSpa 8 automated incubator. Brightfield

---

(objective: 10x, LED intensity: 10, integration time: 13 msec, camera gain: 24) and RFP channel images (Exc. 531 nm, Em. 593 nm, LED intensity: 10, integration time: 55 msec, camera gain: 24) were taken every 2 h over a period of 24 h. About 30 min before the 24 h measurement, the plate was removed from the BioSpa 8 device and 1  $\mu\text{g}/\text{mL}$  Hoechst 33342 dye was added *via* a Tecan D300e digital dispenser for an additional 24 h endpoint DAPI nuclear staining image. Images were processed with the BioTek gen5 data analysis software. The total pHAb dye fluorescence intensity (RFP channel) of each image was normalized to the number of cells determined in the DAPI channel and subtracted by the RFP channel signal at 0 h (background signal). The cell number and background normalized intensities were divided by the pHAb-dye DOL value of each construct and plotted against the time. Data was fitted by linear regression in GraphPad Prism (GraphPad Software, Inc.) and intracellular accumulation rates (slopes) were derived. Finally, the relative intracellular accumulation (%) was calculated for each construct based on the highest intracellular accumulation rate.

#### **6.13.5. Cell Viability Assay**

For the evaluation of MMAE conjugates and related compounds, 40  $\mu\text{L}$  of viable cell suspension were seeded into opaque 384 well plates (cells/well: 6,000 SKBR-3; 3,500 HCC-1954; 2,500 MDA-MB-468; 9,000 A431; 5,000 MCF-7) followed by incubation (37°C, 5% CO<sub>2</sub>) in a humid chamber overnight. Test compounds were added using a D300e digital dispenser. Free MMAE and protein/ protein-conjugate solutions were supplemented with 0.3% Tween-20 (final) and diluted to 6  $\mu\text{M}$  (MMAE) or 10  $\mu\text{M}$  (proteins). Doxorubicin and paclitaxel were used as 10 mM DMSO solutions. All wells were normalized to the maximum amount of Tween-20 added. Cell viability was determined after 4 days using CellTiter-Glo<sup>®</sup> reagent according to the manufacturer's instructions. Luminescence values were normalized to luminescence of non-treated cells and dose-response was fitted using the asymmetric (five parameter) fitting function of GraphPad Prism.

#### **6.13.6. Tumor Spheroid Penetration**

For spheroid formation, BT-474 or HCC-1937 cells were diluted in their appropriate medium and seeded (2,000 cells/well; 40  $\mu\text{L}$ ) into a black clear/round bottom 384 well plate (Corning<sup>®</sup>). The plate was centrifuged for 4 min at 660 x g, rotated by 180° and centrifuged for further 4 min at 660 x g to center the cells in the middle of the wells. Cells were incubated for 96 h at 37°C, 5% CO<sub>2</sub> in a humid chamber to allow formation of spheroids. pHAb-dye constructs were supplemented with 0.3% Tween-20 (final), diluted to 3  $\mu\text{M}$  and added in replicates to the cells (final 50 nM) using a D300e digital dispenser. BT-474 and HCC-1937 spheroids were incubated for 24 h at 37°C, 5% CO<sub>2</sub> in a humid chamber, under exclusion of light. Images were taken with a Leica TCS SP8 confocal laser scanning microscope (20x objective, Exc. 535 nm, Em. 560 – 610 nm, laser power:

---

20, gain: 500). Radial profile plots were created from unprocessed images using the radial profile plot plugin in ImageJ<sup>272</sup> and normalized to the pHAb-dye DOL value of each construct. Mean penetration distances were calculated from ImageJ data as indicated in **Figure 38**.

---

# RESULTS AND DISCUSSION

---

## 7. Results and Discussion

Parts of this work have been published.<sup>277,278</sup>

### 7.1. Design and Generation of Fcabs and Controls

In order to evaluate the Fcab scaffold for the generation of drug conjugates, a literature search was initially performed to identify suitable Fcab variants for this study (section 4.7.2, **Table 2**).

#### 7.1.1. Selection and Design

Fcab variants presented in **Table 5** appeared particularly interesting for several reasons: (1) Their binding to well-known ADC targets overexpressed in solid tumors (HER2, EGFR), (2) their relatively detailed characterization and improved stability compared to other Fcabs, (3) the existence of therapeutical antibodies against the same targets that can be used as references (Trastuzumab, Cetuximab) and (4) in the case of HER2 binding Fcabs, their wide range of binding affinities ( $K_{D,lit}$  0.8 – 109 nM) that allows for studying the impact of affinity on intracellular uptake, cytotoxicity and tumor cell spheroid penetration.

**Table 5. Literature known Fcabs and reference antibodies/ fragments selected for this study.** \*adjacent but not overlapping epitope with Trastuzumab; \*\*no overlapping epitope with Trastuzumab; †no overlapping epitope with Cetuximab.

molecule literature name	type	target	target $K_{D,lit}$ [nM]	target epitope	Engineered C <sub>H</sub> 3 loops	ref.
H10-03-6 CysP2 Cys	Fcab	HER2	69	domain IV*	AB, EF	260
STAB5	Fcab	HER2	19	domain IV*	AB, EF	258
STAB19	Fcab	HER2	109	domain IV*	AB, EF	249,258
FS102	Fcab	HER2	0.8	n.r.**	AB, EF	255
FS1-60	Fcab	EGFR	2.6	†	AB, CD, EF	252
FS1-65	Fcab	EGFR	0.7	†	AB, CD, EF	252
FS1-67	Fcab	EGFR	1.3	†	AB, CD, EF	252
Trastuzumab	IgG1	HER2	0.16	domain IV	-	104,279
Cetuximab	IgG1	EGFR	1.7	domain III	-	101
human Fc portion	IgG1-Fc	-	-	-	-	249

The Fcabs and reference molecules listed in **Table 5** were selected as protein scaffolds and modified for the applicability of various site-specific bioconjugation techniques and Fc $\gamma$ RI, II, III attenuation (**Table 6**). Consequences resulting from non-overlapping target epitopes of Fcabs and references (**Figure 20**) are discussed in section 7.2.1 and 7.2.3.

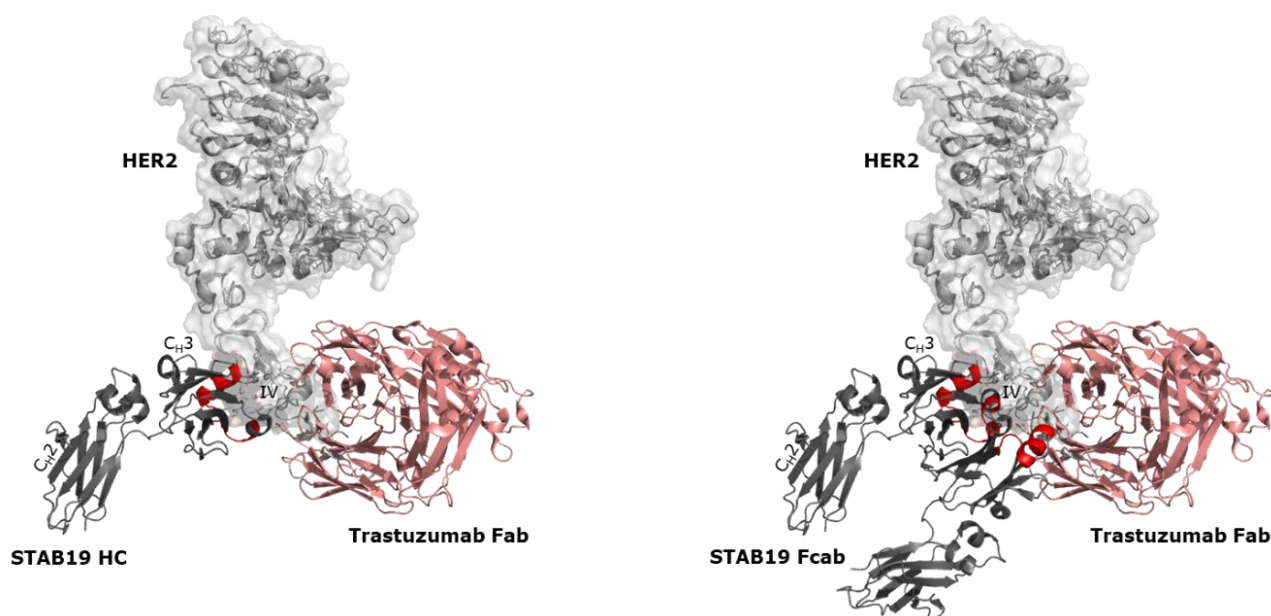


**Figure 20. HER2 targeting Fcabs bind to different HER2 epitopes than Trastuzumab.** Fcabs STAB19 (dark grey) and H10-03-6 bind to the same HER2 (light grey) epitope in domain IV.<sup>249</sup> Fcab STAB5 binds probably to this epitope too. Trastuzumab (salmon) binds to an adjacent epitope in the same HER2 domain IV. The binding site of FS102 is not reported but HER2 binding competition experiments indicated that FS102 and Trastuzumab epitopes do not overlap.<sup>255</sup> STAB19 paratope is marked red.

For site-specific cysteine conjugation, HER2-targeting Fcabs H10-03-6 CysP2 Cys, STAB5 and STAB19 were engineered by incorporation of an addressable cysteine residue at position D265C ( $\alpha$ H-H10<sup>C265</sup>,  $\alpha$ H-S5<sup>C265</sup>,  $\alpha$ H-S19<sup>C265</sup>).<sup>280</sup> Among high and low affinity HER2 binding Fcabs, the intermediate affinity ( $K_D$  19 nM) STAB5 scaffold was chosen as a compromise to further explore site-specific enzymatic conjugation. Therefore, recognition tags (LLQGA<sup>124,281</sup>) that allow for transglutaminase-mediated bioconjugation were genetically fused to the N- and C-terminus of STAB5 to evaluate conjugation on both termini ( $\alpha$ H-S5<sup>LLQGA-N</sup>,  $\alpha$ H-S5<sup>LLQGA-G4S-N</sup>,  $\alpha$ H-S5<sup>C-G4S-LLQGA</sup>,  $\alpha$ H-S5<sup>C-(G4S)2-LLQGA</sup>). LLQGA tags were separated from termini by glycine-serine spacer to facilitate transglutaminase accessibility. Moreover, an effector silencing mutation (D265A<sup>282,283</sup>) was incorporated in all Fcab variants (except  $\alpha$ H-H10<sup>C265</sup>,  $\alpha$ H-S5<sup>C265</sup>,  $\alpha$ H-S19<sup>C265</sup>) to avoid effects mediated by Fc $\gamma$ RI, II, III receptor binding.<sup>149</sup> HER2- and EGFR-targeting Fcabs were also included as variants carrying only the D265A mutation ( $\alpha$ H-H10,  $\alpha$ H-S5,  $\alpha$ H-S19,  $\alpha$ H-FS,  $\alpha$ E-60,  $\alpha$ E-65,  $\alpha$ E-67) aiming for transglutaminase-mediated conjugation to native glutamine Q295 within the C<sub>H</sub>2 region. The EGFR-binding Fcabs ( $\alpha$ E-60,  $\alpha$ E-65,  $\alpha$ E-67) were used as variants lacking the core hinge region (TCPPCP) due to material availability. As a control for subsequent spheroid penetration assays, a full-length 150 kDa STAB5 variant ( $\alpha$ HxH-S5-IgG) was designed with unrelated anti-hen egg lysozyme (HEL) Fab fragments genetically fused onto the Fcab scaffold. Moreover, native human IgG1-Fc (huFc)-based negative controls were designed (huFc, huFc<sup>LLQGA-N</sup>, huFc<sup>LLQGA-G4S-N</sup>, huFc<sup>C-G4S-LLQGA</sup>, huFc<sup>C-(G4S)2-LLQGA</sup>) as well as a Trastuzumab-Fab ( $\alpha$ H-T-Fab) reference carrying two

engineered cysteines (K183C<sup>284</sup>, V205C<sup>120</sup>) for site-specific cysteine conjugation. Cetuximab-IgG ( $\alpha$ E-C-IgG) and Cetuximab-Fab ( $\alpha$ E-C-Fab) reference constructs bearing C-terminal sortase A recognition tags (LPETGS<sup>285</sup>) at light chains were not designed specifically for this work, but were taken from another project.<sup>286</sup> Trastuzumab-IgG ( $\alpha$ H-T-IgG) was used without modification.

**Table 6. Modified Fcabs and controls used in this study.** Engineered conjugation sites are superscripted in Fcab and huFc construct names. Specifications: a – HER2-targeting Fcab; b – EGFR-targeting Fcab; c – non-targeting negative control; d – HER2-targeting reference; e – EGFR-targeting reference; f – HER2-targeting 150 kDa Fcab control.  $\alpha$ E – anti-EGFR,  $\alpha$ H – anti-HER2,  $\alpha$ HxH – anti-HER2xHEL, HC – heavy chain, HEL – hen egg lysozyme, LC – light chain.

construct name	target	protein scaffold	single aa mutation	terminal tag	size [kDa]	specification
$\alpha$ H-H10	HER2	H10-03-6 CysP2	D265A	-	54.4	a
$\alpha$ H-H10 <sup>C265</sup>	HER2	Cys Fcab	D265C	-	54.4	a
$\alpha$ H-S5	HER2	STAB5 Fcab	D265A	-	56.7	a
$\alpha$ H-S5 <sup>C265</sup>	HER2	STAB5 Fcab	D265C	-	56.8	a
$\alpha$ H-S5 <sup>LLQGA-N</sup>	HER2	STAB5 Fcab	D265A	LLQGA-N	59.6	a
$\alpha$ H-S5 <sup>LLQGA-G4S-N</sup>	HER2	STAB5 Fcab	D265A	LLQGA-G4S-N	58.3	a
$\alpha$ H-S5 <sup>C-G4S-LLQGA</sup>	HER2	STAB5 Fcab	D265A	C-G4S-LLQGA	58.7	a
$\alpha$ H-S5 <sup>C-(G4S)2-LLQGA</sup>	HER2	STAB5 Fcab	D265A	C-(G4S) <sub>2</sub> -LLQGA	59.0	a
$\alpha$ H-S19	HER2	STAB19 Fcab	D265A	-	54.2	a
$\alpha$ H-S19 <sup>C265</sup>	HER2	STAB19 Fcab	D265C	-	54.3	a
$\alpha$ H-FS	HER2	FS102 Fcab	D265A	-	53.3	a
$\alpha$ E-60	EGFR	FS1-60 Fcab	D265A	-	52.0	b
$\alpha$ E-65	EGFR	FS1-65 Fcab	D265A	-	52.0	b
$\alpha$ E-67	EGFR	FS1-67 Fcab	D265A	-	51.9	b
huFc	-	IgG1-Fc	D265A	-	53.0	c
huFc <sup>C265</sup>	-	IgG1-Fc	D265C	-	53.1	c
huFc <sup>LLQGA-N</sup>	-	IgG1-Fc	D265A	LLQGA-N	53.6	c
huFc <sup>LLQGA-G4S-N</sup>	-	IgG1-Fc	D265A	LLQGA-G4S-N	54.3	c
huFc <sup>C-G4S-LLQGA</sup>	-	IgG1-Fc	D265A	C-G4S-LLQGA	54.3	c
huFc <sup>C-(G4S)2-LLQGA</sup>	-	IgG1-Fc	D265A	C-(G4S) <sub>2</sub> -LLQGA	55.2	c
$\alpha$ H-T-Fab	HER2	Trastuzumab Fab	K183C, V205C	HC-C-G4S-His <sub>6</sub>	49.0	d
$\alpha$ H-T-IgG	HER2	Trastuzumab IgG1	-	-	148.1	d
$\alpha$ E-C-Fab	EGFR	Cetuximab Fab	-	LC-C-(G4S) <sub>3</sub> -LPETGS, HC-C-G4S-His <sub>6</sub>	50.5	e
$\alpha$ E-C-IgG	EGFR	Cetuximab IgG1	-	LC-C-(G4S) <sub>3</sub> -LPETGS	155.4	e
$\alpha$ HxH-S5-IgG	HEL/ HER2	anti-HEL Fab- STAB5 Fcab	D265A	-	151.5	f

### 7.1.2. Expression and Purification

Fcabs, huFc controls, and  $\alpha$ H-T-Fab reference were produced in mammalian Expi293F cells and purified by standard protein A (**Figure A1**, **Figure A2**) or IMAC (**Figure A3**) affinity chromatography, respectively.

In general, purified protein yields of Fcabs were reduced compared to human Fc controls lacking the engineered antigen binding site (mean yields per culture volume: 84 mg/L vs. 389 mg/L) (**Figure 21**). Reduced binding of the Fcabs to protein A could be excluded as the cause, since SDS-PAGE analysis of the protein A flow through did not detect unbound Fcabs (**Figure A1**, **Figure A2**). The incorporation of the D265C mutation reduced expression yields by approximately 70% compared to constructs carrying the D265A mutation (e.g., huFc vs. huFc<sup>C265</sup> 351 mg/mL vs. 103 mg/mL). After affinity chromatography, monomer content of Fcabs and controls was typically 98 - 100%, except for  $\alpha$ H-H10<sup>C265</sup> and  $\alpha$ H-H10 which showed 4.8% and 22.3% aggregates (MW<sub>app</sub> ~ 700 kDa) by SE-HPLC. In the latter case, aggregates were fully removed by preparative SEC and did not form again, even after a period of ~ 6 months at 4°C. In contrast to human Fc controls huFc<sup>C-G4S-LLQGA</sup> and huFc<sup>C-(G4S)2-LLQGA</sup>, C-terminally tagged Fcabs  $\alpha$ H-S5<sup>C-G4S-LLQGA</sup> and  $\alpha$ H-S5<sup>C-(G4S)2-LLQGA</sup> precipitated during the final protein concentration step and were therefore excluded from following conjugation attempts. N-terminally tagged Fcabs  $\alpha$ H-S5<sup>LLQGA-N</sup> and  $\alpha$ H-S5<sup>LLQGA-G4S-N</sup> did not precipitate but formed 4.2 - 4.6% aggregates after protein concentration (final concentration 5 – 6 mg/mL). Aggregate content increased to 8.2 – 8.5% after a freeze-thaw test cycle.  $\alpha$ H-S5<sup>LLQGA-N</sup> and  $\alpha$ H-S5<sup>LLQGA-G4S-N</sup> were therefore stored at 4°C. Interestingly, huFc<sup>LLQGA-N</sup> and huFc<sup>LLQGA-G4S-N</sup> did not show any aggregation during protein concentration or after freeze-thaw.

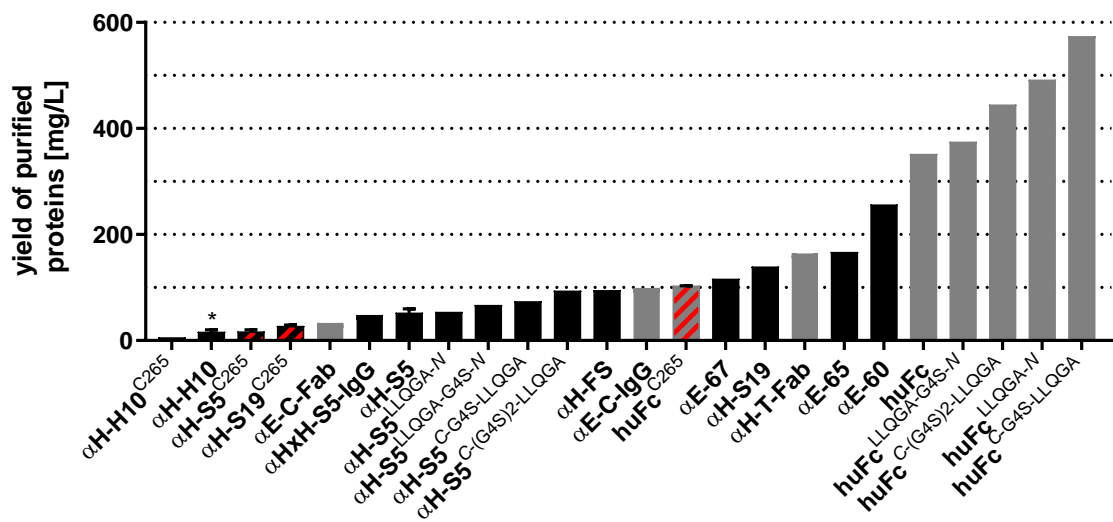


**Figure 21. Purified protein yields.** Yield is given as mass per culture volume. Expi293F expressed Fcabs are shown as black bars while controls are shown as grey bars. Constructs carrying the D265C mutation are marked red. For constructs that were expressed twice, the median ( $\pm$  range) is given. Asterisk marks constructs with aggregate content > 5% that were further purified by preparative SEC after affinity chromatography. Yields of Expi293F expressed  $\alpha$ E-C-IgG and  $\alpha$ E-C-Fab were taken from Roßkopf for comparison.<sup>286</sup>  $\alpha$ H-T-IgG (Trastuzumab) was obtained from pharmacy.

---

All other concentrated Fcabs and controls showed high purity (98 – 100%) confirmed by gel electrophoresis (**Figure A4**) and SE-HPLC (**Figure A5**) after a final freeze-thaw cycle.

### 7.1.3. Biophysical Characterization

The identity and glycosylation patterns of all variants was confirmed by mass spectrometry (LC-MS) (**Table A1**) (**Figure A6**).  $\alpha$ H-S5<sup>LLQGA-N</sup> and huFc<sup>LLQGA-N</sup> are partially O-glycosylated due to a potential O-glycosylation site (LLQGATCPPCP...) generated by genetical fusion of the LLQGA-tag to the hinge region. All STAB5 variants carry an additional Man5 glycosylation which is probably located at the artificial NVS glycosylation site in the engineered C<sub>H3</sub> AB-loop. This artificial glycosylation site was also reported by Traxlmayr *et al.*<sup>258</sup>

Engineering of Fc C<sub>H3</sub> loop regions usually reduces a molecules' thermostability which might result in higher aggregation tendency. Human wildtype Fc portions typically show two transition midpoints ( $T_m$ ) in differential scanning calorimetry (DSC) representing unfolding of the C<sub>H2</sub> ( $T_{m1} \sim 66^\circ\text{C}$ ) and the C<sub>H3</sub> domain ( $T_{m2} \sim 81^\circ\text{C}$ ). In contrast, DSC profiles of Fcabs often show only one broad transition at  $\sim 65^\circ\text{C}$ , indicating that the C<sub>H3</sub> domain is destabilized and its  $T_{m2}$  is shifted toward the  $T_{m1}$  of the C<sub>H2</sub> domain.<sup>258</sup> Rational protein design<sup>259,260</sup> as well as directed evolution<sup>258,261</sup> were applied to restore thermostability of Fcabs. For example, H10-03-6 CysP2 Cys was stabilized by the incorporation of additional disulfide bonds resulting in a human Fc wildtype-like thermostability with C<sub>H2</sub> transition at  $63.5^\circ\text{C}$  and C<sub>H3</sub> transition at  $81.1^\circ\text{C}$ .<sup>260</sup> Unfortunately, variants  $\alpha$ H-H10 and  $\alpha$ H-H10<sup>C265</sup> differing from H10-03-6 CysP2 Cys only at position 265 in the C<sub>H2</sub> region, showed a combined C<sub>H2</sub>, C<sub>H3</sub> transition at  $63 - 64^\circ\text{C}$  in differential scanning fluorimetry (DSF) analysis (**Table 7, Figure A7**) similar to non-stabilized H10-03-6 ( $62$  and  $65^\circ\text{C}$ ).<sup>260</sup> These results indicate that stabilizing disulfide bonds may not be closed in  $\alpha$ H-H10 and  $\alpha$ H-H10<sup>C265</sup> providing also explanation for observed higher aggregation tendency of both molecules. Whether discrepancy to literature is caused by e.g., mutated D265, different analysis techniques (DSC vs. DSF) or different expression host (Expi293F vs. *P. pastoris*) remains unclear.<sup>259,260</sup> In accordance with literature, STAB19 variants  $\alpha$ H-S19 and  $\alpha$ H-S19<sup>C265</sup> showed superior thermostability compared to STAB5 variants, indicated by two separated C<sub>H2</sub> and C<sub>H3</sub> thermal transitions ( $65$  and  $74^\circ\text{C}$ ) *versus* only one combined for STAB5 variants ( $66^\circ\text{C}$ ) (**Table 7, Figure A7**).<sup>258</sup>

EGFR-binding Fcabs  $\alpha$ E-60,  $\alpha$ E-65 and  $\alpha$ E-67 showed reduced C<sub>H2</sub> thermostability ( $T_{m1}$   $57 - 61^\circ\text{C}$ ) compared to all other variants. In contrast,  $\alpha$ E-60,  $\alpha$ E-65 and  $\alpha$ E-67 miss the hinge interchain cysteines ( $H_2N$ -APELLGGPSVF...) and it was speculated whether this causes reduction in C<sub>H2</sub> thermostability. To support this hypothesis, the hinge-cysteine carrying Fcab  $\alpha$ H-FS ( $H_2N$ -TCPPCPAPELLGGPSVF...) was digested with immunoglobulin G-degrading enzyme of *S. pyogenes* (IdeS) (human IgG1 cleavage site: ...TCPPCPAPELLG // GPSVF...)<sup>287</sup> and thermostability of the resultant  $\alpha$ H-FS missing the hinge interchain

cysteines was analyzed. Indeed,  $T_{m1}$  of  $\alpha$ H-FS (w/o hinge) was decreased by 3°C compared to  $\alpha$ H-FS supporting the hypothesis (Table 7, Figure A7).

**Table 7. Thermostability of Fcabs and huFc controls.** Unfolding transition midpoints ( $T_m \pm$  SD) were measured by DSF and are given as mean from duplicates. Typically,  $T_{m1}$  indicates C<sub>H2</sub> transition while  $T_{m2}$  indicates C<sub>H3</sub> transition. In Fcabs the  $T_{m2}$  is often shifted toward the  $T_{m1}$  and only one broad transition is observed. First derivatives of unfolding curves can be found in Figure A7.

	thermal unfolding			thermal unfolding	
	$T_{m1}$ [°C]	$T_{m2}$ [°C]		$T_{m1}$ [°C]	$T_{m2}$ [°C]
<b><math>\alpha</math>H-H10</b>	63.32 ± 0.01	-	<b><math>\alpha</math>H-FS (w/o hinge)</b>	63.13 ± 0.00	74.35 ± 0.02
<b><math>\alpha</math>H-H10<sup>C265</sup></b>	64.00 ± 0.02	-	<b><math>\alpha</math>E-60</b>	59.30 ± 0.03	74.30 ± 0.01
<b><math>\alpha</math>H-S5</b>	66.09 ± 0.02	-	<b><math>\alpha</math>E-65</b>	60.70 ± 0.10	81.99 ± 0.09
<b><math>\alpha</math>H-S5<sup>C265</sup></b>	66.38 ± 0.13	-	<b><math>\alpha</math>E-67</b>	57.13 ± 0.01	-
<b><math>\alpha</math>H-S5<sup>LLQGA-N</sup></b>	66.25 ± 0.05	-	<b>huFc</b>	66.48 ± 0.58	81.71 ± 0.22
<b><math>\alpha</math>H-S5<sup>LLQGA-G4S-N</sup></b>	66.02 ± 0.12	-	<b>huFc<sup>C265</sup></b>	66.29 ± 0.02	81.45 ± 0.02
<b><math>\alpha</math>H-S5<sup>C-G4S-LLQGA</sup></b>	66.08 ± 0.23	-	<b>huFc<sup>LLQGA-N</sup></b>	66.22 ± 0.16	81.93 ± 0.02
<b><math>\alpha</math>H-S5<sup>C-(G4S)2-LLQGA</sup></b>	66.33 ± 0.00	-	<b>huFc<sup>LLQGA-G4S-N</sup></b>	65.89 ± 0.02	81.84 ± 0.01
<b><math>\alpha</math>H-S19</b>	65.19 ± 0.16	74.15 ± 0.28	<b>huFc<sup>C-G4S-LLQGA</sup></b>	66.30 ± 0.12	81.15 ± 0.13
<b><math>\alpha</math>H-S19<sup>C265</sup></b>	65.48 ± 0.01	74.26 ± 0.12	<b>huFc<sup>C-(G4S)2-LLQGA</sup></b>	66.28 ± 0.15	80.97 ± 0.17
<b><math>\alpha</math>H-FS</b>	65.92 ± 0.07	75.23 ± 0.01			

Furthermore, the subset of EGFR-binding variants was selected to analyze protein integrity and hydrodynamic radius ( $r_H$ ) by SE-HPLC coupled multiangle light scattering (MALS) and dynamic light scattering (DLS) (Table 8). Fcabs, huFc, Cetuximab-Fab and IgG showed  $r_H$  in the expected range of globular 50 kDa proteins (3.0 – 3.5 nm) and 150 kDa IgG (5.5 nm), respectively.<sup>288</sup> All samples showed a polydispersity index (PDI) close to 1.00 indicating sample monomer character.

**Table 8. SE-HPLC-MALS-DLS characterization of EGFR-binding Fcabs, huFc and Cetuximab references.**  $M_n$  – number average molar mass;  $M_w$  – mass average molar mass; PDI – polydispersity index ( $PDI = M_w/M_n$ );  $r_H$  – hydrodynamic radius.

construct	$r_H$ [nm]	$M_n$ [g/ml]	$M_w$ [g/ml]	PDI
<b><math>\alpha</math>E-60</b>	3.073 ± 0.177	53.66 ± 0.28	53.84 ± 0.28	1.003 ± 0.007
<b><math>\alpha</math>E-65</b>	3.201 ± 0.139	53.59 ± 0.30	53.78 ± 0.30	1.004 ± 0.008
<b><math>\alpha</math>E-67</b>	3.213 ± 0.144	53.16 ± 0.34	53.56 ± 0.36	1.008 ± 0.009
<b>huFc</b>	3.533 ± 0.139	53.75 ± 0.35	54.10 ± 0.37	1.007 ± 0.010
<b><math>\alpha</math>E-C-Fab</b>	3.121 ± 0.138	50.48 ± 0.33	50.82 ± 0.35	1.007 ± 0.010
<b><math>\alpha</math>E-C-IgG</b>	5.514 ± 0.137	156.2 ± 0.96	157.0 ± 0.99	1.005 ± 0.009

---

## 7.2. Evaluation of Fcab Suitability for ADC Generation

To assess the ADC suitability of selected Fcabs, cellular binding, uptake and accumulation were studied.

### 7.2.1. Cellular Binding of Fcabs to Tumor Cells

Selective binding to target expressing cells is one of the fundamental requisites of antibody-based therapies. HER2- as well as EGFR-targeting variants  $\alpha$ H-H10,  $\alpha$ H-S5,  $\alpha$ H-S19,  $\alpha$ H-FS,  $\alpha$ E-60,  $\alpha$ E-65,  $\alpha$ E-67 were selected and tested for binding to cell surface targets on two target positive (HER2<sup>+</sup>: SKBR-3, HCC-1954; EGFR<sup>+</sup>: MDA-MB-468, A431) and one target negative cell line (HER2<sup>-</sup>: MDA-MB-468; EGFR<sup>-</sup>: MCF-7).  $\alpha$ H-T-IgG,  $\alpha$ H-T-Fab,  $\alpha$ E-C-IgG,  $\alpha$ E-C-Fab references and huFc were included as controls. Binding was assessed by flow cytometry after incubating cells with constructs (100 nM) and subsequent labeling with Fc-specific or anti-LC detection antibody.

Selective cellular binding was observed for  $\alpha$ H-H10,  $\alpha$ H-S5,  $\alpha$ H-S19,  $\alpha$ H-FS,  $\alpha$ E-60,  $\alpha$ E-65 and  $\alpha$ E-67 (**Figure 22**) confirming the reported target-dependent cell binding of corresponding Fcab scaffold variants.<sup>252,255,258,260</sup>

No cellular binding of the huFc negative control was detected indicating the absence of unspecific binding effects. At 100 nM, relative order of fluorescence intensity of distinct variants bound to HER2 positive SKBR-3 and HCC-1954 cells correspond to their reported HER2 binding affinity:  $\alpha$ H-T-IgG ( $K_{D,lit}$  0.16 nM + avidity) <  $\alpha$ H-T-Fab ( $K_{D,lit}$  0.16 nM) <  $\alpha$ H-FS ( $K_{D,lit}$  0.8 nM) <  $\alpha$ H-S5 ( $K_{D,lit}$  19 nM) <  $\alpha$ H-H10 ( $K_{D,lit}$  69 nM) <  $\alpha$ H-S19 ( $K_{D,lit}$  109 nM) (**Figure 22A**) (**Table 5**). For all EGFR-targeting constructs, similar fluorescence signal intensities were observed since their  $K_D$  values are within a very narrow range ( $K_{D,lit}$  0.7 – 2.6 nM). Furthermore, fluorescence signal intensities correspond with reported relative HER2 and EGFR surface expression densities on cell lines (HER2<sup>+</sup>: SKBR-3 > HCC-1954<sup>99</sup>; EGFR<sup>+</sup>: MDA-MB-468 > A431<sup>289</sup>).

In a next step, dissociation constants for the above-mentioned constructs were derived from concentration-dependent cellular binding assays. Therefore, the same cell lines were incubated with serially diluted constructs (**Figure 23**), and  $K_D$  values were derived from inflection points of fitted dose response curves (**Table 9**).  $\alpha$ H-FS,  $\alpha$ E-60,  $\alpha$ E-65,  $\alpha$ E-67,  $\alpha$ H-T-IgG and  $\alpha$ H-T-Fab show a typical dose-response curve pattern where mean fluorescence intensities (MFI) plateau at high concentrations indicating surface receptor saturation (**Figure 23A, B**). Distinct MFI saturation levels between  $\alpha$ H-FS,  $\alpha$ H-T-IgG and  $\alpha$ H-T-Fab may be due to reduced HER2 epitope accessibility for  $\alpha$ H-FS or varying detection antibody labeling caused by fewer addressable binding sites at engineered Fcabs or  $\alpha$ H-T-Fab compared to  $\alpha$ H-T-IgG. Differences in number of attached fluorophore labels to polyclonal detection antibodies would be also a conceivable explanation. Nevertheless,  $K_D$  is independent of the MFI level at receptor saturation and corresponding  $K_D$  for  $\alpha$ H-FS,  $\alpha$ E-60,  $\alpha$ E-65,  $\alpha$ E-67,  $\alpha$ H-T-IgG and  $\alpha$ H-T-Fab (**Table 9**) are in good agreement with literature (**Table 5**).

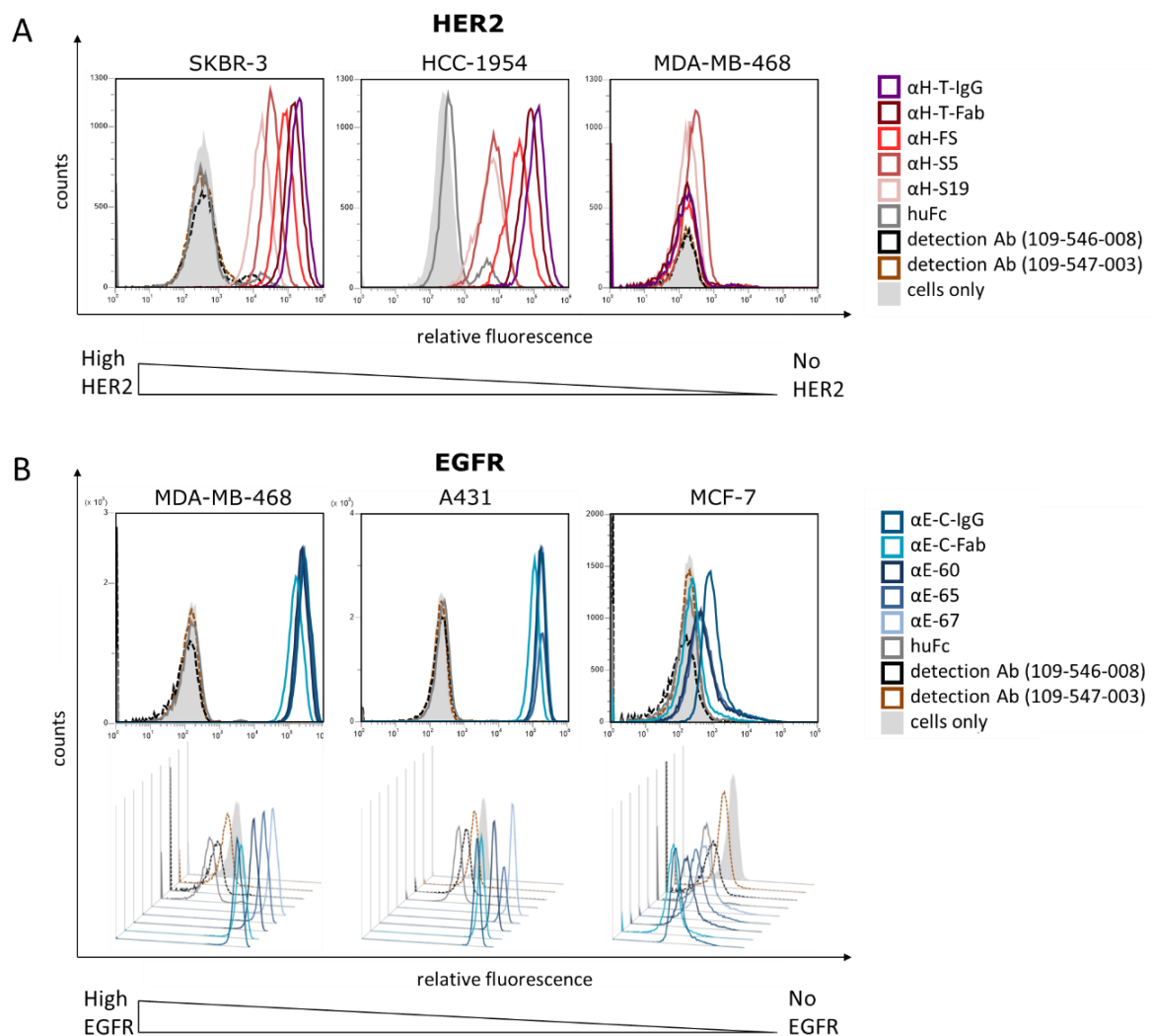


**Figure 22. Cellular binding of Fcabs, huFc and references to several cancer cell lines. (A)** HER2-targeting Fcabs and references bind selectively HER2 positive cells (SKBR-3, HCC-1954). No significant binding to HER2 negative cells (MDA-MB-468) was observed. Relative order of fluorescence intensity of distinct variants on HER2 positive cells correspond to their HER2 binding affinity. **(B)** EGFR-targeting Fcabs and references bind selectively EGFR positive cells (MDA-MB-468, A431). αE-C-IgG binds slightly to EGFR negative MCF-7 cells. Cells were incubated with 100 nM of Fcab/antibody (duplicates) for 60 min at 4°C, washed twice with PBS-1% BSA, incubated for 30 min with 500 nM of AF488-labeled detection antibody at 4°C in darkness, washed twice with PBS-1% BSA, and finally fluorescence intensity was measured by flow cytometry. Fcabs, huFc and IgG references were labeled with Fc-specific polyclonal F(ab')<sub>2</sub>-AF488 mixture (#109-546-008), while Fab references were labeled with IgG-specific polyclonal Fab-AF488 mixture (#109-547-003). Due to different detection antibodies, fluorescence signal intensity of huFc, Fcabs and IgGs cannot be compared directly to αE-C-Fab or αH-T-Fab signal.

In contrast, αH-H10, αH-S5 and αH-S19 apparently do not reach receptor saturation on HER2 positive SKBR-3 and HCC-1954 cells, even at the highest tested concentration (12.8 μM) (**Figure 23B**). At this concentration, negative control huFc did not show significant binding to cells. Neither do αH-H10, αH-S5 and αH-S19 on HER2 negative MDA-MB-468 cells, suggesting that this effect may be HER2 related. It should be noted that this binding behavior was observed in several time- and experimenter-independent replicates and that expected binding behavior of references and αH-FS make a systematic error seem unlikely.

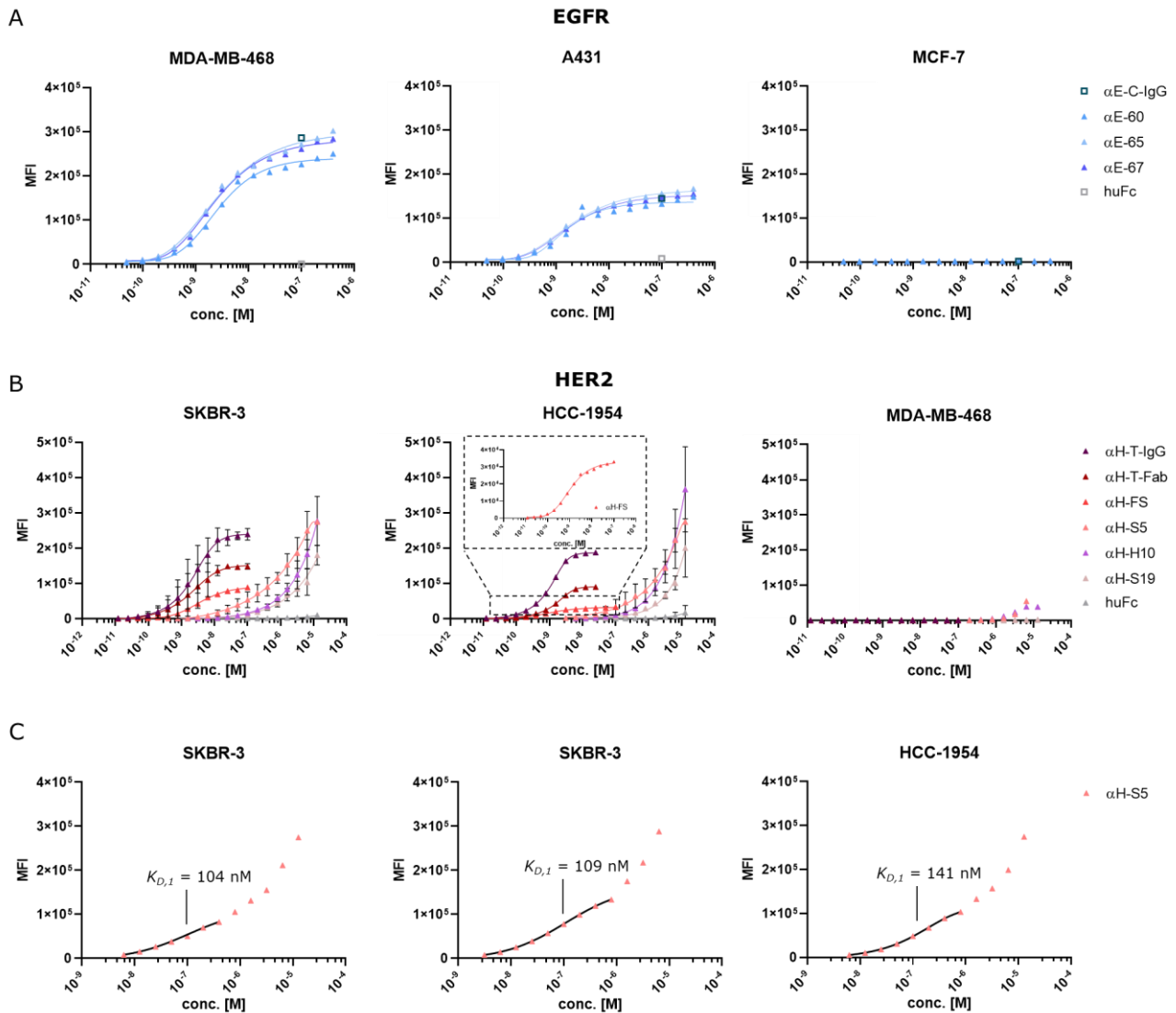


**Figure 23. Concentration-dependent cellular binding of Fcabs, huFc and references to several cancer cell lines.** Dose response (MFI) curves were fitted by asymmetric five parameter function using Graphpad Prism. **(A)** Serial dilution (1:2; 400 – 0.05 nM) of EGFR-targeting Fcabs on EGFR positive (MDA-MB-468, A431) and EGFR negative cells (MCF-7).  $\alpha$ E-C-IgG and huFc controls (100 nM) were included. Varying binding saturation levels between MDA-MB-468 and A431 cells reflect cell specific EGFR expression densities (MDA-MB-468:  $\sim 1.8 \cdot 10^6$  EGFR copies/cell; A431:  $\sim 7 \cdot 10^5$  EGFR copies/cell<sup>289</sup>). **(B)** Binding of HER2-targeting Fcabs and references to HER2 positive (SKBR-3, HCC-1954) and HER2 negative cells (MDA-MB-468) at varying concentration ranges. Mean ( $\pm$  SD) is shown for time- and experimenter-independent replicates:  $\alpha$ H-T-Fab on SKBR-3 (n = 2);  $\alpha$ H-T-IgG,  $\alpha$ H-S5,  $\alpha$ H-H10,  $\alpha$ H-S19 and huFc on SKBR-3 (n = 3);  $\alpha$ H-S5,  $\alpha$ H-H10,  $\alpha$ H-S19 and huFc on HCC-1954 (n = 2).  $\alpha$ H-FS binding on HCC-1954 has been enlarged for better visibility. **(C)**  $\alpha$ H-S5 shows slight turning point near the expected  $K_D$  range. MFI – mean fluorescence intensity.

Data from individual experiments with  $\alpha$ H-S5 suggest that there are two overlapping binding effects taking place (**Figure 23C**). In the lower concentration range ( $< 1 \mu\text{M}$ ) an MFI plateau seem to be reached between 100 – 1000 nM, before MFI values increase more sharply between 1 – 10  $\mu\text{M}$ . When fitting this first binding event,  $K_D$  values in the range of the expected  $K_{D,lit}$  19 nM<sup>258</sup> are obtained ( $K_D \sim 100$  nM). An explanation for the second binding event could be unspecific binding of Fcabs on cell surface which is more pronounced at higher concentration ranges ( $> 1 \mu\text{M}$ ).

**Table 9. Fcab and reference cellular dissociation constants.**  $K_D$  values were derived from inflection points of asymmetric five parameter fitted dose response curves (Graphpad Prism) of concentration-dependent cellular binding experiments. *ambig.* – ambiguous results; *n.d.* – not determined.

construct	cellular $K_D$ [nM]				
	SKBR-3 (HER2 <sup>+</sup> )	HCC-1954 (HER2 <sup>+</sup> )	MDA-MB-468 (HER2 <sup>-</sup> /EGFR <sup>+</sup> )	A431 (EGFR <sup>+</sup> )	MCF-7 (EGFR <sup>-</sup> )
<b>αH-H10</b>	ambig.	ambig.	-	n.d.	n.d.
<b>αH-S5</b>	ambig.	ambig.	-	n.d.	n.d.
<b>αH-S19</b>	ambig.	ambig.	-	n.d.	n.d.
<b>αH-FS</b>	3.54	1.01	-	n.d.	n.d.
<b>αH-T-Fab</b>	1.93	1.66	-	n.d.	n.d.
<b>αH-T-IgG</b>	2.27	1.07	-	n.d.	n.d.
<b>αE-60</b>	n.d.	n.d.	2.58	1.50	-
<b>αE-65</b>	n.d.	n.d.	2.59	1.84	-
<b>αE-67</b>	n.d.	n.d.	2.40	1.75	-
<b>huFc</b>	-	-	-	-	-

### 7.2.2. Generation of pHAb-Dye Labeled Fcabs and Controls

Besides selective binding, other important factors for ADC payload delivery mediated by the antibody component are internalization and intracellular accumulation. Both factors may depend on target epitopes. Since selected Fcabs do not bind to the same HER2 and EGFR epitopes as Trastuzumab and Cetuximab (**Table 5**), it is unclear whether Fcabs show similar cellular uptake profiles than reference antibodies.

To study cellular uptake, selected Fcab variants and controls were labeled with a pH sensor fluorescent dye (pHAb-dye<sup>290</sup>) (**Figure 24A**).

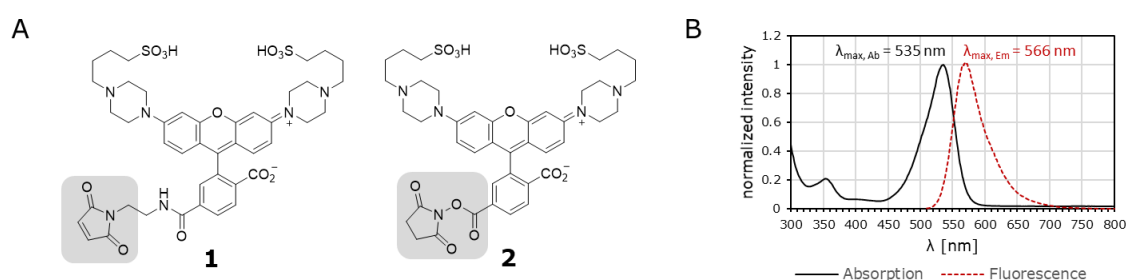


**Figure 24. pHAb-dye-labeling for antibody uptake studies.** (A) Structure of pHAb thiol (**1**) and pHAb amine (**2**) reactive dye. **1** carries a maleimide group (marked grey) which reacts with free thiol groups of cysteines while **2** bears an NHS-active ester (marked grey) which preferentially reacts with amino groups of e.g. lysine side chains. (B) Absorption and fluorescence spectra of pHAb dye in SE-HPLC running buffer (50 mM sodium phosphate, 400 mM sodium perchlorate, pH 6.3). Spectra were recorded on a microplate reader.

pHAb-dye is not fluorescent at neutral pH but becomes highly fluorescent at acidic pH present in endosomal and lysosomal vesicles after internalization.<sup>290</sup> This allows to detect only intracellularly accumulated constructs resulting also in a favorable signal-to-background ratio. Fcabs, references and huFc were labeled with pHAb-dye either *via* site-specific coupling to interchain/ engineered cysteines or in the case of EGFR-targeting Fcabs lacking interchain cysteines by random lysine coupling (**Table 10**).

To ensure comparability between pHAb-dye labeled constructs, fluorescence signals must be normalized to account for varying number of attached pHAb-dye molecules.

Therefore, an SE-HPLC-based method for ADC DAR determination by Wang *et al.* was modified to derive the degree of pHAb-dye labeling (DOL) based on specific pHAb-dye absorption at 535 nm (**Figure 24B**).<sup>276</sup> In addition to DOL determination, the method allows to characterize simultaneously the aggregation and purification (free pHAb-dye) status of the labeled construct from a single SE-HPLC run (**Figure A8**). For the detailed experimental procedure to measure and calculate DOL, the reader is referred to the material and methods section 6.12.20.

**Table 10. pHAb-dye labeled constructs generated for cellular uptake and spheroid penetration studies.** HER2-targeting constructs were labeled by cysteine coupling while EGFR-targeting constructs were labeled by random lysine coupling. DOL values for random lysine coupled constructs are given as mean ( $\pm$  SD) of duplicates. DOL of interchain coupled constructs was calculated from single measurements. Monomer content of pHAb-dye conjugates was derived from SE-HPLC  $A_{280}$  signal. DOL was derived from monomer species. Superscript “C” marks cysteine coupling, while “K” refers to random lysine coupling. *DOL – degree of pHAb-dye labeling.*

pHAb-dye conjugate	conjugation			SE-HPLC monomer content [%]
	substrate	site	DOL	
$\alpha$ H-H10 <sup>C</sup> -pHAb	1	interchain Cys	1.8	33.5
$\alpha$ H-S5 <sup>C</sup> -pHAb	1	interchain Cys	1.9	89.7
$\alpha$ H-S19 <sup>C</sup> -pHAb	1	interchain Cys	2.0	82.3
$\alpha$ H-FS <sup>C</sup> -pHAb	1	interchain Cys	2.5	77.4
$\alpha$ H-T-Fab <sup>C</sup> -pHAb	1	interchain Cys	1.8	87.5
$\alpha$ H-T-IgG <sup>C</sup> -pHAb	1	interchain Cys	2.0	98.8
$\alpha$ HxH-S5-IgG <sup>C</sup> -pHAb	1	interchain Cys	2.0	97.8
$\alpha$ E-60 <sup>K</sup> -pHAb	2	random Lys	1.26 $\pm$ 0.06	98.3
$\alpha$ E-65 <sup>K</sup> -pHAb	2	random Lys	2.28 $\pm$ 0.04	95.3
$\alpha$ E-67 <sup>K</sup> -pHAb	2	random Lys	1.93 $\pm$ 0.02	96.8
$\alpha$ E-C-Fab <sup>K</sup> -pHAb	2	random Lys	1.36 $\pm$ 0.03	95.8
$\alpha$ E-C-IgG <sup>K</sup> -pHAb	2	random Lys	1.94 $\pm$ 0.05	96.5
huFc <sup>K</sup> -pHAb	2	random Lys	4.67 $\pm$ 0.02	98.7

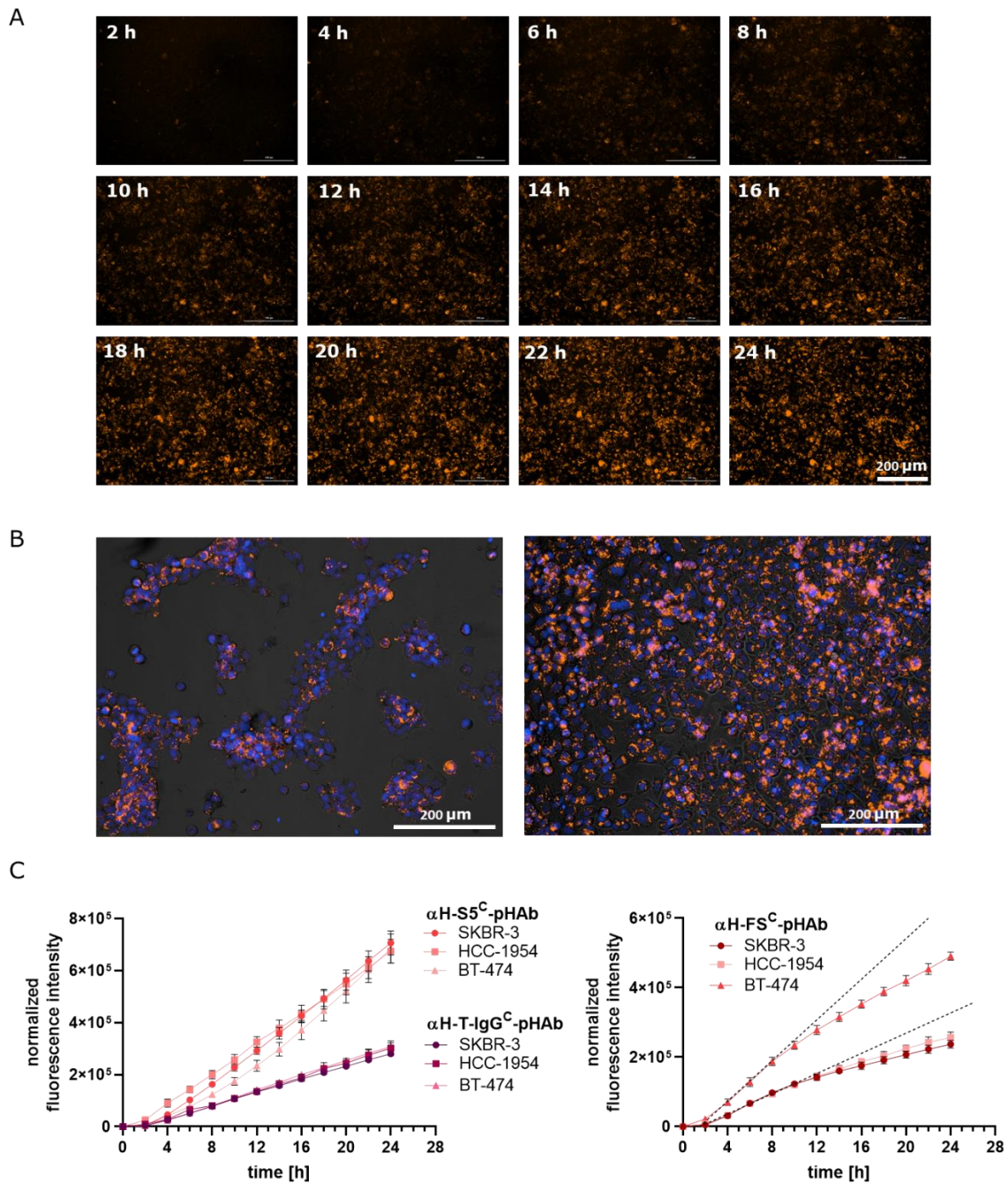
**Table 10** summarizes the generated pHAb-dye conjugates, their DOL and monomer content. Similar degrees of labeling (DOL 1.8 – 2.5 for cysteine coupling; DOL 1.3 – 2.3 for amine coupling) were achieved by carefully adjusting the equivalents of pHAb thiol (**1**) and pHAb amine (**2**) reactive dye added to (previously reduced)

---

proteins. pHAb-dye cysteine coupling of  $\alpha$ H-H10 resulted in protein precipitation. SE-HPLC of the supernatant showed high content of aggregates (66.5%), suggesting that reduction and coupling interfered with the engineered stabilizing cysteines of the H10-03-6 CysP2 Cys scaffold.<sup>260</sup> But also for other constructs, interchain cysteine conjugation led to more aggregates compared to amine coupling ( $\emptyset$  11 vs. 3%). This is potentially caused by the additional DTT reduction and DTT removal step or the conjugation site.

### 7.2.3. Cellular Uptake of Fcabs into Tumor Cells

As already mentioned, Fcabs bind to different target epitopes than Trastuzumab or Cetuximab that may result in altered internalization, lysosomal trafficking and ADC cytotoxicity compared to clinically validated references. To assess ADC suitability of Fcabs, cellular uptake profiles of pH-sensitive pHAb-dye conjugates were studied on target positive (HER2<sup>+</sup>: SKBR-3, HCC-1954, BT-474; EGFR<sup>+</sup>: MDA-MB-468, A431) and target negative tumor cells (HER2<sup>-</sup>: MDA-MB-468; EGFR<sup>-</sup>: MCF-7). References  $\alpha$ H-T-IgG<sup>C</sup>-pHAb,  $\alpha$ H-T-Fab<sup>C</sup>-pHAb,  $\alpha$ E-C-IgG<sup>K</sup>-pHAb and  $\alpha$ E-C-Fab<sup>K</sup>-pHAb were included in these experiments along with huFc<sup>K</sup>-pHAb as a negative control. pHAb-dye labeled constructs were incubated on adherent grown cells for 24 – 26 h and pHAb-dye fluorescence of cell images was continuously recorded throughout the incubation time (**Figure 25A**, **Figure A9A**). After 24 – 26 h, cell nuclei were stained (**Figure 25B**) and a software-assisted visual cell count was performed. The total pHAb-dye fluorescence intensity of images was normalized to the pHAb-dye DOL of the corresponding construct and cell number. Subsequently, cellular uptake kinetics were derived from normalized pHAb-dye fluorescence signals (**Figure 25C**).



Except for  $\alpha\text{H-FS}^{\text{C}}$ -pHAb, normalized pHAb-dye fluorescence signals increased linearly over time indicating constant internalization. Data was fitted by linear regression and normalized intracellular accumulation rates (slopes) were derived (**Figure A10**). For each subset of HER2 and EGFR targeting constructs, the highest normalized intracellular accumulation rate was set 100% and other rates were expressed relative to this rate (**Figure 26**).

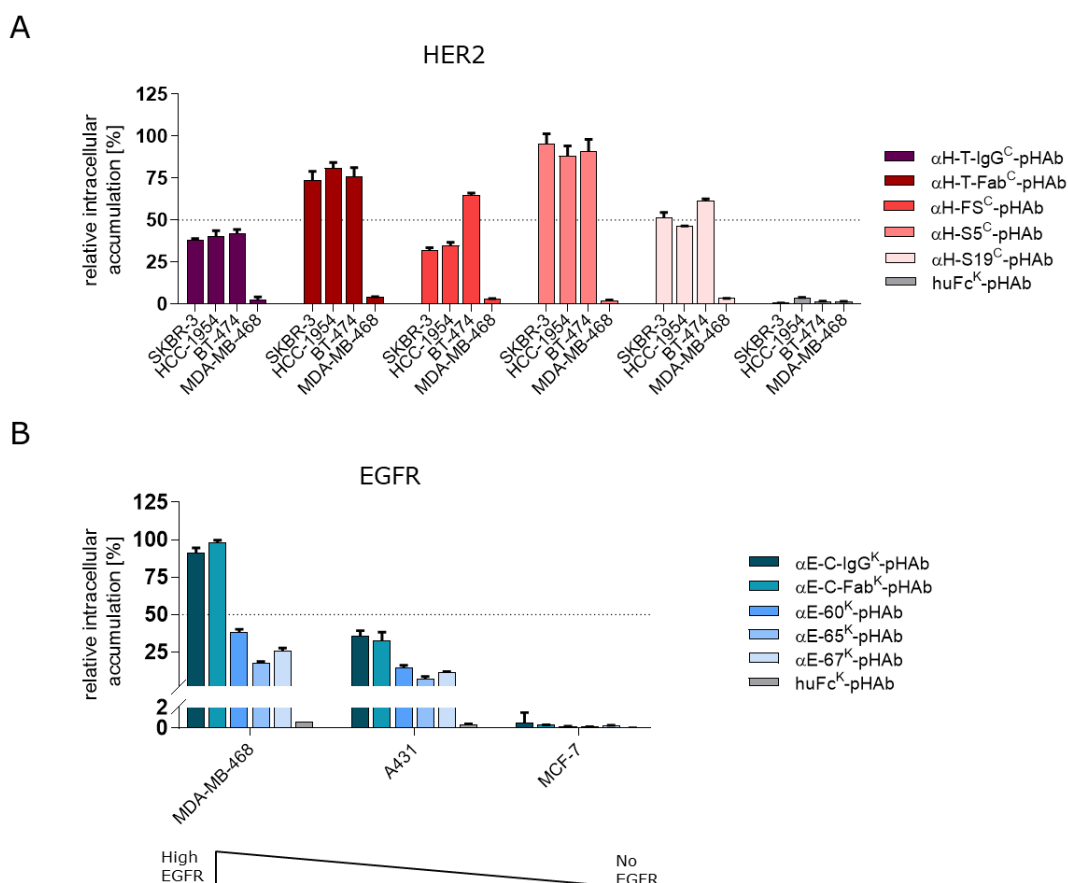


**Figure 26. Relative intracellular accumulation of pHAb-dye labeled constructs.** To obtain relative intracellular accumulation, normalized intracellular accumulation rates were related to the highest normalized intracellular accumulation rate within each subset (HER2, EGFR). Normalized intracellular accumulation rates were derived from 0 - 26 h incubation of pHAb-dye labeled construct (100 nM) on cells. **(A)** Cellular uptake of HER2-targeting constructs into HER2<sup>+</sup> (SKBR-3, HCC-1954, BT-474) and HER2<sup>-</sup> cells (MDA-MB-468). Relative intracellular accumulation ( $\pm$  SD) refers to the highest normalized intracellular accumulation rate:  $\alpha\text{H-S5}^{\text{C}}$ -pHAb on SKBR-3 cells (100%). Cell lines were selected on the basis of HER2 expression levels, with highest expression in SKBR-3, followed by HCC-1954 and BT-474.<sup>99</sup> **(B)** Cellular uptake of EGFR-targeting constructs into EGFR<sup>+</sup> (MDA-MB-468, A431) and EGFR<sup>-</sup> cells (MCF-7). Relative intracellular accumulation ( $\pm$  SD) refers to  $\alpha\text{E-C-IgG}$ -pHAb on MDA-MB-468 (100%). Relative EGFR expression profile is indicated below bar graph.

Both, HER2- and EGFR-targeting Fcab pHAb-dye conjugates as well as Trastuzumab- and Cetuximab pHAb-dye references showed selective intracellular accumulation indicating receptor-mediated endocytosis and endosomal trafficking. No cellular uptake of negative control huFc<sup>K</sup>-pHAb was observed.

For the HER2-targeting subset (**Figure 26A**), intracellular accumulation was most pronounced for  $\alpha\text{H-S5}^{\text{C}}$ -pHAb ( $K_{D,lit}$  19 nM<sup>258</sup>) followed by  $\alpha\text{H-T-Fab}^{\text{C}}$ -pHAb ( $K_{D,lit}$  0.16 nM<sup>279</sup>),  $\alpha\text{H-S19}^{\text{C}}$ -pHAb ( $K_{D,lit}$  109 nM<sup>258</sup>),

---

$\alpha$ H-T-IgG<sup>C</sup>-pHAb ( $K_{D,lit}$  0.16 nM<sup>279</sup> + avidity) and  $\alpha$ H-FS<sup>C</sup>-pHAb ( $K_{D,lit}$  0.8 nM<sup>255</sup>). The lower intracellular accumulation of  $\alpha$ H-S19<sup>C</sup>-pHAb compared to  $\alpha$ H-S5<sup>C</sup>-pHAb reflects reduced target binding by  $\alpha$ H-S19<sup>C</sup>-pHAb at subsaturating antibody concentrations used in this assay (100 nM). High affinity antibodies require lower concentrations for full receptor saturation and thus, show elevated cellular uptake at lower concentrations. Contradictorily,  $\alpha$ H-FS<sup>C</sup>-pHAb showed reduced intracellular accumulation despite high affinity. A possible explanation for this behavior may be provided by an intrinsic mode of action of its scaffold Fcab FS102. Leung *et al.* reported that FS102 induces profound HER2 degradation in HER2 high expressing cell lines, thereby constantly reducing available surface receptors for consecutive internalization cycles.<sup>255</sup> They observed almost 50% reduction in surface and total HER2 levels after incubating SKBR-3 cells for 24 h with 200 nM FS102.<sup>255</sup> In contrast, incubation with 200 nM Trastuzumab reduced SKBR-3 surface and total HER2 levels only by  $\sim$  10% in the same time.<sup>255</sup> The HER2 depletion is also supported by the time dependent reduction of the intracellular accumulation rate (**Figure 25C**). There is no obvious explanation for enhanced intracellular accumulation of  $\alpha$ H-FS<sup>C</sup>-pHAb on BT-474 cells compared to SKBR-3 or HCC-1954.

Slightly higher intracellular accumulation of  $\alpha$ H-S5<sup>C</sup>-pHAb compared to  $\alpha$ H-T-Fab<sup>C</sup>-pHAb may be epitope-driven or may result from increased endosomal HER2 dissociation ( $k_{off, pH7.4}$   $2.61 \cdot 10^{-3} \text{ s}^{-1}$  versus  $0.13 \cdot 10^{-3} \text{ s}^{-1}$ ;  $1/k_{off, pH7.4}$  6.4 min versus 167 min; **Table A2**) enabling unbound  $\alpha$ H-S5<sup>C</sup>-pHAb entry into lysosomal pathway while receptor bound  $\alpha$ H-T-Fab<sup>C</sup>-pHAb is more efficiently recycled back to the surface.<sup>291,292</sup> This is supported by increased recycling rates of Trastuzumab in HER2 high expressing cells described in literature.<sup>99</sup> In contrast to  $\alpha$ H-T-Fab<sup>C</sup>-pHAb,  $\alpha$ H-S5<sup>C</sup>-pHAb dissociation from HER2 is at the same timescale than the predominant immediate recycling pathway of inactivated HER2 ( $\sim$  5 min) and even more rapidly than the prolonged recycling pathway *via* early endosomes ( $>$  15 min) leaving enough time for appreciable dissociation (**Figure 5**).<sup>86</sup>

Compared to  $\alpha$ H-T-Fab<sup>C</sup>-pHAb or  $\alpha$ H-S5<sup>C</sup>-pHAb, relative intracellular accumulation of  $\alpha$ H-T-IgG<sup>C</sup>-pHAb is reduced by approximately 50%. This might be explained by  $\alpha$ H-T-IgG<sup>C</sup>-pHAb bivalency which potentially halve intracellular accumulated  $\alpha$ H-T-IgG<sup>C</sup>-pHAb due to simultaneous occupancy of two HER2 receptors. Endo- and lysosomal trafficking may also depend on the number of expressed surface HER2 receptors for which the following order has been reported: SKBR-3  $>$  HCC-1954  $>$  BT-474.<sup>99</sup>

Regarding the EGFR-targeting subset (**Figure 26B**), bivalent  $\alpha$ E-C-IgG<sup>C</sup>-pHAb and monovalent  $\alpha$ E-C-Fab<sup>C</sup>-pHAb showed similar, but more than 50% increased intracellular accumulation compared to EGFR-binding Fcab-pHAb conjugates. This relationship was confirmed by a second, independent flow cytometry-based cellular uptake assay employing the same pHAb-dye constructs on non-adherent MDA-MB-468 cells (**Figure A9B-D**). Differences may arise from distinct epitopes addressed by Cetuximab and Fcabs<sup>252</sup> since assay concentration (100 nM) exceeds the  $K_D$  values of Fcabs and Cetuximab by a factor of 40 – 50 indicating

---

receptor-saturating conditions. Reduced intracellular uptake of Fcabs indicate that corresponding Fcab-drug conjugates would deliver less payload into a target cell than Cetuximab-drug conjugates, but may have better tumor penetration due to reduced endocytotic clearance as described in section 4.5.2.<sup>171</sup> This could be beneficial for *in vivo* efficacy if the lower amount of intracellularly delivered payload by the Fcab still exceeds the therapeutic threshold for cell death. In other words, instead of hitting and overkilling fewer cells at intracellular payload concentrations highly exceeding the therapeutic threshold, more cells could be targeted and killed at a reduced, but still toxic, intracellular payload concentration.<sup>108,194</sup>

In summary, these results demonstrate that the Fcabs used in this study enable the intracellular accumulation required for ADC applications. Moreover, the study underlines the above-mentioned importance of antibody target epitopes for endosomal trafficking behavior.

### 7.3. Selection, Design and Generation of Fcab-Drug Conjugates

After studying cellular binding and uptake profiles of Fcabs, the most promising Fcab variants were selected for conjugation with cytotoxic payload.  $\alpha$ H-H10 and  $\alpha$ H-H10<sup>C265</sup> were excluded from conjugation experiments due to limited material availability (low expression yield) and their aggregation tendency.  $\alpha$ H-S5<sup>C-G4S-LLQGA</sup> and  $\alpha$ H-S5<sup>C-(G4S)2-LLQGA</sup> were excluded as well, as they mainly precipitated during a protein concentration step.  $\alpha$ H-S5,  $\alpha$ H-S5<sup>C265</sup>,  $\alpha$ H-S5<sup>LLQGA-N</sup>,  $\alpha$ H-S5<sup>LLQGA-G4S-N</sup>,  $\alpha$ H-S19,  $\alpha$ H-S19<sup>C265</sup>,  $\alpha$ H-FS,  $\alpha$ E-60,  $\alpha$ E-65 and  $\alpha$ E-67 were subjected to conjugation along with controls huFc, huFc<sup>C265</sup>, huFc<sup>LLQGA-N</sup>, huFc<sup>LLQGA-G4S-N</sup> and references  $\alpha$ H-T-Fab and  $\alpha$ H-T-IgG.

#### 7.3.1. Design Rationale

It was demonstrated by several authors that the conjugation site can impact stability and therapeutic activity of an ADC.<sup>116–118</sup> Therefore, different sites and conjugation techniques were evaluated for the conjugation of the Fcab scaffold to linker-drugs (**Figure 27A**). For this, a cleavable valine-citrulline (Val-Cit) monomethyl auristatin E (MMAE) construct was chosen as clinically validated microtubule inhibitor ADC linker-drug.<sup>68</sup> Val-Cit-MMAE was equipped with a triple glycine (Gly<sub>3</sub>) handle (**3**) for selective enzymatic transglutaminase conjugation either to genetically fused N-terminal LLQGA tags<sup>124,281</sup> ( $\alpha$ H-S5<sup>LLQGA-N</sup>,  $\alpha$ H-S5<sup>LLQGA-G4S-N</sup>, huFc<sup>LLQGA-N</sup>, huFc<sup>LLQGA-G4S-N</sup>) or to native glutamine Q295<sup>125</sup> within the C<sub>H2</sub> domain ( $\alpha$ H-S5,  $\alpha$ H-S19,  $\alpha$ H-FS,  $\alpha$ E-60,  $\alpha$ E-65,  $\alpha$ E-67, huFc,  $\alpha$ H-T-IgG) (**Figure 27**). In addition, Val-Cit-MMAE carrying a maleimidocaproyl (mc) handle (**4**) was chemically conjugated to engineered cysteine D265C<sup>280</sup> in close proximity to Q295 ( $\alpha$ H-S5<sup>C265</sup>,  $\alpha$ H-S19<sup>C265</sup>, huFc<sup>C265</sup>) or to engineered cysteines K183C and V205C within the LC constant domain of reference  $\alpha$ H-T-Fab

(Figure 27). EGFR-binding references  $\alpha$ E-C-IgG and  $\alpha$ E-C-Fab carrying Gly<sub>3</sub>-Val-Cit-MMAE (**3**) enzymatically conjugated to LC C-terminal LPETGS tags by SrtA were obtained from a related project.<sup>286</sup>

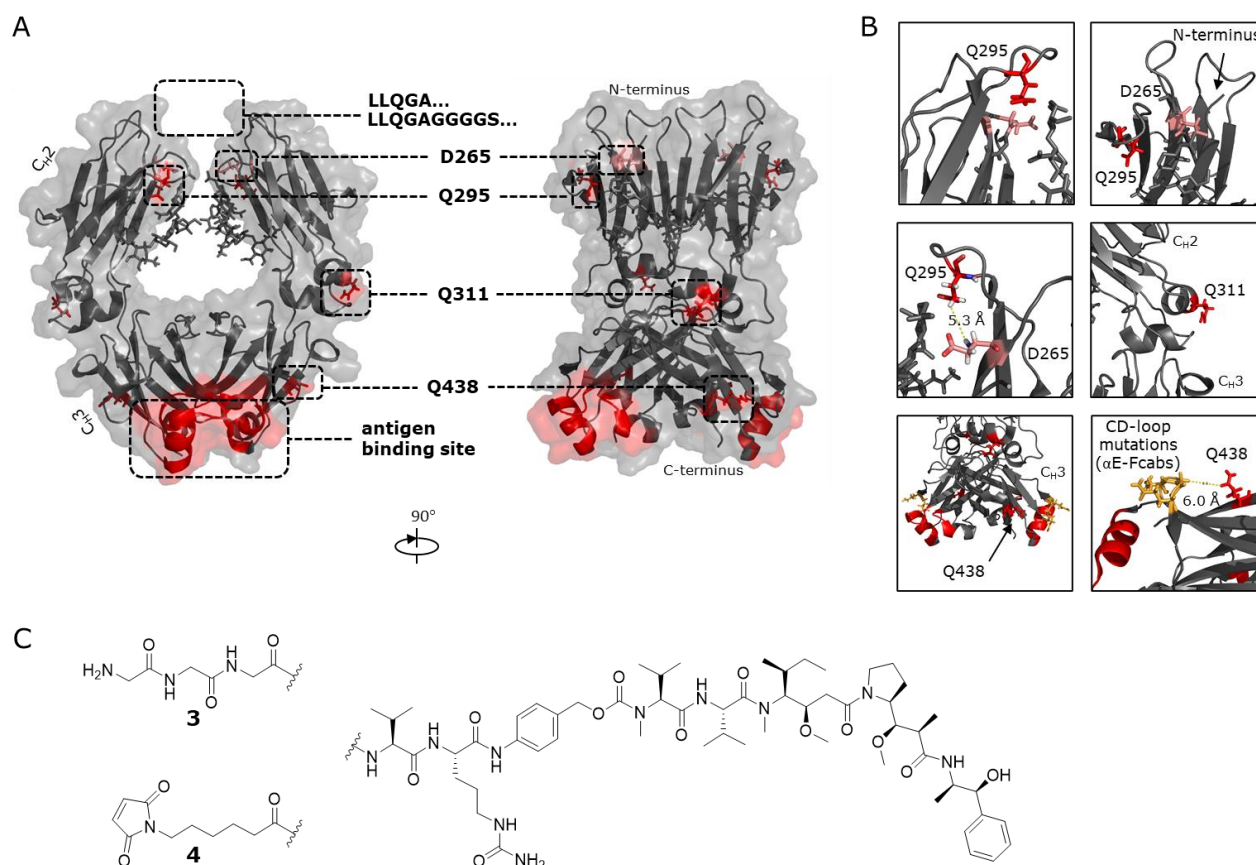


**Figure 27. Fcab conjugation sites and linker-drug structures.** (A) Fcab crystal structure (PDB: 5JIH, STAB19<sup>249</sup>) is shown in cartoon representation with transparent surface. mTG conjugation sites Q295, Q311 and Q438, as well as mutated D265 are depicted as sticks and are highlighted in red and salmon (EU numbering). Amino acids of N-terminal hinge region as well as LLQGA tags are not shown in crystal structure. Engineered amino acids in C<sub>H</sub>3 AB and EF loop forming the paratope are marked in red. (B) Magnification of conjugation sites derived from (A). Closest distance of Q438 and CD-loop side chains (N384, G385, Q386 marked yellow) mutated only in  $\alpha$ E-Fcabs is 6.0 Å. (C) Val-Cit-MMAE cleavable linker-drug possessing either a Gly<sub>3</sub> handle for mTG conjugation (**3**) or a mc handle for cysteine conjugation (**4**).

### 7.3.2. Conjugation, Purification and Biophysical Characterization

**Table 11** summarizes the generated Fcab-, huFc- and reference-drug conjugates and **Figure 28A** details the conjugation, product purification and analysis strategy. After conjugation, excess of linker-drug, reagents and/or mTG was successfully removed by preparative SEC (**Figure 28B**) and analytical SE-HPLC analysis confirmed high monomer content (97 – 100%) for all purified drug-conjugates (**Table 11**, **Figure A11A**, **Figure A12A**). The drug-to-antibody ratio (DAR) was determined from reversed phase (RP-HPLC) (**Figure A11B**, **Figure A12B**) and hydrophobic interaction chromatography (HI-HPLC) (**Figure A11C**) as well as LC-MS data (**Figure A13**, **Figure A14**, **Figure A15**) and is given as the mean (**Table 11**).

Conjugation of **3** to  $\alpha$ H-S5<sup>LLQGA-N</sup>,  $\alpha$ H-S5<sup>LLQGA-G4S-N</sup>, huFc<sup>LLQGA-N</sup> and huFc<sup>LLQGA-G4S-N</sup> was achieved by applying wild-type mTG from *S. mobaraensis* which is reported to not recognize Q295 in IgGs when position N297 is glycosylated.<sup>124</sup> Selective conjugation at both LLQGA tags was expected to yield a maximum DAR of 2.0 which was confirmed for huFc controls (huFc<sup>LLQGA-N</sup>-MMAE DAR 1.4, huFc<sup>LLQGA-G4S-N</sup>-MMAE DAR 2.2). In contrast, the Fcab scaffold surprisingly showed DAR values beyond 2.0 ( $\alpha$ H-S5<sup>LLQGA-N</sup>-MMAE DAR 2.4,  $\alpha$ H-S5<sup>LLQGA-G4S-N</sup>-MMAE DAR 3.0) indicating that another glutamine was coupled by mTG from *S. mobaraensis*. LC-MS peptide mapping was applied to identify the unknown conjugation site but failed to detect a peptidic fragment with linker-drug **3** coupled to a glutamine residue other than Q295 (data not shown).

**Table 11. Generated drug conjugates.** mTG-1 refers to a genetically modified transglutaminase<sup>125</sup>, while mTG-2 is the wild-type transglutaminase from *S. mobaraensis*. For HER2-targeting subset and huFc controls, DAR is given as a mean from HI-HPLC, RP-HPLC and LC-MS analysis. For EGFR-targeting subset, DAR is given as a mean from RP-HPLC and LC-MS analysis. SE-HPLC purity refers to the final monomer drug conjugate and was analyzed after a freeze-thaw cycle. \*kindly provided by J. Roßkopf.<sup>286</sup>

drug conjugate	conjugation				SE-HPLC purity [%]
	site	technique	substrate	DAR	
$\alpha$ H-S5-MMAE	native Q295	mTG-1	3	2.0	100.0
$\alpha$ H-S5 <sup>C265</sup> -MMAE	D265C	cysteine	4	1.5	100.0
$\alpha$ H-S5 <sup>LLQGA-N</sup> -MMAE	LLQGA-N	mTG-2	3	2.4	100.0
$\alpha$ H-S5 <sup>LLQGA-G4S-N</sup> -MMAE	LLQGA-G4S-N	mTG-2	3	3.0	100.0
$\alpha$ H-S19-MMAE	native Q295	mTG-1	3	2.1	100.0
$\alpha$ H-S19 <sup>C265</sup> -MMAE	D265C	cysteine	4	1.1	100.0
$\alpha$ H-FS-MMAE	native Q295	mTG-1	3	2.2	99.8
$\alpha$ E-60-MMAE	Q295, Q311, Q438	mTG-1	3	2.9	96.7
$\alpha$ E-65-MMAE	Q295, Q311, Q438	mTG-1	3	2.7	98.5
$\alpha$ E-67-MMAE	Q295, Q311, Q438	mTG-1	3	2.8	99.7
huFc-MMAE	native Q295	mTG-1	3	2.0	100.0
huFc <sup>C265</sup> -MMAE	D265C	cysteine	4	1.8	100.0
huFc <sup>LLQGA-N</sup> -MMAE	LLQGA-N	mTG-2	3	1.4	100.0
huFc <sup>LLQGA-G4S-N</sup> -MMAE	LLQGA-G4S-N	mTG-2	3	2.2	100.0
$\alpha$ H-T-Fab-MMAE	K183C, V205C	cysteine	4	1.8	99.6
$\alpha$ H-T-IgG-MMAE	native Q295	mTG-1	3	2.0	100.0
$\alpha$ E-C-Fab-MMAE*	LC-C-(G4S) <sub>3</sub> -LPETGS	SrtA	3	0.8	99.5
$\alpha$ E-C-IgG-MMAE*	LC-C-(G4S) <sub>3</sub> -LPETGS	SrtA	3	1.1	99.5

For conjugation of **3** to native Q295 of fully glycosylated Fcabs, huFc and  $\alpha$ H-T-IgG, a genetically engineered mTG was used (see also section 4.4.2).<sup>125</sup> In line with conjugation to native IgGs in literature<sup>125</sup>, homogeneous products with DAR 2.0 – 2.2 were obtained for HER2-targeting Fcabs and controls ( $\alpha$ H-S5-MMAE,  $\alpha$ H-S19-MMAE,  $\alpha$ H-FS-MMAE, huFc-MMAE,  $\alpha$ H-T-IgG-MMAE). In contrast, EGFR-targeting Fcab-MMAE conjugates showed an elevated DAR 2.7 – 2.9 ( $\alpha$ E-60-MMAE,  $\alpha$ E-65-MMAE,  $\alpha$ E-67-MMAE) indicating that

linker-drug **3** had been coupled to additional glutamines in the EGFR-targeting Fcab scaffold only. MS spectra of EGFR-targeting Fcab-MMAE conjugates indicated the presence of overall three conjugation sites (**Figure A13**) which were subsequently identified by LC-MS peptide mapping of digested  $\alpha$ E-60 and  $\alpha$ E-60-MMAE (**Figure 29**) as the already known position Q295 and the novel positions Q311 and Q438. The disappearance of peaks assigned to unconjugated peptides containing Q295 in the digested  $\alpha$ E-60-MMAE mixture (**Figure 29**; peak a, b) indicated that EGFR-targeting Fcabs were nearly completely conjugated at position Q295 while only partially conjugated at position Q311 and Q438 (total 18 – 23% conjugated based on DAR 2.7 – 2.9).

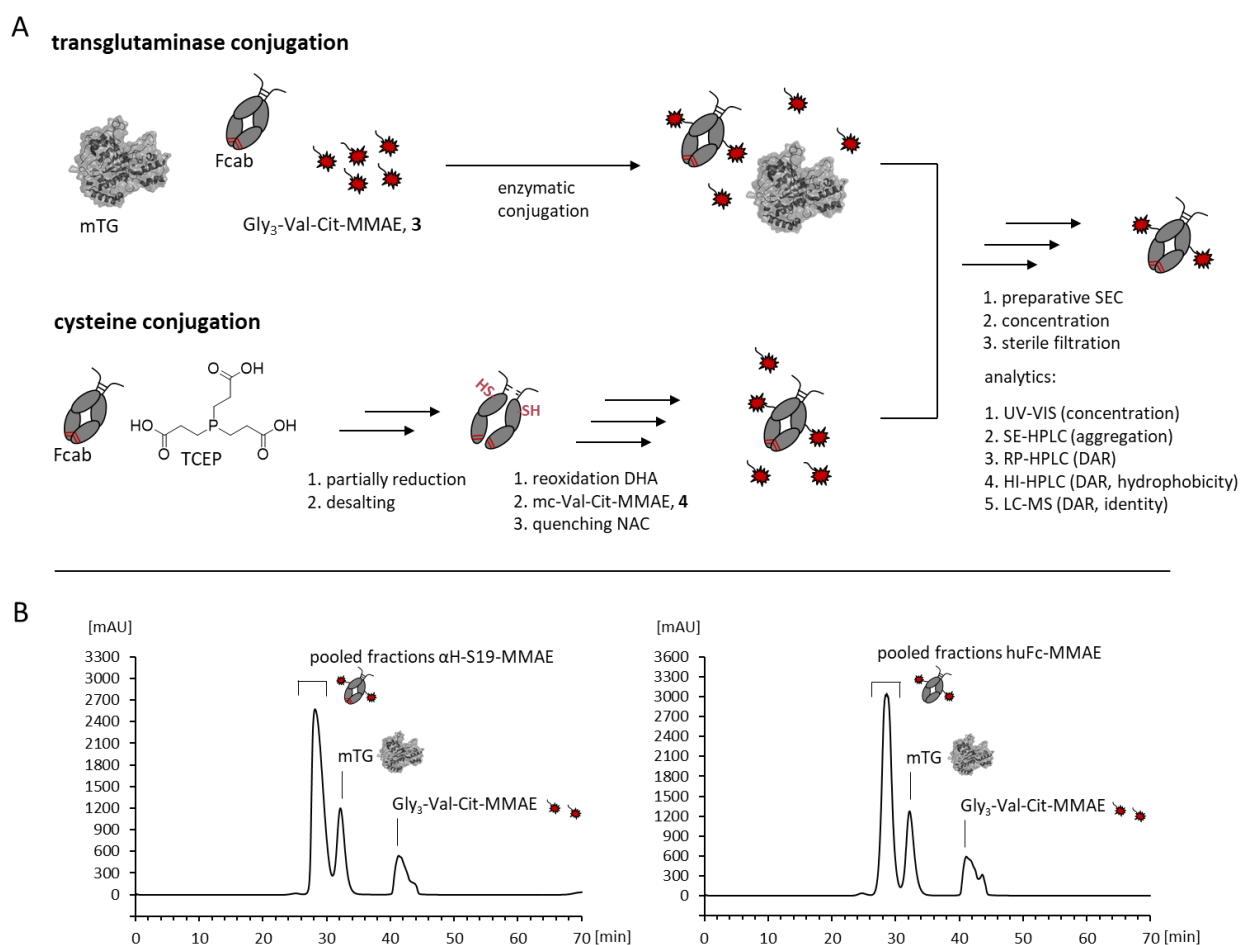
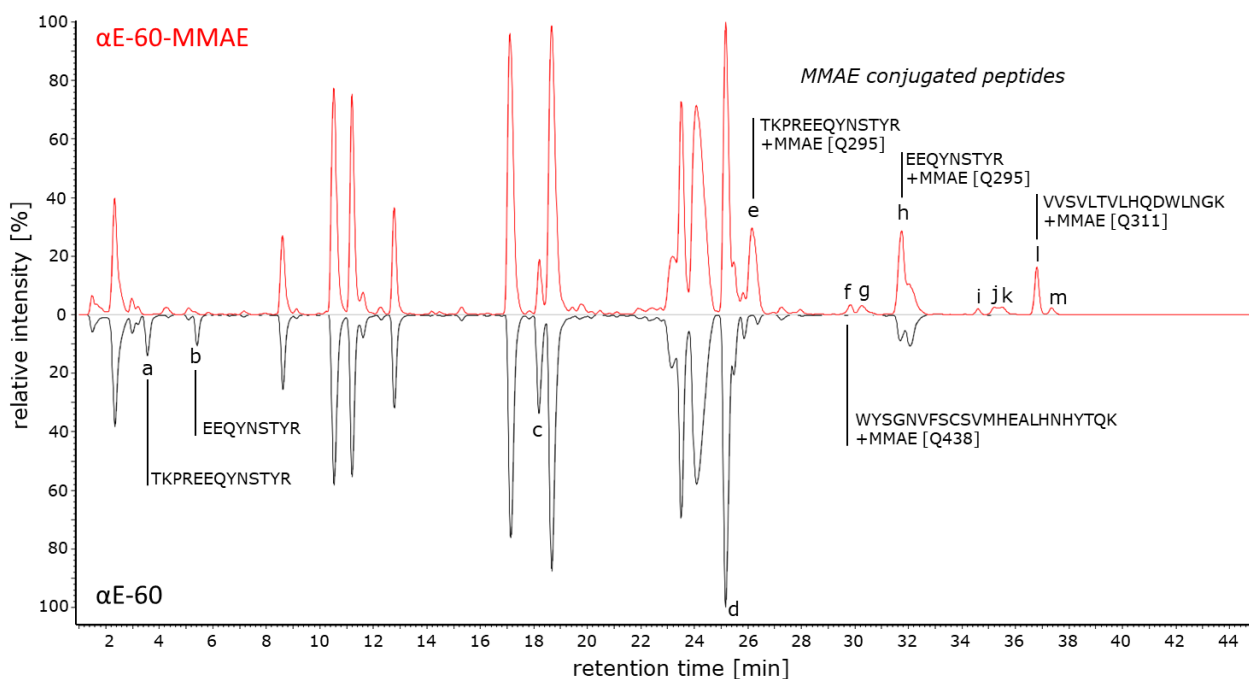


**Figure 28. Conjugation and purification strategy for Fcab-MMAE conjugates.** (A) MMAE conjugates were either generated by enzymatic transglutaminase or engineered cysteine conjugation. After conjugation, excess of microbial transglutaminase (mTG) and Gly<sub>3</sub>-Val-Cit-MMAE (**3**) or dehydroascorbic acid (DHA), *N*-acetylcysteine (NAC) and mc-Val-Cit-MMAE (**4**) were removed by preparative SEC. (B) Exemplary preparative SEC chromatograms illustrating purification of  $\alpha$ H-S19-MMAE (left) and huFc-MMAE (right). Fractions containing conjugated proteins (and non-conjugated species left) were pooled, concentrated, sterile filtered and subjected to analytics. Peak intensities represent absorption at 280 nm.

The accessibility for mTG and altered conjugation has most likely been driven by structural changes or electrostatic effects in adjacent regions. Both Q311 and Q438 lie within the solvent exposed exterior of the

Fcabs (**Figure 27A, B**). Q311 is located at the interface between the C<sub>H</sub>2 and C<sub>H</sub>3 domain and Q438 is situated at the C-terminus in close proximity to three mutated residues in the CD-loop that form part of the EGFR binding paratope (**Figure 27B**) and are not engineered in other Fcabs (**Table 5**).



peak	t <sub>R</sub> [min]	peptide	modification	calculated mass [Da]	m/z	Δmass [Da]
a	3.61	TKPREEQYNSTYR	-	1670.80	557.94	0.00
b	5.47	EEQYNSTYR	GlcNAc-Fuc [N297]	1537.64	769.83	0.00
c	18.31	WYSGNVFSCSVMHEALHNHYTQK	carbamidomethyl [C425]	2794.24	699.57	0.01
d	25.35	VVSVLTVLHQDWLNGK	-	1807.00	603.35	0.01
e	26.33	TKPREEQYNSTYR	MMAE [Q295]	3297.53	825.19	0.80
f	30.00	WYSGNVFSCSVMHEALHNHYTQK	carbamidomethyl [C425], MMAE [Q438]	4071.83	1018.77	0.78
g	30.46	FNWYVDGVEVHNAKTKPREEQYNSTYR	G2FSA2 glycan [N297], MMAE [Q295]	6958.01	994.37	4.50
h	31.92	EEQYNSTYR	MMAE [Q295], GlcNAc-Fuc [N297]	2815.24	1408.23	0.79
i	34.79	VVSVLTVLHQDWLNGKEYK	MMAE [Q311]	3504.79	1169.00	0.79
j	35.38	APELLGGPSVFLFPPKPKDTLMISR	oxidated [M252]	2725.49	682.37	0.03
k	35.57	VVSVLTVLHQDWLNGKEYK	deamidated [N315], MMAE [Q311]	3505.78	1169.34	0.79
l	36.99	VVSVLTVLHQDWLNGK	MMAE [Q311]	3084.59	1542.91	0.79
m	37.52	VVSVLTVLHQDWLNGK	deamidated [N315], MMAE [Q311]	3085.58	1029.27	0.79

**Figure 29. Conjugation site identification of αE-60-MMAE.** LC-MS chromatogram of digested αE-60-MMAE shows conjugated peptides (e-i, k-m) that were not detected in the αE-60 preparation. Conjugated peptides eluted at higher retention times due to hydrophobic MMAE. Matched pairs of unconjugated peptides (a-d) eluted at lower retention times and peaks disappeared (a,b) or showed reduced intensity (c) in the αE-60-MMAE preparation compared to αE-60. The disappearance of peaks assigned to unconjugated peptides containing Q295 (a,b) in the digested αE-60-MMAE mixture indicated that Fcabs were nearly completely conjugated at position Q295 while only partially conjugated at position Q311 and Q438. EU numbering was used.

All three EGFR-targeting Fcabs (αE-60, αE-65, αE-67) harbor the same three amino acid substitutions in the CD-loop (N384T, G385Y, Q386G) and it is tempting to speculate whether altered conjugation is caused by these conserved mutations. However, it is also possible that altered conjugation is due to mutations in other

---

loops (AB, EF) or to the missing core hinge region of EGFR-targeting Fcabs. To elucidate which amino acid exchanges enable mTG-mediated conjugation at position Q311 and/ or Q438, a set of huFc portions with systematically mutated C<sub>H</sub>3 loop regions and/ or a deleted core hinge region needs to be generated and tested for mTG conjugation. Such structure-activity relationship (SAR)-like studies were not part of this work but could be an interesting starting point to generate modified Fc portions or antibodies with increased mTG conjugation efficiency for position Q311 or Q438. Furthermore, SAR studies could guide a rational design of transglutaminases that are able to access positions Q311 and Q438 in native antibodies. In pharmaceutical industry, such a tool enzyme would be of special interest as it would allow to generate high DAR ADCs from existing native antibodies.

In contrast to enzymatic mTG conjugation, site-specific cysteine coupling was less efficient for Fcabs ( $\alpha$ H-S5<sup>C265</sup>-MMAE DAR 1.5,  $\alpha$ H-S19<sup>C265</sup>-MMAE DAR 1.1) compared to the huFc control (huFc<sup>C265</sup>-MMAE DAR 1.8). For the  $\alpha$ H-T-Fab reference, site-specific cysteine conjugation resulted in a DAR value of 1.8 nearly reaching the expected DAR 2.0. Likewise, the expected DAR of 1.0 for the SrtA-conjugated  $\alpha$ E-C-Fab-MMAE was almost reached (DAR 0.8), while SrtA-mediated conjugation was less efficient for  $\alpha$ E-C-IgG-MMAE (DAR 1.1) carrying two possible LPETGS conjugation sites.<sup>286</sup>

In summary, enzymatic conjugation to native Q295 by engineered mTG seems most suitable for Fcabs in terms of conjugation efficiency.

## 7.4. Evaluation of Fcab-Drug Conjugates

Following successful conjugation, Fcab-drug conjugates were evaluated for their hydrophobicity, receptor binding, serum stability and *in vitro* cytotoxicity.

### 7.4.1. Hydrophobicity of Drug Conjugates

Conjugation of hydrophobic payloads such as MMAE usually increases the overall hydrophobicity of the molecule. This can impact construct stability by protein aggregation and accelerate undesired non-specific uptake of ADCs by normal cells.<sup>149</sup> The overall hydrophobicity of a construct can be projected from its HI-HPLC retention time ( $t_R$ ) with longer  $t_R$  indicating higher hydrophobicity due to more pronounced interaction with the hydrophobic stationary phase (**Table 12**).

**Table 12. Hydrophobic interaction chromatography.** HI-HPLC retention times ( $t_R$ ) of unconjugated parental construct and MMAE conjugate DAR 1.0 – 3.0 species. Relative retention time (RRT) refers to the ratio between the  $t_R$  of the DAR species indicated in the table below and the  $t_R$  of the unconjugated parental molecule.

drug conjugate	HI-HPLC $t_R$ [min]				RRT
	parental molecule	DAR 1.0 conjugate	DAR 2.0 conjugate	DAR 3.0 conjugate	
$\alpha$ H-S5-MMAE	15.02	-	15.60	18.91	1.04 (DAR 2.0)
$\alpha$ H-S5 <sup>C265</sup> -MMAE	15.51	15.79	16.11	-	1.04 (DAR 2.0)
$\alpha$ H-S5 <sup>LLQGA-N</sup> -MMAE	16.47	17.36	19.55	22.67	1.19 (DAR 2.0)
$\alpha$ H-S5 <sup>LLQGA-G4S-N</sup> -MMAE	16.49	-	19.49	22.54	1.18 (DAR 2.0)
$\alpha$ H-S19-MMAE	13.22	-	14.39	17.68	1.09 (DAR 2.0)
$\alpha$ H-S19 <sup>C265</sup> -MMAE	13.46	14.43	14.91	-	1.11 (DAR 2.0)
$\alpha$ H-FS-MMAE	13.62	-	15.24	18.67	1.12 (DAR 2.0)
$\alpha$ E-60-MMAE	15.66	15.63	17.07	17.95	1.15 (DAR 3.0)
$\alpha$ E-65-MMAE	13.34	13.48	15.11	15.91	1.19 (DAR 3.0)
$\alpha$ E-67-MMAE	12.42	12.53	14.18	15.13	1.22 (DAR 3.0)
huFc-MMAE	10.63	-	12.33	15.79	1.16 (DAR 2.0)
huFc <sup>C265</sup> -MMAE	10.45	12.34	13.30	-	1.27 (DAR 2.0)
huFc <sup>LLQGA-N</sup> -MMAE	10.35	12.27	14.59	-	1.41 (DAR 2.0)
huFc <sup>LLQGA-G4S-N</sup> -MMAE	10.43	14.09	18.05	18.52	1.73 (DAR 2.0)
$\alpha$ H-T-Fab-MMAE	8.01	13.33	16.99	-	2.12 (DAR 2.0)
$\alpha$ H-T-IgG-MMAE	10.92	12.95	13.11	16.63	1.20 (DAR 2.0)
$\alpha$ E-C-Fab-MMAE	7.89	12.90	-	-	1.63 (DAR 1.0)
$\alpha$ E-C-IgG-MMAE	11.18	13.01	15.36	-	1.37 (DAR 2.0)

Unconjugated Fcab molecules showed higher hydrophobicity ( $t_R$  12.42 – 16.49 min) compared to unconjugated huFc ( $t_R$  10.35 – 10.63 min), Fab ( $t_R$  7.89 – 8.01) and IgG ( $t_R$  10.92 – 11.18) controls (**Figure 30A**) probably caused by the engineered binding site that potentially increases solvent exposure of hydrophobic patches. After conjugation, the hydrophobicity of Fcab-MMAE DAR 2.0 conjugates ( $t_R$  14.18 – 19.55 min) was still increased, but HI-HPLC  $t_R$  indicated more similar hydrophobicity to huFc-MMAE ( $t_R$  12.33 – 18.05 min),  $\alpha$ H-T-Fab-MMAE ( $t_R$  16.99 min), and IgG-MMAE ( $t_R$  13.11 – 15.36 min) DAR 2.0 conjugates (**Figure 30B**). As expected, most pronounced hydrophobicity was observed for variants where MMAE was attached to the N-terminally exposed LLQGA-G4S tag ( $t_R$  18.05 – 19.49 min).

The contribution of the linker-drug to overall hydrophobicity can also be illustrated by the HI-HPLC relative retention time (RRT) of the conjugate and unconjugated parent molecule:

$$RRT = \frac{t_R(\text{conjugate})}{t_R(\text{parent molecule})} \quad (15)$$

More particularly, the RRT allows to judge the shielding effect of protein secondary structures surrounding the hydrophobic linker-drug. Higher RRT indicate better steric accessibility of the linker-drug to the HI-HPLC stationary phase and consequently to serum proteases.<sup>123,125</sup>

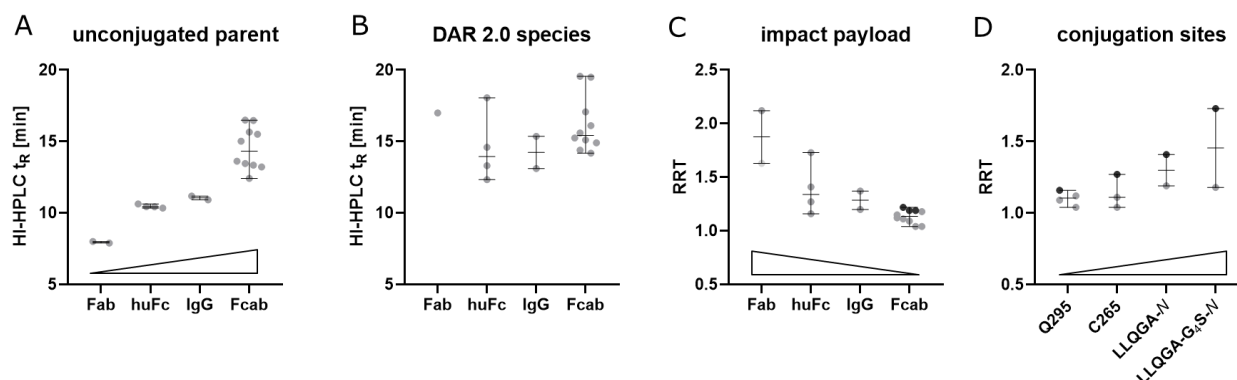


**Figure 30. Hydrophobicity of unconjugated parent molecules and drug conjugates.** (A) HI-HPLC  $t_R$  of unconjugated scaffold proteins increases from Fab < huFc < IgG < Fcab indicating highest intrinsic hydrophobicity for the Fcab scaffold. (B) HI-HPLC  $t_R$  of conjugated DAR 2.0 species are in the same range indicating similar hydrophobicity for Fab-, huFc-, IgG- and Fcab-MMAE DAR 2.0 conjugates. (C) RRT of drug conjugates decreases in the order Fab > huFc > IgG > Fcab suggesting only minor impact of payload hydrophobicity to overall Fcab-drug conjugate hydrophobicity. RRT for DAR 1.0 species (Fab) is marked light grey; RRT for DAR 2.0 species is marked grey; RRT for DAR 3.0 species is marked dark grey. (D) Impact of conjugation site on overall hydrophobicity. RRT of  $\alpha$ H-S5,  $\alpha$ H-S19,  $\alpha$ H-FS and huFc MMAE DAR 2.0 species are shown. huFc variants are marked in dark grey. Median ( $\pm$  range) is given for (A) – (D). Trends are indicated at the bottom of each graph.

Of relevant DAR species, Fcab-MMAE conjugates show the lowest RRT (RRT 1.04 – 1.22) compared to huFc-MMAE (RRT 1.16 – 1.73), Fab-MMAE (RRT 1.63 – 2.12) and IgG-MMAE (RRT 1.20 – 1.37) (Figure 30C), suggesting that MMAE is sufficiently shielded by the Fcab scaffold. It could be speculated whether increased hydrophobicity of Fcabs improves the shielding effect of the payload by hydrophobic Fcab patches. However, it would be also conceivable that lower RRT are not caused by payload shielding but Fcab scaffold hydrophobicity, which may overlap the hydrophobicity added by the payload and thereby determines the overall hydrophobicity of Fcab-MMAE conjugates.

huFc and STAB5-based conjugate HI-HPLC  $t_R$  and RRT increase for positions Q295 < D265C < LLQGA-N < LLQGA-G<sub>4</sub>S-N (Figure 30D) suggesting that position Q295 provides most efficient shielding and overall, most reduced conjugate hydrophobicity. Along with superior conjugation efficiency and product homogeneity ( $\alpha$ H-Fcab-MMAE: DAR 2.0 – 2.2,  $\alpha$ E-Fcab-MMAE: DAR 2.7 – 2.9), position Q295 seems favorable for the generation of Fcab-drug conjugates.

## 7.4.2. Receptor Binding Properties of Drug Conjugates

The conjugation of hydrophobic payloads does not only increase the risk for aggregation or undesired non-specific cellular uptake but also may impact the binding behavior of Fcab-drug conjugates to their target receptor or half-life extending FcRn. This is especially true for the newly discovered conjugation site Q311 that lies within the solvent exposed C<sub>H2</sub>-C<sub>H3</sub> interface (**Figure 27A, B**) proximate to the FcRn binding site (**Figure 3B**).

**Table 13. Target and FcRn binding affinity of unconjugated and conjugated Fcabs and references.** Dissociation constants ( $K_D$ ) were measured by BLI using recombinantly produced HER2, EGFR or FcRn. Binding affinity to FcRn was determined at pH 6.0. Errors are standard errors from fitting using FortéBio data analysis software. On- and off-rates as well as curve fittings are included in the appendix (**Table A2, Table A3, Figure A16, Figure A17, Figure A18**). *n.d.* - not determined.

HER2 subset	non-conjugated		MMAE-conjugates	
	$K_{D,BLI}$ (HER2) [nM]	$K_{D,BLI}$ (FcRn) [nM]	$K_{D,BLI}$ (HER2) [nM]	$K_{D,BLI}$ (FcRn) [nM]
$\alpha$ H-S5-MMAE	2.25 ± 0.03	399 ± 15	3.83 ± 0.04	274 ± 11
$\alpha$ H-S5 <sup>C265</sup> -MMAE	3.52 ± 0.06	376 ± 13	3.36 ± 0.04	350 ± 35
$\alpha$ H-S5 <sup>LLQGA-N</sup> -MMAE	3.52 ± 0.10	389 ± 13	3.24 ± 0.04	284 ± 9
$\alpha$ H-S5 <sup>LLQGA-G4S-N</sup> -MMAE	6.32 ± 0.07	357 ± 12	5.22 ± 0.06	226 ± 8
$\alpha$ H-S19-MMAE	46.6 ± 0.99	383 ± 13	48.5 ± 0.90	609 ± 25
$\alpha$ H-S19 <sup>C265</sup> -MMAE	39.8 ± 0.89	448 ± 15	29.1 ± 2.20	305 ± 36
$\alpha$ H-FS-MMAE	0.34 ± 0.004	346 ± 11	0.73 ± 0.008	339 ± 11
$\alpha$ H-T-Fab-MMAE	0.12 ± 0.001	-	0.40 ± 0.006	-
$\alpha$ H-T-IgG-MMAE	0.18 ± 0.006	303 ± 9	0.43 ± 0.008	387 ± 14
huFc-MMAE	-	524 ± 13	-	501 ± 12
EGFR subset	non-conjugated		MMAE-conjugates	
	$K_{D,BLI}$ (EGFR) [nM]	$K_{D,BLI}$ (FcRn) [nM]	$K_{D,BLI}$ (EGFR) [nM]	$K_{D,BLI}$ (FcRn) [nM]
$\alpha$ E-60-MMAE	2.42 ± 0.01	381 ± 12	2.67 ± 0.02	309 ± 10
$\alpha$ E-65-MMAE	1.07 ± 0.01	329 ± 13	1.37 ± 0.01	362 ± 12
$\alpha$ E-67-MMAE	1.71 ± 0.01	589 ± 22	1.54 ± 0.01	337 ± 12
$\alpha$ E-C-Fab-MMAE	0.82 ± 0.01	-	n.d.	-
$\alpha$ E-C-IgG-MMAE	1.25 ± 0.01	747 ± 24	0.60 ± 0.01	892 ± 31
huFc-MMAE	-	524 ± 13	-	501 ± 12

Therefore, the binding affinity of Fcab-MMAE and control conjugates to recombinant HER2, EGFR and FcRn was analyzed by biolayer interferometry (BLI) and compared to unconjugated parent molecules (**Table 13, Figure 31A, B**). BLI was chosen as it is a fast and well-established method that gives access to binding kinetics ( $K_D$ ,  $k_{off}$ ,  $k_{on}$ ) of protein-protein interactions, often omitting additional protein labeling steps. BLI measurements revealed similar dissociation constants for conjugated and unconjugated variants with differences in  $K_D$  beyond the assay variability (twofold) for target receptor (**Figure 31A**) and FcRn (**Figure 31B**), suggesting that conjugation at position Q295 do not alter receptor binding behavior. However, for Q311

and Q438 it should be noted that effects on EGFR and FcRn binding cannot be assessed robustly *via* the chosen BLI assay setup because of just minor conjugation (18 – 23%). For example, one of the two Q311 residues is statistically unconjugated and the Fcab FcRn 1:1 interaction can take place on the unconjugated site of the Fcab homodimer without detecting any impact of the conjugated second Q311 residue.

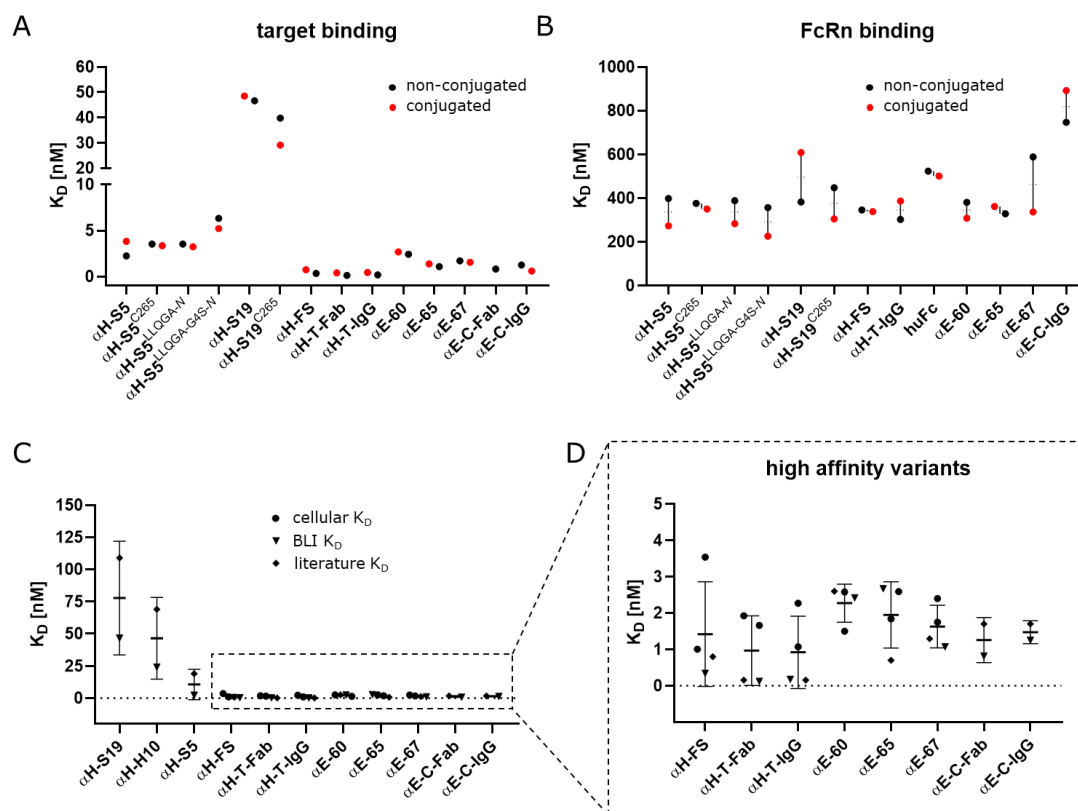


**Figure 31. Target and FcRn dissociation constants.** (A)  $K_D$  values for target binding of unconjugated and conjugated (MMAE) Fcabs and controls. (B)  $K_D$  values for FcRn binding of unconjugated and conjugated (MMAE) Fcabs and controls. Variations in  $K_D$  values are in the typical range of antibody-FcRn interactions observed by this BLI assay.<sup>274</sup> (C) Comparison of target binding  $K_D$  values derived from cellular binding assays, BLI measurements and literature data (Fcab, Trastuzumab and Cetuximab scaffold variants). (D) Enlargement for high affinity binding variants.

For HER2 variants  $\alpha$ H-S5,  $\alpha$ H-H10 and  $\alpha$ H-S19,  $K_D$  values from BLI measurements are lower compared to literature  $K_D$  values derived from cellular binding data (e.g.,  $\alpha$ H-S19:  $K_{D,BLI}$  47 nM vs.  $K_{D,lit}$  109 nM,  $\alpha$ H-S5:  $K_{D,BLI}$  2.2 nM vs.  $K_{D,lit}$  19 nM) (Figure 31C). Differences potentially reflect better accessibility to target epitopes in the BLI setting. For other variants, BLI derived target binding  $K_D$  values are in good agreement with literature or cellular  $K_D$  (Figure 31D). BLI data reveals also that differences in target binding affinity ( $K_D$ ) of Fcabs are mainly accounted by different off-rates (Table A2) as it is typically the case for antibodies.<sup>293</sup>

### 7.4.3. Serum Stability of Drug Conjugates

Based on FcRn binding data, no negative effect of the conjugation on pharmacokinetics (PK) of drug conjugates is expected. However, drug conjugate PK not only depend on FcRn-mediated recycling but also on conjugate stability.<sup>131</sup> For example, it is well documented that premature linker cleavage in circulation largely depends on the conjugation site.<sup>116–118</sup> To anticipate conjugate stability in circulation, Fcab-drug conjugates and reference conjugates were incubated in mouse and human serum for 96 h and payload release was monitored by detection of free MMAE *via* LC-MS/MS (**Table 14**).

**Table 14. Serum stability of Fcab and reference drug conjugates.** Free MMAE was measured *via* LC MS/MS after incubation in mouse and human sera at 37°C for 96 h (n = 3). Numbers show the released fraction relative to initially conjugated MMAE. *n.d.* – *not determined*.

drug conjugate	free MMAE (% total MMAE after 96 h)	
	mouse	human
<b>αH-S5-MMAE</b>	0.5	0.2
<b>αH-S5<sup>C265</sup>-MMAE</b>	1.0	0.0
<b>αH-S5<sup>LLQGA-N</sup>-MMAE</b>	9.6	0.2
<b>αH-S5<sup>LLQGA-G4S-N</sup>-MMAE</b>	34.8	0.0
<b>αH-S19-MMAE</b>	0.6	0.3
<b>αH-S19<sup>C265</sup>-MMAE</b>	1.4	0.0
<b>αH-FS-MMAE</b>	0.4	0.0
-----		
<b>αE-60-MMAE</b>	1.3	0.3
<b>αE-65-MMAE</b>	1.1	0.0
<b>αE-67-MMAE</b>	0.9	0.0
-----		
<b>αH-T-Fab-MMAE</b>	1.6	0.0
<b>αH-T-IgG-MMAE</b>	0.5	0.0
<b>αE-C-Fab-MMAE</b>	n.d.	n.d.
<b>αE-C-IgG-MMAE</b>	n.d.	n.d.

No free MMAE could be detected for conjugates in human serum suggesting high stability for all Fcab-MMAE conjugates in human circulation. In mouse serum, no free MMAE was observed for HER2-targeting variants carrying the linker-drug at position Q295, D265C, K183C or V205C confirming reports on high mouse serum stability of linker-drugs at these positions.<sup>118,122,123,125,294</sup> In contrast, αH-S5<sup>LLQGA-N</sup>-MMAE and αH-S5<sup>LLQGA-G4S-N</sup>-MMAE showed significantly elevated levels of free MMAE already after 2 h in mouse serum (0.9% and 6.2%, respectively) (**Figure 32A**), which further increased during incubation (9.6% and 34.8% after 96 h). Interestingly, both variants carry the linker-drug at the solvent exposed N-terminus with lowest mouse serum stability for variant αH-S5<sup>LLQGA-G4S-N</sup>-MMAE exposing the linker-drug even more by an additional glycine-serine spacer element. Solvent exposure favors serum protease accessibility and it is well described

that the Val-Cit linker motif can undergo cleavage in mouse serum mediated by the murine extracellular carboxylesterase 1c (mCes1c) (see also section 4.4.2).<sup>133</sup> Higher solvent exposure and mCes1c accessibility may also be reflected by higher HI-HPLC RRT of N-terminal linked MMAE constructs described in section 7.4.1.

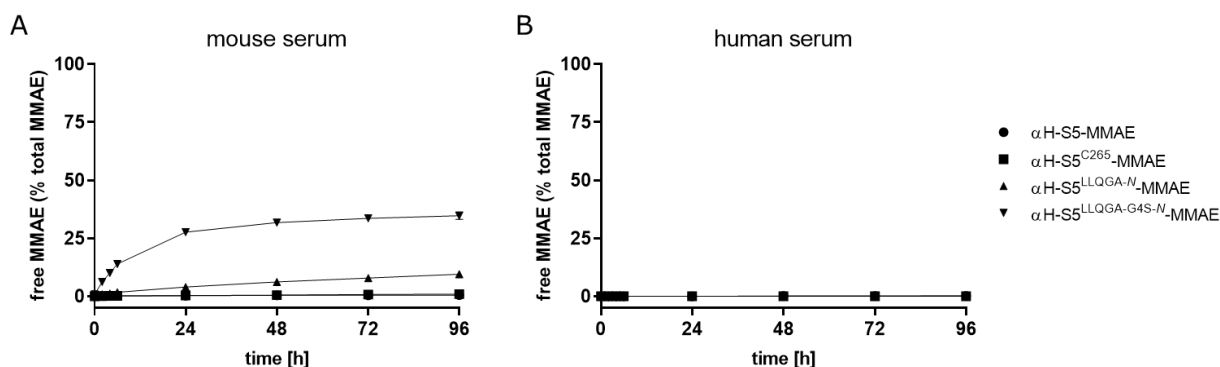


**Figure 32. *In vitro* serum stability exemplarily shown for STAB5-based Fcab-MMAE conjugates.** (A) Mouse serum incubation reveals MMAE release from  $\alpha$ H-S5<sup>LLQGA-N</sup>-MMAE and  $\alpha$ H-S5<sup>LLQGA-G4S-N</sup>-MMAE, while  $\alpha$ H-S5-MMAE and  $\alpha$ H-S5<sup>C265</sup>-MMAE show very low MMAE release and hence excellent conjugate stability. For  $\alpha$ H-S5<sup>LLQGA-G4S-N</sup>-MMAE, free MMAE levels seem to reach a plateau after 24 – 48 h possibly reflecting loss of enzymatic activity. (B) No free MMAE was detected when constructs were incubated in human serum. Free MMAE was measured *via* LC MS/MS after incubation in mouse and human serum at 37°C (n = 3).

Variants  $\alpha$ E-60-MMAE,  $\alpha$ E-65-MMAE and  $\alpha$ E-67-MMAE conjugated at position Q295, Q311 and Q438 did not show reduced mouse serum stability suggesting that position Q311 and Q438 confer sufficient shielding to prevent mCes1c-mediated linker cleavage, despite its solvent exposed localization (**Figure 27A, B**).

In summary, serum stability data confirms Q295, Q311, Q438 and C265 as attractive positions for the generation of Fcab-drug conjugates and disqualifies N-terminal conjugation at least for mCes1c labile linkers.

#### 7.4.4. *In Vitro* Cytotoxicity of Drug Conjugates

The confirmed target binding of Fcab-MMAE conjugates was the essential criteria that supported an *in vitro* cytotoxicity assessment to study whether Fcab-MMAE conjugates selectively deliver and efficiently release MMAE inside tumor cells.

EGFR-targeting conjugates  $\alpha$ E-60-MMAE (DAR 2.9),  $\alpha$ E-65-MMAE (DAR 2.7) and  $\alpha$ E-67-MMAE (DAR 2.8) were incubated on EGFR overexpressing (MDA-MB-468, A431) and EGFR negative cell lines (MCF-7) along with Cetuximab-based reference conjugates  $\alpha$ E-C-Fab-MMAE (DAR 0.8) and  $\alpha$ E-C-IgG-MMAE (DAR 1.1), a huFc-MMAE negative control and unconjugated parent molecules (**Figure 33**). The cell viability was evaluated 4 days post compound addition by quantifying ATP as indicator for metabolic activity. Subsequently, half

---

maximal inhibitory concentrations ( $IC_{50}$ ) were derived from fitted dose-response curves to quantify the potency of the constructs.

All  $\alpha E$ -Fcab-MMAE conjugates showed similar inhibitory activity at sub-nanomolar concentrations on EGFR positive MDA-MB-468 and A431 cells ( $IC_{50}$  0.18 – 0.22 nM and  $IC_{50}$  0.23 – 0.32 nM, respectively) while toxicity against EGFR negative MCF-7 cells was decreased by several orders of magnitude ( $IC_{50} > 100$  nM) indicating target-dependent cell killing (**Figure 33C**). This notion is also supported by the greatly reduced cytotoxicity of non-targeting huFc-MMAE on all cell lines (MDA-MB-468:  $IC_{50} > 300$  nM; A431 and MCF-7:  $IC_{50} > 100$  nM). Interestingly, unconjugated  $\alpha E$ -C-IgG and  $\alpha E$ -C-Fab show approximately 15% reduction in cell viability on MDA-MB-468 cells at  $IC_{50}$  2.0 nM and 6.9 nM, respectively, while no such an effect was observed for  $\alpha E$ -Fcabs on the same cell line (**Figure 33A**). Differences may be caused by individual EGFR epitopes targeted by Cetuximab and  $\alpha E$ -Fcabs.<sup>252</sup> Despite higher cytotoxicity of free MMAE on A431 ( $IC_{50}$  0.17 nM) compared to MDA-MB-468 cells ( $IC_{50}$  0.32 nM),  $\alpha E$ -Fcab-MMAE conjugates as well as reference conjugates showed higher activity on MDA-MB-468 cells (**Figure 33C**) reflecting higher cellular uptake due to increased number of EGFR surface receptors on MDA-MB-468 cells (**Figure 26**). Furthermore, higher potency of  $\alpha E$ -Fcab-MMAE conjugates on EGFR positive cells ( $IC_{50}$  0.18 – 0.32 nM) compared to  $\alpha E$ -C-Fab-MMAE ( $IC_{50}$  0.78 – 0.99 nM) or  $\alpha E$ -C-IgG-MMAE ( $IC_{50}$  0.44 – 0.50 nM) in this 4 day assay suggest that reduced cellular uptake of Fcabs (**Figure 26**) may be compensated by their higher drug load (DAR 2.7 – 2.9 *versus* 0.8 and 1.1, respectively). As already discussed in section 7.2.3, the reduced cellular uptake (i.e. reduced endocytotic clearance) for  $\alpha E$ -Fcab-MMAE may increase their tumor penetration. This, in combination with the here observed sub-nanomolar single-cell therapeutic threshold allows to speculate whether  $\alpha E$ -Fcab-MMAE could enhance therapeutic efficacy as possibly more cells are exposed to a therapeutic dose.

In summary, EGFR-targeting Fcab-MMAE conjugates fulfill the ADC criteria of selective drug delivery and target-mediated cytotoxicity in the for ADCs typical, sub-nanomolar range.

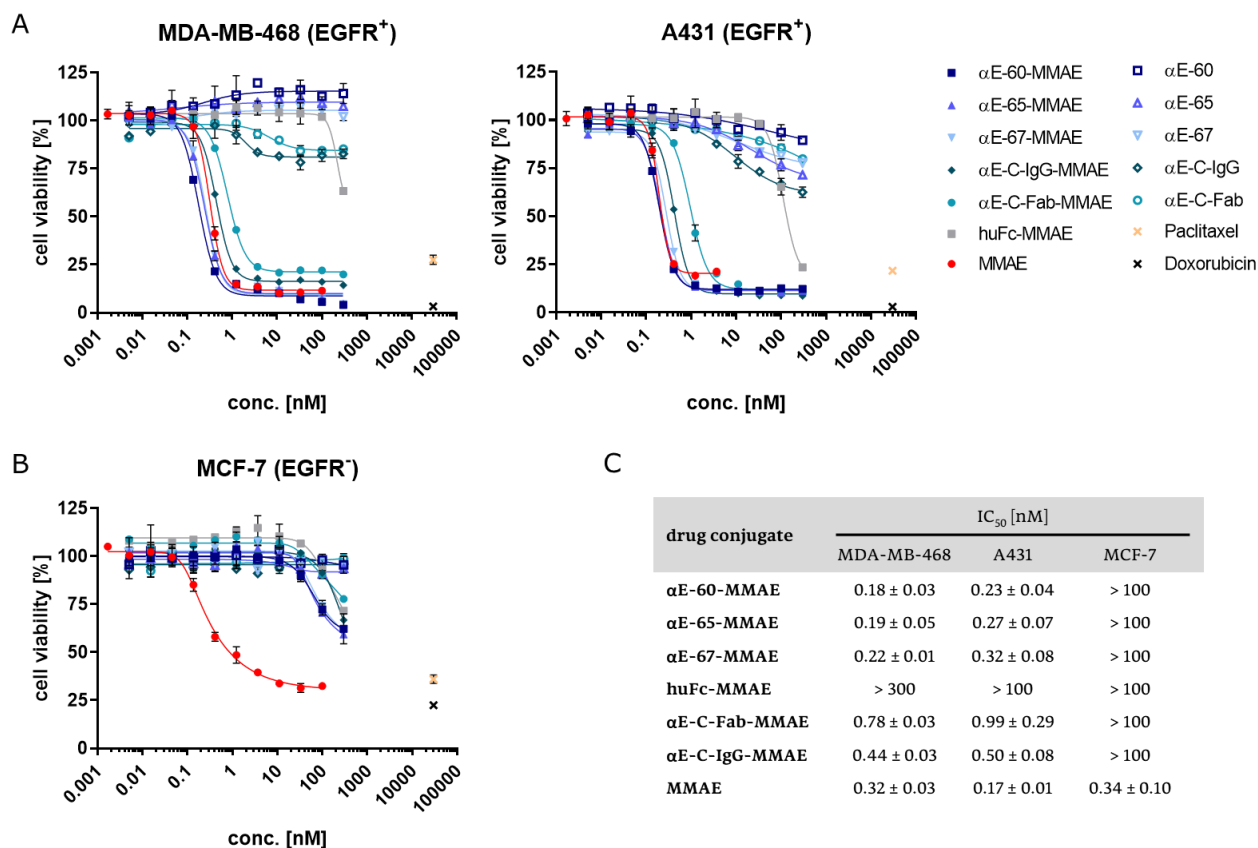


**Figure 33. In vitro cytotoxic activity of EGFR-targeting constructs.** (A) EGFR positive (MDA-MB-468, A431) and (B) EGFR negative cells (MCF-7) were incubated with serial dilution of MMAE conjugates and controls for 4 days before cell viability was analyzed by detection of ATP (CellTiter-Glo luminescent viability assay). Error bars represent standard deviation (SD). (C) Inhibitory activity of MMAE conjugates and free MMAE. IC<sub>50</sub> values are given as mean (± SD) of ≥ 3 independent experiments.

To investigate whether HER2-targeting Fcab-MMAE conjugates induce target-selective cytotoxicity,  $\alpha$ H-S5-MMAE (DAR 2.0),  $\alpha$ H-S5<sup>C265</sup>-MMAE (DAR 1.5),  $\alpha$ H-S5<sup>LLQGA-N</sup>-MMAE (DAR 2.4),  $\alpha$ H-S5<sup>LLQGA-G45-N</sup>-MMAE (DAR 3.0),  $\alpha$ H-S19-MMAE (DAR 2.1),  $\alpha$ H-S19<sup>C265</sup>-MMAE (DAR 1.1) and  $\alpha$ H-FS-MMAE (DAR 2.2) were incubated on HER2 positive (SKBR-3, HCC-1954) and HER2 negative cell lines (MDA-MB-468). Trastuzumab-based references  $\alpha$ H-T-Fab-MMAE (DAR 1.8),  $\alpha$ H-T-IgG-MMAE (DAR 2.0), non-targeting huFc-MMAE, huFc<sup>C265</sup>-MMAE, huFc<sup>LLQGA-N</sup>-MMAE and huFc<sup>LLQGA-G45-N</sup>-MMAE as well as unconjugated parent molecules were included in these experiments. All  $\alpha$ H-Fcab-MMAE conjugates and Trastuzumab reference conjugates induced selective cell killing of HER2 overexpressing cells while huFc MMAE conjugates showed reduced cytotoxicity (IC<sub>50</sub> > 100 nM) on HER2 positive and negative cell lines (Exemplary dose-response curves are given in **Figure 34**).

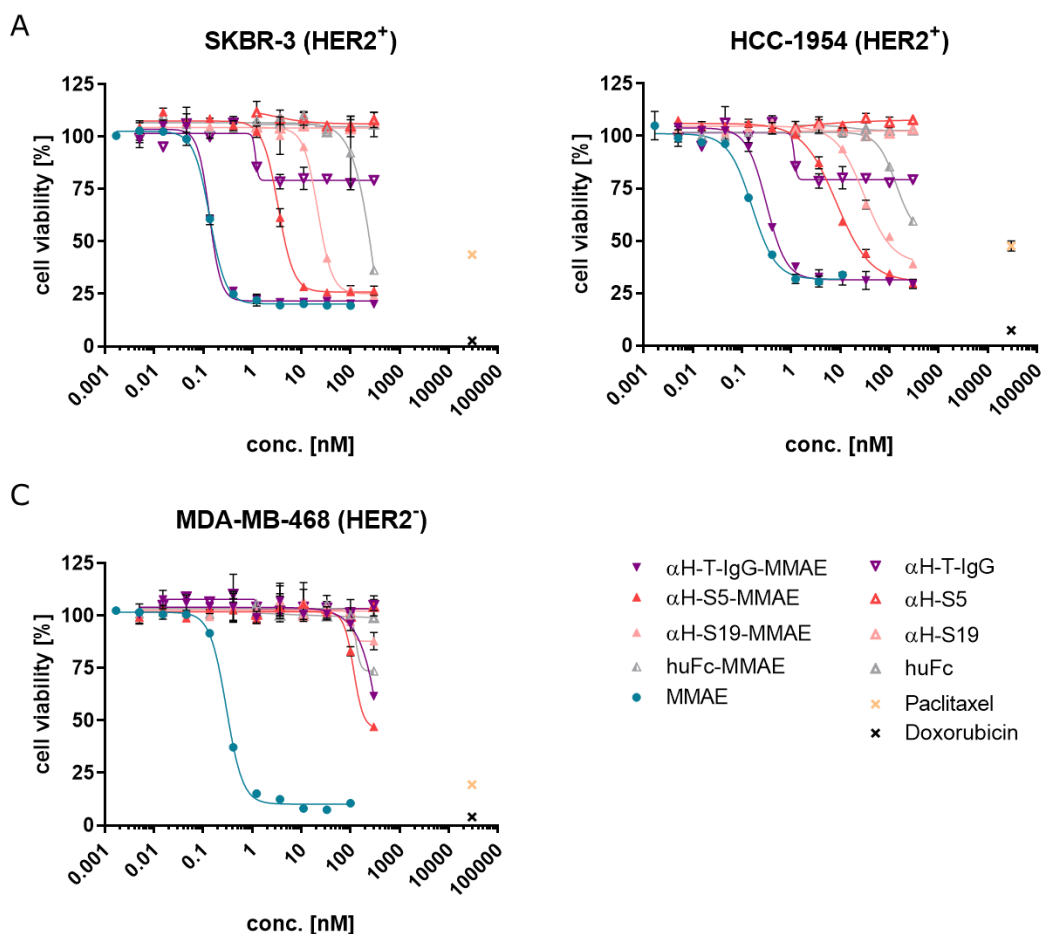


**Figure 34.** *In vitro* cytotoxic activity of HER2-targeting constructs. (A) HER2 positive (SKBR-3, HCC-1954) and (B) HER2 negative cells (MDA-MB-468) were incubated with serial dilution of MMAE conjugates and controls for 4 days before cell viability was analyzed by detection of ATP (CellTiter-Glo luminescent viability assay). Error bars represent standard deviation (SD).

For HER2 positive cells, the  $IC_{50}$  values of  $\alpha$ H-Fcab-MMAE and reference conjugates ranged from sub-nanomolar to double-digit nanomolar concentrations (Figure 35) and correlated with DAR and especially HER2 affinities:  $\alpha$ H-T-IgG-MMAE ( $K_{D,BLI}$  0.43 nM + avidity) >  $\alpha$ H-T-Fab-MMAE ( $K_{D,BLI}$  0.40 nM) >  $\alpha$ H-FS-MMAE ( $K_{D,BLI}$  0.73 nM) > STAB5-based MMAE conjugates ( $K_{D,BLI}$  3.2 – 5.2 nM) > STAB19-based MMAE conjugates ( $K_{D,BLI}$  29.1 – 48.5 nM). For example, the lower HER2 affinity of  $\alpha$ H-S5-MMAE and  $\alpha$ H-S19-MMAE translated into 10- to 100-fold reduced potency ( $IC_{50}$  4 – 8 nM and 27 – 29 nM, respectively) compared to  $\alpha$ H-T-Fab-MMAE ( $IC_{50}$  0.3 nM) (Table A4).

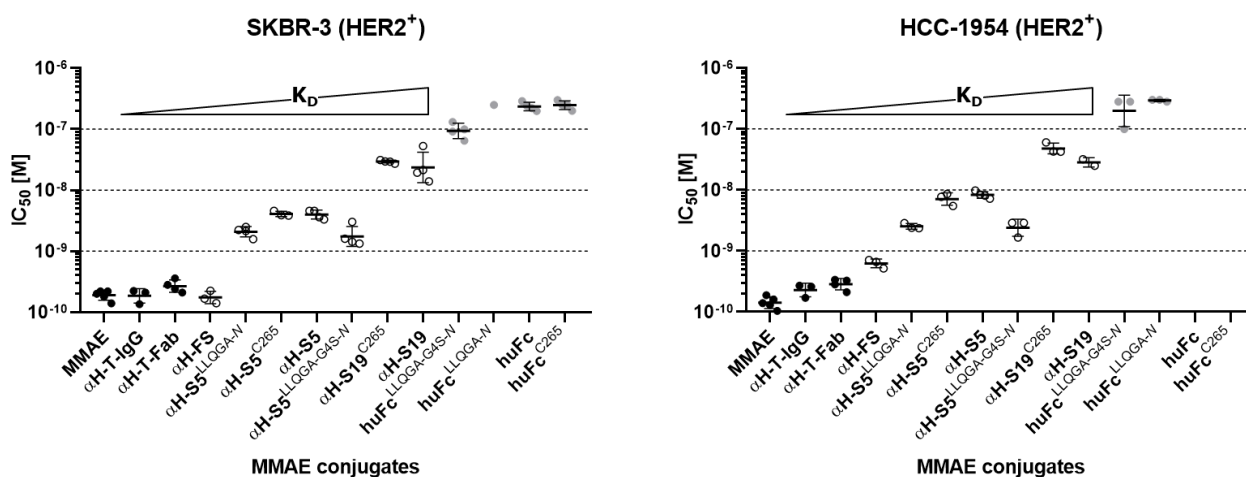


**Figure 35.** *In vitro* cytotoxic activity of HER2-targeting constructs and controls on HER2 positive cells. Fcab-MMAE conjugates (empty circles) as well as Trastuzumab-based reference MMAE conjugates (black dots) and huFc-based negative controls (grey dots) were tested on HER2 expressing SKBR-3 and HCC-1954 cell lines. Each data point in the graph represents the  $IC_{50}$  value from an individual experiment. Bars represent the geometric mean ( $\pm$  SD) calculated from individual  $IC_{50}$ . Constructs were incubated on cells for 4 days before cell viability was measured and  $IC_{50}$  was derived from dose-response. Affinity ( $K_D$ ) is indicated at each graph. Please note that  $\alpha$ H-S5<sup>LLQGA-G4S-N</sup>-MMAE and  $\alpha$ H-S19-MMAE do not strictly follow the  $IC_{50}$ - $K_D$  correlation due to higher DAR values than related conjugates. Unconjugated parent molecules did not show cytotoxicity under assay conditions. Listed  $IC_{50}$  values including HER2 negative MDA-MB-468 cells are given in appendix (Table A4). Corresponding dose response curves are depicted in Figure 34.

The observation that affinity determines *in vitro* potency makes sense considering that the  $K_D$  value is the concentration at half-maximal receptor occupancy. Consequently, high affinity conjugates reach full receptor occupancy at lower concentrations compared to conjugates with weak affinity. This results in enhanced cellular uptake and intracellular payload release for high affinity conjugates until receptor saturation is reached for weak affinity conjugates too.

So far, the affinity-potency relationship has been described for *in vitro* experiments. Which additional implications the lower affinities of  $\alpha$ H-Fcab-MMAE conjugates might have for *in vivo* efficacy will be discussed in the next section 7.5.

In contrast to STAB5 and STAB19-based Fcab-drug conjugates,  $\alpha$ H-FS-MMAE showed cytotoxicity at sub-nanomolar concentrations ( $IC_{50}$  0.18 – 0.63 nM) due to its high HER2 affinity ( $K_{D,BLI}$  0.73 nM). However, lower reduction in cell viability at maximum efficacy was observed for  $\alpha$ H-FS-MMAE compared to other MMAE conjugates or free MMAE (78% versus 87 – 95% on SKBR-3 cells) (Figure 36A). This effect was only observed for  $\alpha$ H-FS-MMAE and was reproduced in three independent experiments, even at a prolonged assay time of 6 days (Figure 36B, C). A possible explanation might provide the unique HER2 degradation mechanism of  $\alpha$ H-FS which was already described in section 7.2.3.<sup>255</sup> The time-dependent depletion of HER2 surface receptors (50% within the first 24 h<sup>255</sup>) could prevent cells from being exposed to a cytotoxic dose of payload resulting in survival of a subpopulation. This would reduce the *in vitro* efficacy of  $\alpha$ H-FS-based drug conjugates as it was observed here but may have a contrary effect *in vivo*. The implications of receptor

downregulation for tumor penetration and *in vivo* efficacy of  $\alpha$ H-FS-MMAE will be discussed in more detail in the next section 7.5.

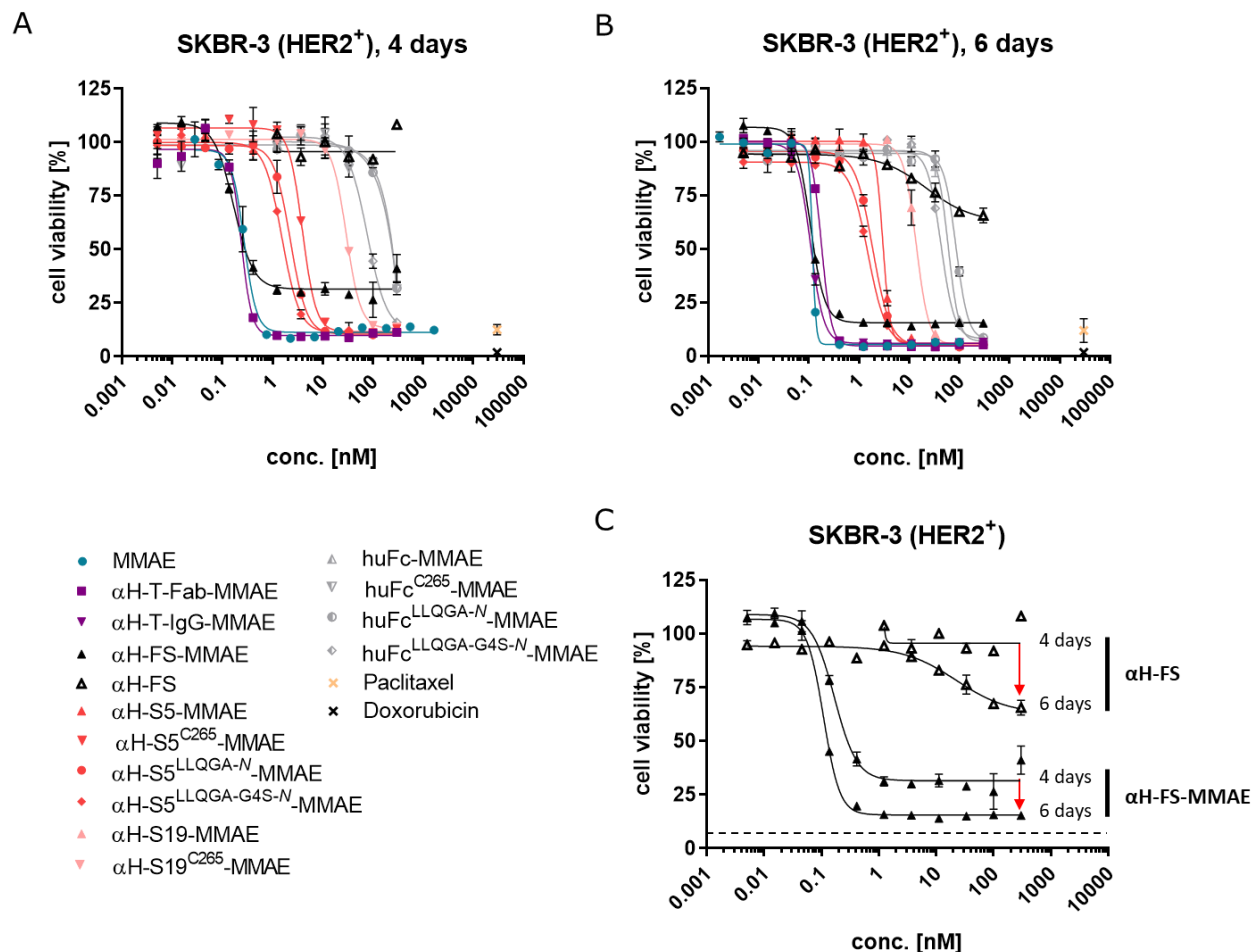


**Figure 36.  $\alpha$ H-FS-MMAE induces lower reduction in cell viability compared to all other investigated MMAE conjugates.** (A) *In vitro* cytotoxic activity of MMAE conjugates on HER2 positive SKBR-3 cells after 4-day and (B) after 6-day treatment in comparison to other Fcab- and reference MMAE conjugates. Interestingly, after 6 day treatment, the reported cell killing effect of unconjugated  $\alpha$ H-FS became visible.<sup>255</sup> (C) For better visualization, only  $\alpha$ H-FS-MMAE and  $\alpha$ H-FS cytotoxicity on SKBR-3 cells after 4 and 6 days are shown. Dashed line represents cell viability levels at maximum effect of free MMAE or other MMAE conjugates after 6 days (B).

Overall, these results demonstrate that Fcab-drug conjugates promise to be safe and efficacious due to selective cell killing and that tuning the affinity heavily impacts *in vitro* cytotoxicity.

---

## 7.5. 3D Tumor Cell Spheroid Penetration Studies

The estimation of efficacy in animal models based on *in vitro* cytotoxicity data is daring as additional effects need to be considered. For example, Nessler and coworkers studied for various single-domain antibody-drug conjugates the impact of target receptor affinity on *in vitro* potency, biodistribution and *in vivo* efficacy in a solid tumor xenograft model.<sup>189</sup> The construct with the lowest affinity ( $K_D$  0.9 nM versus 0.1 – 0.2 nM), longest internalization half-life ( $t_{1/2}$  66 min versus 21 – 40 min) and lowest *in vitro* potency ( $IC_{50}$  1.4 nM versus 0.2 – 0.3 nM), counterintuitively showed the highest *in vivo* efficacy. Biodistribution profiles revealed that lower affinity of variants increased the tumor penetration and *in vivo* activity.<sup>189</sup> Therefore, it is tempting to speculate that Fcab-drug conjugates may show elevated solid tumor penetration, compared to higher affinity ADC variants.

To study and anticipate tumor penetration in an *in vitro* setup, tumor cell spheroids can be used as model of intermediate complexity for solid tumor tissue.<sup>295</sup> Tumor cell spheroids are multicellular spherical aggregates of cancer cells and exhibit many characteristics of solid tumors e.g., the formation of tight junctions between epithelial cells, the development of an ECM and gradients of nutrient concentration.<sup>295–297</sup>

To setup a tumor cell spheroid penetration model, a cell line screening was performed initially to identify target positive and negative cell lines which form round spheroids at reproducible size. Therefore, cells were seeded at different cell numbers in round-bottom microplates, incubated at 37°C, 5% CO<sub>2</sub> in their typical culturing medium and spheroid growth was monitored by brightfield microscopy (**Figure 37**). Several spheroid forming cell lines were identified (HCC-1954, BT-474, LNCaP, HCC-1937, HCC-1143, A431) that all formed spheroids within 24 h, independent of seeded cell number. Prolonged incubation > 24 h did not result in spheroid formation of SKBR-3, MDA-MB-468 or MCF-7 cells, neither did the addition of 0.3% or 1% (w/v) methylcellulose to MDA-MB-468 or MCF-7 cells.

From studied cell lines, BT-474 (HER2<sup>+</sup>) and HCC-1937 (HER2<sup>-</sup>) formed the most spherical shaped spheroids and were therefore selected for further tumor spheroid cell penetration experiments (**Figure A19**). For these experiments a set of HER2 targeting pHAb-dye conjugates ( $\alpha$ H-FS<sup>C</sup>-pHAb,  $\alpha$ H-S5<sup>C</sup>-pHAb,  $\alpha$ H-S19<sup>C</sup>-pHAb, huFc<sup>K</sup>-pHAb,  $\alpha$ H-T-IgG<sup>C</sup>-pHAb,  $\alpha$ H-T-Fab<sup>C</sup>-pHAb,  $\alpha$ HxH-S5-IgG<sup>C</sup>-pHAb) was applied together with confocal microscopy. pHAb-dye was chosen as fluorophore label because of its favorable signal-to-background ratio and more importantly, because it allows to detect spheroid penetration and intracellular uptake simultaneously (see also section 7.2.2).<sup>290</sup> To quantify spheroid penetration, an analysis strategy was developed to calculate the mean penetration distance (MPD) of pHAb-dye labeled constructs (**Figure 38F**) from radial profile plots (**Figure 38E**) of confocal microscopy spheroid images (**Figure 38C**). For penetration experiments, BT-474 and HCC-1937 spheroids were grown for 96 h from initially 2,000 cells. The resulting

BT-474 spheroids had a diameter of usually 370  $\mu\text{m}$ , which allowed to resolve differences in penetration profiles after incubating the spheroids for 24 h with 50 nM pHAb-dye labeled constructs.

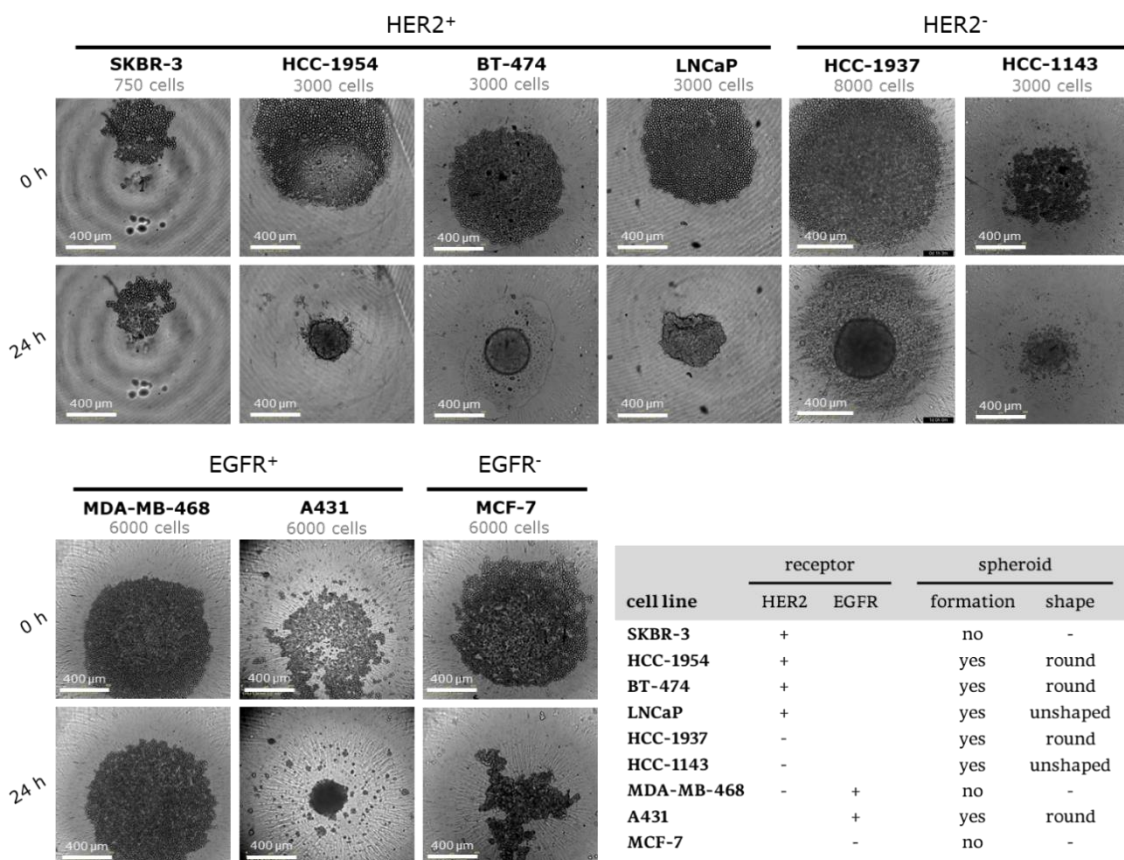


**Figure 37. Spheroid forming cell line screening.** HER2 and EGFR positive and negative cells were seeded without additives into 384 well round-bottom spheroid microplates, centrifuged to center the cells and incubated at 37°C, 5% CO<sub>2</sub> in a cell imaging reader (IncuCyte® S3). Brightfield pictures were taken every 4 h to monitor spheroid formation.

The confocal microscopy focal plane (z-plane) was typically set 60  $\mu\text{m}$  below the top of the spheroid as beyond a depth of approximately 80  $\mu\text{m}$ , fluorescence signals were attenuated in the center of the spheroid which would distort penetration profiles. Signal attenuation is caused by increased light scattering due to the spherical shape and the longer distance that light travels within the center of the spheroid compared to the periphery (**Figure 38B**).

To study the impact of target affinity on penetration and cellular uptake of Fcabs,  $\alpha\text{H-FS}^{\text{C}}$ -pHAb,  $\alpha\text{H-S5}^{\text{C}}$ -pHAb,  $\alpha\text{H-S19}^{\text{C}}$ -pHAb,  $\alpha\text{H-T-Fab}^{\text{C}}$ -pHAb and huFc<sup>K</sup>-pHAb were incubated on HER2 overexpressing BT-474, as well as HER2 negative HCC-1937 spheroids and the distribution of intracellular accumulated constructs was analyzed by fluorescence measurements *via* confocal microscopy (**Figure 39A**). High affinity  $\alpha\text{H-T-Fab}^{\text{C}}$ -pHAb ( $K_{\text{D,BLI}}$  0.12 nM) accumulated in the periphery of the tumor spheroid (MPD  $54 \pm 2 \mu\text{m}$ ). This restricted accumulation is probably caused by extensive binding and internalization which oppose drug

transport towards the center of the spheroid and prevent further penetration – an observation described as “binding site-barrier” in the literature.<sup>170,171</sup> Accordingly, lower affinity variants  $\alpha\text{H-S5}^{\text{C}}\text{-pHAb}$  ( $K_{D,BLI}$  2.25 nM) and  $\alpha\text{H-S19}^{\text{C}}\text{-pHAb}$  ( $K_{D,BLI}$  46.60 nM) demonstrated a more homogenous distribution and elevated MPD ( $69 \pm 2 \mu\text{m}$  and  $63 \pm 4 \mu\text{m}$ ) compared to  $\alpha\text{H-T-Fab}^{\text{C}}\text{-pHAb}$ . In contrast,  $\alpha\text{H-FS}^{\text{C}}\text{-pHAb}$  showed the most homogeneous distribution and highest MPD ( $78 \pm 3 \mu\text{m}$ ) despite its high HER2 affinity ( $K_{D,BLI}$  0.34 nM). The unique receptor degradation mechanism of  $\alpha\text{H-FS}^{\text{C}}\text{-pHAb}$  may lead to decreased endocytotic clearance thereby improving spheroid penetration. When the improved distribution of  $\alpha\text{H-FS}^{\text{C}}\text{-pHAb}$  would overcompensate its reduced cell killing efficacy (**Figure 36**), this could result in homogeneous intra-tumoral concentrations exceeding the single cell therapeutic threshold ( $\text{IC}_{50}$ ). Therefore, it would be interesting to see whether  $\alpha\text{H-FS}^{\text{C}}\text{-pHAb}$  could demonstrate improved *in vivo* efficacy compared to higher affinity variants, e.g.  $\alpha\text{H-T-Fab}^{\text{C}}\text{-pHAb}$  (**Figure 40A, B**).

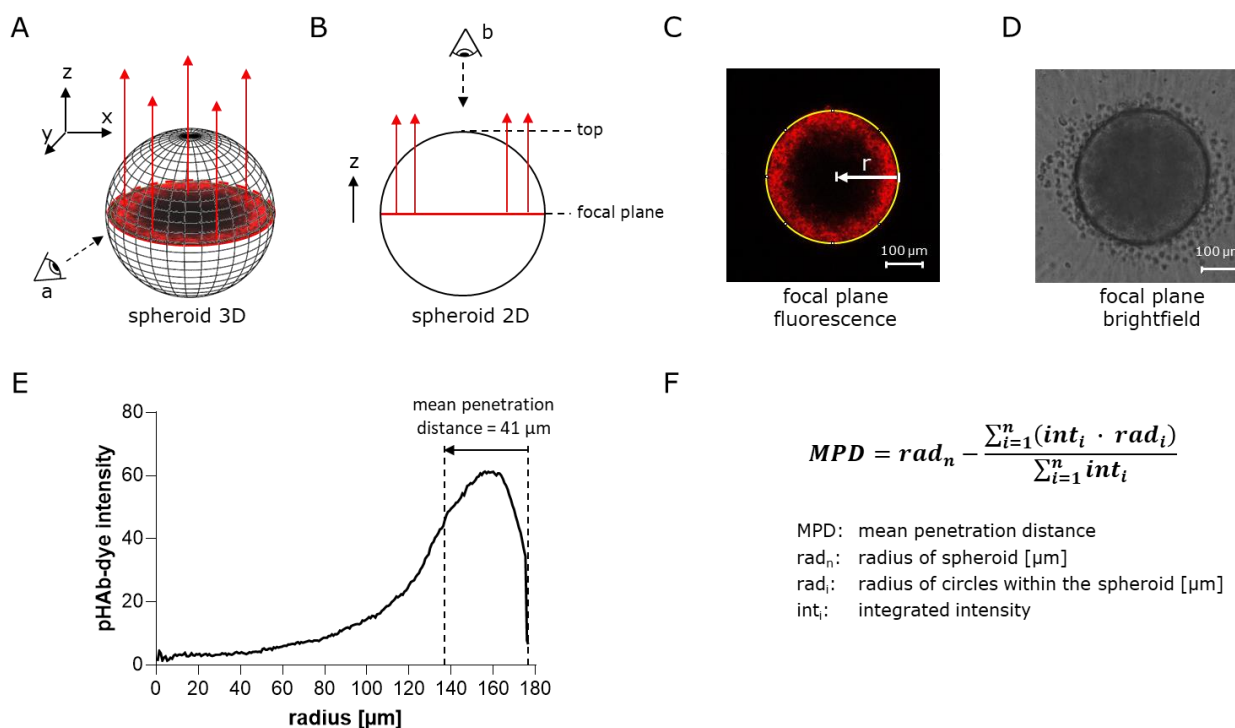


**Figure 38. Quantification strategy for tumor cell spheroid penetration.** (A) Schematic 3D representation of tumor cell spheroid with pHAb-dye fluorescence marked in red. (B) Schematic 2D representation (view a) of tumor cell spheroid with pHAb-dye fluorescence marked in red. (C) Confocal microscopy image of BT-474 spheroid incubated with 50 nM pHAb-dye labeled  $\alpha\text{H-T-IgG}$  for 24 h (view b). The picture was taken 50  $\mu\text{m}$  below the top of the spheroid (z-position). Fluorescence of intracellular accumulated  $\alpha\text{H-T-IgG}^{\text{C}}\text{-pHAb}$  is shown in red. The yellow circle marks the border of the spheroid and was set manually using the radial profile plot plug-in in ImageJ.<sup>272</sup> The radial profile plot plug-in produces a profile plot of normalized integrated intensities around concentric circles as a function of distances from the center of the yellow circle (spheroid) **(D)** Brightfield image of the same spheroid. **(E)** Radial profile plot generated from the BT-474 spheroid by ImageJ. The fluorescence intensity profile of  $\alpha\text{H-T-IgG}^{\text{C}}\text{-pHAb}$  (C) is reflected in the high intensity at larger radii (border of the spheroid). Its limited distribution towards the center of the spheroid produces a sharp decrease of fluorescence intensity towards smaller radii (center of the spheroid). From this radial fluorescence profile, the mean penetration distance (MPD) can be calculated. The MPD allows to compare the spheroid penetration properties of distinct molecules. **(F)** Equation for the calculation of the mean penetration distance from radial profile plots (E).

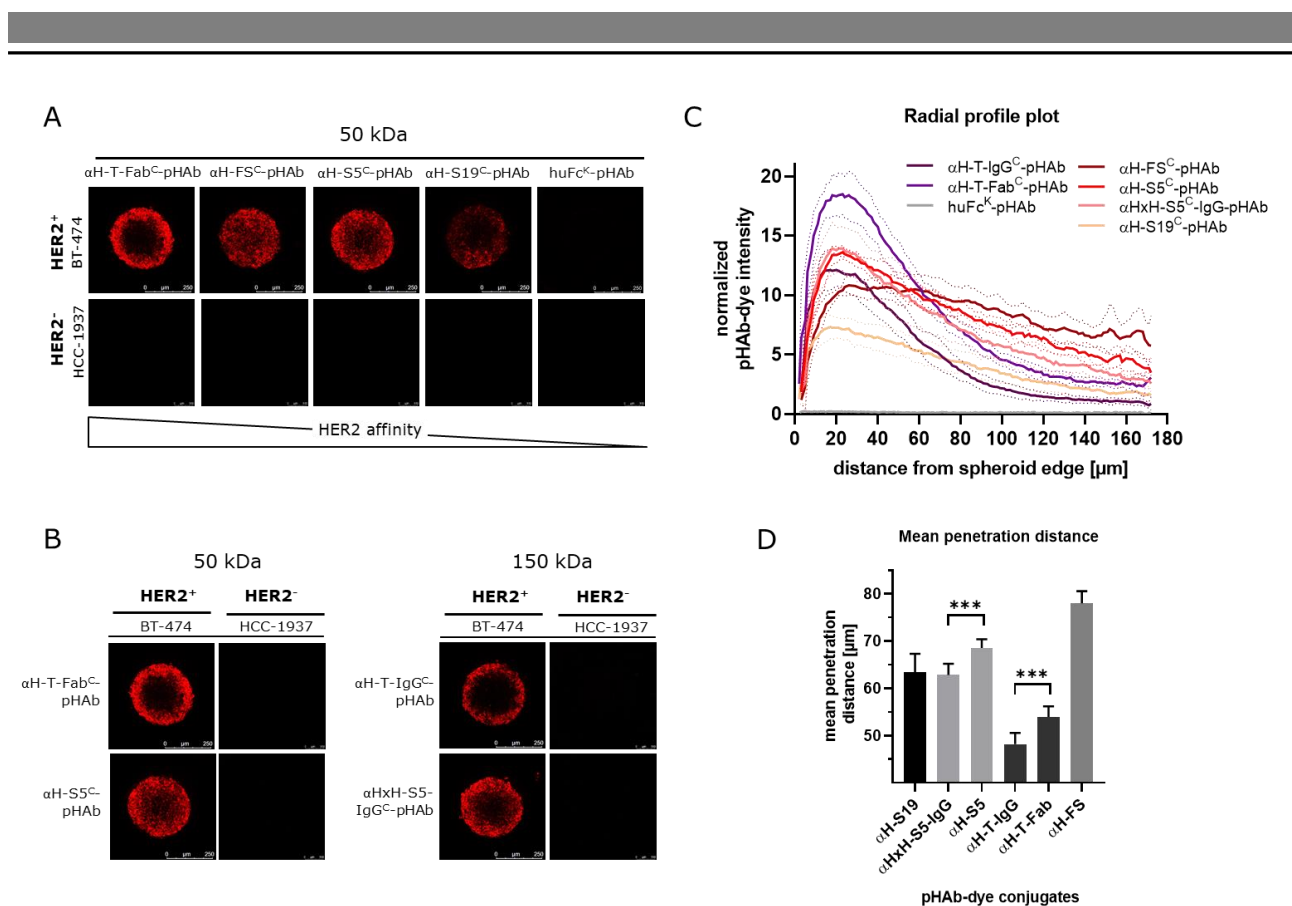


**Figure 39. 3D tumor spheroid penetration model.** (A) Representative confocal microscopy images comparing high affinity versus low affinity distribution of 50 kDa pHAb-dye labeled antibody fragments in HER2 positive BT-474 and HER2 negative HCC-1937 tumor cell spheroids. (B) Representative confocal microscopy images comparing distribution of 50 kDa pHAb-dye labeled antibody fragments versus corresponding 150 kDa IgG variants in BT-474 and HCC-1937 tumor cell spheroids. (C) Radial profile plot derived from confocal microscopy images depicting semiquantitatively the penetration depth. Solid line represents the mean (n = 8 spheroids/group) with SD depicted as dotted lines. Fluorescence intensity was normalized to pHAb-dye DOL. (D) Mean penetration distance (± SD) of 50 kDa antibody fragments and corresponding 150 kDa IgG variants in BT-474 spheroids calculated from radial profile plots (n = 8 spheroids/group). Statistical analysis performed using unpaired, two-tailed t-test, \*\*\* denoted P < 0.001. Spheroids were grown from 2,000 cells for 96 h, incubated for 24 h with 50 nM pHAb-dye labeled constructs and intracellular accumulated pHAb-dye was imaged with a laser scanning confocal microscope (20x). Images were taken at spheroid diameter 341 ± 3 μm and spheroid depth 62 ± 3 μm. Individual spheroid images are depicted in Figure A20. Figure adapted from Jäger *et al.*<sup>277</sup>

Beside αH-FS<sup>C</sup>-pHAb, αH-S5<sup>C</sup>-pHAb showed the highest MPD (69 ± 2 μm), indicating that in these assays a single digit nanomolar binding affinity seems to beneficially balance cellular uptake and spheroid penetration. The importance of the right balance is also evident in negative terms from the greatly reduced intracellular accumulation of αH-S19<sup>C</sup>-pHAb ( $K_{D,BLI}$  46.60 nM) (Figure 39C). Whether the improved distribution profile of αH-S5<sup>C</sup>-pHAb could translate into higher efficacy *in vivo*, depends again on whether increased numbers of targeted cells are exposed to therapeutically active doses of drug (Figure 40C, D). Importantly, no pHAb-dye conjugate showed any signal on HER2 negative HCC-1937 spheroids. Non-targeting huFc<sup>K</sup>-pHAb showed also no signal on BT-474 spheroids.

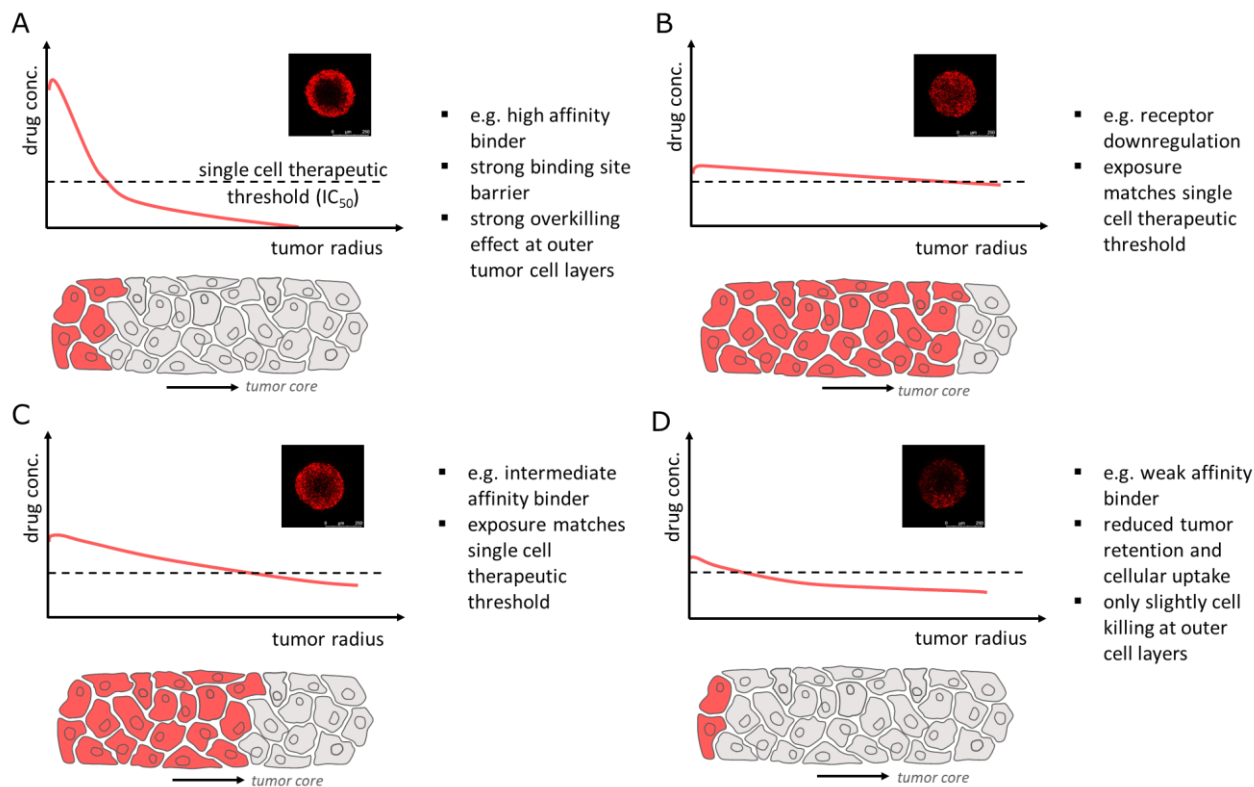


**Figure 40. Hypothetical tumor penetration scenarios derived from spheroid penetration experiments.** The graphic depicts schematically snapshots of different hypothetical scenarios illustrating how experimentally observed tumor spheroid penetration could translate into solid tumor penetration and efficacy if systemic clearance is not limiting. Spheroid images are included for illustration. The single cell therapeutic threshold is set arbitrarily. Tumor cells exposed to drug at concentrations exceeding the single cell therapeutic threshold are marked red. **(A)** High affinity binder showing a pronounced site-barrier effect at the tumor periphery. **(B)** Homogeneous drug distribution. In the depicted scenario the exposure exceeds the single cell therapeutic concentration thereby maximizing efficacy. If concentration in the tumor drops only slightly (below  $IC_{50}$ ), almost no efficacy would be observed. **(C)** Intermediate affinity matches exposure and single cell therapeutic threshold. **(D)** Low affinity binder does not efficiently accumulate at concentrations exceeding the therapeutic threshold at the tumor site resulting in poor efficacy.

As described in section 4.5.2, tumor penetration depends not only on the affinity of a construct, but also on its hydrodynamic radius.<sup>177</sup> 50 kDa Fcabs have an approximately 40% reduced hydrodynamic radius compared to 150 kDa IgG molecules ( $r_H$  3.1 – 3.2 nm *versus* 5.5 nm) (**Table 8**). To elaborate the penetration benefit of Fcabs accounted only to reduced size, the penetration profile of  $\alpha H-S5^C$ -pHAb was compared to a 150 kDa  $\alpha H-S5$  derivative with unrelated anti-HEL Fab arms ( $\alpha HxH-S5-IgG^C$ -pHAb). 50 kDa  $\alpha H-T-Fab^C$ -pHAb and 150 kDa  $\alpha H-T-IgG^C$ -pHAb references were included in these experiments although biased by avidity resulting from  $\alpha H-T-IgG^C$ -pHAb bivalency (**Figure 39B, C**). Smaller-sized  $\alpha H-S5^C$ -pHAb penetrated deeper into BT-474 spheroids (MPD  $69 \pm 2 \mu m$ ) compared to  $\alpha HxH-S5-IgG^C$ -pHAb (MPD  $63 \pm 2 \mu m$ ) confirming the penetration advantage resulting from reduced hydrodynamic radius (**Figure 39D**).

The MPD gain accounted to smaller size ( $\Delta MPD$  6  $\mu m$ ;  $\Delta r_H$  2.3 nm) was inferior to the gain from lower affinity ( $\Delta MPD$  15  $\mu m$ ;  $\alpha H-S5^C$ -pHAb  $K_{D,BLI}$  2.25 nM *versus*  $\alpha H-T-Fab^C$ -pHAb  $K_{D,BLI}$  0.12 nM), suggesting that in this

---

simplified *in vitro* model tumor spheroid penetration is more affected by affinity than by a limited variation in size. The observed relationship is consistent with the analytical derivation of the dependence between maximum penetration depth  $R$  and hydrodynamic radius  $r_H$ , as well as affinity ( $K_D$ ):<sup>171</sup>

$$R \sim \sqrt{\frac{K_D}{r_H}} \quad (15)$$

Equation (15) was derived from equation (3) and (5) in section 4.5.2 and indicates that a higher  $K_D$  value by e.g., factor 18.8 ( $\alpha$ H-S5<sup>C</sup>-pHAb  $K_{D,BLI}$  2.25 nM *versus*  $\alpha$ H-T-Fab<sup>C</sup>-pHAb  $K_{D,BLI}$  0.12 nM) increases  $R$  to a greater extent than a reduced hydrodynamic radius by e.g., factor 1.7 (Fcab  $r_H$  3.1 – 3.2 nm *versus* IgG  $r_H$  5.5 nm). As expected, the bivalent  $\alpha$ H-T-IgG<sup>C</sup>-pHAb reference conjugate (MPD  $48 \pm 2 \mu\text{m}$ ) showed a binding site-barrier effect that was more pronounced compared to monovalent  $\alpha$ H-T-Fab<sup>C</sup>-pHAb (MPD  $54 \pm 2 \mu\text{m}$ ). It remains unclear whether this is mainly due to avidity in binding to cellular HER2 or increased size of bivalent  $\alpha$ H-T-IgG<sup>C</sup>-pHAb.

Taken together, improved penetration capability of  $\alpha$ H-S5<sup>C</sup>-pHAb,  $\alpha$ H-S19<sup>C</sup>-pHAb and  $\alpha$ H-FS<sup>C</sup>-pHAb compared to  $\alpha$ H-T-Fab<sup>C</sup>-pHAb and  $\alpha$ H-T-IgG<sup>C</sup>-pHAb was demonstrated resulting from fine-tuned lower affinity, smaller size and an intrinsic receptor degradation mechanism. Whether this effect translates into better efficacy *in vivo* needs to be investigated in carefully designed animal models considering additional effects such as systemic clearance and tumor tissue extravasation.

---

---

## 8. Conclusion

---

The aim of the work presented herein was to evaluate for the first time Fcabs as novel ADC scaffold by assessing the generation and functionality of Fcab-based drug conjugates.

Fcabs incorporate an engineered antigen binding and half-life extending native FcRn binding site in a small ~ 50 kDa Fc fragment. This combination provides Fcabs with the potential to enhance efficacy of conventional IgG-based ADCs in solid tumors by increasing tumor exposure due to a smaller size accounting for better tumor penetration and a favorable pharmacokinetics profile.

For proof of concept, an initial literature search yielded seven distinct HER2- or EGFR-targeting Fcabs that were considered as relevant for solid tumor indications and thus, selected for the feasibility study. Fcab scaffolds were genetically engineered to attenuate FcγR binding (D265A) and to enable site-specific conjugation (N-terminal mTG tags, D265C). The expression yields and thermostability of Fcabs were inferior to human Fc controls lacking the engineered antigen binding site but still acceptable. For all Fcab scaffold variants, target- and affinity-dependent cell binding could be verified on several cancer cell lines. To study the cellular uptake as a prerequisite for the targeting molecule of an ADC, Fcabs were labeled *via* random lysine coupling or interchain cysteines with a pH sensitive dye that becomes fluorescent only at acidic pH present in endosomal and lysosomal vesicles after internalization. All selected Fcabs showed receptor-mediated endocytosis which classified them as possible ADC targeting vehicles and allowed for their conjugation to cytotoxic linker-drugs. Fcabs were successfully conjugated at different positions (native Q295, N-terminally, D265C) to the clinically validated microtubule inhibitor Val-Cit-MMAE employing microbial transglutaminase or cysteine coupling techniques. Two additional unknown conjugation sites within the EGFR-targeting Fcab scaffolds could be identified as glutamine Q311 and Q438 leading to an unexpected high DAR of ~ 2.9 for these constructs. The MMAE conjugates were profiled for their hydrophobicity, target and FcRn binding kinetics as well as serum stability. No undesirable impact on the Fcab binding properties was observed for any conjugation site. For the Fcab scaffold, conjugation to native Q295 seems to be very well suited due to high conjugation efficiency and the generation of homogenous, stable and functional Fcab-drug conjugates. Moreover, Q295 coupled conjugates showed lower overall hydrophobicity compared to N-terminally or C265 coupled conjugates. Subsequently, target-dependent cytotoxicity was demonstrated for all generated Fcab-MMAE conjugates with  $IC_{50}$  values ranging from sub-nanomolar to double digit nanomolar concentrations, depending on target affinity of the Fcab.

In addition, a 3D tumor cell spheroid model was set up to anticipate the impact of target affinity and molecular size on tumor penetration. Target binding affinity could be confirmed as more critical for penetration than the reduction in size. Using this model, an Fcab with single digit nanomolar HER2 affinity

---

( $\alpha$ H-S5) showed a favorable balance between spheroid penetration and cellular uptake. Moreover, the same 50 kDa Fcab demonstrated enhanced spheroid penetration compared to its 150 kDa derivative with unrelated Fab arms or to clinically applied Trastuzumab. The most homogeneous spheroid distribution was observed for an Fcab ( $\alpha$ H-FS) that induced profound HER2 degradation highlighting the positive effect of reduced endocytotic uptake on spheroid penetration. Whether the beneficial spheroid penetration of Fcabs translates into improved overall tumor exposure for Fcab-drug conjugates and ultimately a better efficacy than IgG-based ADCs in solid tumors, needs to be evaluated in carefully designed *in vivo* xenograft studies. Taken together, the herein presented work emphasizes the Fcab format as novel scaffold for the generation of drug conjugates illustrating the functionality and the potential of Fcab-drug conjugates as new therapeutic modality.

---

---

## 9. Outlook

---

### 9.1. Solid Tumor Penetration and Efficacy Predictions by Mechanistic Modelling

Predictions on solid tumor disposition of protein therapeutics from classical simulation approaches unfortunately do not apply to Fcabs, since such simulations assume extremely short half-lives for 50 kDa sized molecules.<sup>79,177</sup> Currently, there exist no modeling data that predicts or excludes an improved solid tumor exposure for Fcabs or a comparable scaffold. To justify a further development of this format, modeling data or *in vivo* experiments supporting the projected potential are urgently needed. From a developer's point of view, a mechanistic model would be more beneficial for conceptual understanding and more ethically justifiable than animal studies at this early stage of development.

Over the last five years, mechanistic models for ADC tumor distribution<sup>108,162</sup> and *in vivo* efficacy<sup>159–161</sup> have been developed whose predictions have become increasingly accurate as shown by comparison with experimental data by these authors. A strength of these models is that every mechanistic step is based on experimentally determined data (e.g. target expression levels) and rate constants (e.g., target turnover, linker cleavage).

To better understand the influence of size, intermediate half-life and affinity on Fcab tumor distribution each individually but also in dependency to each other, a mechanistic model would be tremendously helpful. In order to maximize efficacy, a model would allow to identify key factors that limit tumor penetration of Fcab-drug conjugates and to adjust for example, the Fcab affinity or half-life (e.g. by introducing a half-life extending M252Y, S254T, T256E “YTE” mutation<sup>298</sup>) according to a certain solid tumor type. Guided by modelling data, fine-tuned Fcab-drug conjugates could be designed and generated in a more rational way. To finally prove the potential of Fcab-drug conjugates and to verify results from modelling and simulation, the most promising candidates should be tested in carefully designed animal studies.

### 9.2. *In Vivo* Evaluation of Fcab-Drug Conjugates

The *in vivo* concept evaluation follows two principle strategies and can be either performed by (1) tumor distribution or (2) tumor shrinkage studies. In both studies, xenograft models would be selected, and the tumor cells transplanted into immunodeficient mice. Animals would then be treated with the Fcab-drug and reference conjugates. Depending on the evaluation strategy, tumors would be either cut out to analyze tumor sections for conjugate distribution or remain implanted to monitor tumor size over the period of treatment. Both studies can be supported by an initial pharmacokinetics study to determine Fcab-drug conjugate plasma half-life and possibly refine modelling input data and dosing schedules.

Different study designs are conceivable. For example, a 50 kDa Fcab-drug conjugate could be compared to its 150 kDa (Fab)<sub>2</sub>-Fcab-drug conjugate derivative with unrelated Fab arms to assess the impact of reduced size on tumor distribution or growth. Similarly, an Fcab-drug conjugate could be compared to its FcRn-silenced analog (e.g. I253A, H310A, H435A mutation<sup>79,299</sup>) to elucidate the impact of extended half-life. IgG-based ADCs could be included as references in all studies to rank Fcab-drug conjugates according to established technologies.

### 9.3. Cleavable (Fab)<sub>2</sub>-Fcab-drug conjugates – Reducing Size Right at the Tumor Site

If the intermediate plasma half-life ( $t_{1/2,\beta}$  60 – 85 h in mice) of Fcabs is still too short to expose the tumor to a therapeutically active concentration for a sufficiently long time, a modified molecular design may provide a solution. For this, Fab arms could be fused onto the Fcab scaffold obtaining an IgG-like antibody format (termed mAb<sup>2</sup>) that should have a circulatory half-life in the range of classical antibodies due to an increased molecular size. To not lose advantages for tumor penetration resulting from Fcabs' small size, a protease recognition site can be engineered into the hinge region that allows for specific proteolytic cleavage by extracellular proteases upregulated in the tumor microenvironment (**Figure 41**).<sup>286</sup> The molecule would benefit from the long plasma half-life of the circulating (Fab)<sub>2</sub>-Fcab fusion until it reaches the tumor site where small Fcab- and Fab-drug conjugates are released upon proteolytic cleavage. Subsequently, the small fragments would penetrate deeper into the solid tumor mass.

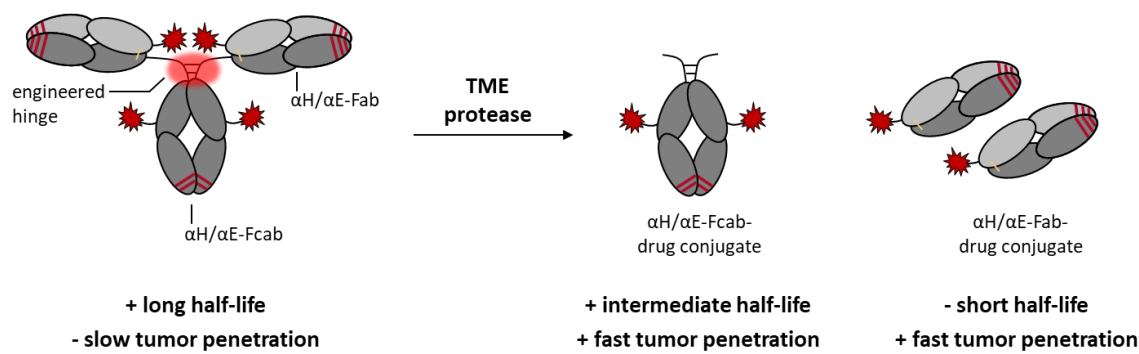


**Figure 41. Proposed tetraivalent (Fab)<sub>2</sub>-Fcab fusions with engineered hinge cleavage site.** The hinge region contains an engineered cleavage site that is specifically recognized by extracellular proteases (matriptase and uPA) upregulated in the tumor microenvironment (TME). Hinge cleavage results in the release of two 50 kDa Fab-drug conjugates and one 50 kDa Fcab-drug conjugate at the tumor site. Released fragment-drug conjugates should show improved solid tumor penetration compared to the tetraivalent 150 kDa parent mAb<sup>2</sup>.

In a feasibility study conducted by Roßkopf, a matriptase and uPA cleavage site<sup>300</sup> was genetically engineered into the hinge region of Trastuzumab.<sup>286</sup> The biophysical behavior and target binding of the engineered antibody was similar to its unmodified form and specific enzymatic Fab release demonstrated protease

---

accessibility and validated the functionality of the *de novo* antibody design.<sup>286</sup> Initial experiments suggest that analog molecules based on Trastuzumab Fab arms fused to the Fcabs STAB5 or STAB19 efficiently release Fab fragments and the Fcab upon matriptase and uPA digestion (**Figure A21**).

---

## 10. References

---

1. World Health Organization. *WHO Report on Cancer: setting priorities, investing wisely and providing care for all.* (2020).
2. Dillekås, H., Rogers, M. S. & Straume, O. Are 90% of deaths from cancer caused by metastases? *Cancer Med.* **8**, 5574–5576 (2019).
3. Loeb, L. A., Loeb, K. R. & Anderson, J. P. Multiple mutations and cancer. *Proc. Natl. Acad. Sci. U. S. A.* **100**, 776–781 (2003).
4. Hanahan, D. & Weinberg, R. A. The Hallmarks of Cancer. *Cell* **100**, 57–70 (2000).
5. Hanahan, D. & Weinberg, R. A. Hallmarks of Cancer: The Next Generation. *Cell* **144**, 646–674 (2011).
6. Negrini, S., Gorgoulis, V. G. & Halazonetis, T. D. Genomic instability an evolving hallmark of cancer. *Nat. Rev. Mol. Cell Biol.* **11**, 220–228 (2010).
7. Ford, D., Easton, D. F., Bishop, D. T., Narod, S. A. & Goldgar, D. E. Risks of cancer in BRCA1-mutation carriers. *Lancet* **343**, 692–695 (1994).
8. Ford, D. *et al.* Genetic Heterogeneity and Penetrance Analysis of the BRCA1 and BRCA2 Genes in Breast Cancer Families. *Am. J. Hum. Genet.* **62**, 676–689 (1998).
9. Sjöblom, T. *et al.* The consensus coding sequences of human breast and colorectal cancers. *Science* **314**, 268–274 (2006).
10. Wood, L. D. *et al.* The Genomic Landscapes of Human Breast and Colorectal Cancers. *Science* **318**, 1108–1113 (2007).
11. Jones, S. *et al.* Core Signaling Pathways in Human Pancreatic Cancers Revealed by Global Genomic Analyses. *Science* **321**, 1801–1806 (2008).
12. Parsons, D. W. *et al.* An Integrated Genomic Analysis of Human Glioblastoma Multiforme. *Science* **321**, 1807–1812 (2008).
13. Halazonetis, T. D., Gorgoulis, V. G. & Bartek, J. An oncogene-induced DNA damage model for cancer development. *Science* **319**, 1352–1355 (2008).
14. Lane, D. P. p53, guardian of the genome. *Nature* **358**, 15–16 (1992).
15. Gorgoulis, V. G. *et al.* Activation of the DNA damage checkpoint and genomic instability in human precancerous lesions. *Nature* **434**, 907–913 (2005).
16. Bartkova, J. *et al.* DNA damage response as a candidate anti-cancer barrier in early human tumorigenesis. *Nature* **434**, 864–870 (2005).
17. Olivier, M., Hollstein, M. & Hainaut, P. TP53 Mutations in Human Cancers: Origins, Consequences, and Clinical Use. *Cold Spring Harb. Perspect. Biol.* **2**, a001008–a001008 (2010).
18. Kandoth, C. *et al.* Mutational landscape and significance across 12 major cancer types. *Nature* **502**, 333–339 (2013).
19. Dvorak, H. F. Tumors: Wounds that do not heal-redux. *Cancer Immunol. Res.* **3**, 1–11 (2015).
20. Sporn, M. B. & Todaro, G. J. Autocrine secretion and malignant transformation of cells. *N. Engl. J. Med.* **303**, 878–880 (1980).
21. Cheng, N., Chytil, A., Shyr, Y., Joly, A. & Moses, H. L. Transforming growth factor-beta signaling-deficient fibroblasts enhance hepatocyte growth factor signaling in mammary carcinoma cells to promote scattering and invasion. *Mol. Cancer Res.* **6**, 1521–1533 (2008).

- 
22. DeSantis, C. E. *et al.* Breast cancer statistics, 2019. *CA. Cancer J. Clin.* **69**, 438–451 (2019).
  23. Harbeck, N. *et al.* Breast cancer. *Nat. Rev. Dis. Prim.* **5**, 66 (2019).
  24. Thomas, R. & Weihua, Z. Rethink of EGFR in Cancer With Its Kinase Independent Function on Board. *Front. Oncol.* **9**, 800 (2019).
  25. Yan, M. *et al.* HER2 expression status in diverse cancers: review of results from 37,992 patients. *Cancer Metastasis Rev.* **34**, 157–164 (2015).
  26. Shay, J. W. & Wright, W. E. Hayflick, his limit, and cellular ageing. *Nat. Rev. Mol. Cell Biol.* **1**, 72–76 (2000).
  27. Kim, N. W. *et al.* Specific association of human telomerase activity with immortal cells and cancer. *Science* **266**, 2011–2015 (1994).
  28. Hanahan, D. & Folkman, J. Patterns and emerging mechanisms of the angiogenic switch during tumorigenesis. *Cell* **86**, 353–364 (1996).
  29. Berx, G. & van Roy, F. Involvement of members of the cadherin superfamily in cancer. *Cold Spring Harb. Perspect. Biol.* **1**, a003129 (2009).
  30. Tabariès, S. & Siegel, P. M. The role of claudins in cancer metastasis. *Oncogene* **36**, 1176–1190 (2017).
  31. Talmadge, J. E. & Fidler, I. J. AACR Centennial Series: The Biology of Cancer Metastasis: Historical Perspective. *Cancer Res.* **70**, 5649–5669 (2010).
  32. Fadaka, A. *et al.* Biology of glucose metabolism in cancer cells. *J. Oncol. Sci.* **3**, 45–51 (2017).
  33. Dunn, G. P., Old, L. J. & Schreiber, R. D. The three Es of cancer immunoediting. *Annu. Rev. Immunol.* **22**, 329–360 (2004).
  34. Chen, D. S., Irving, B. A. & Hodi, F. S. Molecular Pathways: Next-Generation Immunotherapy—Inhibiting Programmed Death-Ligand 1 and Programmed Death-1. *Clin. Cancer Res.* **18**, 6580–6587 (2012).
  35. Duan, Q., Zhang, H., Zheng, J. & Zhang, L. Turning Cold into Hot: Firing up the Tumor Microenvironment. *Trends in Cancer* **6**, 605–618 (2020).
  36. Anderson, N. M. & Simon, M. C. The tumor microenvironment. *Curr. Biol.* **30**, R921–R925 (2020).
  37. Dagogo-Jack, I. & Shaw, A. T. Tumour heterogeneity and resistance to cancer therapies. *Nat. Rev. Clin. Oncol.* **15**, 81–94 (2018).
  38. Cleary, A. S., Leonard, T. L., Gestl, S. A. & Gunther, E. J. Tumour cell heterogeneity maintained by cooperating subclones in Wnt-driven mammary cancers. *Nature* **508**, 113–117 (2014).
  39. Balkwill, F. R., Capasso, M. & Hagemann, T. The tumor microenvironment at a glance. *J. Cell Sci.* **125**, 5591–5596 (2012).
  40. Sahai, E. *et al.* A framework for advancing our understanding of cancer-associated fibroblasts. *Nat. Rev. Cancer* **20**, 174–186 (2020).
  41. Naito, H., Iba, T. & Takakura, N. Mechanisms of new blood-vessel formation and proliferative heterogeneity of endothelial cells. *Int. Immunol.* **32**, 295–305 (2020).
  42. Ribatti, D., Nico, B., Crivellato, E. & Vacca, A. The structure of the vascular network of tumors. *Cancer Lett.* **248**, 18–23 (2007).
  43. De Palma, M., Biziato, D. & Petrova, T. V. Microenvironmental regulation of tumour angiogenesis. *Nat. Rev. Cancer* **17**, 457–474 (2017).

- 
44. Sevick, E. M. & Jain, R. K. Geometric resistance to blood flow in solid tumors perfused ex vivo: effects of tumor size and perfusion pressure. *Cancer Res.* **49**, 3506–3512 (1989).
  45. Dewhirst, M. W. & Secomb, T. W. Transport of drugs from blood vessels to tumour tissue. *Nat. Rev. Cancer* **17**, 738–750 (2017).
  46. Hashizume, H. *et al.* Openings between Defective Endothelial Cells Explain Tumor Vessel Leakiness. *Am. J. Pathol.* **156**, 1363–1380 (2000).
  47. Fitzgerald, G., Soro-Arnaiz, I. & De Bock, K. The Warburg Effect in Endothelial Cells and its Potential as an Anti-angiogenic Target in Cancer. *Front. Cell Dev. Biol.* **6**, 100 (2018).
  48. Padera, T. P. *et al.* Cancer cells compress intratumour vessels. *Nature* **427**, 695–695 (2004).
  49. Padera, T. P. *et al.* Lymphatic metastasis in the absence of functional intratumor lymphatics. *Science* **296**, 1883–1886 (2002).
  50. Wartiovaara, U. *et al.* Peripheral Blood Platelets Express VEGF-C and VEGF which Are Released during Platelet Activation. *Thromb. Haemost.* **80**, 171–175 (1998).
  51. Schoppmann, S. F. *et al.* VEGF-C expressing tumor-associated macrophages in lymph node positive breast cancer: impact on lymphangiogenesis and survival. *Surgery* **139**, 839–846 (2006).
  52. Mohammed, R. A. A. *et al.* Prognostic significance of vascular endothelial cell growth factors -A, -C and -D in breast cancer and their relationship with angio- and lymphangiogenesis. *Br. J. Cancer* **96**, 1092–1100 (2007).
  53. Neuchrist, C. *et al.* Vascular endothelial growth factor C and vascular endothelial growth factor receptor 3 expression in squamous cell carcinomas of the head and neck. *Head Neck* **25**, 464–474 (2003).
  54. Stylianopoulos, T., Munn, L. L. & Jain, R. K. Reengineering the Physical Microenvironment of Tumors to Improve Drug Delivery and Efficacy: From Mathematical Modeling to Bench to Bedside. *Trends in Cancer* **4**, 292–319 (2018).
  55. Heldin, C.-H., Rubin, K., Pietras, K. & Östman, A. High interstitial fluid pressure - an obstacle in cancer therapy. *Nat. Rev. Cancer* **4**, 806–813 (2004).
  56. Henke, E., Nandigama, R. & Ergün, S. Extracellular Matrix in the Tumor Microenvironment and Its Impact on Cancer Therapy. *Front. Mol. Biosci.* **6**, 1–24 (2020).
  57. Wei, S. C. *et al.* Matrix stiffness drives epithelial–mesenchymal transition and tumour metastasis through a TWIST1–G3BP2 mechanotransduction pathway. *Nat. Cell Biol.* **17**, 678–688 (2015).
  58. Rice, A. J. *et al.* Matrix stiffness induces epithelial–mesenchymal transition and promotes chemoresistance in pancreatic cancer cells. *Oncogenesis* **6**, e352–e352 (2017).
  59. Falzone, L., Salomone, S. & Libra, M. Evolution of Cancer Pharmacological Treatments at the Turn of the Third Millennium. *Front. Pharmacol.* **9**, 1300 (2018).
  60. Urruticoechea, A. *et al.* Recent Advances in Cancer Therapy: An Overview. *Curr. Pharm. Des.* **16**, 3–10 (2009).
  61. Baumann, M. *et al.* Radiation oncology in the era of precision medicine. *Nat. Rev. Cancer* **16**, 234–249 (2016).
  62. DeVita, V. T. & Chu, E. A history of cancer chemotherapy. *Cancer Res.* **68**, 8643–8653 (2008).
  63. Kaye, S. B. New antimetabolites in cancer chemotherapy and their clinical impact. *Br. J. Cancer* **78**, 1–7 (1998).

- 
64. Zhou, J. & Giannakakou, P. Targeting Microtubules for Cancer Chemotherapy. *Curr. Med. Chem. Agents* **5**, 65–71 (2005).
  65. Yardley, D. A. Drug Resistance and the Role of Combination Chemotherapy in Improving Patient Outcomes. *Int. J. Breast Cancer* **2013**, 1–15 (2013).
  66. Schirrmacher, V. From chemotherapy to biological therapy: A review of novel concepts to reduce the side effects of systemic cancer treatment. *Int. J. Oncol.* **54**, 407–419 (2019).
  67. Talwar, V., Pradeep Babu, K. V. & Raina, S. An overall review of targeted therapy in solid cancers. *Curr. Med. Res. Pract.* **7**, 99–105 (2017).
  68. Tarcsa, E., Guffroy, M. R., Falahatpisheh, H., Phipps, C. & Kalvass, J. C. Antibody-drug conjugates as targeted therapies: Are we there yet? A critical review of the current clinical landscape. *Drug Discov. Today Technol.* (2020) doi:10.1016/j.ddtec.2020.07.002.
  69. Ledford, H., Else, H. & Warren, M. Cancer immunologists scoop medicine Nobel prize. *Nature* **562**, 20–21 (2018).
  70. Ribas, A. & Wolchok, J. D. Cancer immunotherapy using checkpoint blockade. *Science* **359**, 1350–1355 (2018).
  71. Ke, X. & Shen, L. Molecular targeted therapy of cancer: The progress and future prospect. *Front. Lab. Med.* **1**, 69–75 (2017).
  72. Vidarsson, G., Dekkers, G. & Rispens, T. IgG subclasses and allotypes: From structure to effector functions. *Front. Immunol.* **5**, 1–17 (2014).
  73. Harris, L. J., Larson, S. B., Hasel, K. W. & McPherson, A. Refined structure of an intact IgG2a monoclonal antibody. *Biochemistry* **36**, 1581–1597 (1997).
  74. Lobner, E., Traxlmayr, M. W., Obinger, C. & Hasenhindl, C. Engineered IgG1-Fc - one fragment to bind them all. *Immunol. Rev.* **270**, 113–131 (2016).
  75. Ryman, J. T. & Meibohm, B. Pharmacokinetics of Monoclonal Antibodies. *CPT Pharmacometrics Syst. Pharmacol.* **6**, 576–588 (2017).
  76. Roopenian, D. C. *et al.* The MHC Class I-Like IgG Receptor Controls Perinatal IgG Transport, IgG Homeostasis, and Fate of IgG-Fc-Coupled Drugs. *J. Immunol.* **170**, 3528–3533 (2003).
  77. Chaudhury, C. *et al.* The major histocompatibility complex-related Fc receptor for IgG (FcRn) binds albumin and prolongs its lifespan. *J. Exp. Med.* **197**, 315–322 (2003).
  78. Kim, J., Hayton, W. L., Robinson, J. M. & Anderson, C. L. Kinetics of FcRn-mediated recycling of IgG and albumin in human: Pathophysiology and therapeutic implications using a simplified mechanism-based model. *Clin. Immunol.* **122**, 146–155 (2007).
  79. Li, Z. *et al.* Effect of size on solid tumor disposition of protein therapeutics. *Drug Metab. Dispos.* **47**, 1136–1145 (2019).
  80. Roopenian, D. C. & Akilesh, S. FcRn: The neonatal Fc receptor comes of age. *Nat. Rev. Immunol.* **7**, 715–725 (2007).
  81. Oganessian, V. *et al.* Structural Insights into Neonatal Fc Receptor-based Recycling Mechanisms. *J. Biol. Chem.* **289**, 7812–7824 (2014).
  82. Hynes, N. E. & MacDonald, G. ErbB receptors and signaling pathways in cancer. *Curr. Opin. Cell Biol.* **21**, 177–184 (2009).
  83. Ciardiello, F. & Tortora, G. EGFR Antagonists in Cancer Treatment. *N. Engl. J. Med.* **358**, 1160–1174 (2008).

- 
84. Yarden, Y. Biology of HER2 and its importance in breast cancer. *Oncology* **61**, 1–13 (2001).
  85. Graus-Porta, D., Beerli, R. R., Daly, J. M. & Hynes, N. E. ErbB-2, the preferred heterodimerization partner of all ErbB receptors, is a mediator of lateral signaling. *EMBO J.* **16**, 1647–1655 (1997).
  86. Wiley, H. S. Trafficking of the ErbB receptors and its influence on signaling. in *The EGF Receptor Family* 81–91 (Elsevier, 2003). doi:10.1016/B978-012160281-9/50007-4.
  87. Wiley, H. S. *et al.* The role of tyrosine kinase activity in endocytosis, compartmentation, and down-regulation of the epidermal growth factor receptor. *J. Biol. Chem.* **266**, 11083–11094 (1991).
  88. Chang, C. P. *et al.* Ligand-induced internalization of the epidermal growth factor receptor is mediated by multiple endocytic codes analogous to the tyrosine motif found in constitutively internalized receptors. *J. Biol. Chem.* **268**, 19312–19320 (1993).
  89. Resat, H., Ewald, J. A., Dixon, D. A. & Wiley, H. S. An integrated model of epidermal growth factor receptor trafficking and signal transduction. *Biophys. J.* **85**, 730–743 (2003).
  90. Stoscheck, C. M. & Carpenter, G. Down regulation of epidermal growth factor receptors: direct demonstration of receptor degradation in human fibroblasts. *J. Cell Biol.* **98**, 1048–1053 (1984).
  91. Beguinot, L., Lyall, R. M., Willingham, M. C. & Pastan, I. Down-regulation of the epidermal growth factor receptor in KB cells is due to receptor internalization and subsequent degradation in lysosomes. *Proc. Natl. Acad. Sci.* **81**, 2384–2388 (1984).
  92. Stoscheck, C. M. & Carpenter, G. Characterization of the metabolic turnover of epidermal growth factor receptor protein in A-431 cells. *J. Cell. Physiol.* **120**, 296–302 (1984).
  93. Baulida, J., Kraus, M. H., Alimandi, M., Di Fiore, P. P. & Carpenter, G. All ErbB receptors other than the epidermal growth factor receptor are endocytosis impaired. *J. Biol. Chem.* **271**, 5251–5257 (1996).
  94. Bou-Assaly, W. & Mukherji, S. Cetuximab (Erbix). *Am. J. Neuroradiol.* **31**, 626–627 (2010).
  95. Sunada, H., Magun, B. E., Mendelsohn, J. & MacLeod, C. L. Monoclonal antibody against epidermal growth factor receptor is internalized without stimulating receptor phosphorylation. *Proc. Natl. Acad. Sci. U. S. A.* **83**, 3825–3829 (1986).
  96. Sunada, H., Yu, P., Peacock, J. S. & Mendelsohn, J. Modulation of tyrosine, serine, and threonine phosphorylation and intracellular processing of the epidermal growth factor receptor by antireceptor monoclonal antibody. *J. Cell. Physiol.* **142**, 284–292 (1990).
  97. Adams, G. P. & Weiner, L. M. Monoclonal antibody therapy of cancer. *Nat. Biotechnol.* **23**, 1147–1157 (2005).
  98. Molina, M. A. *et al.* Trastuzumab (herceptin), a humanized anti-Her2 receptor monoclonal antibody, inhibits basal and activated Her2 ectodomain cleavage in breast cancer cells. *Cancer Res.* **61**, 4744–4749 (2001).
  99. Ram, S., Kim, D., Ober, R. J. & Ward, E. S. The level of HER2 expression is a predictor of antibody-HER2 trafficking behavior in cancer cells. *MAbs* **6**, 1211–1219 (2014).
  100. Hudis, C. A. Trastuzumab - Mechanism of action and use in clinical practice. *N. Engl. J. Med.* **357**, 39–51 (2007).
  101. Li, S. *et al.* Structural basis for inhibition of the epidermal growth factor receptor by cetuximab. *Cancer Cell* **7**, 301–311 (2005).
  102. Stamos, J., Sliwkowski, M. X. & Eigenbrot, C. Structure of the Epidermal Growth Factor Receptor Kinase Domain Alone and in Complex with a 4-Anilinoquinazoline Inhibitor. *J. Biol. Chem.* **277**, 46265–46272 (2002).

- 
103. Lu, C. *et al.* Structural Evidence for Loose Linkage between Ligand Binding and Kinase Activation in the Epidermal Growth Factor Receptor. *Mol. Cell. Biol.* **30**, 5432–5443 (2010).
  104. Cho, H.-S. *et al.* Structure of the extracellular region of HER2 alone and in complex with the Herceptin Fab. *Nature* **421**, 756–760 (2003).
  105. Clynes, R. A., Towers, T. L., Presta, L. G. & Ravetch, J. V. Inhibitory Fc receptors modulate in vivo cytotoxicity against tumor targets. *Nat. Med.* **6**, 443–446 (2000).
  106. Mullard, A. FDA approves ADC Therapeutics' loncastuximab tesirine, ushering in a new cytotoxic payload. *Nat. Rev. Drug Discov.* **20**, 414–414 (2021).
  107. Staudacher, A. H. & Brown, M. P. Antibody drug conjugates and bystander killing: is antigen-dependent internalisation required. *Br. J. Cancer* **117**, 1736–1742 (2017).
  108. Khera, E., Cilliers, C., Bhatnagar, S. & Thurber, G. M. Computational transport analysis of antibody-drug conjugate bystander effects and payload tumoral distribution: Implications for therapy. *Mol. Syst. Des. Eng.* **3**, 73–88 (2018).
  109. Khera, E. *et al.* Quantifying ADC bystander payload penetration with cellular resolution using pharmacodynamic mapping. *Neoplasia* **23**, 210–221 (2021).
  110. Joubert, N., Beck, A., Dumontet, C. & Denevault-Sabourin, C. Antibody–Drug Conjugates: The Last Decade. *Pharmaceuticals* **13**, 245 (2020).
  111. Khongorzul, P., Ling, C. J., Khan, F. U., Ihsan, A. U. & Zhang, J. Antibody–Drug Conjugates: A Comprehensive Review. *Mol. Cancer Res.* **18**, 3–19 (2020).
  112. Leung, D. *et al.* Antibody Conjugates-Recent Advances and Future Innovations. *Antibodies* **9**, 2 (2020).
  113. Bargh, J. D., Isidro-Llobet, A., Parker, J. S. & Spring, D. R. Cleavable linkers in antibody-drug conjugates. *Chem. Soc. Rev.* **48**, 4361–4374 (2019).
  114. Yaghoubi, S. *et al.* Potential drugs used in the antibody–drug conjugate (ADC) architecture for cancer therapy. *J. Cell. Physiol.* **235**, 31–64 (2020).
  115. Beck, A., Goetsch, L., Dumontet, C. & Corvaia, N. Strategies and challenges for the next generation of antibody-drug conjugates. *Nat. Rev. Drug Discov.* **16**, 315–337 (2017).
  116. Shen, B. *et al.* Conjugation site modulates the in vivo stability and therapeutic activity of antibody-drug conjugates. *Nat. Biotechnol.* **30**, 184–189 (2012).
  117. Strop, P. *et al.* Location Matters: Site of Conjugation Modulates Stability and Pharmacokinetics of Antibody Drug Conjugates. *Chem. Biol.* **20**, 161–167 (2013).
  118. Dorywalska, M. *et al.* Effect of attachment site on stability of cleavable antibody drug conjugates. *Bioconjug. Chem.* **26**, 650–659 (2015).
  119. Junutula, J. R. *et al.* Site-specific conjugation of a cytotoxic drug to an antibody improves the therapeutic index. *Nat. Biotechnol.* **26**, 925–932 (2008).
  120. Vollmar, B. S. *et al.* Attachment Site Cysteine Thiol pKa Is a Key Driver for Site-Dependent Stability of THIOMAB Antibody–Drug Conjugates. *Bioconjug. Chem.* **28**, 2538–2548 (2017).
  121. Sussman, D. *et al.* Engineered cysteine antibodies: An improved antibody-drug conjugate platform with a novel mechanism of drug-linker stability. *Protein Eng. Des. Sel.* **31**, 47–54 (2018).
  122. Ohri, R. *et al.* High-Throughput Cysteine Scanning To Identify Stable Antibody Conjugation Sites for Maleimide- and Disulfide-Based Linkers. *Bioconjug. Chem.* **29**, 473–485 (2018).

- 
123. Tumej, L. N. *et al.* Site Selection: a Case Study in the Identification of Optimal Cysteine Engineered Antibody Drug Conjugates. *AAPS J.* **19**, 1123–1135 (2017).
  124. Schneider, H., Deweid, L., Avrutina, O. & Kolmar, H. Recent progress in transglutaminase-mediated assembly of antibody-drug conjugates. *Anal. Biochem.* **595**, 113615 (2020).
  125. Dickgiesser, S. *et al.* Site-Specific Conjugation of Native Antibodies Using Engineered Microbial Transglutaminases. *Bioconjug. Chem.* **31**, 1070–1076 (2020).
  126. Oller-Salvia, B., Kym, G. & Chin, J. W. Rapid and Efficient Generation of Stable Antibody–Drug Conjugates via an Encoded Cyclopropene and an Inverse-Electron-Demand Diels–Alder Reaction. *Angew. Chemie - Int. Ed.* **57**, 2831–2834 (2018).
  127. Duivelshof, B. L. *et al.* Glycan-Mediated Technology for Obtaining Homogeneous Site-Specific Conjugated Antibody–Drug Conjugates: Synthesis and Analytical Characterization by Using Complementary Middle-up LC/HRMS Analysis. *Anal. Chem.* **92**, 8170–8177 (2020).
  128. Yamada, K. *et al.* AJICAP: Affinity Peptide Mediated Regiodivergent Functionalization of Native Antibodies. *Angew. Chemie - Int. Ed.* **58**, 5592–5597 (2019).
  129. Muguruma, K. *et al.* Development of a High-Affinity Antibody-Binding Peptide for Site-Specific Modification. *ChemMedChem* **16**, 1814–1821 (2021).
  130. Gupta, N. *et al.* Computationally designed antibody–drug conjugates self-assembled via affinity ligands. *Nat. Biomed. Eng.* **3**, 917–929 (2019).
  131. Su, D. & Zhang, D. Linker Design Impacts Antibody-Drug Conjugate Pharmacokinetics and Efficacy via Modulating the Stability and Payload Release Efficiency. *Front. Pharmacol.* **12**, 1–8 (2021).
  132. Caculitan, N. G. *et al.* Cathepsin B is dispensable for cellular processing of cathepsin B-cleavable antibody–drug conjugates. *Cancer Res.* **77**, 7027–7037 (2017).
  133. Dorywalska, M. *et al.* Molecular Basis of Valine-Citrulline-PABC Linker Instability in Site-Specific ADCs and Its Mitigation by Linker Design. *Mol. Cancer Ther.* **15**, 958–970 (2016).
  134. Pabst, M. *et al.* Modulation of drug-linker design to enhance in vivo potency of homogeneous antibody-drug conjugates. *J. Control. Release* **253**, 160–164 (2017).
  135. Anami, Y. *et al.* Glutamic acid–valine–citrulline linkers ensure stability and efficacy of antibody–drug conjugates in mice. *Nat. Commun.* **9**, 2512 (2018).
  136. Jeffrey, S. C. *et al.* Development and Properties of  $\beta$ -Glucuronide Linkers for Monoclonal Antibody–Drug Conjugates. *Bioconjug. Chem.* **17**, 831–840 (2006).
  137. Jeffrey, S. C., De Brabander, J., Miyamoto, J. & Senter, P. D. Expanded utility of the  $\beta$ -glucuronide linker: ADCs that deliver phenolic cytotoxic agents. *ACS Med. Chem. Lett.* **1**, 277–280 (2010).
  138. Kolodych, S. *et al.* Development and evaluation of  $\beta$ -galactosidase-sensitive antibody-drug conjugates. *Eur. J. Med. Chem.* **142**, 376–382 (2017).
  139. Miller, J. T., Vitro, C. N., Fang, S., Benjamin, S. R. & Tumej, L. N. Enzyme-Agnostic Lysosomal Screen Identifies New Legumain-Cleavable ADC Linkers. *Bioconjug. Chem.* **32**, 842–858 (2021).
  140. Dal Corso, A., Cazzamalli, S., Gébleux, R., Mattarella, M. & Neri, D. Protease-Cleavable Linkers Modulate the Anticancer Activity of Noninternalizing Antibody–Drug Conjugates. *Bioconjug. Chem.* **28**, 1826–1833 (2017).
  141. Rossin, R. *et al.* Chemically triggered drug release from an antibody-drug conjugate leads to potent antitumour activity in mice. *Nat. Commun.* **9**, 1–11 (2018).

- 
142. Pahl, A., Lutz, C. & Hechler, T. Amanitins and their development as a payload for antibody-drug conjugates. *Drug Discov. Today Technol.* **30**, 85–89 (2018).
  143. Pillow, T. H. *et al.* Antibody Conjugation of a Chimeric BET Degrader Enables *in vivo* Activity. *ChemMedChem* **15**, 17–25 (2020).
  144. Dragovich, P. S. *et al.* Antibody-mediated delivery of chimeric protein degraders which target estrogen receptor alpha (ER $\alpha$ ). *Bioorg. Med. Chem. Lett.* **30**, 126907 (2020).
  145. Maneiro, M. *et al.* Antibody–PROTAC Conjugates Enable HER2-Dependent Targeted Protein Degradation of BRD4. *ACS Chem. Biol.* **15**, 1306–1312 (2020).
  146. Dragovich, P. S. *et al.* Antibody-Mediated Delivery of Chimeric BRD4 Degraders. Part 1: Exploration of Antibody Linker, Payload Loading, and Payload Molecular Properties. *J. Med. Chem.* **64**, 2534–2575 (2021).
  147. Dragovich, P. S. *et al.* Antibody-Mediated Delivery of Chimeric BRD4 Degraders. Part 2: Improvement of *In Vitro* Antiproliferation Activity and *In Vivo* Antitumor Efficacy. *J. Med. Chem.* **64**, 2576–2607 (2021).
  148. Lai, A. C. & Crews, C. M. Induced protein degradation: An emerging drug discovery paradigm. *Nat. Rev. Drug Discov.* **16**, 101–114 (2017).
  149. Mahalingaiah, P. K. *et al.* Potential mechanisms of target-independent uptake and toxicity of antibody-drug conjugates. *Pharmacol. Ther.* **200**, 110–125 (2019).
  150. Yurkovetskiy, A. V. *et al.* A polymer-based antibody-vinca drug conjugate platform: Characterization and preclinical efficacy. *Cancer Res.* **75**, 3365–3372 (2015).
  151. Schneider, H. *et al.* Dextramabs: A Novel Format of Antibody-Drug Conjugates Featuring a Multivalent Polysaccharide Scaffold. *ChemistryOpen* **8**, 354–357 (2019).
  152. De Goeij, B. E. C. G. *et al.* Efficient payload delivery by a bispecific antibody-drug conjugate targeting HER2 and CD63. *Mol. Cancer Ther.* **15**, 2688–2697 (2016).
  153. Anderl, J. M1231: A first-in-class bispecific antibody-drug conjugate targeting EGFR and MUC1. in *Emerging Mechanisms of Resistance to Targeted Therapies* (AACR Virtual Annual Meeting II, 2020).
  154. Gébleux, R., Stringhini, M., Casanova, R., Soltermann, A. & Neri, D. Non-internalizing antibody–drug conjugates display potent anti-cancer activity upon proteolytic release of monomethyl auristatin E in the subendothelial extracellular matrix. *Int. J. Cancer* **140**, 1670–1679 (2017).
  155. Gébleux, R., Wulfhard, S., Casi, G. & Neri, D. Antibody format and drug release rate determine the therapeutic activity of noninternalizing antibody-drug conjugates. *Mol. Cancer Ther.* **14**, 2606–2612 (2015).
  156. Perrino, E. *et al.* Curative properties of noninternalizing antibody-drug conjugates based on maytansinoids. *Cancer Res.* **74**, 2569–2578 (2014).
  157. Singh, A. P. & Shah, D. K. Measurement and mathematical characterization of cell-level pharmacokinetics of antibody-drug conjugates: A case study with trastuzumab-vc-MMAE. *Drug Metab. Dispos.* **45**, 1120–1132 (2017).
  158. Sharma, S., Li, Z., Bussing, D. & Shah, D. K. Evaluation of Quantitative Relationship Between Target Expression and Antibody-Drug Conjugate Exposure Inside Cancer Cells. *Drug Metab. Dispos.* **48**, 368–377 (2020).
  159. Singh, A. P., Guo, L., Verma, A., Wong, G. G. L. & Shah, D. K. A cell-level systems PK-PD model to characterize *in vivo* efficacy of ADCs. *Pharmaceutics* **11**, 1–18 (2019).

- 
160. Singh, A. P. *et al.* Evolution of the Systems Pharmacokinetics-Pharmacodynamics Model for Antibody-Drug Conjugates to Characterize Tumor Heterogeneity and In Vivo Bystander Effect. *J. Pharmacol. Exp. Ther.* **374**, 184–199 (2020).
  161. Singh, A. P. *et al.* Antibody Coadministration as a Strategy to Overcome Binding-Site Barrier for ADCs: a Quantitative Investigation. *AAPS J.* **22**, 28 (2020).
  162. Cilliers, C., Guo, H., Liao, J., Christodolu, N. & Thurber, G. M. Multiscale Modeling of Antibody-Drug Conjugates: Connecting Tissue and Cellular Distribution to Whole Animal Pharmacokinetics and Potential Implications for Efficacy. *AAPS J.* **18**, 1117–1130 (2016).
  163. Bussing, D., Sharma, S., Li, Z., Meyer, L. F. & Shah, D. K. Quantitative Evaluation of the Effect of Antigen Expression Level on Antibody–Drug Conjugate Exposure in Solid Tumor. *AAPS J.* **23**, 10–12 (2021).
  164. Betts, A. *et al.* Use of translational modeling and simulation for quantitative comparison of PF-06804103, a new generation HER2 ADC, with Trastuzumab-DM1. *J. Pharmacokinet. Pharmacodyn.* **47**, 513–526 (2020).
  165. Weddell, J., Chiney, M. S., Bhatnagar, S., Gibbs, J. P. & Shebley, M. Mechanistic Modeling of Intra-Tumor Spatial Distribution of Antibody-Drug Conjugates: Insights into Dosing Strategies in Oncology. *Clin. Transl. Sci.* **14**, 395–404 (2021).
  166. Donaghy, H. Effects of antibody, drug and linker on the preclinical and clinical toxicities of antibody-drug conjugates. *MAbs* **8**, 659–671 (2016).
  167. Guffroy, M., Falahatpisheh, H. & Finkelstein, M. Improving the Safety Profile of ADCs. in *Innovations for Next-Generation Antibody-Drug Conjugates* (ed. Damelin, M.) 45–71 (Springer International Publishing, 2018). doi:10.1007/978-3-319-78154-9\_3.
  168. Bartelink, I. H. *et al.* Tumor Drug Penetration Measurements Could Be the Neglected Piece of the Personalized Cancer Treatment Puzzle. *Clin. Pharmacol. Ther.* **106**, 148–163 (2019).
  169. Beckman, R. A., Weiner, L. M. & Davis, H. M. Antibody constructs in cancer therapy. *Cancer* **109**, 170–179 (2007).
  170. Thurber, G. M., Schmidt, M. M. & Wittrup, K. D. Factors determining antibody distribution in tumors. *Trends Pharmacol. Sci.* **29**, 57–61 (2008).
  171. Thurber, G. M., Schmidt, M. M. & Wittrup, K. D. Antibody tumor penetration: Transport opposed by systemic and antigen-mediated clearance. *Adv. Drug Deliv. Rev.* **60**, 1421–1434 (2008).
  172. Xenaki, K. T., Oliveira, S. & van Bergen en Henegouwen, P. M. P. Antibody or Antibody Fragments: Implications for Molecular Imaging and Targeted Therapy of Solid Tumors. *Front. Immunol.* **8**, 1287 (2017).
  173. Maeda, H. Macromolecular therapeutics in cancer treatment: The EPR effect and beyond. *J. Control. Release* **164**, 138–144 (2012).
  174. Um, W. *et al.* A Comparative Study on Albumin-Binding Molecules for Targeted Tumor Delivery through Covalent and Noncovalent Approach. *Bioconjug. Chem.* **30**, 3107–3118 (2019).
  175. Wong, A. D., Ye, M., Ulmschneider, M. B. & Searson, P. C. Quantitative Analysis of the Enhanced Permeation and Retention (EPR) Effect. *PLoS One* **10**, e0123461 (2015).
  176. Michel, C. C. & Curry, F. E. Microvascular permeability. *Physiol. Rev.* **79**, 703–761 (1999).
  177. Schmidt, M. M. & Wittrup, K. D. A modeling analysis of the effects of molecular size and binding affinity on tumor targeting. *Mol. Cancer Ther.* **8**, 2861–2871 (2009).

- 
178. Thurber, G. M. & Weissleder, R. A Systems Approach for Tumor Pharmacokinetics. *PLoS One* **6**, e24696 (2011).
  179. Adams, G. P. *et al.* High Affinity Restricts the Localization and Tumor Penetration of Single-Chain Fv Antibody Molecules. *Cancer Res.* **61**, 4750–4755 (2001).
  180. Graff, C. P. & Wittrup, K. D. Theoretical analysis of antibody targeting of tumor spheroids: Importance of dosage for penetration, and affinity for retention. *Cancer Res.* **63**, 1288–1296 (2003).
  181. Thurber, G. M. & Wittrup, K. D. Quantitative spatiotemporal analysis of antibody fragment diffusion and endocytic consumption in tumor spheroids. *Cancer Res.* **68**, 3334–3341 (2008).
  182. Nielsen, U. B., Adams, G. P., Weiner, L. M. & Marks, J. D. Targeting of bivalent anti-ErbB2 diabody antibody fragments to tumor cells is independent of the intrinsic antibody affinity. *Cancer Res.* **60**, 6434–6440 (2000).
  183. Adams, G. P. *et al.* Avidity-mediated enhancement of in vivo tumor targeting by single-chain Fv dimers. *Clin. Cancer Res.* **12**, 1599–1605 (2006).
  184. Rudnick, S. I. *et al.* Influence of Affinity and Antigen Internalization on the Uptake and Penetration of Anti-HER2 Antibodies in Solid Tumors. *Cancer Res.* **71**, 2250–2259 (2011).
  185. Muchekehr, R. *et al.* The Effect of Molecular Weight, PK, and Valency on Tumor Biodistribution and Efficacy of Antibody-Based Drugs. *Transl. Oncol.* **6**, 562–572 (2013).
  186. Debie, P. *et al.* Size and affinity kinetics of nanobodies influence targeting and penetration of solid tumours. *J. Control. Release* **317**, 34–42 (2020).
  187. Song, Y. *et al.* Dissecting the impact of target-binding kinetics of protein binders on tumor localization. *iScience* **24**, 102104 (2021).
  188. Tsumura, R. *et al.* Influence of the dissociation rate constant on the intra-tumor distribution of antibody-drug conjugate against tissue factor. *J. Control. Release* **284**, 49–56 (2018).
  189. Nessler, I. *et al.* Increased Tumor Penetration of Single-Domain Antibody–Drug Conjugates Improves In Vivo Efficacy in Prostate Cancer Models. *Cancer Res.* **80**, 1268–1278 (2020).
  190. Wong, O. K. *et al.* RN765C, a low affinity EGFR antibody drug conjugate with potent anti-tumor activity in preclinical solid tumor models. *Oncotarget* **9**, 33446–33458 (2018).
  191. Zwaagstra, J. C. *et al.* Binding and functional profiling of antibody mutants guides selection of optimal candidates as antibody drug conjugates. *PLoS One* **14**, e0226593 (2019).
  192. Ackerman, M. E., Pawlowski, D. & Wittrup, K. D. Effect of antigen turnover rate and expression level on antibody penetration into tumor spheroids. *Mol. Cancer Ther.* **7**, 2233–2240 (2008).
  193. Sutherland, R., Buchegger, F., Schreyer, M., Vacca, A. & Mach, J. P. Penetration and Binding of Radiolabeled Anti-Carcinoembryonic Antigen Monoclonal Antibodies and Their Antigen Binding Fragments in Human Colon Multicellular Tumor Spheroids. *Cancer Res.* **47**, 1627–1633 (1987).
  194. Cilliers, C., Menezes, B., Nessler, I., Linderman, J. & Thurber, G. M. Improved tumor penetration and single-cell targeting of antibody–drug conjugates increases anticancer efficacy and host survival. *Cancer Res.* **78**, 758–768 (2018).
  195. Lu, G. *et al.* Co-administered antibody improves penetration of antibody–dye conjugate into human cancers with implications for antibody–drug conjugates. *Nat. Commun.* **11**, 1–11 (2020).
  196. Bordeau, B. M., Yang, Y. & Balthasar, J. P. Transient competitive inhibition bypasses the binding site barrier to improve tumor penetration of trastuzumab and enhance T-DM1 efficacy. *Cancer Res.* **81**, 4145–4154 (2021).

- 
197. Li, Z., Krippendorff, B. & Shah, D. K. Influence of Molecular size on the clearance of antibody fragments. *Pharm. Res.* **34**, 2131–2141 (2017).
  198. Dennis, M. S. *et al.* Imaging tumors with an albumin-binding Fab, a novel tumor-targeting agent. *Cancer Res.* **67**, 254–261 (2007).
  199. Thurber, G. M., Zajic, S. C. & Wittrup, K. D. Theoretic criteria for antibody penetration into solid tumors and micrometastases. *J. Nucl. Med.* **48**, 995–999 (2007).
  200. Deonarain, M. P. Miniaturised ‘antibody’-drug conjugates for solid tumours? *Drug Discov. Today Technol.* **30**, 47–53 (2018).
  201. Deonarain, M. *et al.* Small-Format Drug Conjugates: A Viable Alternative to ADCs for Solid Tumours? *Antibodies* **7**, 16 (2018).
  202. Aguiar, S. *et al.* Chimeric Small Antibody Fragments as Strategy to Deliver Therapeutic Payloads. *Adv. Protein Chem. Struct. Biol.* **112**, 143–182 (2018).
  203. Deonarain, M. P. & Xue, Q. Tackling solid tumour therapy with small-format drug conjugates. *Antib. Ther.* **3**, 237–245 (2020).
  204. Deonarain, M. P. & Yahioglu, G. Current strategies for the discovery and bioconjugation of smaller, targetable drug conjugates tailored for solid tumor therapy. *Expert Opin. Drug Discov.* **16**, 613–624 (2021).
  205. Zhou, Z., Zhang, J., Zhang, Y., Ma, G. & Su, Z. Specific Conjugation of the Hinge Region for Homogeneous Preparation of Antibody Fragment-Drug Conjugate: A Case Study for Doxorubicin-PEG-anti-CD20 Fab’ Synthesis. *Bioconjug. Chem.* **27**, 238–246 (2016).
  206. Badescu, G. *et al.* Bridging Disulfides for Stable and Defined Antibody Drug Conjugates. *Bioconjug. Chem.* **25**, 1124–1136 (2014).
  207. Ruddle, B. T., Fleming, R., Wu, H., Gao, C. & Dimasi, N. Characterization of Disulfide Bond Rebridged Fab–Drug Conjugates Prepared Using a Dual Maleimide Pyrrolbenzodiazepine Cytotoxic Payload. *ChemMedChem* **14**, 1185–1195 (2019).
  208. Liu, W. *et al.* High antitumor activity of Sortase A-generated anti-CD20 antibody fragment drug conjugates. *Eur. J. Pharm. Sci.* **134**, 81–92 (2019).
  209. Li, Q. *et al.* Improved Inhibition of Tumor Growth by Diabody-Drug Conjugates via Half-Life Extension. *Bioconjug. Chem.* **30**, 1232–1243 (2019).
  210. Kim, K. M. *et al.* Anti-CD30 diabody-drug conjugates with potent antitumor activity. *Mol. Cancer Ther.* **7**, 2486–2497 (2008).
  211. Lillo, A. M. *et al.* A Human Single-Chain Antibody Specific for Integrin  $\alpha 3\beta 1$  Capable of Cell Internalization and Delivery of Antitumor Agents. *Chem. Biol.* **11**, 897–906 (2004).
  212. Woitok, M. *et al.* Comparison of a mouse and a novel human scFv-SNAP-auristatin F drug conjugate with potent activity against EGFR-overexpressing human solid tumor cells. *Onco. Targets. Ther.* **10**, 3313–3327 (2017).
  213. Aubrey, N. *et al.* Site-Specific Conjugation of Auristatins onto Engineered scFv Using Second Generation Maleimide to Target HER2-positive Breast Cancer in Vitro. *Bioconjug. Chem.* **29**, 3516–3521 (2018).
  214. Cao, L. *et al.* HER2-specific immunotoxins constructed based on single-domain antibodies and the improved toxin PE24X7. *Int. J. Pharm.* **574**, 118939 (2020).
  215. Sochaj-Gregorczyk, A. M. *et al.* Design and in vitro evaluation of a cytotoxic conjugate based on the anti-HER2 affibody fused to the Fc fragment of IgG1. *Int. J. Mol. Sci.* **18**, 1688 (2017).

- 
216. Altai, M. *et al.* Affibody-derived drug conjugates: Potent cytotoxic molecules for treatment of HER2 over-expressing tumors. *J. Control. Release* **288**, 84–95 (2018).
  217. Brandl, F., Busslinger, S., Zangemeister-Wittke, U. & Plückthun, A. Optimizing the anti-tumor efficacy of protein-drug conjugates by engineering the molecular size and half-life. *J. Control. Release* **327**, 186–197 (2020).
  218. Xu, T. *et al.* Drug Conjugates Based on a Monovalent Affibody Targeting Vector Can Efficiently Eradicate HER2 Positive Human Tumors in an Experimental Mouse Model. *Cancers* **13**, 85 (2020).
  219. Zhu, G., Niu, G. & Chen, X. Aptamer-Drug Conjugates. *Bioconjug. Chem.* **26**, 2186–2197 (2015).
  220. Dickgiesser, S. *et al.* Self-Assembled Hybrid Aptamer-Fc Conjugates for Targeted Delivery: A Modular Chemoenzymatic Approach. *ACS Chem. Biol.* **10**, 2158–2165 (2015).
  221. Deng, Z. *et al.* Polymeric Engineering of Aptamer–Drug Conjugates for Targeted Cancer Therapy. *Bioconjug. Chem.* **31**, 37–42 (2020).
  222. Tan, Y. *et al.* Aptamer Enables Consistent Maytansine Delivery through Maintaining Receptor Homeostasis for HER2 Targeted Cancer Therapy. *Bioconjug. Chem.* **31**, 1766–1774 (2020).
  223. Cochran, J. R., Smith, M., Grant, G. A., Cox, N. & Kintzing, J. R. Integrin-Targeting Knottin Peptide-Drug Conjugates are Potent Inhibitors of Tumor Cell Proliferation. *Angew. Chemie Int. Ed.* **55**, 9894–9897 (2016).
  224. Cartwright, O. C., Beekman, A. M., Cominetti, M. M. D., Russell, D. A. & Searcey, M. A Peptide–Duocarmycin Conjugate Targeting the Thomsen-Friedenreich Antigen has Potent and Selective Antitumor Activity. *Bioconjug. Chem.* **31**, 1745–1749 (2020).
  225. Mudd, G. E. *et al.* Identification and Optimization of EphA2-Selective Bicycles for the Delivery of Cytotoxic Payloads. *J. Med. Chem.* **63**, 4107–4116 (2020).
  226. Bennett, G. *et al.* MMAE Delivery Using the Bicycle Toxin Conjugate BT5528. *Mol. Cancer Ther.* **19**, 1385–1394 (2020).
  227. Michigami, M. *et al.* A “ligand-targeting” peptide-drug conjugate: Targeted intracellular drug delivery by VEGF-binding helix-loop-helix peptides via receptor-mediated endocytosis. *PLoS One* **16**, 1–16 (2021).
  228. Srinivasarao, M., Galliford, C. V. & Low, P. S. Principles in the design of ligand-targeted cancer therapeutics and imaging agents. *Nat. Rev. Drug Discov.* **14**, 203–219 (2015).
  229. Vergote, I. & Leamon, C. P. Vintafolide: A novel targeted therapy for the treatment of folate receptor expressing tumors. *Ther. Adv. Med. Oncol.* **7**, 206–218 (2015).
  230. Zhuang, C. *et al.* Small molecule-drug conjugates: A novel strategy for cancer-targeted treatment. *Eur. J. Med. Chem.* **163**, 883–895 (2019).
  231. Cazzamalli, S., Dal Corso, A., Widmayer, F. & Neri, D. Chemically defined antibody- and small molecule-drug conjugates for in vivo tumor targeting applications: A comparative analysis. *J. Am. Chem. Soc.* **140**, 1617–1621 (2018).
  232. Whalen, K. A. *et al.* Targeting the somatostatin receptor 2 with the miniaturized drug conjugate, PEN-221: A potent and novel therapeutic for the treatment of small cell lung cancer. *Mol. Cancer Ther.* **18**, 1926–1936 (2019).
  233. Patel, T. K. *et al.* Small molecule drug conjugates (SMDCs): an emerging strategy for anticancer drug design and discovery. *New J. Chem.* **45**, 5291–5321 (2021).
  234. Huang, H. *et al.* Modular design of nanobody–drug conjugates for targeted-delivery of platinum anticancer drugs with an MRI contrast agent. *Chem. Commun.* **55**, 5175–5178 (2019).

- 
235. Glassman, P. M. *et al.* Molecularly Engineered Nanobodies for Tunable Pharmacokinetics and Drug Delivery. *Bioconjug. Chem.* **31**, 1144–1155 (2020).
  236. Pilati, D. & Howard, K. A. Albumin-based drug designs for pharmacokinetic modulation. *Expert Opin. Drug Metab. Toxicol.* **16**, 783–795 (2020).
  237. Tijink, B. M. *et al.* Improved tumor targeting of anti-epidermal growth factor receptor Nanobodies through albumin binding: taking advantage of modular Nanobody technology. *Mol. Cancer Ther.* **7**, 2288–2297 (2008).
  238. Simon, M., Frey, R., Zangemeister-Wittke, U. & Plückthun, A. Orthogonal assembly of a designed ankyrin repeat protein-cytotoxin conjugate with a clickable serum albumin module for half-life extension. *Bioconjug. Chem.* **24**, 1955–1966 (2013).
  239. Hirasawa, S. *et al.* Facile and Efficient Chemoenzymatic Semisynthesis of Fc-Fusion Compounds for Half-Life Extension of Pharmaceutical Components. *Bioconjug. Chem.* **30**, 2323–2331 (2019).
  240. Sharma, P. *et al.* Drug Conjugates for Targeting Eph Receptors in Glioblastoma. *Pharmaceuticals* **13**, 77 (2020).
  241. Gallo, F. *et al.* Enhancing the Pharmacokinetics and Antitumor Activity of an  $\alpha$ -Amanitin-Based Small-Molecule Drug Conjugate via Conjugation with an Fc Domain. *J. Med. Chem.* **64**, 4117–4129 (2021).
  242. Brandl, F. *et al.* Influence of size and charge of unstructured polypeptides on pharmacokinetics and biodistribution of targeted fusion proteins. *J. Control. Release* **307**, 379–392 (2019).
  243. Gehlsen, K. R. *et al.* Pharmacokinetics of engineered human monomeric and dimeric CH2 domains. *MAbs* **4**, 466–474 (2012).
  244. Xenaki, K. T. *et al.* Homogeneous tumor targeting with a single dose of HER2-targeted albumin-binding domain-fused nanobody-drug conjugates results in long-lasting tumor remission in mice. *Theranostics* **11**, 5525–5538 (2021).
  245. Gong, R. *et al.* Engineered human antibody constant domains with increased stability. *J. Biol. Chem.* **284**, 14203–14210 (2009).
  246. Gong, R., Wang, Y., Feng, Y., Zhao, Q. & Dimitrov, D. S. Shortened Engineered Human Antibody CH2 Domains. *J. Biol. Chem.* **286**, 27288–27293 (2011).
  247. Peretti, S. Abdurin-Drug Conjugates: A New Generation of Targeted Therapies. in *Abdurin-Drug Conjugates - Small Size and Long Half-Life to Improve Drug Concentration in the Target Tissue* (PEGS Europe, 2017).
  248. Wozniak-Knopp, G. *et al.* Introducing antigen-binding sites in structural loops of immunoglobulin constant domains: Fc fragments with engineered HER2/neu-binding sites and antibody properties. *Protein Eng. Des. Sel.* **23**, 289–297 (2010).
  249. Lobner, E. *et al.* Fcab-HER2 Interaction: a M $\acute{e}$ nage  $\grave{a}$  Trois. Lessons from X-Ray and Solution Studies. *Structure* **25**, 878–889 (2017).
  250. Wozniak-Knopp, G. *et al.* Designing Fcabs: Well-expressed and stable high affinity antigen-binding Fc fragments. *Protein Eng. Des. Sel.* **30**, 567–581 (2017).
  251. Lobner, E. *et al.* Two-faced Fcab prevents polymerization with VEGF and reveals thermodynamics and the 2.15 Å crystal structure of the complex. *MAbs* **9**, 1088–1104 (2017).
  252. Tuna, M., Leung, K.-M., Sun, H., Medcalf, M. & Isaac, S. EGFR binding molecules. CA3030505A1. (2018).

- 
253. Kainer, M. *et al.* Correlation between CD16a binding and immuno effector functionality of an antigen specific immunoglobulin Fc fragment (Fcab). *Arch. Biochem. Biophys.* **526**, 154–158 (2012).
254. Jez, J. *et al.* Significant Impact of Single N -Glycan Residues on the Biological Activity of Fc-based Antibody-like Fragments. *J. Biol. Chem.* **287**, 24313–24319 (2012).
255. Leung, K. M. *et al.* A HER2-specific Modified Fc Fragment (Fcab) induces antitumor effects through degradation of HER2 and apoptosis. *Mol. Ther.* **23**, 1722–1733 (2015).
256. Traxlmayr, M. W. *et al.* Integrin binding human antibody constant domains - Probing the C-terminal structural loops for grafting the RGD motif. *J. Biotechnol.* **155**, 193–202 (2011).
257. Woisetschläger, M. *et al.* In vivo and in vitro activity of an immunoglobulin Fc fragment (Fcab) with engineered Her-2/neu binding sites. *Biotechnol. J.* **9**, 844–851 (2014).
258. Traxlmayr, M. W. *et al.* Directed evolution of Her2/neu-binding IgG1-Fc for improved stability and resistance to aggregation by using yeast surface display. *Protein Eng. Des. Sel.* **26**, 255–265 (2013).
259. Wozniak-Knopp, G., Stadlmann, J. & Rüker, F. Stabilisation of the Fc Fragment of Human IgG1 by Engineered Intradomain Disulfide Bonds. *PLoS One* **7**, e30083 (2012).
260. Wozniak-Knopp, G. & Rüker, F. A C-terminal interdomain disulfide bond significantly stabilizes the Fc fragment of IgG. *Arch. Biochem. Biophys.* **526**, 181–187 (2012).
261. Traxlmayr, M. W. *et al.* Directed evolution of stabilized IgG1-Fc scaffolds by application of strong heat shock to libraries displayed on yeast. *Biochim. Biophys. Acta - Proteins Proteomics* **1824**, 542–549 (2012).
262. Hasenhindl, C. *et al.* Stability assessment on a library scale: A rapid method for the evaluation of the commutability and insertion of residues in C-terminal loops of the CH3 domains of IgG1-Fc. *Protein Eng. Des. Sel.* **26**, 675–682 (2013).
263. Traxlmayr, M. W. *et al.* Construction of pH-sensitive Her2-binding IgG1-Fc by directed evolution. *Biotechnol. J.* **9**, 1013–1022 (2014).
264. Everett, K. L. *et al.* Generation of Fcabs targeting human and murine LAG-3 as building blocks for novel bispecific antibody therapeutics. *Methods* **154**, 60–69 (2019).
265. Kraman, M. *et al.* FS118, a Bispecific Antibody Targeting LAG-3 and PD-L1, Enhances T-Cell Activation Resulting in Potent Antitumor Activity. *Clin. Cancer Res.* **26**, 3333–3344 (2020).
266. Kariolis, M. S. *et al.* Brain delivery of therapeutic proteins using an Fc fragment blood-brain barrier transport vehicle in mice and monkeys. *Sci. Transl. Med.* **12**, eaay1359 (2020).
267. Batey, S. *et al.* HER2 Binding Agent Therapies. WO2016/162505A1. (2016).
268. F-star. F-star Scientific Approach. <http://www.f-star.com/scientific-approach/overview/>.
269. Benedetti, F. *et al.* Bispecific antibodies with Fab-arms featuring exchanged antigen-binding constant domains. *Biochem. Biophys. Reports* **26**, 100959 (2021).
270. Benedetti, F., Stadlbauer, K., Stadlmayr, G., Rüker, F. & Wozniak-Knopp, G. A Tetravalent Biparatopic Antibody Causes Strong HER2 Internalization and Inhibits Cellular Proliferation. *Life* **11**, 1157 (2021).
271. Trastuzumab amino acid sequence on DrugBank database (accession number: DB00072). <https://www.drugbank.ca/drugs/DB00072>.
272. Baggethun, P. Radial Profile Plot for ImageJ. <https://imagej.nih.gov/ij/plugins/radial-profile.html> (2002).
273. Bioinformatics, S. I. of. Expasy ProtParam Tool. <https://web.expasy.org/protparam/>.

- 
274. Tobias, R. & Ma, W. Forté Bio Application Note 19: Analysis of FcRn-Antibody Interactions on the Octet Platform.
275. Chen, I., Dorr, B. M. & Liu, D. R. A general strategy for the evolution of bond-forming enzymes using yeast display. *Proc. Natl. Acad. Sci.* **108**, 11399–11404 (2011).
276. Wang, C. *et al.* Chromatography-based methods for determining molar extinction coefficients of cytotoxic payload drugs and drug antibody ratios of antibody drug conjugates. *J. Chromatogr. A* **1455**, 133–139 (2016).
277. Jäger, S. *et al.* Generation and Biological Evaluation of Fc Antigen Binding Fragment-Drug Conjugates as a Novel Antibody-Based Format for Targeted Drug Delivery. *Bioconjug. Chem.* **32**, 1699–1710 (2021).
278. Jäger, S. *et al.* EGFR binding Fc domain-drug conjugates: stable and highly potent cytotoxic molecules mediate selective cell killing. *Biol. Chem.* (2021) doi:10.1515/hsz-2021-0321.
279. Lakayan, D., Haselberg, R., Gahoual, R., Somsen, G. W. & Kool, J. Affinity profiling of monoclonal antibody and antibody-drug-conjugate preparations by coupled liquid chromatography-surface plasmon resonance biosensing. *Anal. Bioanal. Chem.* **410**, 7837–7848 (2018).
280. Anderl, J., Torsten, H., Müller, C. & Pahl, A. Amatoxin-antibody conjugates. US20180043033A1. (2018).
281. Strop, P. *et al.* Engineered polypeptide conjugates and methods for making thereof using transglutaminase. WO2012059882A2. (2012).
282. Baudino, L. *et al.* Crucial Role of Aspartic Acid at Position 265 in the CH2 Domain for Murine IgG2a and IgG2b Fc-Associated Effector Functions. *J. Immunol.* **181**, 6664–6669 (2008).
283. Shields, R. L. *et al.* High Resolution Mapping of the Binding Site on Human IgG1 for FcγRI, FcγRII, FcγRIII, and FcRn and Design of IgG1 Variants with Improved Binding to the FcγR. *J. Biol. Chem.* **276**, 6591–6604 (2001).
284. Marquette, K. *et al.* Engineered antibody constant regions for site-specific conjugation and methods and uses therefor. EP2794653B1. (2019).
285. Gébleux, R., Briendl, M., Grawunder, U. & Beerli, R. R. Sortase A Enzyme-Mediated Generation of Site-Specifically Conjugated Antibody–Drug Conjugates. in *Enzyme-Mediated Ligation Methods* (eds. Nuijens, T. & Schmidt, M.) 1–13 (Humana, New York, NY, 2019). doi:10.1007/978-1-4939-9546-2\_1.
286. Roßkopf, J. Improved Drug Delivery of next-generation Antibody-Drug Conjugates by utilizing tumor-associated proteases. (Technische Universität Darmstadt, 2019). doi:10.25534/tuprints-00009685.
287. Von Pawel-Rammingen, U., Johansson, B. P. & Björck, L. IdeS, a novel streptococcal cysteine proteinase with unique specificity for immunoglobulin G. *EMBO J.* **21**, 1607–1615 (2002).
288. Armstrong, J. K., Wenby, R. B., Meiselman, H. J. & Fisher, T. C. The hydrodynamic radii of macromolecules and their effect on red blood cell aggregation. *Biophys. J.* **87**, 4259–4270 (2004).
289. Sellmann, C. Balancing Efficacy and Selectivity of Bispecific c-METxEGFR Antibodies. (Technische Universität Darmstadt, 2016).
290. Nath, N. *et al.* Homogeneous plate based antibody internalization assay using pH sensor fluorescent dye. *J. Immunol. Methods* **431**, 11–21 (2016).
291. Owen, S. C. *et al.* Targeting HER2+ breast cancer cells: Lysosomal accumulation of anti-HER2 antibodies is influenced by antibody binding site and conjugation to polymeric nanoparticles. *J. Control. Release* **172**, 395–404 (2013).

- 
292. Kang, J. C. *et al.* Engineering a HER2-specific antibody–drug conjugate to increase lysosomal delivery and therapeutic efficacy. *Nat. Biotechnol.* **37**, 523–526 (2019).
  293. Schwesinger, F. *et al.* Unbinding forces of single antibody-antigen complexes correlate with their thermal dissociation rates. *Proc. Natl. Acad. Sci.* **97**, 9972–9977 (2000).
  294. Benjamin, S. R. *et al.* Thiolation of Q295: Site-Specific Conjugation of Hydrophobic Payloads without the Need for Genetic Engineering. *Mol. Pharm.* **16**, 2795–2807 (2019).
  295. Minchinton, A. I. & Tannock, I. F. Drug penetration in solid tumours. *Nat. Rev. Cancer* **6**, 583–592 (2006).
  296. Sutherland, R. M. & Durand, R. E. Radiation response of multicell spheroids - an in vitro tumour model. *Curr. Top. Radiat. Res. Q.* **11**, 87–139 (1976).
  297. Sutherland, R. M. Cell and environment interactions in tumor microregions: the multicell spheroid model. *Science* **240**, 177–184 (1988).
  298. Dall’Acqua, W. F., Kiener, P. A. & Wu, H. Properties of Human IgG1s engineered for enhanced binding to the neonatal Fc Receptor (FcRn). *J. Biol. Chem.* **281**, 23514–23524 (2006).
  299. Schlothauer, T. *et al.* Analytical FcRn affinity chromatography for functional characterization of monoclonal antibodies. *MAbs* **5**, 576–586 (2013).
  300. Desnoyers, L. R. *et al.* Tumor-Specific Activation of an EGFR-Targeting Probody Enhances Therapeutic Index. *Sci. Transl. Med.* **5**, 207ra144 (2013).
  301. Brezski, R. J., Knight, D. M. & Jordan, R. E. The Origins, Specificity, and Potential Biological Relevance of Human Anti-IgG Hinge Autoantibodies. *Sci. World J.* **11**, 1153–1167 (2011).

## 11. Appendix

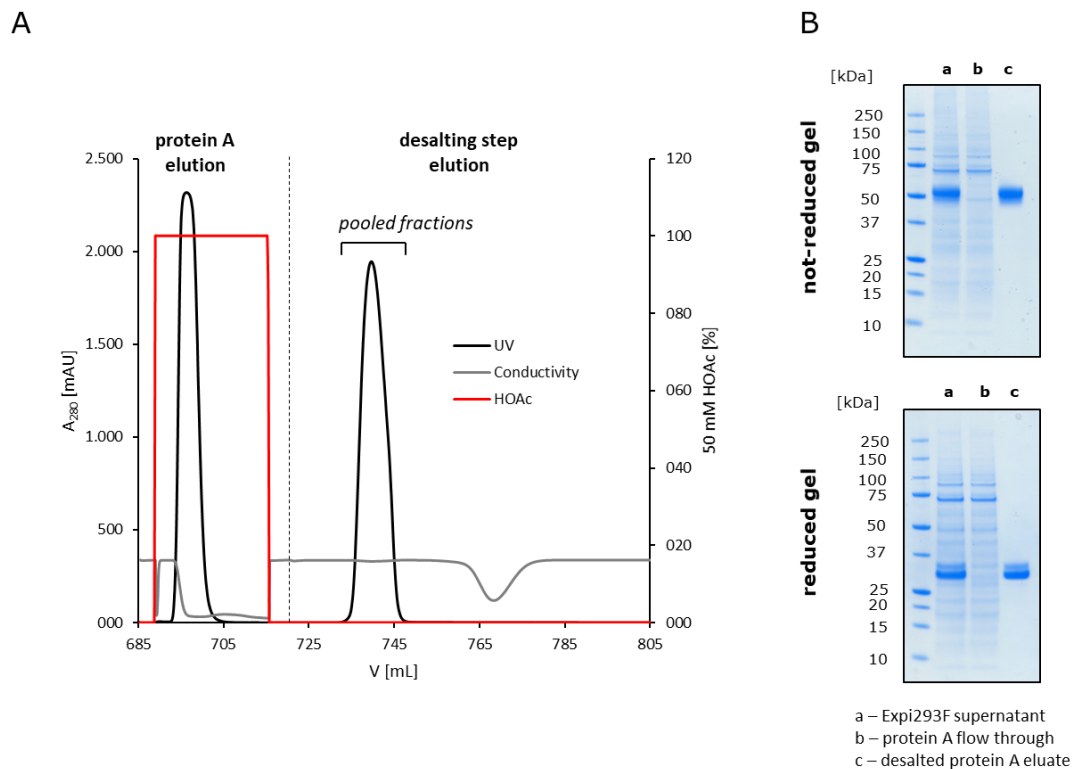


**Figure A1. Protein A purification process exemplarily shown for HER2 targeting Fcab  $\alpha$ H-FS.** (A) ÄKTA Xpress (HiTrap™ MabSelect SuRe 5 mL and HiPrep™ 26/10 desalting column) chromatogram showing protein peak after elution from Protein A column (50 mM acetic acid (HOAc), pH 3.2) and a second protein peak after a subsequent buffer change step. (B) SDS-PAGE analysis of reduced and not-reduced cell supernatant, protein A flow through and purified  $\alpha$ H-FS shows high efficiency of protein A purification for Fcabs.

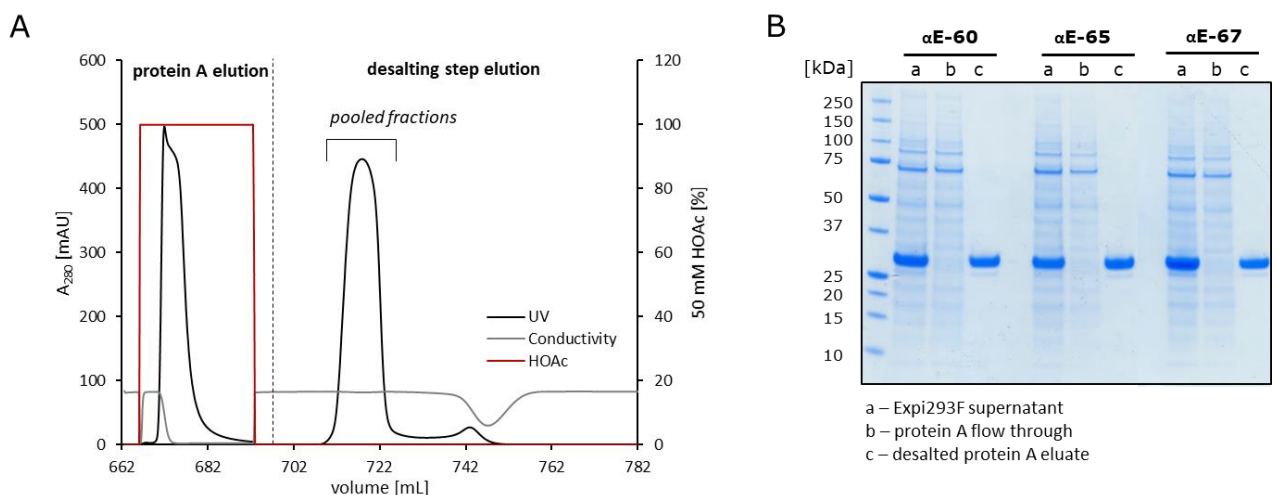
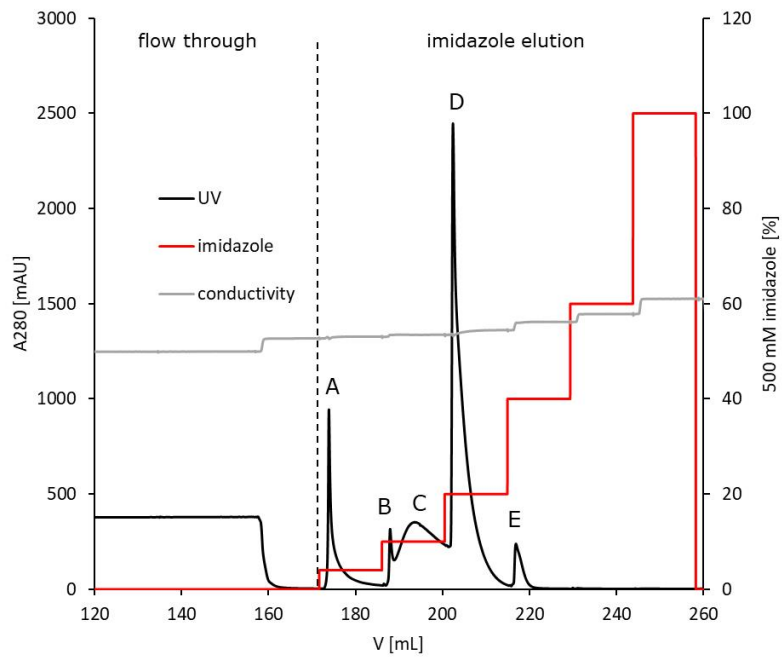


**Figure A2. Protein A purification process exemplarily shown for EGFR targeting Fcabs.** (A) Exemplary ÄKTA Xpress (HiTrap™ MabSelect SuRe 5 mL and HiPrep™ 26/10 desalting column) chromatogram showing  $\alpha$ E-65 protein peak after elution from protein A column (50 mM acetic acid (HOAc), pH 3.2) and a second protein peak after a subsequent buffer change step. (B) SDS-PAGE analysis of reduced cell supernatant, protein A flow through and purified Fcabs shows high efficiency of protein A purification for Fcabs.

A



B

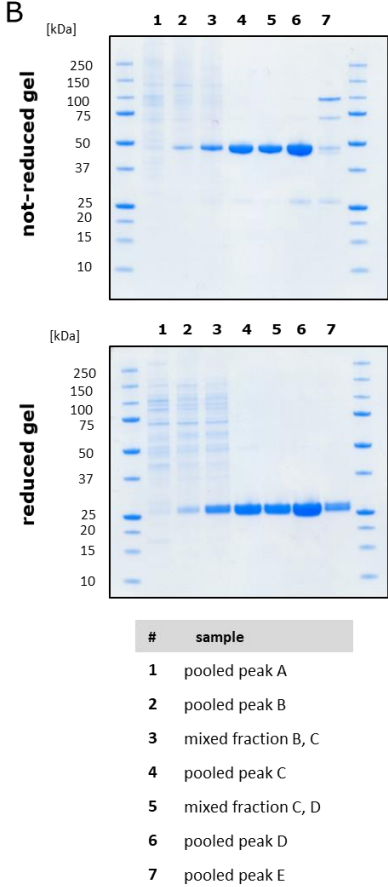


**Figure A3. Immobilized metal affinity chromatography (IMAC) purification of His<sub>6</sub>-tagged  $\alpha$ H-T-Fab.** (A) ÄKTA Pure (1 mL HisTrap™ HP column, GE Healthcare) chromatogram showing eluted protein fractions by increasing concentrations of imidazole. (B) SDS-PAGE analysis of not-reduced and reduced pooled peaks and mixed fractions. Here, peak C and D were pooled yielding pure  $\alpha$ H-T-Fab (SE-HPLC purity: 99.0%).

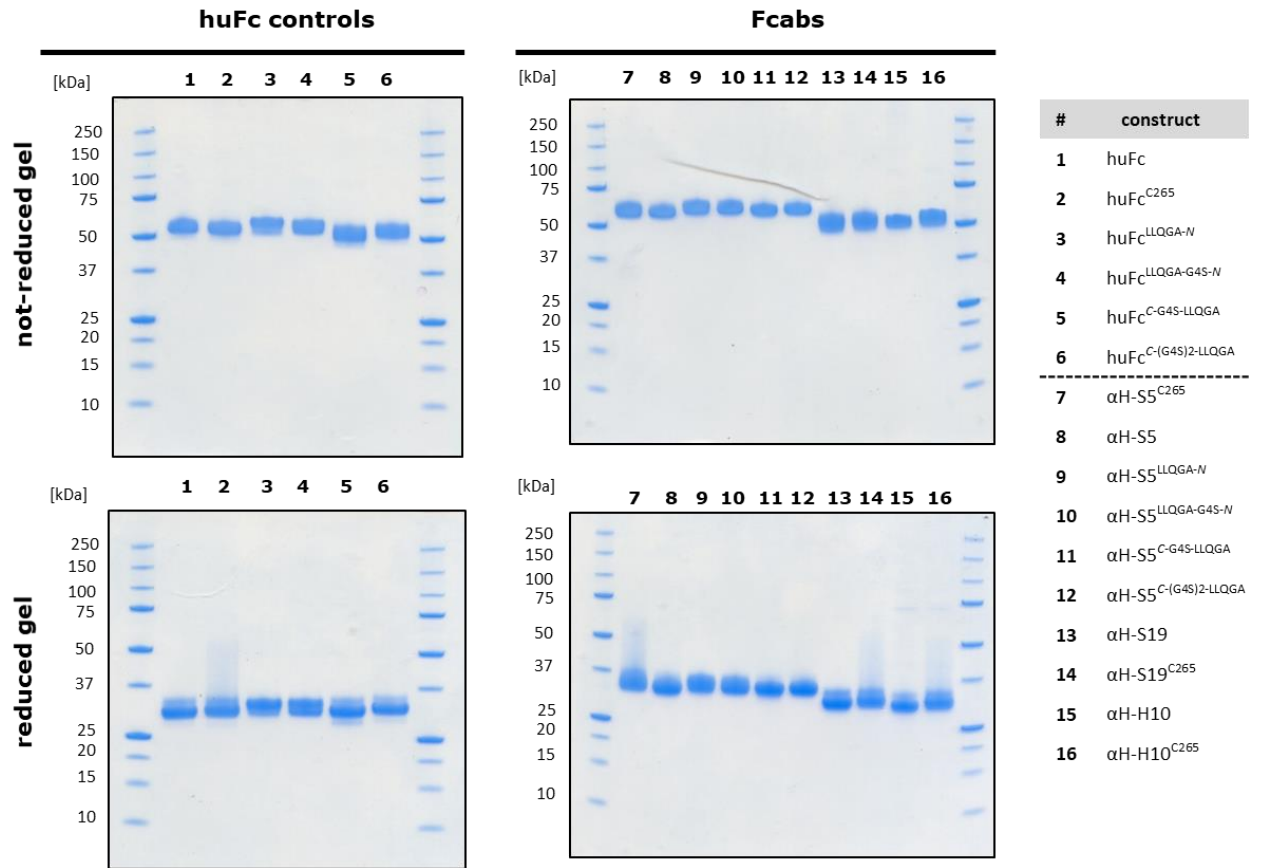


**Figure A4. SDS-PAGE exemplarily showing not-reduced and reduced purified huFc controls and HER2-targeting Fcab variants.** The bands of not-reduced constructs appear around the expected 50 kDa. When reduced, monomeric heavy chains appear at approx. 30 kDa. Higher apparent molecular weights of STAB5 variants (lane 7 – 12) compared to huFc, STAB19 or H10-03-6 CysP2 Cys variants (lane 1 – 6, 13 – 16) are probably caused by an additional glycosylation at an artificial NVS site in the engineered C<sub>H</sub>3 AB-loop of STAB5 which was also reported by Traxlmayr *et al.*<sup>258</sup>

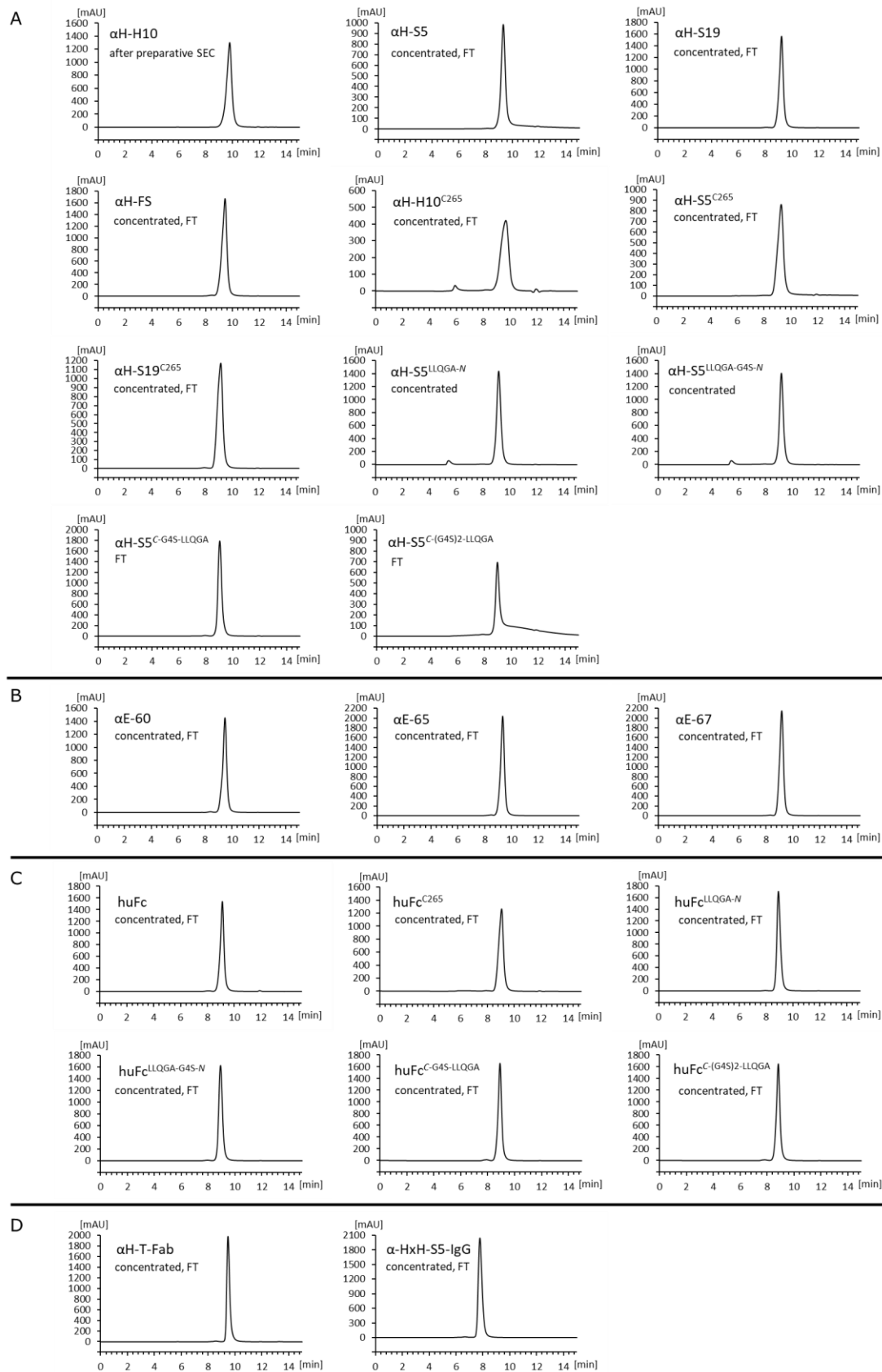


**Figure A5. Analytical SE-HPLC chromatograms (Abs. 214 nm) of purified Fcabs (A, B), human Fc controls (C) and references (D). Single peaks show high monomeric content and the absence of significant quantities of aggregates. FT – after freeze-thaw cycle.**

**Table A1. LC-MS analysis confirms the identity of Fcabs, huFc controls and references.** Mass variations between calculated and observed masses account for glycosylation patterns and standard measurement deviations. Only the most intense glycosylation patterns are listed.  $\alpha$ H-S5<sup>LLQGA-N</sup> and huFc<sup>LLQGA-N</sup> are partially O-glycosylated due to a potential O-glycosylation site (LLQGATCPPCP...) generated by the genetically introduced N-terminal LLQGA-tag. All STAB5 variants carry an additional Man5 glycosylation which is probably located at the artificial NVS glycosylation site in the engineered C<sub>H</sub>3 AB-loop. This artificial glycosylation site was also reported by Traxlmayr *et al.*<sup>258</sup>

<b>heavy chain</b>				
	calculated mass [kDa]	measured mass [kDa]	$\Delta$ mass [kDa]	most intense modifications
<b><math>\alpha</math>H-H10</b>	25.738	27.184	1.446	G0F (+1445 Da)
<b><math>\alpha</math>H-H10<sup>C265</sup></b>	25.770	27.378	1.608	G1F (+1607 Da)
<b><math>\alpha</math>H-S5</b>	25.546	28.370	2.824	Man5 (+1217 Da), G1F (+1607 Da)
<b><math>\alpha</math>H-S5<sup>C265</sup></b>	25.578	28.565	2.987	Man5 (+1217 Da), G2F (+1770 Da)
<b><math>\alpha</math>H-S5<sup>LLQGA-N</sup></b>	26.029	29.800	3.771	Man5 (+1217 Da), G1F (+1607 Da), partially O-glycosylated
<b><math>\alpha</math>H-S5<sup>LLQGA-G4S-N</sup></b>	26.344	29.166	2.822	Man5 (+1217 Da), G1F (+1607 Da)
<b><math>\alpha</math>H-S5<sup>C-G4S-LLQGA</sup></b>	26.344	29.332	2.988	Man5 (+1217 Da), G2F (+1770 Da)
<b><math>\alpha</math>H-S5<sup>C-(G4S)2-LLQGA</sup></b>	26.659	29.485	2.826	Man5 (+1217 Da), G1F (+1607 Da)
<b><math>\alpha</math>H-S19</b>	25.492	27.100	1.608	G1F (+1607 Da)
<b><math>\alpha</math>H-S19<sup>C265</sup></b>	25.524	27.130	1.606	G1F (+1607 Da)
<b><math>\alpha</math>H-FS</b>	25.067	26.671	1.604	G1F (+1607 Da)
<b><math>\alpha</math>E-60</b>	24.403	26.008	1.605	G1F (+1607 Da)
<b><math>\alpha</math>E-65</b>	24.378	25.984	1.606	G1F (+1607 Da)
<b><math>\alpha</math>E-67</b>	24.359	25.964	1.605	G1F (+1607 Da)
<b>huFc</b>	24.894	26.502	1.608	G1F (+1607 Da)
<b>huFc<sup>C265</sup></b>	24.926	26.695	1.769	G2F (+1770 Da)
<b>huFc<sup>LLQGA-N</sup></b>	25.377	26.820	1.443	G0F (+1445 Da), partially O-glycosylated
<b>huFc<sup>LLQGA-G4S-N</sup></b>	25.692	27.137	1.445	G0F (+1445 Da)
<b>huFc<sup>C-G4S-LLQGA</sup></b>	25.692	27.139	1.447	G0F (+1445 Da)
<b>huFc<sup>C-(G4S)2-LLQGA</sup></b>	26.007	27.615	1.608	G1F (+1607 Da)
<b><math>\alpha</math>H-T-Fab</b>	25.541	25.541	0.000	-
<b><math>\alpha</math>HxH-S5-IgG</b>	49.400	52.205	2.805	-pGlu (-17 Da), G1F (+1607 Da), Man5 (+1217 Da)
<b>light chain</b>				
	calculated mass [kDa]	measured mass [kDa]	$\Delta$ mass [kDa]	most intense modifications
<b><math>\alpha</math>H-T-Fab</b>	23.422	23.420	0.002	-
<b><math>\alpha</math>HxH-S5-IgG</b>	23.541	23.540	0.001	-

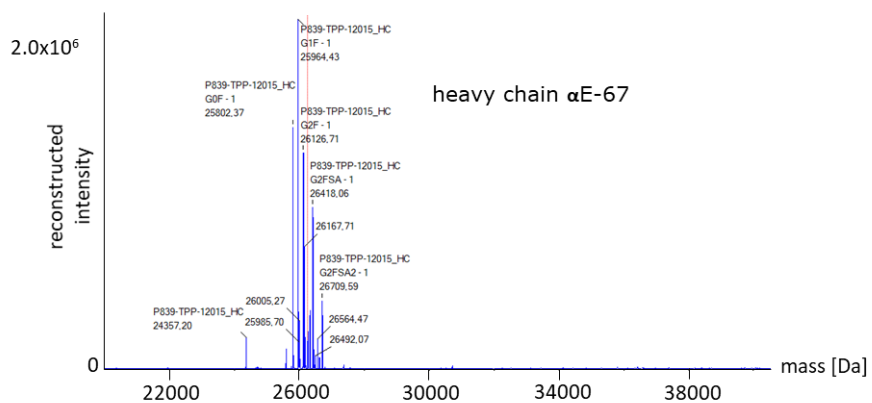
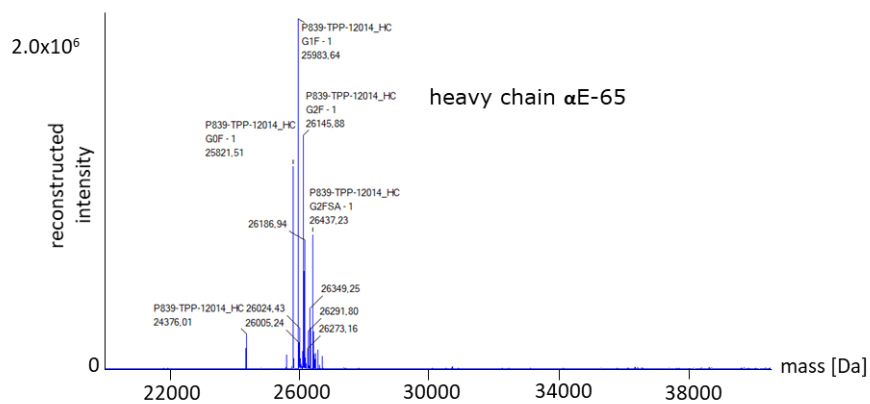
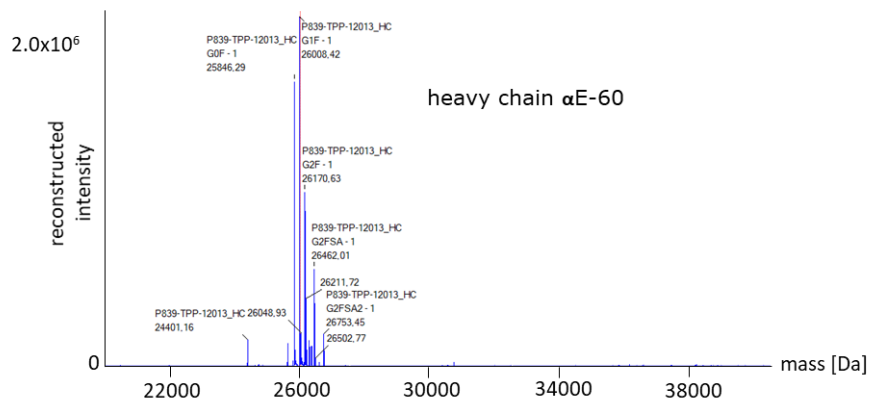


**Figure A6. Exemplary deconvoluted MS spectra of EGFR-targeting Fcabs.** Peaks represent heavy chains with distinct glycosylation patterns.

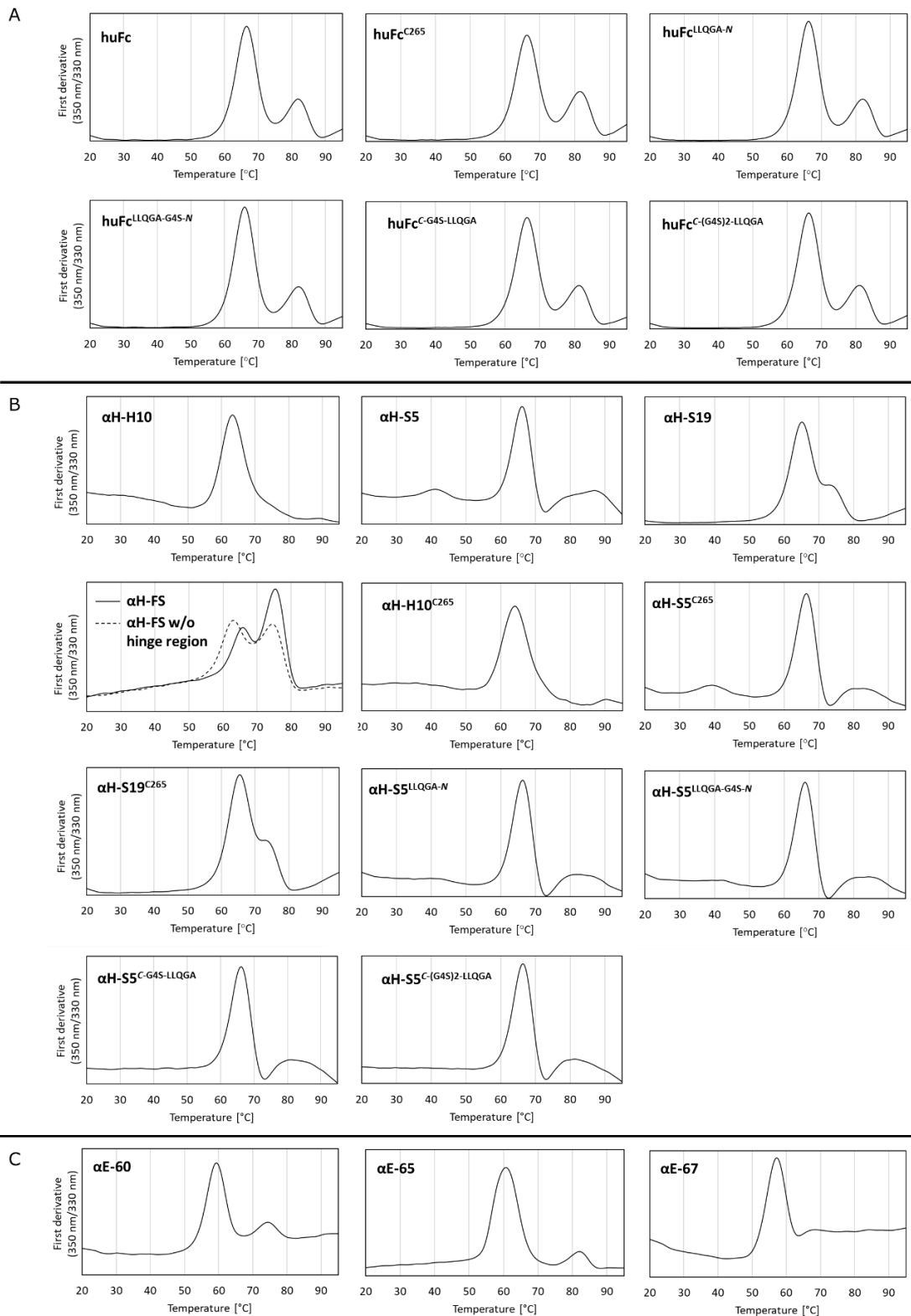


**Figure A7. Thermal stability of Fcabs and huFc control molecules. (A)** Typically, an Fc portion shows two unfolding transition midpoints  $T_m$  (peaks). The first  $T_{m1}$  between 60–70°C shows unfolding of the  $C_H2$  region while the second  $T_{m2}$  at > 80°C marks unfolding of the  $C_H3$  region. **(B)** HER2-binding Fcabs often do not show clear  $T_{m2}$ , probably due to the engineered antigen binding site in the  $C_H3$  region. **(C)** EGFR-binding Fcabs show reduced  $T_{m1}$  compared to huFc controls and HER2-binding Fcabs. This is probably due to the missing hinge interchain cysteines of  $\alpha E-60$ ,  $\alpha E-65$ ,  $\alpha E-67$ . Cleavage of hinge region by IdeS reduces  $T_{m1}$  as shown for  $\alpha H-FS$ .

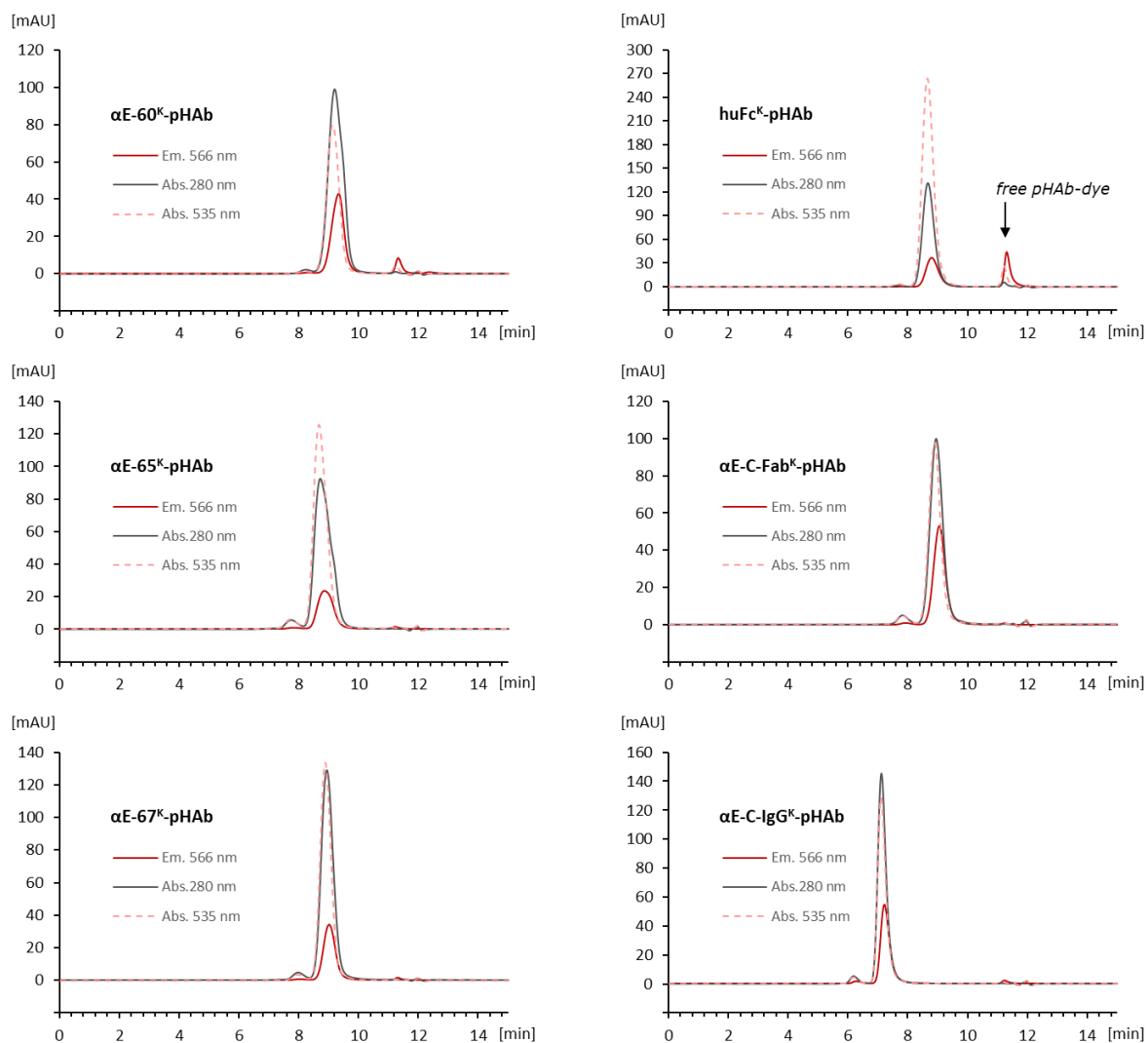


**Figure A8. SE-HPLC characterization of pAb-dye conjugates exemplarily shown for EGFR-targeting subset.** SE-HPLC of purified amine-coupled pAb-dye conjugates showing absorption at 280 nm (protein and pAb-dye) and 535 nm (pAb-dye) as well as pAb-dye fluorescence (Exc. 535 nm, Em. 566 nm). At  $t_R$  11 – 12 min unconjugated pAb-dye may elute. Degree of pAb-dye labeling (DOL) can be derived from individual peak areas as described in section 6.12.20.

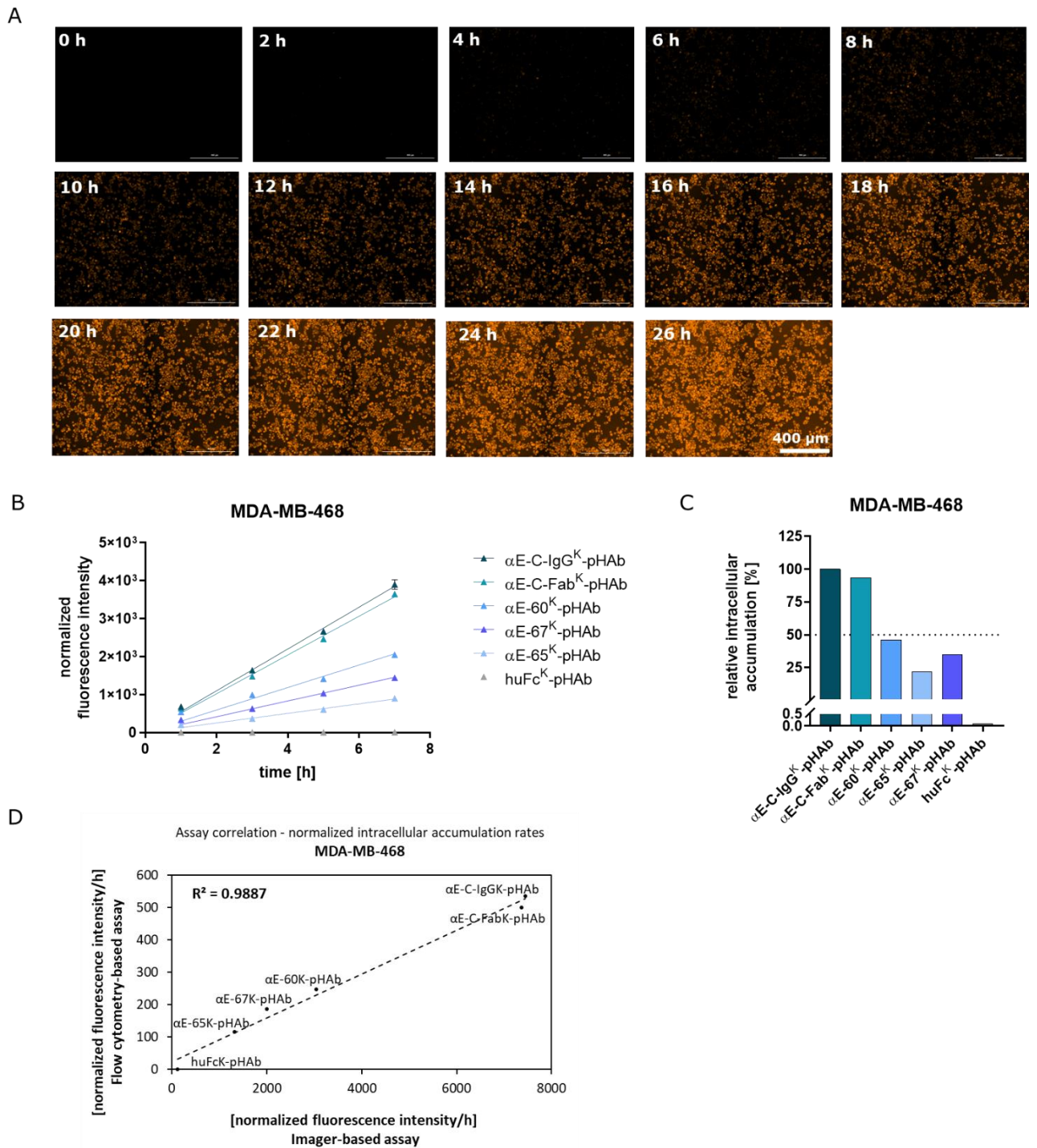


**Figure A9. Cellular uptake kinetics of pHAb-dye labeled EGFR-targeting constructs.** (A) Cellular accumulation time series exemplarily shown for  $\alpha$ E-60<sup>K</sup>-pHAb on MDA-MB-468 cells. Cells were incubated at 37°C, 80% humidity and 5% CO<sub>2</sub> with 100 nM  $\alpha$ E-60<sup>K</sup>-pHAb and RFP channel images (Exc. 531 nm, Em. 593 nm) were recorded every 2 h for 26 h using a cell imaging reader equipped with an automated incubator. (B) Cell number and pHAb-dye DOL normalized intracellular accumulation rates measured by a flow cytometry-based cellular uptake assay. pHAb-dye labeled constructs (100 nM) were incubated in the dark on non-adherent MDA-MB-468 cells at 37°C and 4°C (reference) for 1, 3, 5 and 7 h (duplicates). Cells were washed twice with PBS-1% BSA, and finally pHAb-dye fluorescence intensity was measured by flow cytometry. Fluorescence of cells incubated at 4°C was subtracted from fluorescence of cells incubated at 37°C. (C) Flow cytometry assay relative intracellular accumulation derived from normalized intracellular accumulation rates by setting the highest rate 100% ( $\alpha$ E-C-IgG<sup>K</sup>-pHAb) (D) Relative intracellular accumulation in MDA-MB-468 cells derived from flow cytometry-based assay confirms the imaging-based cellular uptake data for MDA-MB-468 cells.

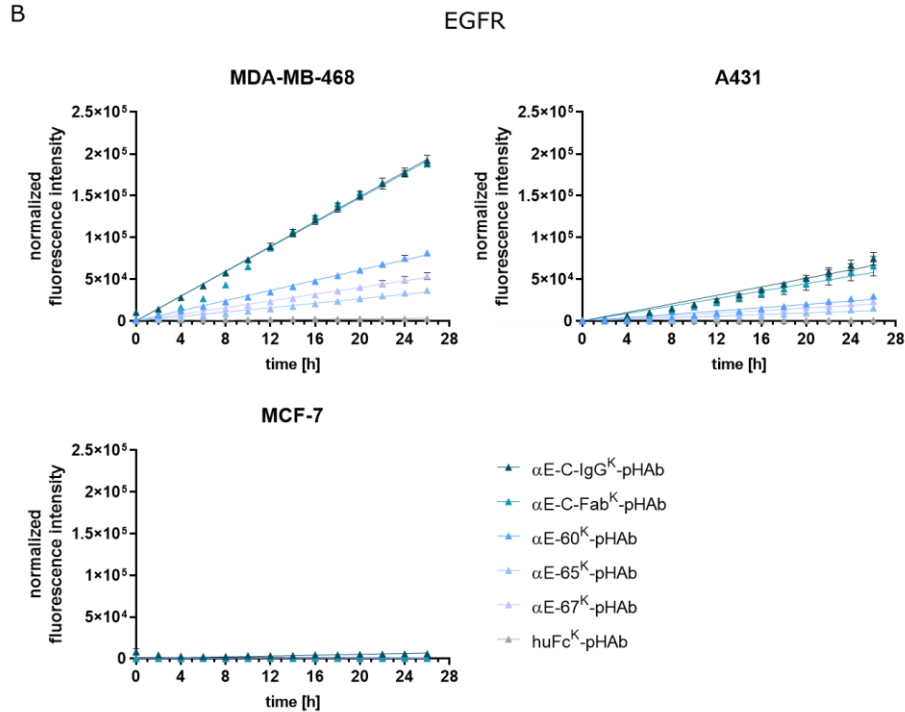
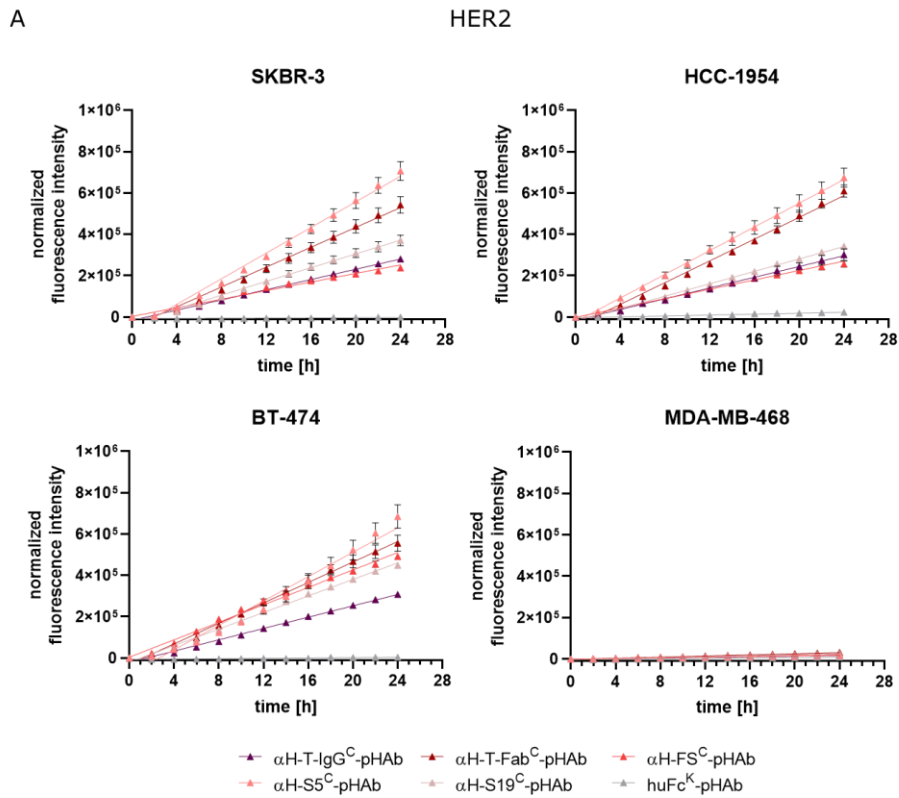


**Figure A10. Cellular uptake kinetics of pHAb-dye labeled constructs.** Intracellular accumulation was monitored for 24-26 h at 100 nM in triplicates. The total fluorescence intensity of recorded images is normalized to the cell-number and the DOL of the pHAb-dye labeled construct and plotted over time to derive normalized intracellular accumulation rates from slopes of a linear regression. Subsequently, the relative intracellular accumulation can be calculated from these rates.

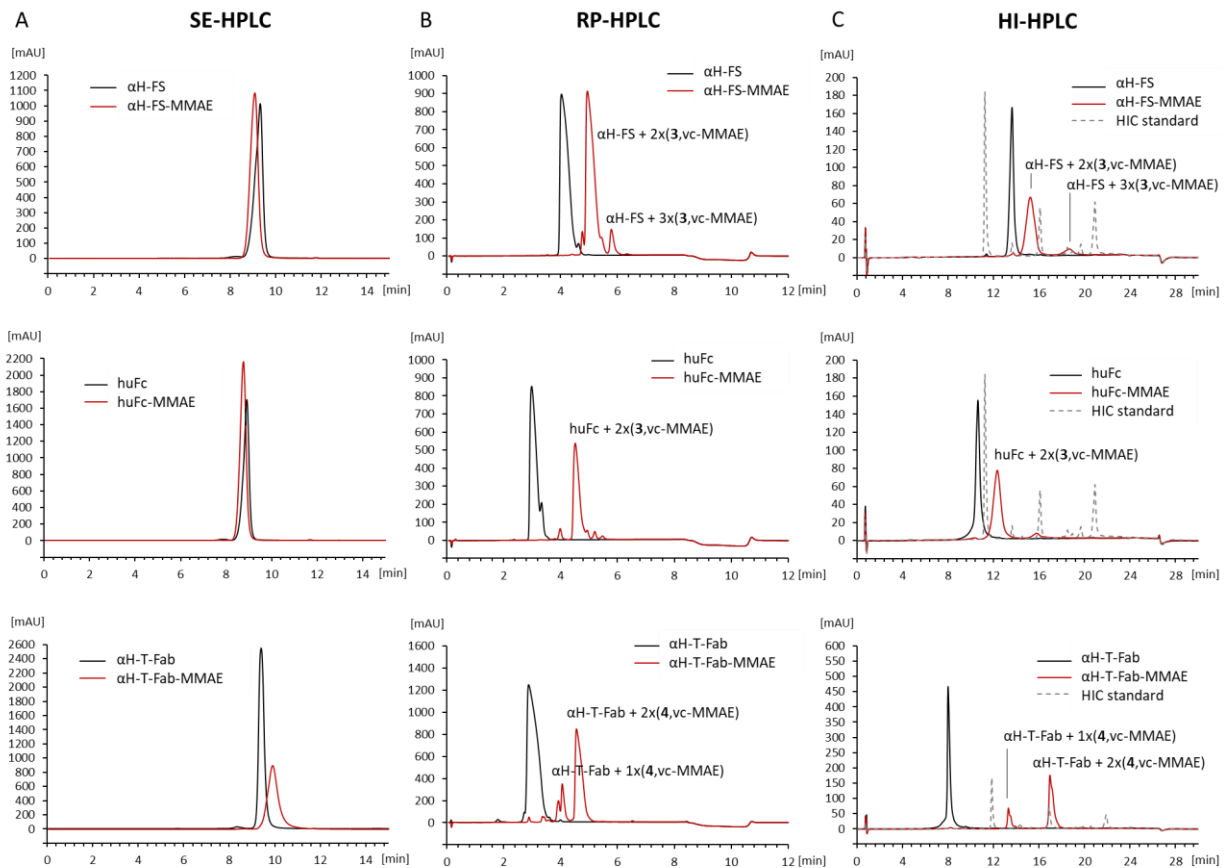


**Figure A11. Chromatographic characterization of generated MMAE conjugates exemplarily shown for  $\alpha$ H-FS-MMAE, huFc-MMAE and  $\alpha$ H-T-Fab-MMAE.** (A) Analytical size exclusion SE-HPLC shows a distinct single peak demonstrating formation of monomeric drug conjugates without aggregates. Signal intensity represents absorption at 214 nm (B) Reversed phase RP-HPLC reveals conjugation of Gly<sub>3</sub>-Val-Cit-MMAE (3) or mc-Val-Cit-MMAE (4). RP-DAR is calculated from peak areas of individual DAR species. For example, 25% relative peak area of DAR 1 species  $\alpha$ H-T-Fab-MMAE and 75% relative peak area of DAR 2 species  $\alpha$ H-T-Fab-MMAE reveals a final RP-DAR of 1.75. Signal intensity represents absorption at 214 nm. (C) Hydrophobic interaction HI-HPLC separates distinct DAR species according to their hydrophobicity. HIC-DAR can be calculated from peak areas just as RP-DAR. Moreover, relative retention times (RRT) can be calculated from HIC data to characterize the intrinsic hydrophobicity of an ADC. RRT were calculated from the elution times of e.g., the DAR 2.0 drug conjugate and the parental antibody emphasizing the hydrophobicity added by linker-drug to each construct. Signal intensity represents absorption at 280 nm.

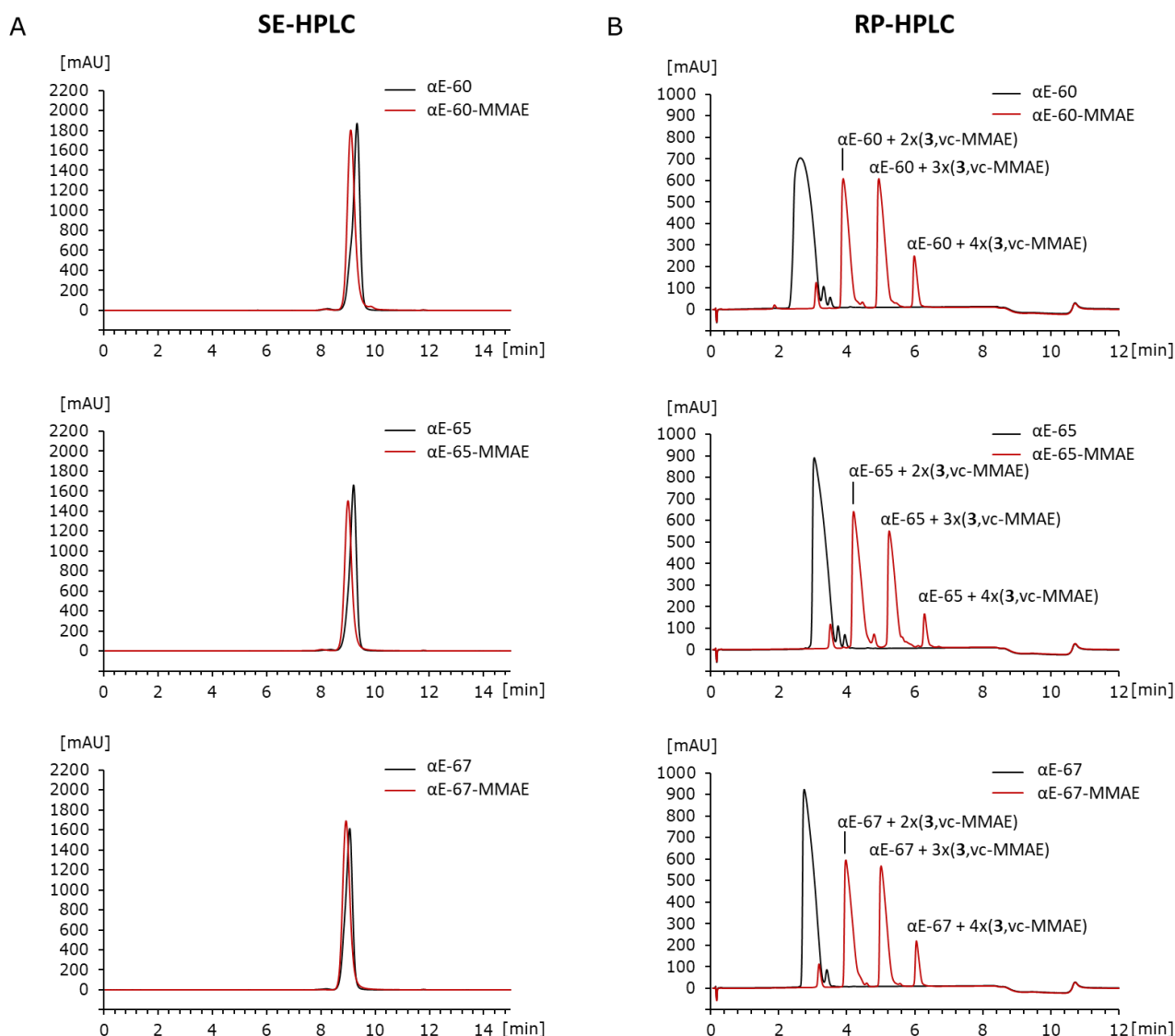


**Figure A12. Chromatographic characterization of EGFR-targeting Fcab-MMAE conjugates.** (A) Analytical size exclusion SE-HPLC shows a distinct single peak demonstrating formation of monomeric drug conjugates without aggregates. Signal intensity represents absorption at 214 nm (B) Reversed phase RP-HPLC reveals conjugation of Gly<sub>3</sub>-Val-Cit-MMAE (3). RP-DAR is calculated from peak areas of individual DAR species (αE-60-MMAE RP-DAR 2.6; αE-65-MMAE RP-DAR 2.5; αE-67-MMAE RP-DAR 2.5). Signal intensity represents absorption at 214 nm.

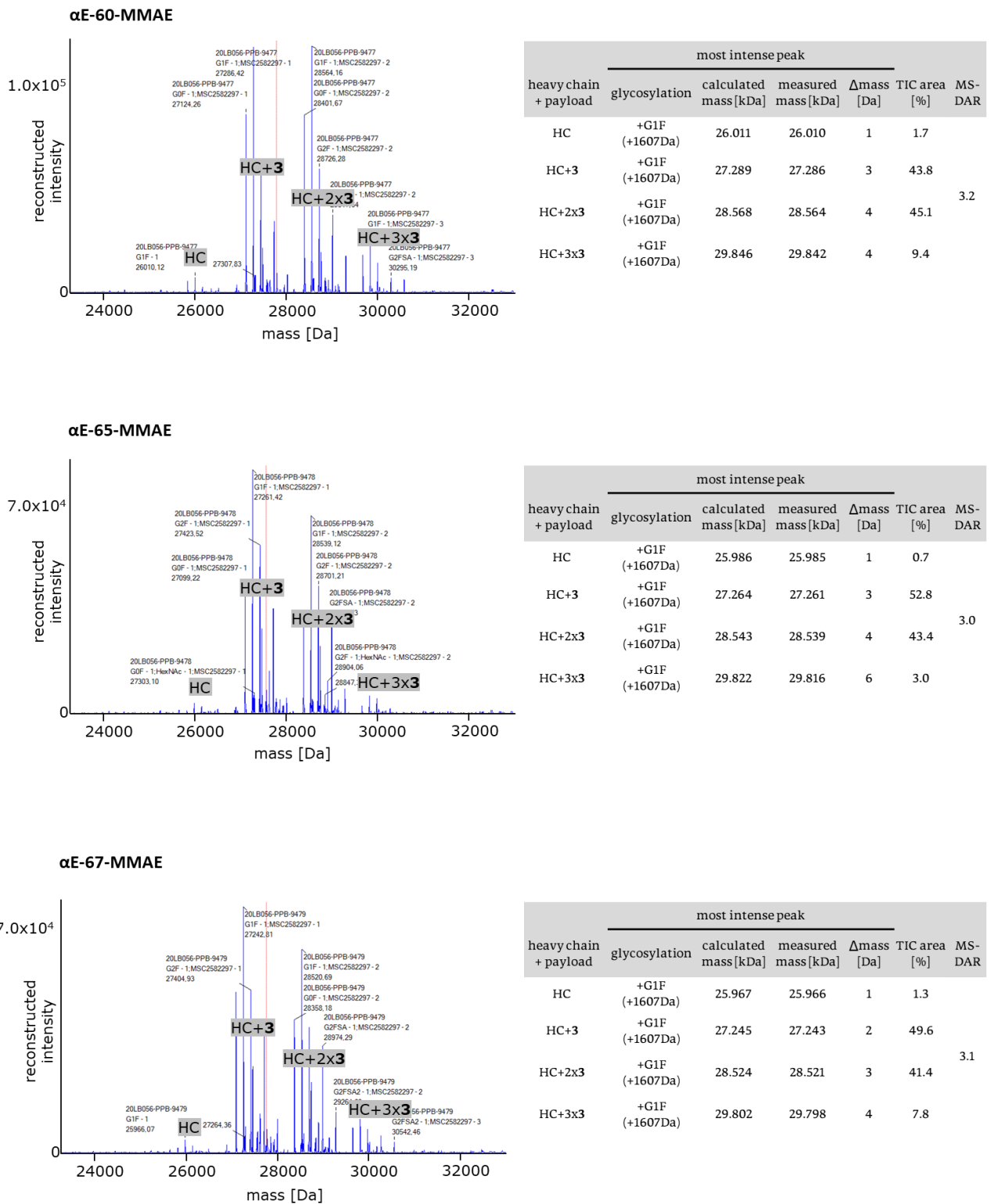


**Figure A13. MS-DAR determination of EGFR-targeting Fcab-MMAE conjugates from TIC area.** Deconvoluted MS spectra showing groups of differently glycosylated heavy chains (HC) carrying 0 – 3 Gly<sub>3</sub>-Val-Cit-MMAE (3). Total ion count (TIC) area of HC species carrying 0 – 3 linker payloads were used to calculate the MS-DAR as shown in tables on the right side.

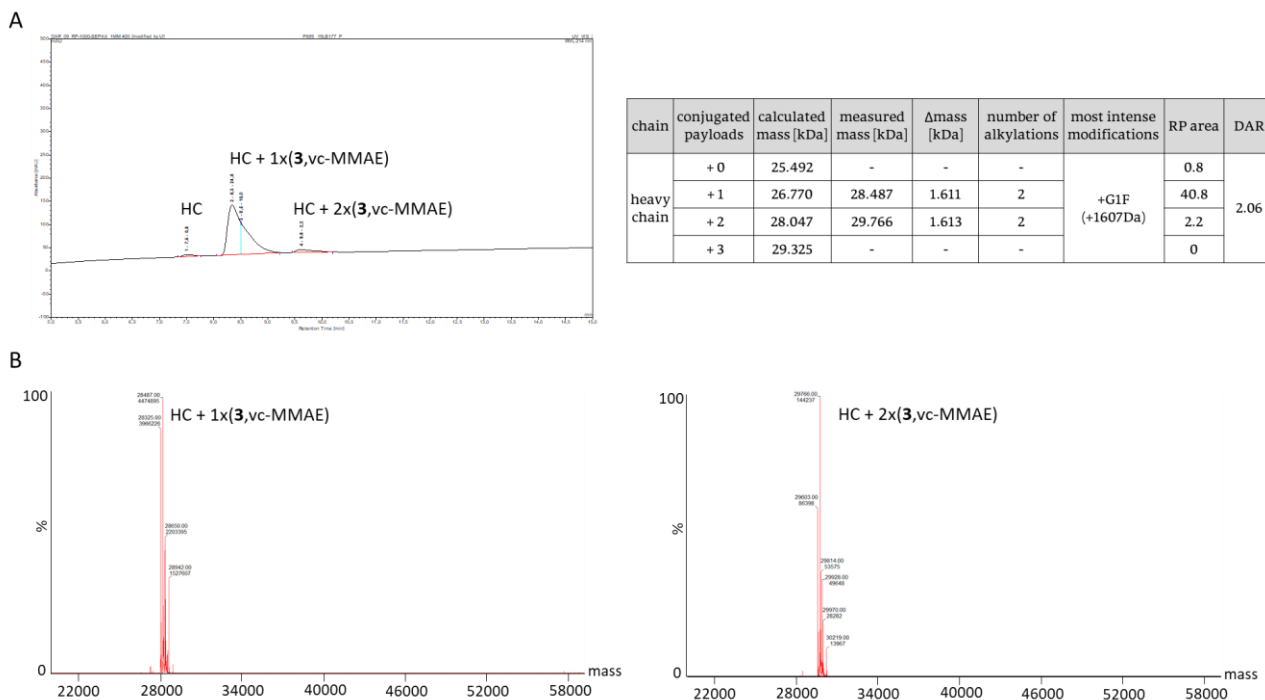


**Figure A14 Exemplary LC-MS DAR determination of  $\alpha$ H-S19-MMAE.** (A) Reversed phase chromatogram of reduced drug conjugate and DAR calculation from RP peak areas. (B) Deconvoluted MS spectra were used to assign RP peaks to individual heavy chain species conjugated with Gly<sub>3</sub>-Val-Cit-MMAE (3).

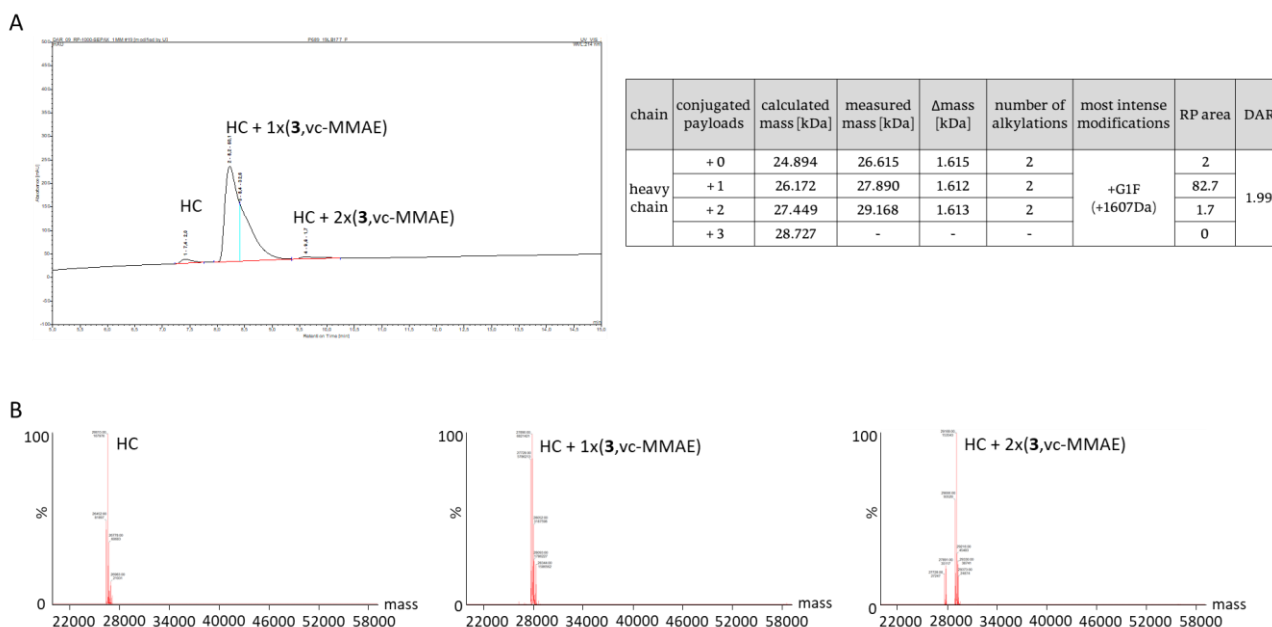


**Figure A15. Exemplary LC-MS-DAR determination of huFc-MMAE.** (A) Reversed phase chromatogram of reduced drug conjugate and DAR calculation from RP peak areas. (B) Deconvoluted MS spectra were used to assign RP peaks to individual heavy chain species conjugated with Gly<sub>3</sub>-Val-Cit-MMAE (3).

**Table A2. Kinetic parameters for target binding.** Dissociation constants ( $K_D$ ), on- ( $k_{on}$ ) and off-rates ( $k_{off}$ ) were measured at pH 7.4 by BLI using recombinantly produced HER2 or EGFR. Errors are standard errors from fitting using FortéBio data analysis software. Fitting quality is characterized by  $R^2$ .

HER2 subset	HER2						
	$K_{D,BLI}$ [nM]	$K_D$ error [nM]	$k_{on}$ [ $10^6$ /Ms]	$k_{on}$ error [ $10^6$ /Ms]	$k_{off}$ [ $10^{-3}$ /s]	$k_{off}$ error [ $10^{-3}$ /s]	full fitting $R^2$
$\alpha$ H-S5	2.25	0.029	1.158	0.014	2.605	0.011	0.9768
$\alpha$ H-S5-MMAE	3.83	0.041	0.837	0.009	3.210	0.011	0.9865
$\alpha$ H-S5 <sup>C265</sup>	3.52	0.057	1.430	0.009	5.040	0.076	0.9977
$\alpha$ H-S5 <sup>C265</sup> -MMAE	3.36	0.041	1.042	0.012	3.499	0.012	0.9797
$\alpha$ H-S5 <sup>LLQGA-N</sup>	3.52	0.104	0.836	0.005	5.430	0.079	0.9976
$\alpha$ H-S5 <sup>LLQGA-N</sup> -MMAE	3.24	0.038	0.928	0.010	3.002	0.011	0.9812
$\alpha$ H-S5 <sup>LLQGA-G4S-N</sup>	6.32	0.067	0.965	0.005	6.090	0.057	0.9985
$\alpha$ H-S5 <sup>LLQGA-G4S-N</sup> -MMAE	5.22	0.055	0.595	0.006	3.105	0.011	0.9855
$\alpha$ HxH-S5-IgG	7.86	0.092	0.424	0.005	3.337	0.012	0.9903
$\alpha$ H-S19	46.60	0.994	1.230	0.021	57.500	0.716	0.9952
$\alpha$ H-S19-MMAE	48.52	0.900	0.531	0.007	25.760	0.311	0.9960
$\alpha$ H-S19 <sup>C265</sup>	39.80	0.885	1.270	0.025	50.300	0.549	0.9934
$\alpha$ H-S19 <sup>C265</sup> -MMAE	29.06	2.198	0.745	0.047	21.640	0.918	0.9742
$\alpha$ H-H10	24.13	0.462	0.254	0.005	6.117	0.032	0.9789
$\alpha$ H-FS	0.34	0.004	1.331	0.009	0.450	0.005	0.9953
$\alpha$ H-FS-MMAE	0.73	0.008	0.756	0.005	0.554	0.005	0.9930
$\alpha$ H-T-Fab	0.12	<0.001	1.100	0.004	0.131	0.001	0.9986
$\alpha$ H-T-Fab-MMAE	0.40	0.006	0.379	0.001	0.150	0.002	0.9987
$\alpha$ H-T-IgG	0.18	0.006	0.307	0.001	0.055	0.002	0.9900
$\alpha$ H-T-IgG-MMAE	0.43	0.008	0.287	0.001	0.123	0.002	0.9986
EGFR subset	EGFR						
	$K_{D,BLI}$ [nM]	$K_D$ error [nM]	$k_{on}$ [ $10^6$ /Ms]	$k_{on}$ error [ $10^6$ /Ms]	$k_{off}$ [ $10^{-3}$ /s]	$k_{off}$ error [ $10^{-3}$ /s]	full fitting $R^2$
$\alpha$ E-60	2.42	0.01	0.311	0.001	0.752	0.001	0.9995
$\alpha$ E-60-MMAE	2.67	0.02	0.346	0.002	0.924	0.003	0.9979
$\alpha$ E-65	1.07	0.01	0.371	0.001	0.397	0.001	0.9991
$\alpha$ E-65-MMAE	1.37	0.01	0.385	0.001	0.528	0.002	0.9991
$\alpha$ E-67	1.71	0.01	0.332	0.001	0.568	0.002	0.9991
$\alpha$ E-67-MMAE	1.54	0.01	0.405	0.001	0.622	0.001	0.9993
$\alpha$ E-C-Fab	0.82	0.00	0.713	0.003	0.585	0.002	0.9995
$\alpha$ E-C-IgG	1.25	0.01	1.172	0.008	1.462	0.004	0.9959
$\alpha$ E-C-IgG-MMAE	0.60	0.01	1.451	0.012	0.868	0.004	0.9941

**Table A3. Kinetic parameters for FcRn binding.** Dissociation constants ( $K_D$ ), on- ( $k_{on}$ ) and off-rates ( $k_{off}$ ) were measured by BLI using recombinantly produced FcRn. Binding affinity to FcRn was determined at pH 6.0. Errors are standard errors from fitting using FortéBio data analysis software. Fitting quality is characterized by  $R^2$ .

HER2 subset	FcRn						
	$K_{D,BLI}$ [nM]	$K_D$ error [nM]	$k_{on}$ [10 <sup>6</sup> /Ms]	$k_{on}$ error [10 <sup>6</sup> /Ms]	$k_{off}$ [10 <sup>-3</sup> /s]	$k_{off}$ error [10 <sup>-3</sup> /s]	full fitting $R^2$
<b>αH-S5</b>	399	15	0.300	0.009	120	3	0.9949
<b>αH-S5-MMAE</b>	274	11	0.328	0.010	90	3	0.9917
<b>αH-S5<sup>C265</sup></b>	376	13	0.378	0.011	142	3	0.9953
<b>αH-S5<sup>C265</sup>-MMAE</b>	350	35	0.327	0.022	115	9	0.9435
<b>αH-S5<sup>LLQGA-N</sup></b>	389	13	0.377	0.010	147	3	0.9956
<b>αH-S5<sup>LLQGA-N</sup>-MMAE</b>	284	9	0.321	0.008	91	2	0.9942
<b>αH-S5<sup>LLQGA-G4S-N</sup></b>	357	12	0.390	0.011	139	3	0.9951
<b>αH-S5<sup>LLQGA-G4S-N</sup>-MMAE</b>	226	8	0.374	0.009	85	2	0.9935
<b>αH-S19</b>	383	13	0.421	0.012	161	3	0.9958
<b>αH-S19-MMAE</b>	609	25	0.203	0.007	123	3	0.9944
<b>αH-S19<sup>C265</sup></b>	448	15	0.354	0.009	159	3	0.9965
<b>αH-S19<sup>C265</sup>-MMAE</b>	305	36	0.440	0.037	134	11	0.9046
<b>αH-H10</b>	399	15	0.300	0.010	99	2	0.9946
<b>αH-FS</b>	346	11	0.403	0.010	139	3	0.9949
<b>αH-FS-MMAE</b>	339	11	0.426	0.012	144	3	0.9949
<b>αH-T-IgG</b>	303	9	0.482	0.012	146	3	0.9965
<b>αH-T-IgG-MMAE</b>	387	11	0.372	0.009	144	3	0.9967
EGFR subset	FcRn						
	$K_{D,BLI}$ [nM]	$K_D$ error [nM]	$k_{on}$ [10 <sup>6</sup> /Ms]	$k_{on}$ error [10 <sup>6</sup> /Ms]	$k_{off}$ [10 <sup>-3</sup> /s]	$k_{off}$ error [10 <sup>-3</sup> /s]	full fitting $R^2$
<b>αE-60</b>	381	12	0.292	0.007	111	2	0.9958
<b>αE-60-MMAE</b>	309	10	0.232	0.006	72	2	0.9971
<b>αE-65</b>	329	13	0.339	0.011	112	2	0.9954
<b>αE-65-MMAE</b>	362	12	0.210	0.005	76	2	0.9958
<b>αE-67</b>	589	22	0.289	0.009	170	3	0.9952
<b>αE-67-MMAE</b>	337	12	0.232	0.007	78	2	0.9964
<b>αE-C-IgG</b>	747	24	0.219	0.006	164	2	0.9975
<b>αE-C-IgG-MMAE</b>	892	31	0.185	0.006	165	3	0.9974
<b>huFc</b>	524	13	0.407	0.009	213	2	0.9982

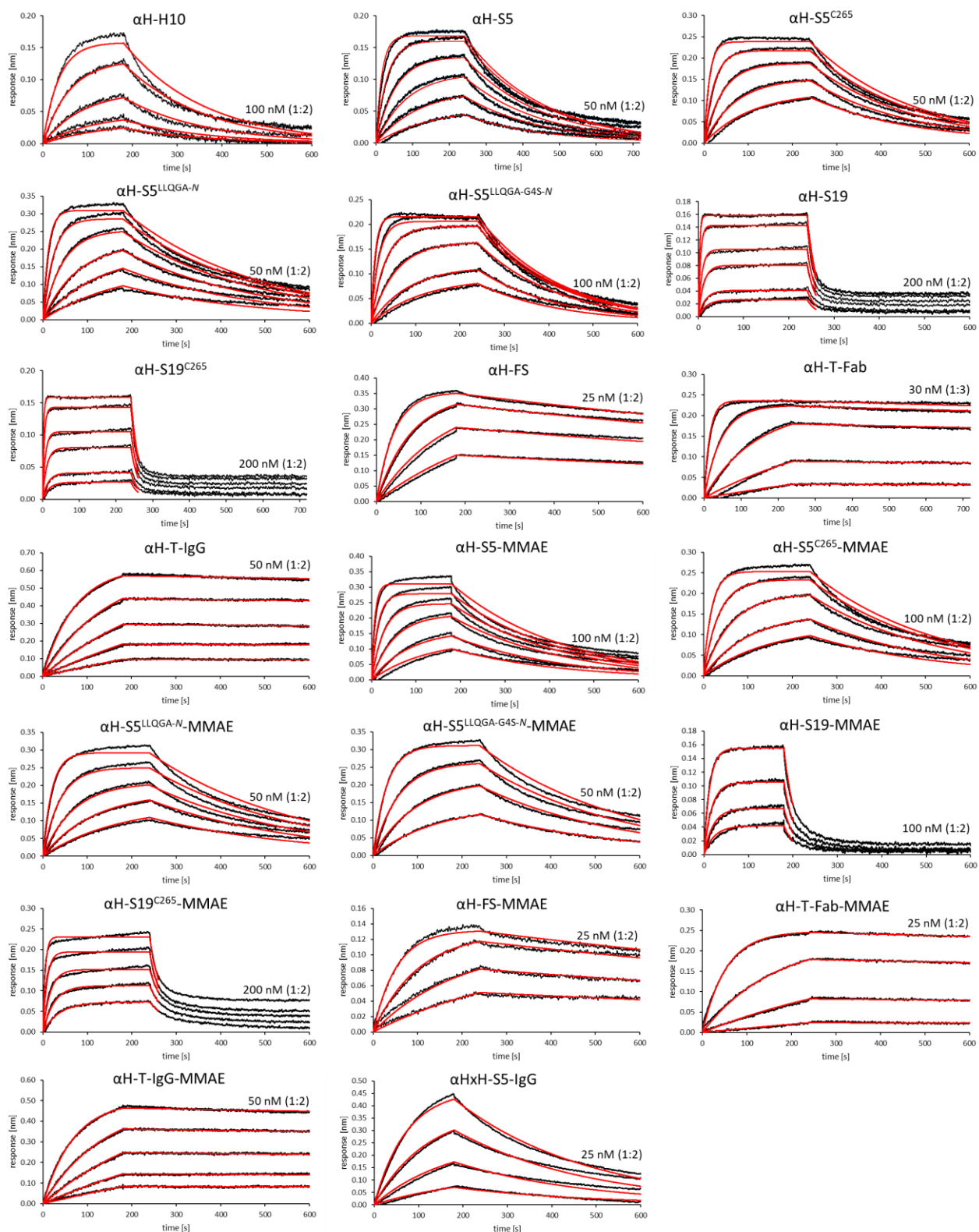


**Figure A16.** HER2 binding analysis of unconjugated Fcabs, Trastuzumab variants and corresponding MMAE conjugates *via* BLI. Association and dissociation were either fitted by a 1:1 global full-fit binding model or by a 1:1 global partial-dissociation model (only S19 variants). Fittings are shown in red. For each sensorgram, the highest concentration of analyte during association and its dilution factor are given.

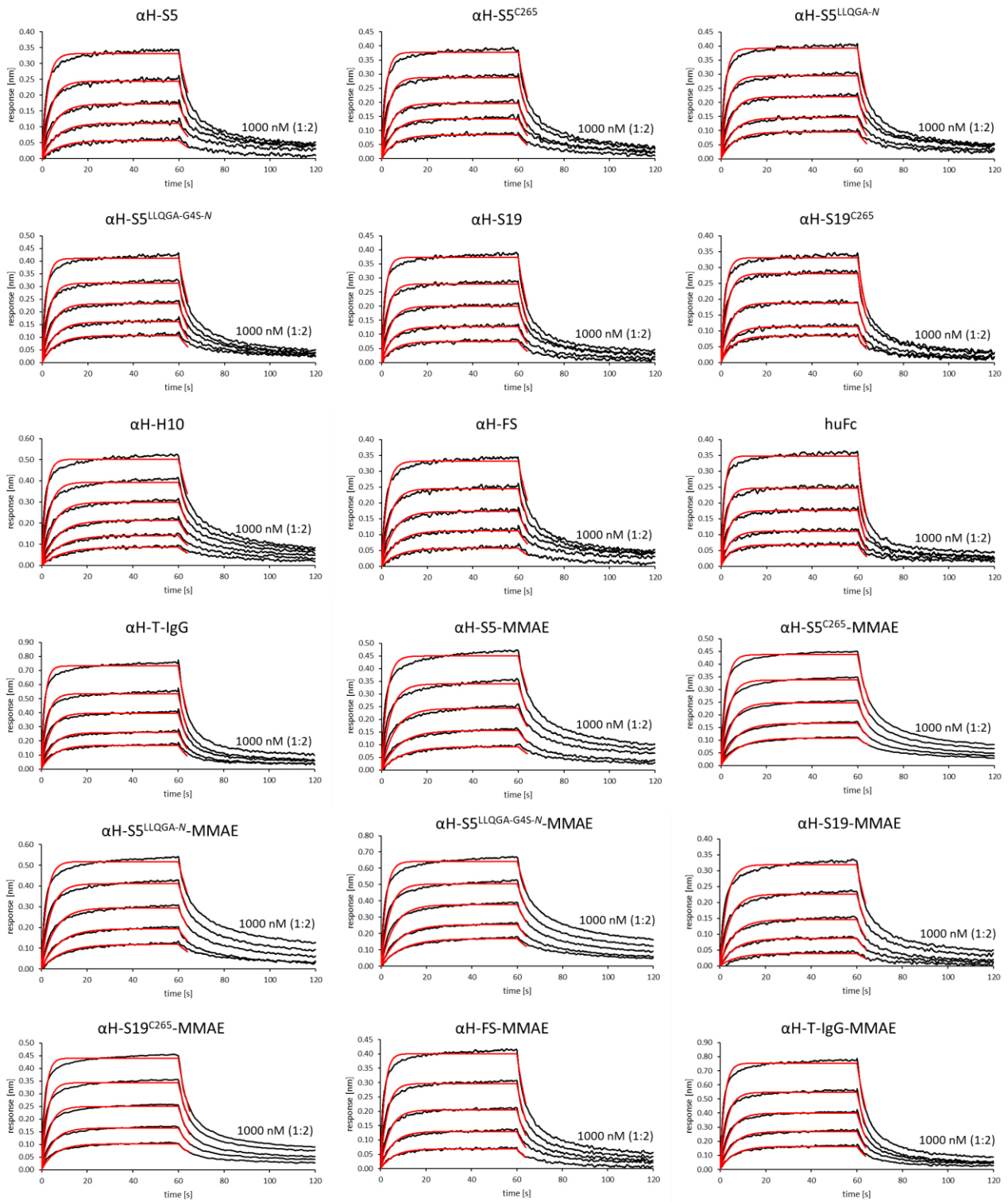


**Figure A17. FcRn binding analysis of HER2-targeting subset *via* BLI.** Association and dissociation of analytes (1  $\mu$ M; 1:2 serially diluted) were recorded at pH 6.0 and fitted by a 1:1 global partial-dissociation model. Fittings are shown in red.

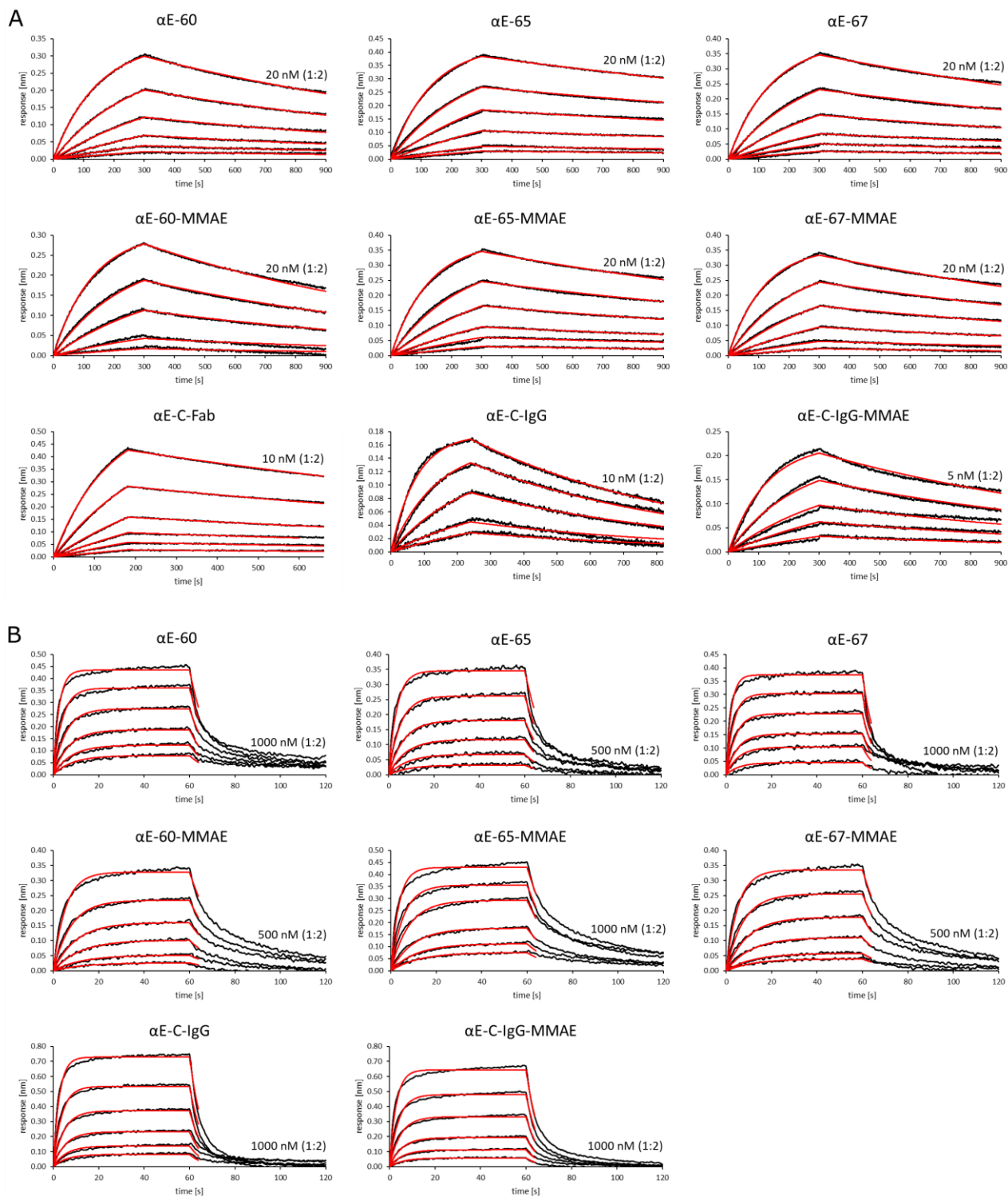


**Figure A18. Receptor binding BLI sensorgrams of EGFR-targeting subset. (A)** EGFR binding analysis. Association and dissociation were recorded at pH 7.4 and fitted by a 1:1 global full-fit binding model. **(B)** FcRn binding analysis. Association and dissociation of analytes were recorded at pH 6.0 and fitted by a 1:1 global partial-dissociation model. Fittings are shown in red. For each sensorgram, the highest concentration of analyte during association and its dilution factor are given.

**Table A4. *In vitro* potency of Fcab-drug conjugates and controls.** Inhibitory concentrations at 50% cell viability ( $IC_{50}$ ) are given as the mean ( $\pm$  SD) of  $\geq 3$  independent experiments of which each experiment was performed in duplicates. Cell viability was measured after 4 days incubation. To judge  $IC_{50}$  values, DAR values and target dissociation constants ( $K_{D,BLI}$ ) are listed as well.

HER2 subset	$K_{D,BLI}$ (HER2) [nM]	DAR	$IC_{50}$ [nM]		
			SKBR-3 (HER2 <sup>+</sup> )	HCC-1954 (HER2 <sup>+</sup> )	MDA-MB-468 (HER2 <sup>-</sup> )
<b><math>\alpha</math>H-S5-MMAE</b>	3.8	2.0	4.04 $\pm$ 0.66	8.38 $\pm$ 1.09	267 $\pm$ 20
<b><math>\alpha</math>H-S5<sup>C265</sup>-MMAE</b>	3.4	1.5	4.12 $\pm$ 0.41	7.26 $\pm$ 1.61	> 300
<b><math>\alpha</math>H-S5<sup>LLQGA-N</sup>-MMAE</b>	3.2	2.4	2.11 $\pm$ 0.39	2.55 $\pm$ 0.28	> 100
<b><math>\alpha</math>H-S5<sup>LLQGA-G4S-N</sup>-MMAE</b>	5.2	3.0	1.85 $\pm$ 0.80	2.49 $\pm$ 0.72	> 100
<b><math>\alpha</math>H-S19-MMAE</b>	48.5	2.1	27.0 $\pm$ 17.6	28.5 $\pm$ 4.95	> 300
<b><math>\alpha</math>H-S19<sup>C265</sup>-MMAE</b>	29.1	1.1	29.4 $\pm$ 1.64	48.5 $\pm$ 10.4	> 300
<b><math>\alpha</math>H-FS-MMAE</b>	0.7	2.2	0.18 $\pm$ 0.04	0.63 $\pm$ 0.10	> 300
<b>huFc-MMAE</b>	-	2.0	237 $\pm$ 39	> 100	> 300
<b>huFc<sup>C265</sup>-MMAE</b>	-	1.8	250 $\pm$ 41	> 300	> 300
<b>huFc<sup>LLQGA-N</sup>-MMAE</b>	-	1.4	250	> 100	> 300
<b>huFc<sup>LLQGA-G4S-N</sup>-MMAE</b>	-	2.2	96.8 $\pm$ 27.3	> 100	> 300
<b><math>\alpha</math>H-T-Fab-MMAE</b>	0.4	1.8	0.27 $\pm$ 0.07	0.29 $\pm$ 0.06	> 100
<b><math>\alpha</math>H-T-IgG-MMAE</b>	0.4	2.0	0.19 $\pm$ 0.05	0.23 $\pm$ 0.06	> 100
<b>MMAE</b>	-	-	0.19 $\pm$ 0.03	0.14 $\pm$ 0.03	0.33 $\pm$ 0.04
<b><math>\alpha</math>H-S5</b>	2.2	-	> 300	> 300	> 300
<b><math>\alpha</math>H-S5<sup>C265</sup></b>	3.5	-	> 300	> 300	> 300
<b><math>\alpha</math>H-S5<sup>LLQGA-N</sup></b>	3.5	-	> 300	> 300	> 300
<b><math>\alpha</math>H-S5<sup>LLQGA-G4S-N</sup></b>	6.3	-	> 300	> 300	> 300
<b><math>\alpha</math>H-S19</b>	46.6	-	> 300	> 300	> 300
<b><math>\alpha</math>H-S19<sup>C265</sup></b>	39.8	-	> 300	> 300	> 300
<b><math>\alpha</math>H-FS</b>	0.3	-	> 300	> 300	> 300
<b>huFc</b>	-	-	> 300	> 300	> 300
<b><math>\alpha</math>H-T-Fab</b>	0.1	-	> 300	> 300	> 300
<b><math>\alpha</math>H-T-IgG</b>	0.2	-	1.17	1.17	> 300
EGFR subset	$K_{D,BLI}$ (EGFR) [nM]	DAR	$IC_{50}$ [nM]		
			MDA-MB-468 (EGFR <sup>+</sup> )	A431 (EGFR <sup>+</sup> )	MCF-7 (EGFR <sup>-</sup> )
<b><math>\alpha</math>E-60-MMAE</b>	2.7	2.9	0.18 $\pm$ 0.03	0.23 $\pm$ 0.04	> 100
<b><math>\alpha</math>E-65-MMAE</b>	1.4	2.7	0.19 $\pm$ 0.05	0.27 $\pm$ 0.07	> 100
<b><math>\alpha</math>E-67-MMAE</b>	1.5	2.8	0.22 $\pm$ 0.01	0.32 $\pm$ 0.08	> 100
<b>huFc-MMAE</b>	-	2.0	> 300	> 100	> 100
<b><math>\alpha</math>E-C-Fab-MMAE</b>	n.d.	0.8	0.78 $\pm$ 0.03	0.99 $\pm$ 0.29	> 100
<b><math>\alpha</math>E-C-IgG-MMAE</b>	0.6	1.1	0.44 $\pm$ 0.03	0.50 $\pm$ 0.08	> 100
<b>MMAE</b>	-	-	0.32 $\pm$ 0.03	0.17 $\pm$ 0.01	0.34 $\pm$ 0.10
<b><math>\alpha</math>E-60</b>	2.4	-	> 300	> 300	> 300
<b><math>\alpha</math>E-65</b>	1.1	-	> 300	> 300	> 300
<b><math>\alpha</math>E-67</b>	1.7	-	> 300	> 300	> 300
<b><math>\alpha</math>E-C-Fab</b>	0.82	-	6.32 $\pm$ 5.71	> 300	> 300
<b><math>\alpha</math>E-C-IgG</b>	1.25	-	1.13 $\pm$ 0.59	> 300	> 300

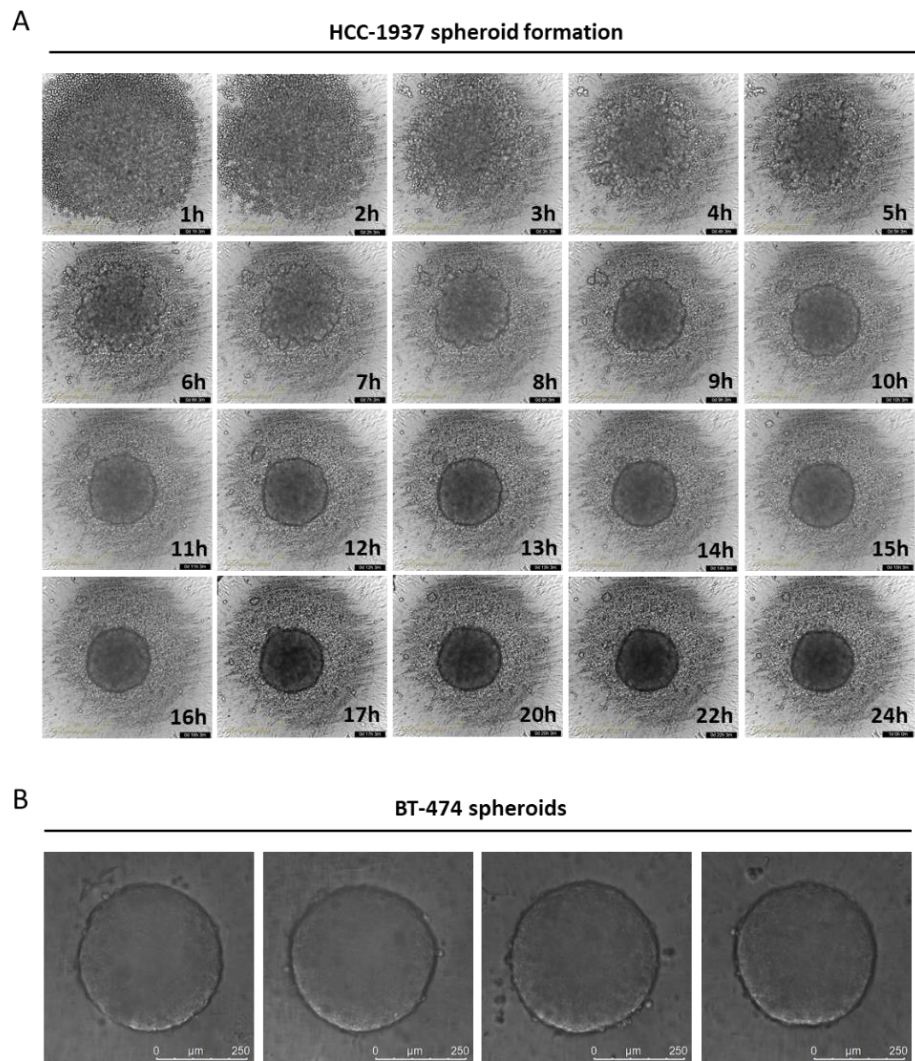


**Figure A19. Formation of tumor cell spheroids.** (A) Wide field images showing exemplarily tumor cell spheroid formation of 8000 HCC-1937 cells over 24 h at 37°C, 80% humidity and 5% CO<sub>2</sub>. Wide field images were taken with an IncuCyte® S3 live-cell analysis system (Sartorius). (B) Confocal microscopy images showing 4 different BT-474 cell spheroids with reproducible size (2,000 cells were grown for 96 h at 37°C, 80% humidity and 5% CO<sub>2</sub>). Confocal microscopy images were taken at 20-fold magnification with a confocal laser scanning microscope TCS SP8 (Leica).

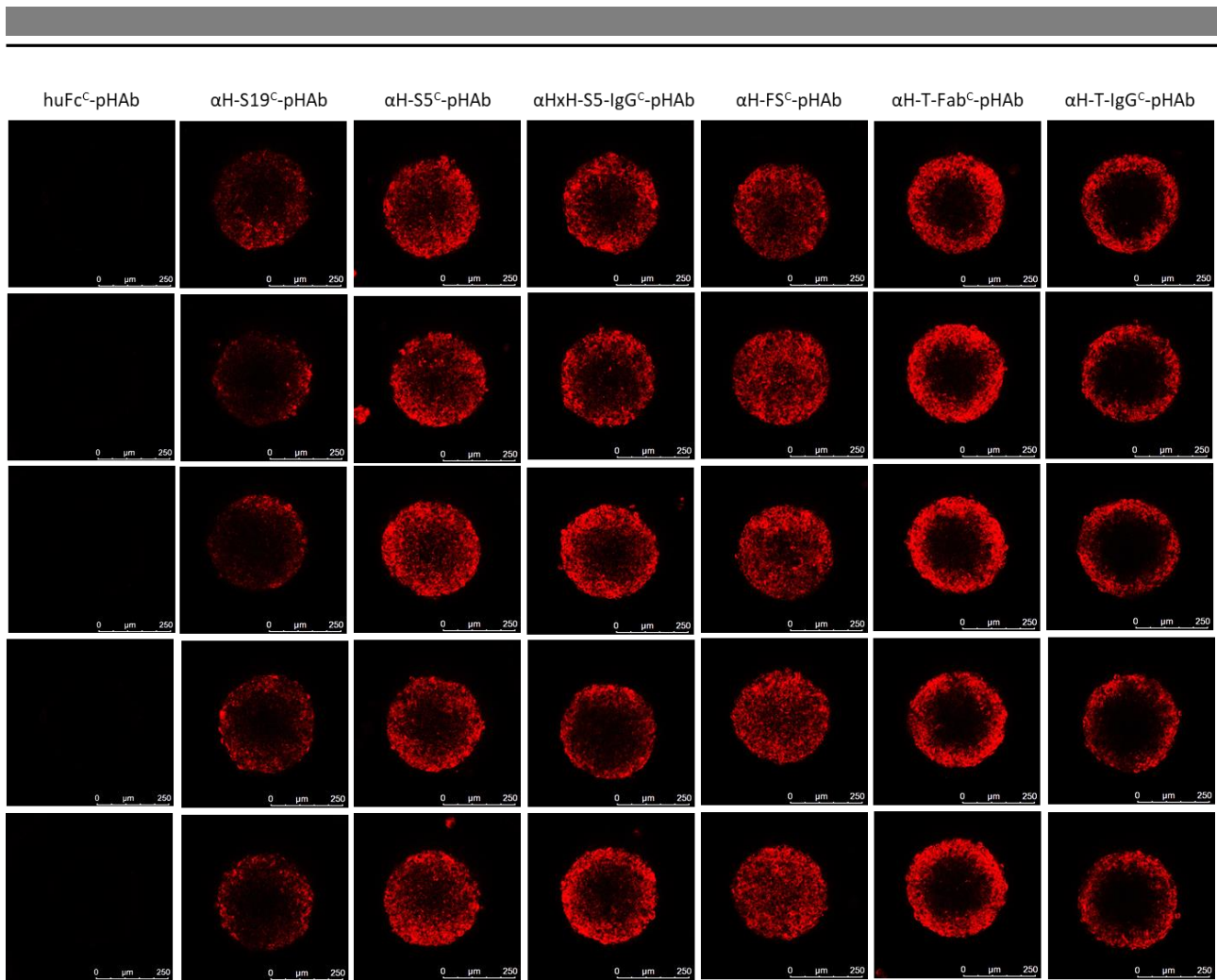


**Figure A20. Confocal microscopy of tumor spheroids treated with pHAb-dye labeled constructs.** BT-474 tumor cell spheroids (2,000 cells grown for 96 h at 37°C, 80% humidity and 5% CO<sub>2</sub>) were incubated with 50 nM pHAb-dye labeled constructs for 24 h. Images were taken with a confocal laser scanning microscope TCS SP8 (Leica, 20-fold magnification) at spheroid diameter 341 ± 3 μm and spheroid depth 62 ± 3 μm. For visual comparability the brightness of images was adjusted to compensate differences resulting from distinct pHAb-dye labeling degrees. For better visualization, the contrast of all images was increased by 40%. Radial profile plots and MPD were derived from unprocessed images.

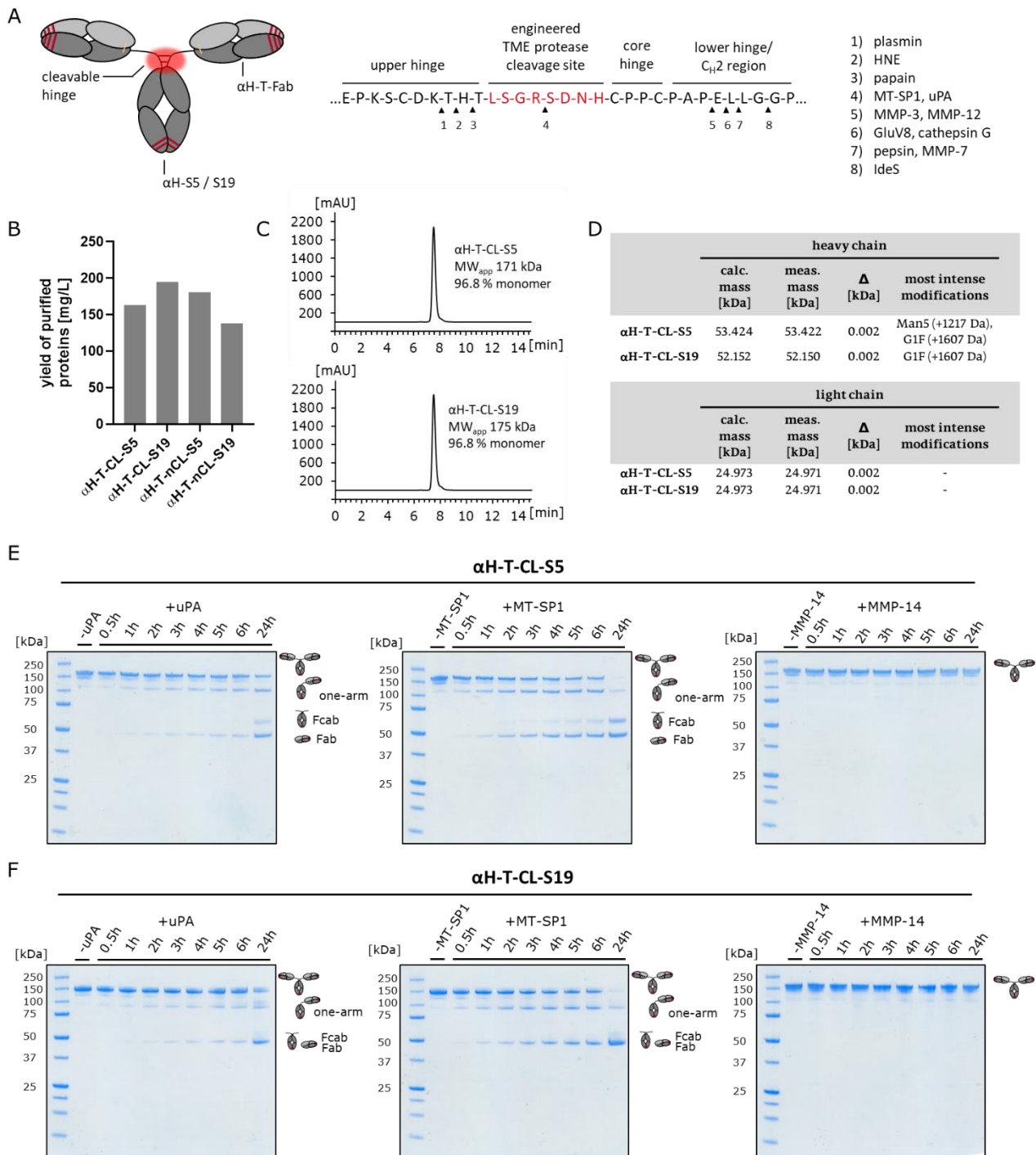


**Figure A21. HER2-targeting tetraivalent (Fab)<sub>2</sub>-Fcab fusions with engineered hinge cleavage site.** (A) Antibody design consisting of Trastuzumab Fab arms containing LC-C-terminal-(G<sub>4</sub>S)<sub>3</sub>-LPETGS SrtA conjugation tags, HER2-targeting Fcabs S5 ( $\alpha$ H-T-CL-S5) or S19 ( $\alpha$ H-T-CL-S19), and an engineered cleavage site in the hinge region (LSGRSDNH) that is recognized by TME extracellular proteases matriptase (MT-SP1) and urokinase-type plasminogen activator (uPA).<sup>286,300</sup> Other specific protease cleavage sites within IgG1 hinge region are depicted as well.<sup>301</sup> (B) Protein expression was not altered by the introduced cleavage site in  $\alpha$ H-T-CL-S5 and  $\alpha$ H-T-CL-S19. For comparison, constructs  $\alpha$ H-T-nCL-S5 and  $\alpha$ H-T-nCL-S19 lacking hinge modifications are shown. (C) SE-HPLC after freeze-thaw cycle confirmed high purity and absence of aggregates. (D) LC-MS confirmed protein identity. (E) SDS-PAGE analysis demonstrated specific cleavage of  $\alpha$ H-T-CL-S5 when incubated with uPA or MT-SP1. Digestion resulted in the formation of expected ~100 kDa (one-arm) and ~50 kDa (Fab, Fcab) protein bands. As already described, the Fcab S5 shows higher MW<sub>app</sub> (Figure A4). Digestion by non-related MMP-14 did not show any cleavage products. (F) SDS-PAGE analysis demonstrated specific cleavage of  $\alpha$ H-T-CL-S19 by uPA and MT-SP1. CL – cleavable by MT-SP1 and uPA; nCL – not cleavable by MT-SP1 and uPA.

---

## 11.1. Abbreviations

aa	Amino acid
Ab	Antibody
ABD	Albumin-binding domain
Abs.	Absorption
ADC	Antibody-drug conjugate
ADCC	Antibody-dependent cellular cytotoxicity
$\alpha$ E	Anti-EGFR
AF488	Alexa Fluor 488
$\alpha$ H	Anti-HER2
$\alpha$ HxH	Anti-HER2 and anti-HEL
ALCL	Anaplastic large-cell lymphoma
ALL	Acute lymphoblastic leukemia
AML	Acute myeloid leukemia
Amp	Ampicillin
ATCC	American Type Culture Collection
ATP	Adenosine triphosphate
BCMA	B-cell maturation antigen
BLI	Biolayer interferometry
BRCA1/2	Breast cancer susceptibility 1/2
BSA	Bovine serum albumin
bsAb	Bispecific antibody
CAF	Cancer-associated fibroblast
CDC	Complement dependent cytotoxicity
CDR	Complementarity determining region
C <sub>H</sub> 1, 2, 3	Constant domain 1, 2, 3 of the heavy chain
CL	Cleavable
C <sub>L</sub>	Constant domain of the light chain
CV	Column volume
<i>D</i>	Diffusion coefficient
$\Delta$	delta, difference
Da	Dalton
DAR	Drug-to-antibody ratio

---

DLS	Dynamic light scattering
DMEM medium	Dulbecco's modified eagle's medium
DNA	Deoxyribonucleic acid
DOL	Degree of labeling
DTT	Dithiothreitol
ECM	Extracellular matrix
<i>E. coli</i>	<i>Escherichia coli</i>
EGF(R)	Epidermal growth factor (receptor)
EGFR <sup>+/-</sup>	EGFR positive / negative
Em.	Emission
Exc.	Excitation
Fab	Fragment antigen binding
FBS	Fetal bovine serum
Fc	Fragment crystallizable
Fcab	Fc antigen binding
FcRn	Neonatal Fc receptor
FcγR	Fc gamma receptor
FDA	Food and Drug Administration
FT	After freeze-thaw
HC	Heavy chain
HER1, 2, 3, 4	Human epidermal growth factor receptor 1, 2, 3, 4
HER2 <sup>+/-</sup>	HER2 positive / negative
HI-HPLC	Analytical hydrophobic interaction chromatography
His-tag	Histidine tag, usually composed of six histidines
HL	Hodgkin lymphoma
HPLC	High performance liquid chromatography
hu	Human, <i>homo sapiens</i>
IC <sub>50</sub>	Half maximal inhibitory concentration
IFP	Interstitial fluid pressure
Ig	Immunoglobulin
IGN	Indolinobenzodiazepine
IMAC	Immobilized metal affinity chromatography
KB	Kinetics buffer

---

$K_D$	Equilibrium dissociation constant
kDa	Kilo dalton
$k_{off}$	Dissociation rate constant (off-rate)
$k_{on}$	Association rate constant (on-rate)
LB medium	Luria-Bertani medium
LC	Light chain
LC-MS	Liquid chromatography-mass spectrometry
mAb	Monoclonal antibody
MALDI-TOF	Matrix-assisted laser desorption/ionization time of flight mass spectrometry
MALS	Multiangle light scattering
MAPK	Mitogen-activated protein kinase
mc	Maleimidocaproyl
mCes1c	Murine carboxylesterase 1c
MEC	Molar extinction coefficient
MED	Minimal effective dose
MES	2-(N-morpholino)ethanesulfonic acid
MFI	Mean fluorescence intensity
MMAE	Monomethyl auristatin E
MMAF	Monomethyl auristatin F
MMP	Matrix metalloproteinase
MoA	Mode of action
MPD	Mean penetration distance
MS	Mass spectrometry
MTD	Maximum tolerated dose
mTG	Microbial transglutaminase
MT-SP1	Matriptase
mu	Murine, <i>mus musculus</i>
MW	Molecular weight
MW <sub>app</sub>	Apparent molecular weight
MWCO	Molecular weight cut-off
n.d.	Not determined
n.r.	Not reported
nCL	Noncleavable

---

NHS	<i>N</i> -hydroxy succinimide
NK cells	Natural killer cells
<i>P</i>	Permeability coefficient
pAb	polyclonal antibody
PABC	Para-aminobenzyloxycarbonyl
PAGE	Polyacrylamide gel electrophoresis
PBD	Pyrrrolobenzodiazepine
PBS	Phosphate buffered saline
PD-1	Programmed cell death protein 1
PD-L1	Programmed cell death protein ligand 1
PDB	Protein Data Bank
PDI	Polydispersity index
PDX	Patient derived xenograft
PEG	Polyethylene glycol
pI	Isoelectric point
PI3K	Phosphatidylinositol 3-kinase
<i>P. pastoris</i>	<i>Pichia pastoris</i>
R <sup>2</sup>	Coefficient of determination
<i>r<sub>H</sub></i>	Hydrodynamic radius
RP-HPLC	Analytical reversed phase chromatography
rpm	Revolutions per minute
RPMI medium	Roswell Park Memorial Institute medium
RRT	Relative retention time
RT	Room temperature
<i>S. aureus</i>	<i>Staphylococcus aureus</i>
scFv	Single-chain variable fragment
SD	Standard deviation
sdAb	Single-domain antibody
SDS	Sodium dodecylsulfate
SEC	Size exclusion chromatography
SE-HPLC	Analytical size exclusion chromatography
SMDC	Small molecule–drug conjugate
<i>S. mobaraensis</i>	<i>Streptomyces mobaraensis</i>

---

SrtA	Sortase A
$t_{1/2}$	Half-life
TCEP	Tris(2-carboxyethyl)phosphine
TGF- $\beta$	Transforming growth factor beta
TI	Therapeutic index
TIC	Total ion count
$T_m$	Melting temperature
TME	Tumor microenvironment
TNBC	Triple negative breast cancer
TNF- $\alpha$	Tumor necrosis factor alpha
$t_R$	Retention time
uPA	Urokinase-type plasminogen activator
v/v	Volume per volume
vc	Valine-citrulline
VEGF(R)	Vascular endothelial growth factor receptor
$V_H$	Variable domain of the heavy chain
$V_L$	Variable domain of the light chain
w/v	Weight per volume
wt	Wild type

---

## 11.2. List of Figures

Figure 1. Therapeutic index.....	14
Figure 2. Antibody structure. ....	16
Figure 3. IgG half-life extension by FcRn. ....	18
Figure 4. HER receptors, ligands and major downstream signal transduction pathways.....	19
Figure 5. Trafficking of HER receptors.....	20
Figure 6. Cetuximab and Trastuzumab mode of action.. ....	22
Figure 7. ADC structure and mode of action.....	23
Figure 8. ADC linker structures.....	25
Figure 9. Novel ADC payloads. ....	26
Figure 10. Solid tumor exposure and efficacy.....	29
Figure 11. Factors influencing antibody tumor penetration.....	30
Figure 12. IgG- and antibody fragment-based drug conjugates. ....	37
Figure 13. Small drug conjugates based on non-antibody alternative binding scaffolds. ....	38
Figure 14. Small format-based drug conjugates with half-life extending function.....	40
Figure 15. Fcab structure and binding.....	43
Figure 16. Amino acid sequence of human IgG1-Fc and HER2 targeting Fcabs H10-03-6, STAB19 and FS102. .....	44
Figure 17. Conceptual representation of potential advantages of Fcab-drug conjugates over other small antibody-fragment based drug conjugates and conventional IgG-based ADCs. ....	47
Figure 18. Exemplary pTT5 vector for mammalian expression.....	55
Figure 19. SE-HPLC analysis for the determination of pHAb-dye DOL, exemplarily shown for a pHAb-dye conjugated Fcab. ....	73
Figure 20. HER2 targeting Fcabs bind to different HER2 epitopes than Trastuzumab.. ....	81
Figure 21. Purified protein yields. ....	83
Figure 22. Cellular binding of Fcabs, huFc and references to several cancer cell lines. ....	87
Figure 23. Concentration-dependent cellular binding of Fcabs, huFc and references to several cancer cell lines. ....	88
Figure 24. pHAb-dye-labeling for antibody uptake studies. ....	89
Figure 25. Cellular uptake kinetics of pHAb-dye-labeled HER2-targeting constructs.....	92
Figure 26. Relative intracellular accumulation of pHAb-dye labeled constructs. ....	93
Figure 27. Fcab conjugation sites and linker-drug structures.....	96

---

Figure 28. Conjugation and purification strategy for Fcab-MMAE conjugates. ....	98
Figure 29. Conjugation site identification of $\alpha$ E-60-MMAE.....	99
Figure 30. Hydrophobicity of unconjugated parent molecules and drug conjugates.....	102
Figure 31. Target and FcRn dissociation constants. ....	104
Figure 32. <i>In vitro</i> serum stability exemplarily shown for STAB5-based Fcab-MMAE conjugates.....	106
Figure 33. <i>In vitro</i> cytotoxic activity of EGFR-targeting constructs. ....	108
Figure 34. <i>In vitro</i> cytotoxic activity of HER2-targeting constructs. ....	109
Figure 35. <i>In vitro</i> cytotoxic activity of HER2-targeting constructs and controls on HER2 positive cells. ....	110
Figure 36. $\alpha$ H-FS-MMAE induces lower reduction in cell viability compared to all other investigated MMAE conjugates.....	111
Figure 37. Spheroid forming cell line screening. ....	113
Figure 38. Quantification strategy for tumor cell spheroid penetration.....	114
Figure 39. 3D tumor spheroid penetration model. ....	115
Figure 40. Hypothetical tumor penetration scenarios derived from spheroid penetration experiments. ....	116
Figure 41. Proposed tetravalent (Fab) <sub>2</sub> -Fcab fusions with engineered hinge cleavage site. ....	121

---

### 11.3. List of Tables

Table 1. Main characteristics of approved ADCs.....	28
Table 2. Overview of published and characterized Fcab variants.....	45
Table 3. Mammalian cell lines used in this work.....	49
Table 4. Molar extinction coefficient at different wavelengths.....	74
Table 5. Literature known Fcabs and reference antibodies/ fragments selected for this study. ....	80
Table 6. Modified Fcabs and controls used in this study. ....	82
Table 7. Thermostability of Fcabs and huFc controls.....	85
Table 8. SE-HPLC-MALS-DLS characterization of EGFR-binding Fcabs, huFc and Cetuximab references. ....	85
Table 9. Fcab and reference cellular dissociation constants.....	89
Table 10. pHAb-dye labeled constructs generated for cellular uptake and spheroid penetration studies.....	90
Table 11. Generated drug conjugates. ....	97
Table 12. Hydrophobic interaction chromatography.....	101
Table 13. Target and FcRn binding affinity of unconjugated and conjugated Fcabs and references. ....	103
Table 14. Serum stability of Fcab and reference drug conjugates.....	105

---

## 11.4. Acknowledgements

Mein besonderer Dank gilt Prof. Dr. Harald Kolmar für die akademische Betreuung meiner Dissertation an der TU Darmstadt, seinem stetigen Interesse und Unterstützung meines Forschungsvorhabens, die konstruktiven Ratschläge und dem mir entgegengebrachten Vertrauen. Erwähnen möchte ich in diesem Zusammenhang auch unsere Arbeitsgruppen-Seminare und die Ausflüge ins Kleinwalsertal, welche den wissenschaftlichen Austausch, die Integration in die Arbeitsgruppe und die akademische Forschung nochmals in besonderer Weise gestärkt haben.

Prof. Dr. Dr. Siegfried Neumann danke ich für die bereitwillige Übernahme des Korreferats. Prof. Dr. Boris Schmidt und Prof. Dr. Dominik Niopek möchte ich für die Bereitschaft danken, sich als Fachprüfer bereitzustellen.

Insbesondere möchte ich mich ganz herzlich bei Dr. Christian Schröter für die wissenschaftliche Betreuung, die vielen wertvollen fachlichen und außerfachlichen Ratschläge, seine motivierende Art und die tolle Arbeitsatmosphäre in seinem Team bedanken. Außerdem möchte ich ihm dafür danken, dass er mich von Anfang an unterstützt hat, dieses und weitere Forschungsvorhaben in die Tat umzusetzen.

Gleichermaßen möchte ich mich bei Dr. Stefan Hecht und Dr. Jan Anderl dafür bedanken, dass sie mir die Möglichkeit gaben, mich in meinem Forschungsvorhaben in ihrer Abteilung frei entfalten zu können. Auch danke ich ihnen und Dr. Stephan Dickgiesser für das Ausrichten des Merck Biopharma Mini Symposiums, wodurch ich in Kontakt zu Prof. Dr. Florian Rüker kam. Ihm danke ich dafür, dass er mich auf die sehr spannenden Fcab Moleküle aufmerksam gemacht hat.

Ich möchte mich auch bei M.Sc. Tim Wagner für seine wertvolle Mitarbeit und Unterstützung bei der Charakterisierung der Fcabs bedanken, welche maßgeblich zum Erfolg dieser Arbeit beigetragen hat. Insbesondere unsere gemeinsamen Mittagspausen, welche oft die Forschung von Michael F. Holick zum Thema hatte, habe ich sehr geschätzt.

Dr. Janis Roßkopf möchte ich dafür danken, dass er mich bereitwillig als Verwalter aller Moleküle und Überbleibsel aus seiner Promotionszeit eingesetzt hat. Insbesondere die Cetuximab Konstrukte und Proteasen waren mir eine große Hilfe. Auch möchte ich ihm für seine inspirierende Forschung danken.

Des Weiteren möchte ich mich bei Dr. Nicolas Rasche und seinem Team für die Bereitstellung der MMAE-Konjugate bedanken. Hier gilt mein Dank insbesondere B.Sc. Laura Basset, welche unter großem Einsatz die Konjugation der Moleküle übernommen hat. Außerdem danke ich Dr. Stephan Dickgiesser für seine fachliche Unterstützung und das Interesse an meinem Forschungsvorhaben.

Selbstverständlich gilt mein großer Dank Stephan Keller und Alexander Müller aus dem Labor von Dirk Müller-Pompalla, welche mir jederzeit mit fachlichem Rat und großer Hilfsbereitschaft hinsichtlich der Proteinreinigung zur Seite standen. Die freundschaftliche Aufnahme auch abseits des Laboralltags war mir eine große Stütze.

Ihrem Auszubildenden Cristian Brunori danke ich für die Aufreinigung einiger Konstrukte dieser Arbeit.

---

Mein besonderer Dank gilt auch Deniz Demir, B.Sc. Iris Willenbücher, Ramona Gaa, Kerstin Hallstein und Dr. Simon Krah für die exzellente Schulung zu Hefezelldisplay und FACS Antikörper Screening im Rahmen meines ursprünglichen Promotionsprojektes. Auch danke ich ihnen für die offene Art und freundschaftliche Aufnahme ins Team sowie all die lustigen Unternehmungen außerhalb des Labors.

Des Weiteren danke ich dem gesamten Team des LC-MS Labors von Dr. Roland Kellner für die immer sehr zeitnahe Analytik. Hier möchte ich insbesondere Jennifer Schanz und M.Sc. Amanda Friedrich für die Übernahme der Messungen danken. Dr. Jason Tonillo und Jennifer Schanz danke ich außerdem für ihre Hilfe zur Identifizierung von „Mr. Q“.

Weiterer Dank gebührt außerdem B.Sc. Konstanze Waurisch und Kirstin Leidinger aus dem Labor von Dr. Birgit Piater für die fachliche und hilfsbereite Unterstützung zu den pHAb-dye basierten Internalisierungsexperimenten.

Überdies danke ich Dr. Sakshi Garg für die Einweisung und Nutzung des Konfokalmikroskops. Hier gilt der Dank insbesondere M.Sc. Jasmin Hunsrücker und Bianca Roth für die praktischen Tipps zum Arbeiten mit Spheroïden.

Mein besonderer Dank gilt Dr. Marcel Rieker für seine in jeglicher Hinsicht inspirierende und motivierende Art. Auch möchte ich ihm dafür danken, dass er mir während des schriftlichen Verfassens dieser Arbeit innerhalb unseres gemeinsamen Innospire Projektes stets den Rücken freigehalten hat.

Nicht zu vergessen ist natürlich auch der Rest unseres Innospire Teams um Dr. Doreen Könning, Dr. Christian Schröter, Dr. Nicolas Rasche und M.Sc. Michaela Fesenfeld, denen ich meinen Dank für den Support, die reibungslose Zusammenarbeit und die wertvollen Erfahrungen aussprechen möchte.

Allen meinen ehemaligen und aktuellen Doktoranden-Kollegen bei Merck, Dr. Tim Hofmann, M.Sc. Marie Quillmann, M.Sc. Anna Kaempffe, Dr. Marcel Rieker, Dr. Janis Roßkopf, Dr. Lukas Pekar, M.Sc. Tanja Lehmann, Dr. Martina Zimmermann, Dr. Markus Lubda, M.Sc. Sandra Müller, Dr. Gregory Som und M.Sc. Janina Klemm danke ich für die tolle gemeinsame Zeit, unsere erfrischenden Mittagessen, lustigen Kaffeepausen und die fortwährende Unterstützung während der langen Abende im Labor.

Meinen Freunden Hendrik, Lilith, Lorena und Tobias, sowie meinen Mitbewohnerfreunden Kira, Katha, Mitko und Alejandro danke ich dafür, dass sie mir in den letzten drei Jahren und darüber hinaus, immer unterstützend und rücksichtsvoll zur Seite standen.

Außerdem möchte ich meinen Eltern Andrea und Helmut sowie meiner Schwester Lena für ihre uneingeschränkte Unterstützung während meiner Promotion und meinem gesamten Studium danken. Vielen Dank für euer aller Verständnis während so manch stressiger Phasen.

Zu guter Letzt danke ich ganz besonders Marisol. Dafür, dass sie immer an mich geglaubt hat und mir den nötigen Rückhalt gab, um diese Arbeit anzufertigen.

Muchísimas gracias por todo tu apoyo y tu comprensión durante los últimos tres años. Este trabajo no hubiera sido posible sin ti.

---

---

## 12. Affirmations

---

### Erklärungen laut Promotionsordnung

#### §8 Abs. 1 lit. c PromO

Ich versichere hiermit, dass die elektronische Version meiner Dissertation mit der schriftlichen Version übereinstimmt und für die Durchführung des Promotionsverfahrens vorliegt.

#### §8 Abs. 1 lit. d PromO

Ich versichere hiermit, dass zu einem vorherigen Zeitpunkt noch keine Promotion versucht wurde und zu keinem früheren Zeitpunkt an einer in- oder ausländischen Hochschule eingereicht wurde. In diesem Fall sind nähere Angaben über Zeitpunkt, Hochschule, Dissertationsthema und Ergebnis dieses Versuchs mitzuteilen.

#### §9 Abs. 1 PromO

Ich versichere hiermit, dass die vorliegende Dissertation selbstständig und nur unter Verwendung der angegebenen Quellen verfasst wurde.

#### §9 Abs. 2 PromO

Die Arbeit hat bisher noch nicht zu Prüfungszwecken gedient.

Ort, Datum:

Darmstadt, 16. November 2021

Unterschrift:



---

Sebastian Michael Jäger